

# Naval Research Laboratory

Washington, DC 20375-5320

NRL/PU/6730-94-264

June 1994



# NIKE KrF Laser Facility

**NIKE KrF Laser Annual Report  
August 1993**

19950803 008

Approved for public release; distribution is unlimited.

## DISCLAIMER

This work was prepared as an account of work conducted by the Laser Plasma Branch, Plasma Physics Division, and the Laboratory for Computational Fluid Dynamics, both of the Naval Research Laboratory, and associated contractors, sponsored by the U.S. Department of Energy and the Office of Naval Research. Neither the above named sponsors, nor any of their employees, makes any warranty, expressed or implied, or assumes any legal liability or responsibility for the accuracy, completeness, or usefulness of any information, apparatus, product, or process disclosed, or represents that its use would not infringe privately owned rights. Reference herein to any specific commercial product, process, or service by trade name, mark, manufacturer, or otherwise, does not necessarily constitute or imply its endorsement, recommendation, or favoring by the United States Government of any agency thereof or any sponsor. Results reported in the Nike KrF Laser Annual Report should not be taken as necessarily final results as they represent active research. The views and opinions of the authors expressed herein do not necessarily state or reflect those of the above sponsoring entities.

For questions or comments, contact Jill Dahlburg, *Editor*, Laboratory for Computational Physics & Fluid Dynamics, Naval Research Laboratory, Washington, DC.

### TID Production Staff

Layout and Production	<i>Dora Wilbanks, Judy Kogok, Donna Gloystein, Marsha Bray, and Barbara Jolliffe</i>
Printing Assistance	<i>Kathy Parrish</i>

**ABOUT THE COVER:** The first goal of the Nike Laser program is the development of an ultra-uniform, flat-top laser focal profile, for application to direct-drive laser fusion. The laser-target program will then use Nike to evaluate methods of uniformly accelerating a foil that has the mass thickness of a high gain pellet. The top-hat profile on the cover of this report symbolizes the objectives of both the laser-development and the laser-target programs.

NRL



Accession For	
NTIS	CRA&I
DTIC	TAB
Unannounced	
Justification	
By _____	
Distribution / _____	
Availability Codes	
Dist	Avail and/or Special
A-1	

**NIKE KrF Laser Annual Report  
August 1993**

# **Table of Contents**

## CONTENTS

Section		Page
<b>EXECUTIVE SUMMARY</b>		
1	Nike Laser Facility, <i>S. Bodner</i> . . . . .	3
2	Nike Laser-Target Experiments, <i>S. Bodner</i> . . . . .	7
3	From Nike to a Laboratory Microfusion Facility, <i>S. Bodner</i> . . . . .	9
<b>HISTORY</b>		
4	Program History, <i>S. Bodner</i> . . . . .	15
5	The Idea of ISI, <i>R. Lehmberg</i> . . . . .	19
6	Filamentation in ICF Plasmas with Nonlocal Thermal Conductivity, <i>A. Schmitt</i> . . . . .	21
7	Suppression of Plasma Instabilities by ISI: Experiments, <i>A. Mostovych</i> . . . . .	33
8	Suppression of Parametric Instability by ISI: Theory, <i>P. Guzdar</i> . . . . .	47
<b>LASER DESIGN CONCEPT</b>		
9	Nike Optical Design, <i>R. Lehmberg</i> . . . . .	53
10	Nike Amplifier Staging, <i>S. Obenschain</i> . . . . .	57
11	Analysis of Nike Image Quality, <i>T. Lehecka</i> . . . . .	61
12	Scaling Laws for Nike Targets, <i>J. Gardner</i> . . . . .	65
<b>NIKE LASER FACILITY AND PROGRESS</b>		
13	Floor Plan and Introduction, <i>S. Obenschain</i> . . . . .	69
14	The Oscillator and Pulse Slicing System, <i>A. Deniz</i> . . . . .	71
15	Large-Aperture Discharge-Pumped Laser Amplifier, <i>M. Pronko</i> . . . . .	75
16	Amplifier Lasing Model, <i>M. McGeoch</i> . . . . .	89
17	20 cm Aperture Amplifier and Initial System Test, <i>C. Pawley</i> . . . . .	113
18	The 60 cm Amplifier, <i>J. Sethian</i> . . . . .	123
19	Propagation Bay, <i>T. Lehecka</i> . . . . .	131
20	Automatic Beam Positioning System, <i>J. Hardgrove</i> . . . . .	135
21	Nike Target Facility, <i>J. Stamper</i> . . . . .	139
22	Control System, <i>O. Barr</i> . . . . .	147
<b>PLANNED LASER-TARGET EXPERIMENTS</b>		
23	Planned Target Experiments and Diagnostics, <i>S. Obenschain</i> . . . . .	155
24	Nike Target Modeling, <i>J. Gardner</i> . . . . .	165
25	Targets for Nike, <i>J. Sethian</i> . . . . .	177
<b>TARGET PHYSICS MODELING</b>		
26	Edge Effects, <i>J. Dahlburg</i> . . . . .	183
27	STA Opacity Modeling, <i>M. Klapisch</i> . . . . .	189
28	Radiative Preheat in Strongly Coupled, Laser Accelerated Plasmas, <i>J. Giuliani</i> . . . . .	195
29	Start-up Imprinting and Shock Dynamics, <i>M. Emery</i> . . . . .	201
30	RAD3D_CM, <i>D. Fyfe</i> . . . . .	211
31	Three-Dimensional Multimode Results, <i>J. Dahlburg</i> . . . . .	215
<b>AUTHOR INDEX</b> . . . . .		
		225

# **Executive Summary**

- 3      **Nike Laser Facility**  
*Stephen E. Bodner*
- 7      **Nike Laser-Target Experiments**  
*Stephen E. Bodner*
- 9      **From Nike to a Laboratory Microfusion Facility**  
*Stephen E. Bodner*

## Section 1 NIKE LASER FACILITY

Stephen E. Bodner  
*Laser Plasma Branch  
Plasma Physics Division  
Naval Research Laboratory*

For the past four years, the Naval Research Laboratory has been developing a new krypton fluoride laser called Nike as our next step in the evaluation of direct-drive laser fusion. The fundamental near-term justification for KrF is its potential to produce a very smooth laser profile using the optical smoothing technique called ISI (induced spatial incoherence). For longer-term power plant applications, KrF also appears to be the most attractive laser option.

In general, any laser nonuniformity tends to degrade the performance of a high gain pellet design, because the laser nonuniformity seeds the Rayleigh-Taylor hydrodynamic instability. This instability can be ameliorated by preheating the fuel, but the preheat then reduces the thermonuclear yield. To obtain the highest possible yield, one generally wants the least possible laser nonuniformity.

The first phase of Nike is now operating, and its performance has exceeded our expectations. At the time of this report, August 1993, we had experimentally measured a 1.4% rms fluctuation in a 4 nsec pulse, along with a beam tilt of less than 2%. By the Spring of 1994, the rms nonuniformity had been reduced to 1.0% in one beam. This uniformity is the best in the world with short-wavelength lasers, and it justifies our shift to KrF technology. The results are also in near perfect agreement with our independent theoretical prediction. Figure 1.1 shows the August 1993 measurement and the theoretical prediction.

This uniformity was measured using just one of the Nike beams. Later in 1994 we plan

to overlap 44 beams in the full system. This overlap will produce an additional statistical averaging, because the various laser beams encounter different optical surfaces that introduce statistically independent phase distortions. For the completed Nike we expect the rms non-uniformity to drop to  $\sim 0.2\text{--}0.4\%$  in a 4 nsec pulse, and  $\sim 0.4\text{--}0.8\%$  in a 1 nsec pulse.

According to our hydrodynamic computer simulations, this laser nonuniformity is equivalent to an initial pellet surface finish of 100 Å in a transverse wavelength of 50 microns. Our hypothesis is that this level of laser non-uniformity is necessary to produce target gains of more than 100 with a few megajoule laser. The Nike laser-target experiments will be used to evaluate the sufficiency of this hypothesis, and to provide the target physics foundation for a high gain facility (LMF) of potential use for both military and civilian applications.

Figure 1.2 compares the uniformity of one beam of Nike, the projection for the complete Nike, and the estimated requirements for a high gain target. Figure 1.3 is an illustration of the basic ISI optical smoothing technique: an incoherent object is imaged through the laser onto the target without the need for a phase plate or echelon. Since the laser optics is placed near the Fourier transform plane of the object, there is minimal distortion at the image plane. (As an analogy, note that a fingerprint on a camera lens does not have a major effect on the clarity of the photo.)

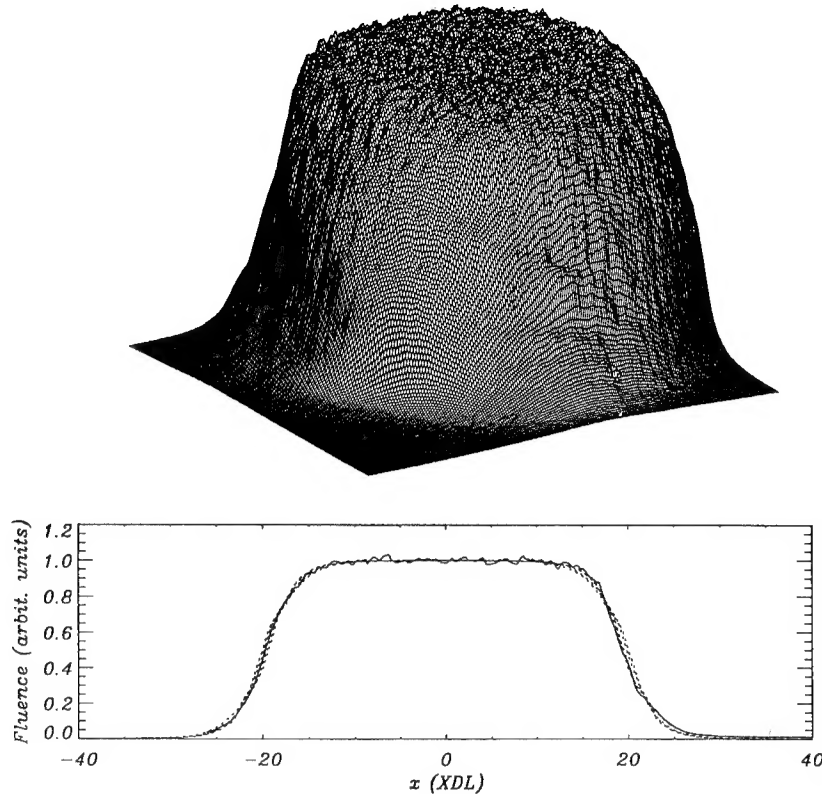


Fig. 1.1 — The measured laser beam profile in the far field after propagating through the 20 cm E-beam amplifier. This is one of 28 multiplexed laser beams. One lineout through this profile is plotted along with the independent theoretical prediction. The solid line is the theory, the dashed line the data.

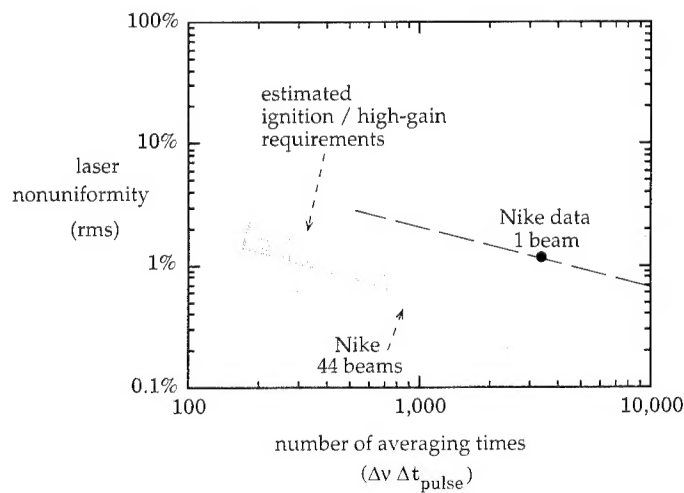


Fig. 1.2 — The rms laser nonuniformity in the far field for 1 of the 26 beams in the current Nike, plus the projection for a 44 beam overlap with the completed Nike, and the estimated requirements for a high gain pellet. The current and projected data fit a  $\sqrt{t}$  slope because of the statistical averaging of incoherent beams. The pellet gains should be higher with lower laser nonuniformity.

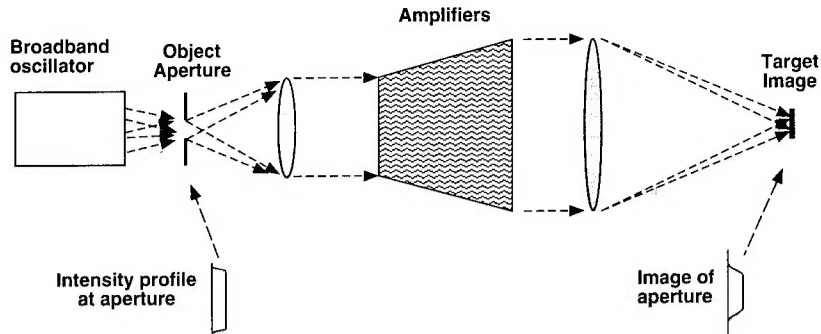


Fig. 1.3 — The ISI concept relays a relatively incoherent object through the laser onto the image. If the laser amplifiers are approximately in the Fourier transform plane of the object, then the amplifier gain and phase distortions will not have a large effect on the shape of the image profile.

The Nike laser chain is schematically shown in Fig. 1.4. It consists of an oscillator, object aperture, several discharge amplifiers, two E-beam amplifiers, and a set of multiplexing and demultiplexing optics. The system has been operating since June 1993 through the first E-beam amplifier with 28 beams. The uniform beam profile shown in Fig. 1.1 was measured in July 1993 using one of those beams.

The Nike laser has been designed to produce at least 3000 Joules on target, of which 2200 Joules in 44 beams are used for target

acceleration experiments, and 800 Joules in 12 beams are used for an x-ray backlighter diagnostic. The pulse duration of the main beams is 4 nsec at high power, plus a typically 6 nsec exponentially rising foot in front of the pulse. Reliability of KrF lasers had been a concern in earlier systems, but current KrF systems in Britain and Japan can now fire hundreds of shots between routine maintenance, and our experience with Nike through the 20 cm amplifier leads us to expect a similar robustness.

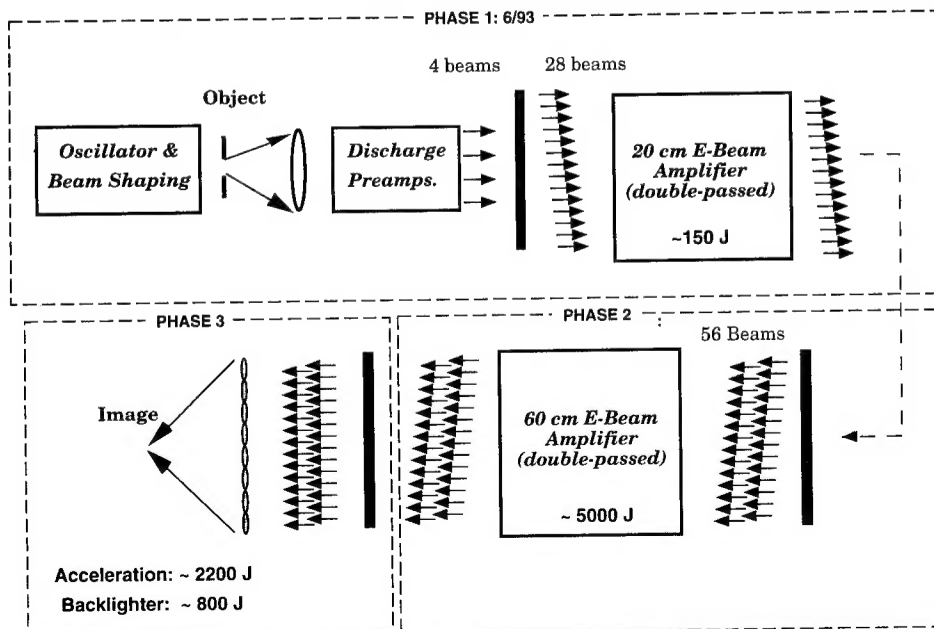


Fig. 1.4 — The Nike laser is being completed and tested in phases. The system is fully operational through the 20 cm E-beam amplifier, and should be completed through the target area in 1994.

## Section 2

### NIKE LASER-TARGET EXPERIMENTS

Stephen E. Bodner  
*Laser Plasma Branch*  
*Plasma Physics Division*  
*Naval Research Laboratory*

There are two ways of scaling down from a high gain pellet to near term experiments with less laser energy. One can maintain the spherically converging geometry and just reduce the pellet size and the laser pulse duration by the same ratio. Or, one can accelerate a planar foil with a pulse duration and target thickness that are similar to a high gain target, but without the spherical effects. Each approach has its advantages and limitations. Both geometries are a necessary component of any near-term evaluation of laser fusion.

The Nike facility is designed to accelerate planar targets. Some of the basic parameters are indicated in Fig. 2.1. It is perhaps worthwhile to review the advantages and limitations of flat foil experiments:

- Since the most dangerous Rayleigh-Taylor perturbations have wavelengths that are comparable to the pellet shell thickness, which is much less than the pellet radius, the spherical effects are not dominant for these perturbations.
- Radiation is one of the major methods under consideration to control hydrodynamic instabilities. The absorption distance for radiation cannot be scaled correctly with the laser's pulse duration. With planar targets one can use roughly the same target thickness as in a high gain pellet, and therefore one can better evaluate radiation effects.
- The surface finish on the pellet does not scale with pellet size. With planar foils one can easily scale and control the surface finish.

~ 2200 Joules in 44 beam overlap  
top-hat spatial profile  
~ 600  $\mu\text{m}$  spot size  
~ 6 nsec exponentially rising foot,  
plus a 4 nsec high power pulse

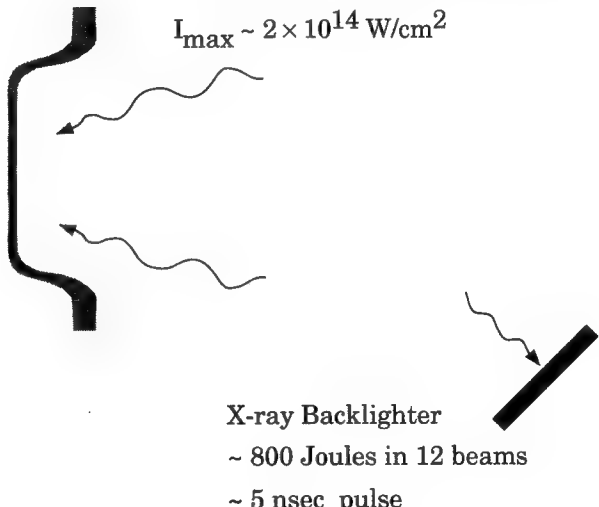


Fig. 2.1 — The Nike laser will be used to accelerate flat foils. Some of the laser conditions are listed here.

- The coherence time of the laser cannot be decreased in proportion to the duration of the pellet implosion. Temporal averaging and beam smoothing are therefore more easily evaluated in planar geometry.
- Many diagnostics are more successful in planar geometry. For example, the rear inner surface temperature and the time-dependent mass variations of the foil are more easily accessed. Because of this, flat foils have become the standard tool for

evaluating short-wavelength Rayleigh-Taylor growth.

The disadvantages of planar targets are:

- Longer wavelength perturbations cannot be evaluated because of the lack of spherical convergence.
- Edge effects limit the distance that the target can be accelerated. With two kilojoules, one can only investigate the early portion of the acceleration of a high gain target, with therefore less e-folds of growth than in a spherical target. Planar targets should however suffice if there are at least 3-4 e-folds of the instability. If one understands the early stages of the growth of the instability, then one can probably extrapolate for the remaining e-folds.
- One cannot directly evaluate how the kinetic energy of a pellet shell couples its energy into the hot ignitor region.
- One cannot evaluate the physics of the deceleration of the pellet shell.

The Nike laser will be used primarily to evaluate the ablative Rayleigh-Taylor instability. The most dangerous perturbation wavelengths of interest are believed to be comparable to the shell thickness, and much less than the pellet radius. We estimate that we can accelerate a planar foil a distance of almost 300 microns before edge effects dominate. For a 50 micron perturbation, this would provide about 8 e-foldings of classical growth. This is more than enough growth experimentally to evaluate various stabilization techniques, and to project the net growth for an imploding high gain pellet.

For a successful implosion, the amplitude of the Rayleigh-Taylor perturbation  $A(t)$  must be significantly less than the pellet shell thickness  $\Delta R(t)$ . In a simplified form, assuming just one perturbation mode, this can be written:

$$A(t) = A_0 e^{\gamma t} \leq \frac{1}{2} \Delta R(t).$$

The Nike laser optical smoothing system has been designed to minimize the effective  $A_0$ . The Nike laser-target experiments will then investi-

gate ways of minimizing the growth rate  $\gamma$ , under conditions relevant to a high gain target. One known way of reducing  $\gamma$  is to preheat the fuel. Preheating increases the velocity of the plasma through the ablation surface; this convectively stabilizes the Rayleigh-Taylor growth. Of course preheating the fuel also reduces the thermonuclear yield of the pellet, which is why we want to minimize  $A_0$ .

One of the first successful measurements of the Rayleigh-Taylor growth rate was performed at NRL in the mid 1980s using one micron light with ISI optical smoothing. Since then, there have been a variety of direct-drive Rayleigh-Taylor experiments at several labs, using optically-smoothed half-micron laser light, with laser nonuniformities in the range of 4-12% rms. These experiments provided very useful data to compare with theory and codes, but those laser nonuniformities have prevented the use of pulse shaping, and have prevented the use of third-micron light. With a shorter laser wavelength, or with pulse shaping, the 4-12% rms laser nonuniformities would have destroyed the target. Thus until now short wavelength experiments have been limited to high-isentrope, shock-like accelerations, without pulse shaping.

With its improved beam uniformity Nike will, for the first time in the laser fusion program, be able directly to accelerate a target on the low isentropes necessary for laser fusion. Hydrodynamic calculations at NRL predict that the Nike beam, with pulse shaping and with a quarter-micron laser wavelength, will be able successfully to accelerate a cold foil target without destroying it. The top-hat laser focal profile will also be flatter than in previous experiments. Parameter studies will include various dopants in the foil for radiation preheat control, various target materials and layerings for hydrodynamic shock studies, and various laser pulse shapes. Eventually we plan to use cryogenic targets, with a  $D_2$  payload and a plastic ablator, so that we can also evaluate the classical Rayleigh-Taylor interface instability at the  $CH/D_2$  interface. This is necessary, since some target designs transfer the Rayleigh-Taylor problem from the ablator itself to the ablator/fuel interface.

### Section 3

## FROM NIKE TO A LABORATORY MICROFUSION FACILITY

Stephen E. Bodner  
*Laser Plasma Branch  
Plasma Physics Division  
Naval Research Laboratory*

There are three major potential applications of laser fusion: weapons effects simulation, weapons physics research, and electrical energy production. Although each of these applications is very valuable, there are of course limits to what it can justifiably cost. Let us consider each of the applications in turn.

If a direct-drive pellet were to achieve a yield of  $\sim 200$  MJ, then a few percent of this yield will be in a broad spectrum of x-rays. The conversion is small, but the useful x-rays would nonetheless provide an enhancement over any existing or planned nuclear weapons simulator, with the limitations of a short pulse duration of the x-rays and an inevitably accompanying neutron pulse. We also must keep in mind the performance and cost limitations: (1) The pellet must produce a yield of  $\sim 200$  MJ, not  $\sim 20$  MJ to justify a change from conventional pulsed power technology. (2) Both the construction and the operating costs of the facility must be moderate, or it would probably not be attractive solely for weapons effects studies.

If a direct-drive pellet could achieve a yield of 200-1000 MJ, then it would also be of use in the study of various fundamental physics associated with nuclear weapons design, helping to maintain basic scientific competence with a nuclear test ban. It is now generally agreed that there is not any significant advantage of indirect drive targets over direct drive targets for this application. The proper question is, which concept really works?

If a direct-drive pellet could achieve a gain of  $\sim 100$  with modest laser energy, then the overall system is potentially useful as a reactor for a power plant. A team of engineers and scientists recently developed a 1000 MWe fusion power plant design they called "Sombremo" using a KrF laser with a direct drive pellet.<sup>1</sup> In their baseline design, the pellet gain was 118, the laser energy 3.4 MJ, and the pellet yield 400 MJ. The estimated cost of electricity was 6-8 cents/kWh, which is comparable to an advanced tokamak design and to future coal plants. (Note that the product of laser efficiency times pellet gain was only 8, which is less than the old rule of thumb of 10, yet the system was still attractive.)

For all three applications, we will have to meet a similar requirement: high gain at a few megajoules, with a modest capital cost. To achieve just ignition should be viewed as an intermediate step. Our long term goal of ICF is the achievement of at least gain 100, with a laser energy of no more than about 2 MJ. A direct drive target with an ultra smooth KrF laser has the potential of obtaining gains of more than 100 and yields of more than 200 MJ, thereby meeting all three of the long term goals of laser fusion. In the nearer term, our ICF concept will have to demonstrate success in several physics and engineering areas, as illustrated in Fig. 3.1 and in Table 3.1.

<sup>1</sup>Article in *Fusion Technology*, May 1992.

Table 3.1 — Necessary Components to Prepare for a KrF Laboratory Microfusion Facility

Foil Acceleration Experiments	Nike will evaluate the methods of limiting the ablative Rayleigh-Taylor instability, scaled to a high gain pellet.
Spherical Implosion Experiments	Glass lasers at Omega Upgrade (U. Rochester) and Gekko XII (Osaka U.) are best suited to evaluate the lower-mode perturbations ( $\ell \leq 40$ ) where spherical effects are most important.
High Gain Target Design	Some high gain target designs have been proposed. Further, detailed, robust, high-gain point designs will be needed that are consistent with the above laser-target experiments and with the available laser beam quality. Calculations of high gain targets are in progress at several ICF laboratories, including NRL.
Cryogenic Target Fabrication	Significant progress has been made in the development of uniform cryogenic targets, but success has not yet been achieved. An aggressive research and development effort is currently underway at several laboratories.
Megajoule Laser System Design	A new detailed optical design for a megajoule KrF laser system is required, to estimate total cost and to provide guidance for near-term laser research. These design studies are in progress at several laboratories, including NRL.
KrF Beamline Development	The Nike laser is too small to serve as a prototype for a megajoule system. The building block for a megajoule system would be an amplifier with laser energy in the range of 30-100 kJ. To minimize the cost and performance risk of a megajoule system, a single large amplifier module should be designed, built, and evaluated. No such effort is yet underway. We estimate that the development cost would be a small fraction of the existing ICF program, and it could be constructed in a few years.
Efficient, High Rep-Rate Amplifier	Although KrF lasers are probably the ideal system for an inertial fusion reactor, there has not yet been a demonstration of an E-beam KrF amplifier with 5-7% efficiency, 5-10 hertz rep rate, and long life time. The current KrF programs use single-pulse lasers, with an optimization for reliable operation, not efficiency or cost. The development of an efficient, reliable, 500-1000 J/pulse amplifier would provide an important verisimilitude for the ICF program. The laser might also have significant commercial spin-off applications, depending upon its eventual cost and reliability. No such effort is yet underway. The development cost for this amplifier would also be a small fraction of the existing ICF program.

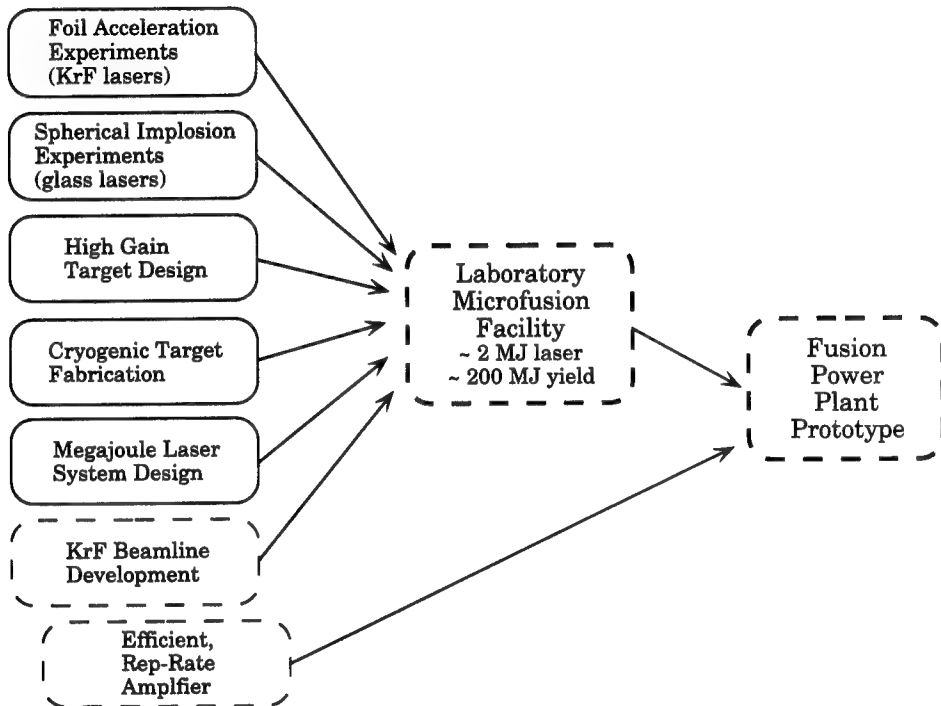


Fig. 3.1 — The necessary components of a KrF program to prepare for a Laboratory Microfusion Facility and a Prototype Fusion Power Plant. The items in the dashed lines are not in the existing ICF program.

# History

15      **Program History**  
            *Stephen E. Bodner*

19      **The Idea of ISI**  
            *R. H. Lehmberg*

21      **Filamentation in ICF Plasmas With Nonlocal  
            Thermal Conductivity**  
            *Andrew J. Schmitt*

33      **Suppression of Plasma Instabilities by ISI: Experiments**  
            *Andrew Mostovych*

47      **Suppression of Parametric Instability by ISI: Theory**  
            *P. N. Guzdar*

## Section 4

### PROGRAM HISTORY

Stephen E. Bodner  
*Laser Plasma Branch*  
*Plasma Physics Division*  
*Naval Research Laboratory*

The direct-drive approach to laser fusion is inherently attractive for two fundamental reasons:

1. **Simplicity.** Because the laser beams shine directly upon the pellet, without the complication of a hohlraum, the target geometry is, to lowest order, spherically symmetric. Simpler systems have fewer modes of failure.
2. **Efficiency.** Because the laser beams shine directly upon the pellet, the overall coupling efficiency of laser energy to imploding fuel can be 3-5 times higher than for a hohlraum geometry. For a given yield from the pellet, the laser energy and cost can be 3-5 times less, and the pellet gain 3-5 times higher. Because of the high cost and low efficiency of all laser systems, this improved efficiency can be critical to the viability of laser fusion.

Along with these inherent advantages there have been some inherent difficulties that have had to be surmounted. Because the laser light shines directly upon the pellet, the implosion is very sensitive to laser nonuniformities. In the 1970s, before the development of optical smoothing techniques, the direct-drive concept used thermal transport in the corona of the pellet to smooth out the laser nonuniformities. If we define  $\delta r$  to be the distance between the laser absorption radius and the ablation radius, and  $\lambda$  to be the wavelength of the transverse per-

turbation around the pellet, then laser nonuniformities would be thermally smoothed if  $\delta r > \lambda$ . The distance  $\delta r$  is a function of the laser wavelength, and is only sufficiently large when the laser wavelength is in the infrared, near 1  $\mu\text{m}$ . NRL scientists published detailed articles that developed scaling laws for  $\delta r$  under various conditions, and utilized the Pharos III glass laser to test and verify those scaling laws. We confirmed the smoothing of laser beams that could be obtained with infrared laser light.

By the late 1970s however, it became clear from research at other labs that a short laser wavelength laser would be required to control the various laser-plasma instabilities (decay, two-plasmon, Raman, and Brillouin). See Fig. 4.1, which indicates the threshold for one particular instability, the backward convective Stimulated Raman Scatter. For infrared laser light, the threshold for significant backscatter was rather low:  $\sim 10^{14} \text{ W/cm}^2$ . The same graph shows the laser intensity required to produce 50 Mbar of ablation pressure—a typical value for an ICF target with a moderately-thick value for the aspect ratio  $\Delta R/R$  of a pellet shell.

The inherent conflict between the need for both short and long laser wavelengths was resolved by the inventions of optical smoothing. The inventions were based upon the observation that a laser beam can focus to a spot size that is much smaller than a high gain pellet. Typically, a laser can focus to tens of microns, while a high gain pellet has a radius of a few thousand microns. The trick then was to trade off the ability to focus a laser beam for an improved laser beam quality.

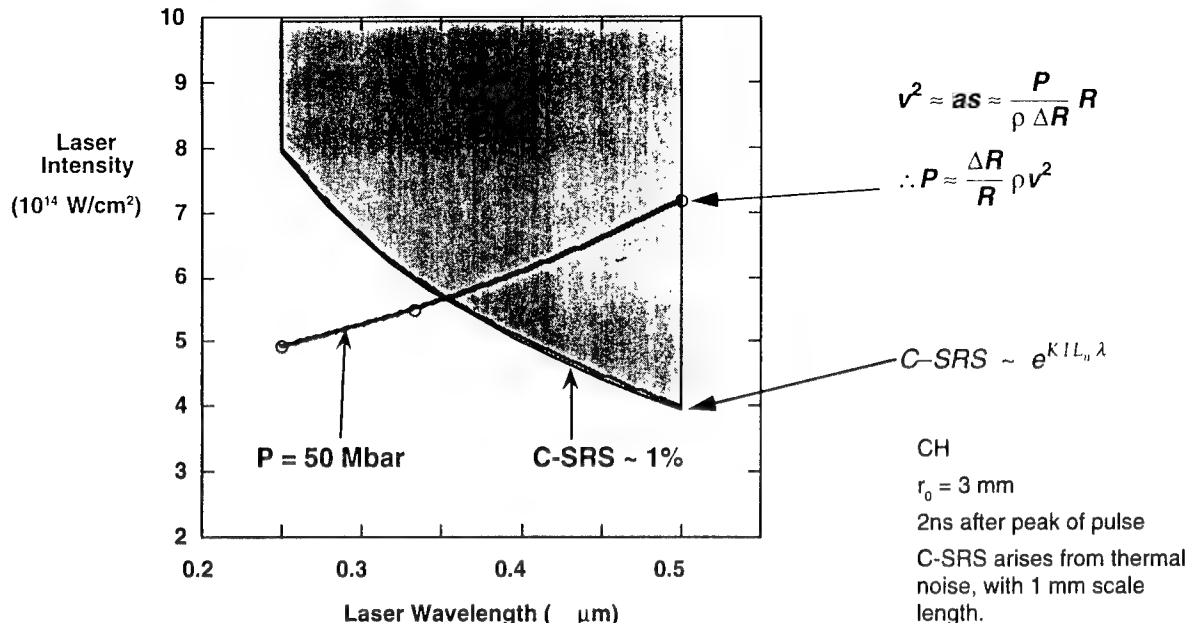


Fig. 4.1 — Controlling the various plasma instabilities requires a short wavelength laser such as KrF. Producing sufficient ablation pressure to implode the pellet requires a minimum laser intensity. Both of these constraints can be satisfied with a KrF laser.

The two inventions in 1982 were ISI, developed at NRL, and RPP (Random Phase Plate), developed at Osaka. Both techniques were attempts to produce a smoother ablation profile on the target, but with a difference: the RPP technique produced a *stationary* speckle pattern in the target plane, while the ISI technique produced a statistically *time-varying* pattern that smoothed with time. Since the hydrodynamic response time of the pellet was much longer than the laser's coherence time, we expected that the time variations would average out, effectively leaving only the time-averaged smooth pattern.

The next major question to be addressed was the impact of optical smoothing upon the various laser-plasma instabilities. In a series of laser-target experiments through the mid-1980s, NRL evaluated the effect of ISI. To our delight, we found that ISI with a short laser wavelength produced orders of magnitude reduction in the various laser-plasma instabilities. As an example, Fig. 4.2 shows the effect of ISI on the convective Raman instability. In parallel experiments using RPP, at Osaka and elsewhere, no significant reduction was found in the various

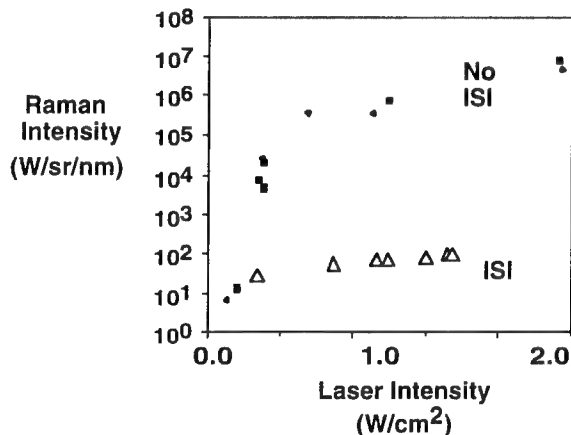


Fig. 4.2 — Induced Spatial Incoherence (ISI) reduced the convective Stimulated Raman Scatter by orders of magnitude, because ISI controlled the filamentation mode. Similar effects were seen with the other laser-plasma instabilities.

laser-plasma instabilities, except for a small effect when one used very fast focusing optics (of no long term relevance to ICF).

The favorable results with ISI were partially explained at NRL in terms of the filamentation instability. Using both two- and three-dimensional laser propagation codes, we showed that

ordinary laser beams with hot spots were self-focusing in the plasma, and increasing the laser intensity by orders of magnitude. With ISI, the laser hot spots moved about too rapidly for significant self-focusing. With RPP, the residual speckle was stationary in time, and self focused, unless the filament length was very short due to the use of fast focusing optics. (Temporal averaging was then incorporated into various other optical smoothing schemes, especially SSD developed at the U. of Rochester.)

With the favorable results of ISI, the direct drive program could now shift to a short laser wavelength, reaping the advantages in laser-plasma instability control and higher coupling efficiency, without inducing a fundamental problem in symmetry. There were however some basic limitations to the original ISI concept. Although it worked well at  $1\omega$  (infrared) and  $2\omega$  (green), the frequency conversion to the third harmonic was lower. In addition, the technique required aligning a large number of echelons (optical mirrors). In a small laser such as Pharos III that was not a problem. However when we extrapolated to a high-gain target, the number of mirrors rose into the hundreds of

thousands. This seemed inconsistent with the basic appeal of direct drive—its simplicity.

In 1987 NRL invented and proposed a new optical smoothing scheme, called echelon-free ISI. In this approach the echelons at the end of the laser were replaced by an optical smoothing mechanism at the laser oscillator. The smooth beam was then optically relayed through the laser chain. Detailed theoretical analysis indicated that the Object could be imaged onto the Target if nonlinear optical effects could be minimized. With a gas laser such as KrF instead of glass, the lasing medium would not produce significant nonlinear effects. Using optical multiplexing with mirrors, we would not be dominated by chromatic aberration or nonlinear self-focusing. With its inherently broad bandwidth, KrF also seemed to be ideally matched to the needs of optical smoothing. With its very short wavelength,  $1/4 \mu\text{m}$ , the laser light would couple efficiently to the pellet with minimal risk of plasma instabilities. For all of these reasons, NRL shifted its program from a frequency-converted glass laser (Pharos III) to a KrF laser (Nike).

---

## Section 5 THE IDEA OF ISI

R.H. Lehmberg  
*Laser Plasma Branch  
Plasma Physics Division  
Naval Research Laboratory*

One requirement for high-gain direct-drive laser fusion is uniform illumination of the spherical fuel pellet. Calculations indicate that high pellet gain requires peak-valley ablation pressure nonuniformities to be limited to less than 2%.<sup>5.1</sup> This requirement becomes especially challenging for shorter wavelength lasers, which couple more efficiently to the target, but allow less thermal smoothing of the ablation pressure. For direct-drive, it requires a laser whose focal spot profile is highly smooth and controllable.

To produce such a beam, Nike is implementing a modified version<sup>5.2</sup> of the induced spatial incoherence (ISI) technique<sup>5.3</sup> (Fig. 1.3). An object aperture is uniformly illuminated by broad bandwidth  $\Delta\nu \sim 1$  THz, spatially incoherent light. This aperture is imaged onto the target by relaying its optical Fourier transform plane (pupil plane) through the laser system. The time-averaged focal profile at the target is therefore controlled directly by adjusting the object aperture; for example, it can be shaped to a non-flat profile by using a *soft* aperture. Light from each point in the object aperture illuminates the Fourier plane with a different ray angle, but the same time-averaged intensity distribution. If each amplifier stage is located at or near an image of the Fourier plane, the image of the object formed at the target will be insensitive to the amplifier gain nonuniformities.<sup>5.4</sup>

The time-averaged focal profile will remain relatively insensitive to large scale phase non-uniformities imposed by the laser system if its angular width is many times diffraction-limited (XDL), and large compared to the angular perturbations introduced by the phase aberration. The Nike optical design, which is described in

Section 9, allows nearly complete compensation of all systematic phase aberrations, such as astigmatism, coma, and spherical aberration. Distortion due to *random* phase aberration (e.g., arising from optical surface imperfections) is examined in detail in Reference 5.4. For the 30-100 XDL flat-top profiles to be used in Nike planar target experiments, the main effect of random phase aberration is to round-off the edges of the profile. Distortion of non-flat profiles can be pre-compensated at the object aperture as long as the angular perturbations remain relatively small and reproducible.

The *instantaneous* focal spot intensity produced by incoherent beam smoothing schemes such as ISI is highly nonuniform speckle. It approaches a smooth profile only when averaged over time intervals  $t_{av}$  much larger than the laser coherence time  $t_c \approx 1/\Delta\nu$ . Under this condition, the standard deviation of the residual speckle nonuniformity is well approximated by the expression<sup>5.3</sup>  $\sigma \approx (t_c/t_{av})^{1/2}$ . For fusion applications,  $t_c$  must be much shorter than the time required for the target to react hydrodynamically to the speckle. Calculations indicate that  $t_c \sim 1$  psec is short enough to provide the required ablation pressure uniformity once the steady-state blowoff plasma is formed; however, shorter coherence times are desirable to reduce imprinting of the laser nonuniformities onto the target *before* this plasma is fully developed.<sup>5.5</sup> KrF amplifiers have sufficient  $\Delta\nu$  to achieve  $t_c < 0.3$  psec,<sup>5.6</sup> but the optical system must be capable of transporting such bandwidths without distorting the focal profile. The Nike optical system is designed to accommodate  $\Delta\nu$  up to 5 THz ( $t_c = 0.2$  psec) with negligible chromatic

aberration. It achieves this by using mostly reflective optics at the larger apertures, and by using large F-number lenses and chromatic correction in the front end optics.

## REFERENCES

- 5.1. S.E. Bodner, J. Fusion Energy **1**, 221 (1981)
- 5.2. R.H. Lehmberg, and J. Goldhar, Fusion Technology **11**, 532 (1987)
- 5.3. R.H. Lehmberg and S.P. Obenschain, Opt. Commun. **46**, 27 (1983); R.H. Lehmberg, A.J. Schmitt and S.E. Bodner, J. Appl. Phys. **62**, 2680 (1987)
- 5.4. R.H. Lehmberg, S.P. Obenschain, C.J. Pawley, M.S. Pronko, A.V. Deniz, and T. Lehecka, *Laser Coherence Control: Technology and Applications*. Proc. SPIE **1870**, 163 (1993), Edited by H.T. Powell and T.J. Kessler
- 5.5. M.H. Emery, J.H. Gardner, R.H. Lehmberg, and S.P. Obenschain, Phys. Fluids B **3**, 2640 (1991)
- 5.6. R.C. Sze, S.J. Thomas, N.A. Kurnit, and C.W. Patterson, *1990 Conference on Lasers and Electro-Optics*, OSA Technical Digest Series, Vol. 7, paper CWF46 (Optical Society of America, Wash. DC, 1990)

## Section 6

### FILAMENTATION IN ICF PLASMAS WITH NONLOCAL THERMAL CONDUCTIVITY

Andrew J. Schmitt  
*Laser Plasma Branch  
Plasma Physics Division  
Naval Research Laboratory*

#### I. INTRODUCTION

The filamentation instability is caused by localized "hot spots" of laser light intensity that create density channels in a plasma. The local index of refraction is greater in these channels, which causes the hot spots to focus and enhances the filamentation effect. This phenomenon is particularly important in inertial confinement fusion [ICF] plasmas because the typical ICF laser has hot spots that are many times the average laser intensity. The ponderomotive force and thermal gradients driven by inverse-bremsstrahlung heating are the common causes of filamentation in ICF plasmas.

In previous work modeling three-dimensional [3d] laser-plasma filamentation,<sup>6.1,6.2</sup> we attempted to assess the relative importance of ponderomotive and thermal filamentation in laboratory and reactor-scale ICF plasmas. We concluded that ponderomotive was not dominant in the short-wavelength collisional plasmas favored in ICF, and that thermal filamentation, while a possible problem in large reactor-scale plasmas, could be controlled with optical smoothing techniques such as induced-spatial-incoherence (ISI). ISI suppresses filamentation by randomly moving the position of the laser hot spots on the timescale of the laser coherence time. If the coherence time is small compared to the plasma response time, the plasma will respond to a time-average of the laser intensity, which can be quite smooth.

Since the previous work was completed, analyses of energy flow in plasmas using

Fokker-Planck codes<sup>6.3,6.4</sup> have shown that heat transport can be nonlocal in the underdense corona of ICF targets under conditions where filamentation is important. We have updated the 3d laser-plasma propagation code by including a generic non-local heat transport model. This model predicts reduction of electron thermal conductivity and an associated enhancement in thermal filamentation. Applying the model to short-wavelength reactor-scale ICF plasmas, we find that the importance of and necessity for optical smoothing is increased.

#### II. THE MODIFIED 3-D CODE

The basis of this analysis is a modified form of the thermal conductivity coupled with our earlier 3d laser propagation code. The modified thermal conductivity is defined most easily and generally in Fourier space:

$$\kappa(k) = \kappa_0^{SP} / (1 + (\beta \lambda_e k)^\alpha), \quad (6.1)$$

where  $\kappa_0^{SP}$  is the Spitzer-Härm conductivity,  $\lambda_e$  is the electron mean free path,  $k$  is the Fourier space wavenumber of the temperature perturbation, and  $\beta$  and  $\alpha$  are empirically chosen parameters, which depend upon the problem being solved. In the examples presented here, we use  $\beta = 30$  and  $\alpha = 4/3$ , which describes temperature distributions produced by inverse bremsstrahlung heating.<sup>6.4</sup>

Using the formula (6.1) for the thermal conductivity gives the linearized energy balance equation as:

$$2\pi\gamma_R \bar{n}_e \frac{\partial}{\partial t} \bar{T}(k_{\perp}, t) = k_{\perp}^2 \kappa_0^{-SP} \left[ 1 + \left( \frac{1}{2\pi} \Gamma k_{\perp} \right)^{\alpha} \right]^{-1} \bar{T}(k_{\perp}, t) \quad (6.2)$$

$$+ 4\pi^2 \gamma_T \bar{\psi} * \bar{\psi}(k_{\perp}, t).$$

These equations are non-dimensionalized by defining all length and time units in terms of laser wavelength ( $\lambda_0$ ) and acoustic time ( $\lambda_0/c_s$ ). All quantities shown with an overbar (i.e.,  $\bar{n}$ ) have been normalized to their undisturbed value. The non-dimensional coupling terms  $\gamma_R$  and  $\gamma_T$  have been derived previously:<sup>6,1</sup>

$$\gamma_T = \frac{\text{heating rate}}{\text{conduction cooling rate}} = \frac{c^2 \kappa_b I_0}{\omega_0^2 \kappa_e^{SH} T_e}$$

$$= 9 \times 10^{-9} \frac{I_0 (10^{14} \text{W/cm}^2) Z^2 \ln \Lambda_c \ln \Lambda_b}{T_e^5 (\text{keV}) \sqrt{\epsilon_0} \phi(Z)} \frac{n_e^2}{n_c^2}$$

$$\gamma_R = \frac{\text{conduction time}}{\text{acoustic transit time}} = \frac{3c_s n_e c}{2\kappa_e \omega_0}$$

$$= 1.4 \times 10^{-5} \frac{(n_e/n_c) \ln \Lambda_c Z}{T_e^2 (\text{keV}) \lambda_0 \phi(Z)} \left( \frac{Z+1}{A} \right)^{1/2}$$

Along with these parameters, there is a new independent parameter describing the non-locality of the thermal conductivity; it is the normalized electron mean-free path defined as  $\Gamma \equiv \beta \lambda_e k_0$ . When  $\Gamma$  is larger than one, the conductivity can be significantly nonlocal.

The other basic equations that are solved in this 3d laser propagation code remain unchanged, and are shown here for completeness. They include the laser propagation equation based upon the slowly-varying envelope approximation:

$$\left[ 4\pi i \frac{\partial}{\partial \eta} + k_{\perp}^2 \right] \psi = 4\pi^2 \delta \epsilon(\eta, k_x, k_y, t) \psi, \quad (6.3)$$

( $\psi$  is the laser electric field envelope,  $\epsilon$  is the plasma dielectric constant,  $\delta \epsilon$  is the change in the dielectric constant due to the laser, and  $\eta = \int^z dz' / \sqrt{\epsilon_0(z')}$ ) and the driven ion-acoustic wave equation,

$$\left[ \frac{\partial^2}{\partial t^2} + q k_{\perp} \frac{\partial}{\partial t} + k_{\perp}^2 \right] \ln(\bar{n}_e) = - \left[ \frac{Z}{1+Z} \right] k_{\perp}^2 \bar{T} - \gamma_p k_{\perp}^2 \bar{\psi} * \bar{\psi} \quad (6.4)$$

where  $q$  is the ratio of the ion-acoustic wave damping to its real frequency, and  $Z$ ,  $T$  and  $n_e$  are the plasma ionization, temperature and density, respectively. We assume quasi-neutralilty and a one-temperature plasma model. Finally, the parameter  $\gamma_p$  is:

$$\gamma_p = \frac{\text{ponderomotive pressure}}{\text{plasma thermal pressure}}$$

$$= \frac{e^2 \psi_0^* \psi_0}{4m_e \omega_0^2 T_e (1 + 1/Z)}$$

$$= 9.3 \times 10^{-3} \frac{\lambda_0^2 (\mu m) I_0 (10^{14} \text{W/cm}^2)}{\sqrt{\epsilon_0} (1 + 1/Z) T_e (\text{keV})}.$$

### III. PERTURBATION ANALYSIS

Linearizing the basic equations (in the steady state limit) and assuming sinusoidal intensity perturbations, we find analytic expressions for spatial growth rates (Table 6.1). The formulas reduce to the earlier Spitzer-Härm results<sup>6,1,6,2</sup> in the limit  $\Gamma \rightarrow 0$ . The main differences are that the growth rate can be larger and the wavenumber range of unstable perturbations is broadened (Fig. 6.1). The ratio of the minimum Spitzer-Härm growth length to the nonlocal growth length is:

$$\frac{k_{\parallel-\max}^{FP}}{k_{\parallel-\max}^{SH}} = \left[ 1 + \frac{2}{3} \left( \frac{2}{3} \tilde{n} \gamma_T \right)^{1/2} \Gamma^2 \right]. \quad (6.5)$$

Table 6.1 — Growth Rates and Perturbation Wavenumbers for Non-local Thermal Filamentation: Steady State and ISI Incident Light

general thermal conductivity model:

$$\kappa_{FP} = \kappa_{SH} \left[ 1 + (\Gamma \tilde{k}_\perp)^\alpha \right]^{-1}$$

$$(\tilde{k} = ck/\omega_0; \tilde{n} = n_e/n_{crit}, \epsilon = 1 - \tilde{n}, \tau_c = t_c c_s \lambda_0)$$

$$\gamma_T = \frac{c^2 \kappa_b I_0}{\omega_0^2 \kappa_e^{SH} T_e}$$

	Steady State ( $\tau_c = \infty$ )	ISI
Spatial growth rate $\tilde{k}_\parallel$	$\frac{1}{2\sqrt{\epsilon}} \left[ 2\tilde{n}\gamma_T \left( 1 + [\Gamma \tilde{k}_\perp]^\alpha \right) - \tilde{k}_\perp^4 \right]^{\frac{1}{2}}$	$\frac{1}{2\sqrt{\epsilon}} \left[ 2\tilde{n}\gamma_T \tau_c^{1/2} \tilde{k}_\perp^{1/2} \left( 1 + [\Gamma \tilde{k}_\perp]^\alpha \right) - \tilde{k}_\perp^4 \right]^{\frac{1}{2}}$
Threshold perturbation wavenumber $\tilde{k}_{\perp-Threshold}$	$\frac{\tilde{k}_{\perp-Threshold}^4}{\left( 1 + [\Gamma \tilde{k}_{\perp-Threshold}]^\alpha \right)} = 2\tilde{n}\gamma_T ;$ $\lim_{\Gamma \tilde{k}_\perp \gg 1} \tilde{k}_{\perp-Threshold} = (2\tilde{n}\gamma_T \Gamma^\alpha)^{\frac{1}{4-\alpha}}$	$\frac{\tilde{k}_{\perp-Threshold}^{7/2}}{\left( 1 + [\Gamma \tilde{k}_{\perp-Threshold}]^\alpha \right)} \leq 2\tilde{n}\gamma_T \tau_c^{1/2} ;$ $\lim_{\Gamma \tilde{k}_\perp \gg 1} \tilde{k}_{\perp-Threshold} \leq (2\tilde{n}\gamma_T \tau_c^{1/2} \Gamma^\alpha)^{\frac{2}{7-2\alpha}}$
Fastest growing wavenumber $\tilde{k}_{\perp-maximum}$	$\left( \frac{1}{2} \tilde{n}\gamma_T \Gamma^\alpha \alpha \right)^{\frac{1}{4-\alpha}}$	$\left[ \frac{2\alpha+1}{4} \tilde{n}\gamma_T \tau_c^{1/2} \Gamma^\alpha \right]^{\frac{2}{7-2\alpha}}$ $\left( \lim \Gamma \tilde{k}_\perp \gg 1 \right)$
Fastest spatial growth rate $\tilde{k}_{\parallel-maximum}$	$\left( \frac{\tilde{n}\gamma_T}{2\epsilon} \right)^{\frac{1}{2}} \left[ 1 + \left( \frac{4-\alpha}{4} \right) \left( \frac{1}{2} \tilde{n}\gamma_T \alpha \Gamma^4 \right)^{\frac{\alpha}{4-\alpha}} \right]^{\frac{1}{2}}$	$\frac{1}{2} \left( \frac{1}{\epsilon_0} \left\{ \frac{7-2\alpha}{1+2\alpha} \right\} \right)^{\frac{1}{2}} \left( \frac{(2\alpha+1)}{4} \tilde{n}\gamma_T \tau_c^{1/2} \Gamma^\alpha \right)^{\frac{4}{7-2\alpha}}$ $\left( \lim \Gamma \tilde{k}_\perp \gg 1 \right)$

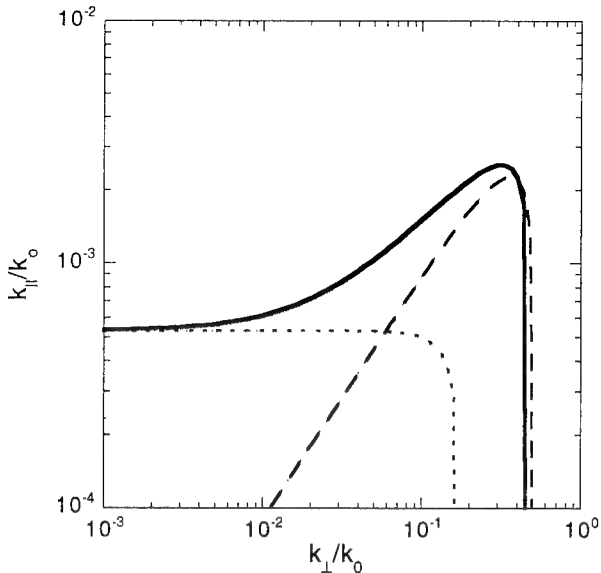


Fig. 6.1 — A comparison of the typical behavior of the growth rates for filamentation due to ponderomotive (dashed line), Spitzer-Härm thermal conduction dominated heating (dotted line) and Fokker-Planck thermal conduction dominated heating (solid line). (For thermal filamentation,  $\gamma_T = 5.3 \times 10^{-6}$  and (for Fokker-Planck)  $\Gamma = 293$ , and for ponderomotive filamentation  $\gamma_p = 6.4 \times 10^{-3}$ .)

Aside from the quantitative difference in growth lengths, there is also a qualitative difference in the wavenumber dependence. The non-local thermal conductivity enhances small-scale temperature and density perturbations (compared to Spitzer-Härm) and causes thermal filamentation to behave like ponderomotive filamentation (which also favors small-scale density perturbations). With nonlocal conductivity active, the most unstable mode increases from  $k_\perp = 0$  to the region close to the unstable mode cutoff ( $k_{\perp\text{-threshold}}^{\text{FP}} \approx 1.5 k_{\perp\text{-max}}^{\text{FP}}$ ), and grows appreciably faster than surrounding modes. This is similar to ponderomotive growth, where the threshold mode is 1.4 times the most unstable mode.

A similar perturbation analysis can be done when the incident beam is optically smoothed with ISI. This model<sup>6,1</sup> assumes that the response of the plasma to a perturbation in the laser profile is determined by the linearly-time-averaged laser perturbation. The time-averaging occurs over the characteristic hydrodynamic response time, which depends upon the plasma parameters and the size of the perturbation. For a random process like ISI, the time averaging

reduces the perturbation driving intensity by the factor  $(t_c/t_{av})^{1/2}$  where  $t_c$  and  $t_{av}$  are the laser coherence time ( $2\pi/\Delta\omega_0$ ) and the hydro response time, respectively. This response time is the greater of the acoustic time  $\tau_A = (k_\perp c_s)^{-1}$  and the temperature response time  $\tau_T = n_e \kappa k_\perp^2$ , where  $k_\perp^{-1}$  is the intensity perturbation wave-number. The acoustic time is greater when  $\gamma_R k_0/k_\perp < [1 + (\Gamma k_\perp)^\alpha]^{-1}$ , and this is assumed in the results presented in Table 6.1. This model assumes the coherence time to be finite yet significantly less than the averaging time, in contrast to the model used by Rose et al.<sup>6,5,6</sup> that assumes the limit  $t_c \rightarrow 0$ .

## IV. RESULTS AND DISCUSSION

### IV.A. Homogeneous Nonabsorbing Plasmas

We begin with a direct comparison between the simulations and the simple theory presented in Section III. For these comparisons we use a homogeneous fully ionized CH plasma with density  $n/n_{\text{crit}} = 0.5$  and  $T_e = T_i = 750$  eV, for which  $\lambda_e \sim \lambda_0$  and  $\Gamma \approx 175$ . The transverse size of the simulation is fixed at  $400\lambda_0$ . Because the perturbation analysis of Section 6.III ignores absorption, we artificially set the em wave damping to zero in the simulations. The intensity of the incident  $0.25\ \mu\text{m}$  wavelength laser is varied from  $10^{12}$  to mid- $10^{13}$   $\text{W/cm}^2$ , giving coupling strengths  $\gamma_T$  in the range of  $5 \times 10^{-9}$  to  $2 \times 10^{-7}$ . The incident beam intensity profiles are "generic" in the sense described in our earlier work,<sup>6,1</sup> and are focused into the plasma with  $f/20$  optics and a nonuniformity of  $\sigma_{\text{RMS}} = 1$  (the incident intensity peaks are about 10 times the average intensity). Growth lengths (determined by the position of the first intensity maximum) and intensity maximums from these simulations are shown in Fig. 6.2, along with previous results using classical Spitzer-Härm conductivity. The main difference between the nonlocal (finite  $\Gamma$ ) and classical ( $\Gamma = 0$ ) simulations are that the coupling strengths ( $\gamma_T$ ) producing similar values of filamentation differ by about a factor of  $\sim 10$ -50. Figure 6.2 also shows the minimum growth

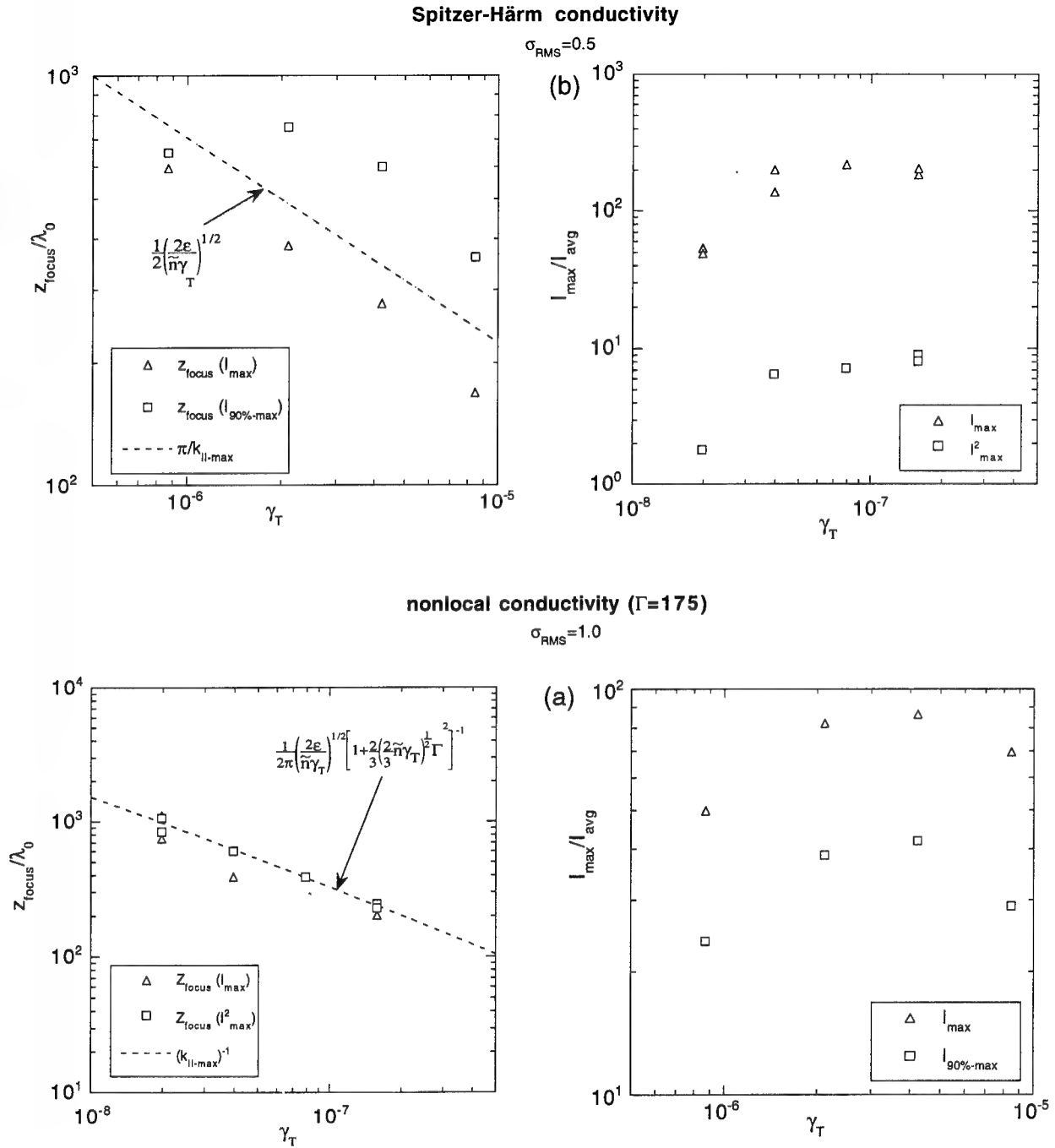


Fig. 6.2 — Growth lengths and maximum intensities vs coupling strength ( $\gamma_T$ ) from simulations of thermal conduction dominated filamentation using (a) the Fokker-Planck model with  $\Gamma = 175$ , and (b) the Spitzer-Härm model ( $\Gamma = 0$ ). All simulations use  $f/20$  optics and a  $400\lambda_0$  wide simulation mesh. The Fokker-Planck simulations used a beam quality of  $\sigma_{\text{RMS}} = 1$ , while the Spitzer-Härm model used  $\sigma_{\text{RMS}} = 0.5$ . The measurement  $I_{90\%-\text{max}}$  refers to the maximum of the 90% energy distribution contour<sup>2</sup>.

lengths from the theory in Section III: the scalings generally agree with the simulation.

Other simulations were done in which only  $\Gamma$  was varied and  $\gamma_T$  was fixed at  $1.58 \times 10^{-7}$  (see Fig. 6.3). The theory is a fairly good fit when  $\Gamma > 50$ , but is shorter by a factor of  $\sim 2$  at smaller values of  $\Gamma$ . This is consistent with the previous Spitzer-Härm simulations (cf. Fig. 6.2b). This empirical result suggest that the formula given by eqn. (6.5) be increased by the factor 2 for  $\Gamma \gg 1$ :

$$\left. \frac{k_{||-\max}^{FP}}{k_{||-\max}^{SH}} \right|_{\text{empirical}} = 2 \left[ 1 + \frac{2}{3} \left( \frac{2}{3} \bar{n} \gamma_T \right)^{1/2} \Gamma^2 \right] \quad (6.6)$$

Simulations of ISI beam behavior were also performed in these homogeneous nonabsorptive plasmas. The behavior is a little more complex because both time and spatial averages are used to characterize the filamentation growth lengths and intensity increases.<sup>6,2</sup> In the simulations, summarized in Fig. 6.4,  $\gamma_T$  was varied between  $10^{-7}$  to  $2 \times 10^{-6}$  and coherence times ( $\tau_c \equiv t_c \lambda_0 / C_s$ ) varied from 1/4, 1, and 4. Again, note that nonlocal conductivity increases the filamentation strength significantly for fixed values of

$\gamma_T \tau_c^{1/2}$ . The theoretical curve given by  $1/k_{||-\max}$  is also shown; it appears to be a good fit at the higher values of  $\gamma_T \tau_c^{1/2}$ , although the scatter among the different measurements of focal length is significant. At the smaller values of  $\gamma_T \tau_c^{1/2}$ , filamentation is weak and linear scattering dominates the focal length.

#### IV.B. Inhomogeneous Absorbing Plasmas

Filamentation in realistic plasmas also competes with absorption, and both vary in magnitude due to inhomogeneity in the plasma. As a representative example, we use a long-scale-length directly-driven plasma used in our previous 3d studies.<sup>6,2</sup> The plasma is created by a KrF laser focused by an  $f/40$  lens to an intensity  $3 \times 10^{14} \text{ W/cm}^2$  on a CH target. The initial plasma is inhomogeneous only in the axial direction, and we simulate a  $500\lambda_0$  wide area.

In steady-state simulations, the quality of the generic beam ( $\sigma_{\text{RMS}}$ ) is varied to determine the threshold quality that produces little or no filamentation. The results are shown in Fig. 6.5. For  $\Gamma = 0$  (Spitzer-Härm), we find that  $\sigma_{\text{RMS}} \sim 0.1$  is needed to eliminate filamentation (somewhat arbitrarily defined as limiting the maximum intensity to  $I_{\max} < 20I_{\text{avg}}$ ). This

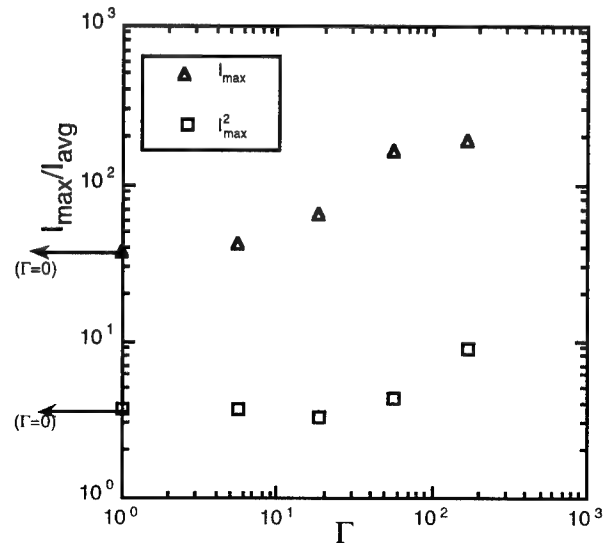
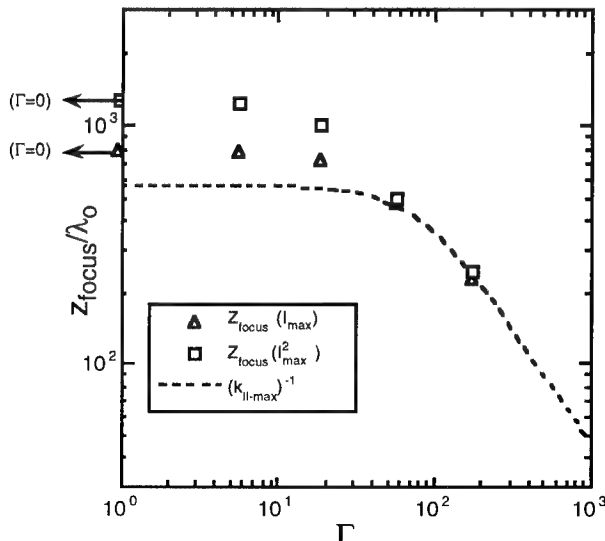


Fig. 6.3 — Growth lengths and maximum intensities vs nonlocality parameter  $\Gamma$ , from simulations of thermal conduction dominated filamentation. Parameters are the same as in Fig. 6.2, with  $\gamma_T$  fixed at  $1.58 \times 10^{-7}$ . The theoretical curve  $(1/k_{||-\max} \lambda_0)$  agrees well for  $\Gamma > 50$ , while for  $\Gamma \rightarrow 0$ , the simulation values are about a factor of 2 larger (see also Fig. 6.2b). The points on the left axis with the arrows pointing left are  $\Gamma = 0$  simulations.

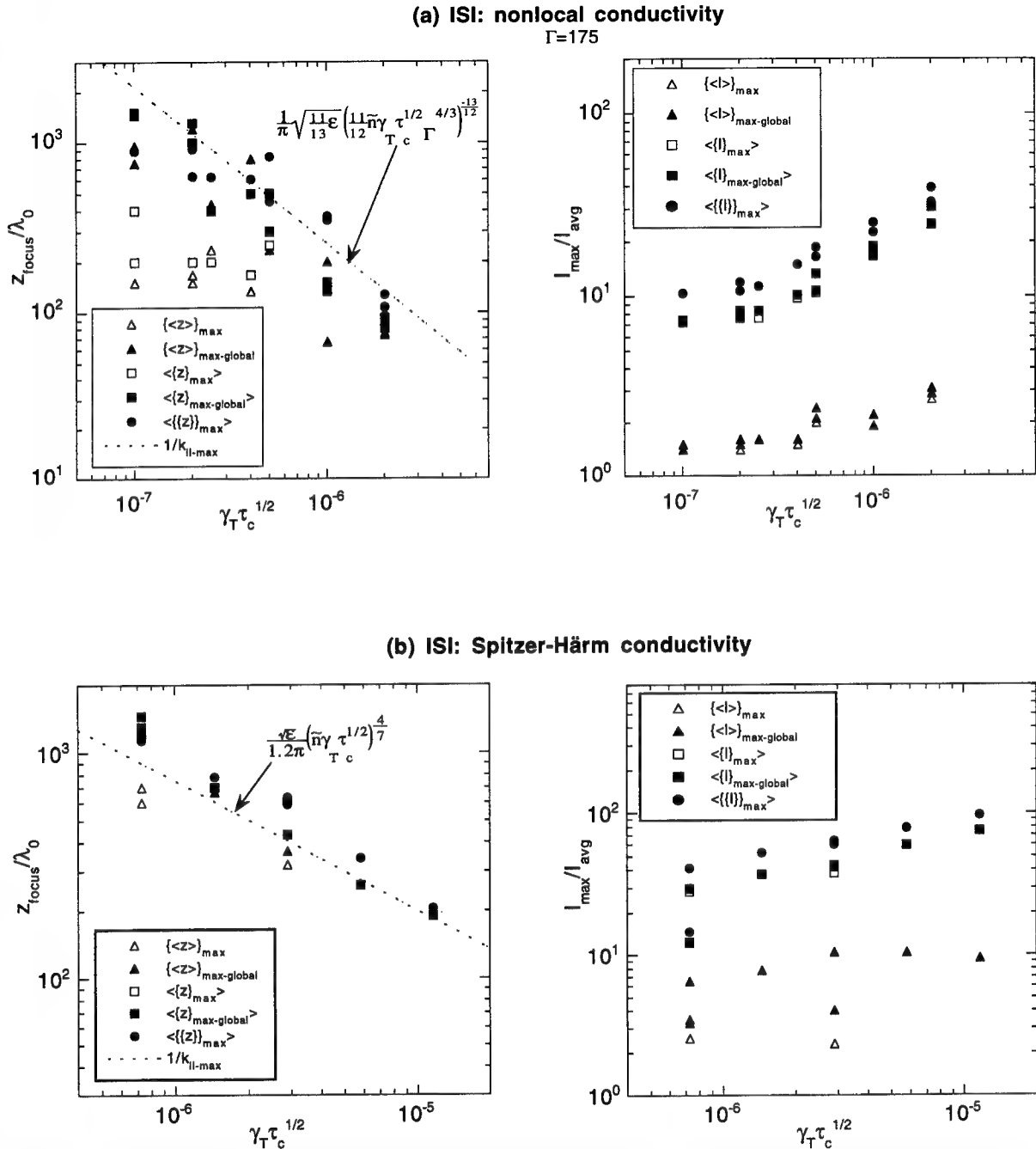


Fig. 6.4 — Growth lengths and maximum intensities found in simulations of thermal conduction dominated filamentation using (a) the Fokker-Planck model with  $\Gamma = 175$ , and (b) the Spitzer-Härm model ( $\Gamma = 0$ ). The laser light has been smoothed with ISI. All simulations use  $f/10$  optics and a  $100\lambda_0$  wide simulation mesh.

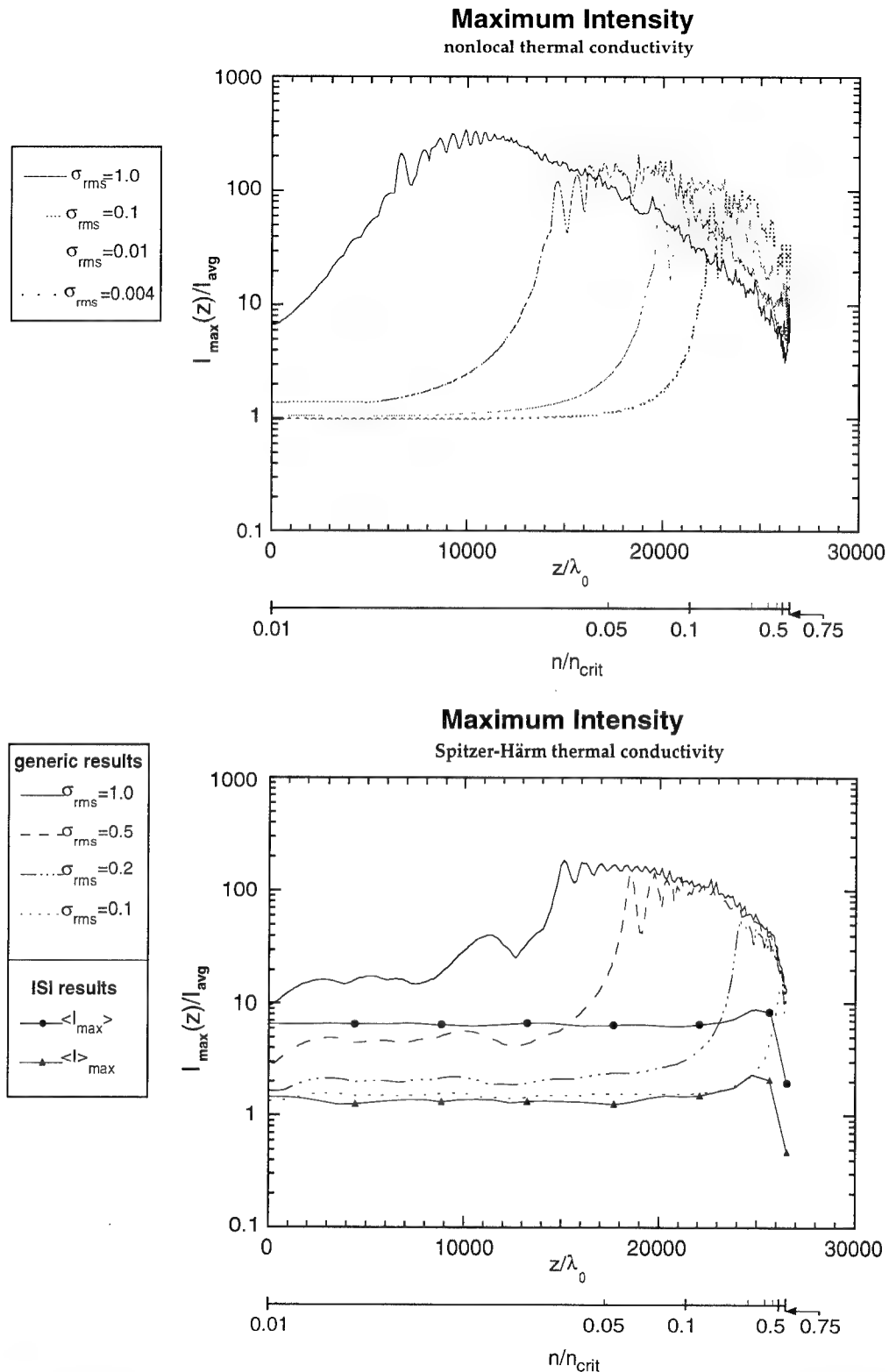


Fig. 6.5 — Increasing the initial beam quality can reduce the severity of filamentation when propagating through an inhomogeneous plasma created by a KrF laser ( $\lambda_0 = 0.25 \mu\text{m}$ ) at  $3.5 \times 10^{-14} \text{ W/cm}^2$ . For the classical Spitzer-Härm case ( $\Gamma = 0$ ) significant filamentation reduction is found for high quality beams ( $\sigma_{\text{RMS}} < 0.1$ ), but when nonlocal thermal conduction is accounted for, the quality may be impossible to achieve. In the  $\Gamma = 0$  simulations almost all of the filamentation is due to ponderomotive effects.  $f/40$  optics and  $500\lambda_0$  or  $1000\lambda_0$  wide simulation meshes were used.

is a very clean beam by ICF laser standards. Including the effect of finite  $\Gamma$  produces much more filamentation.  $\Gamma$  in this plasma varies from  $3 \times 10^4$  at  $n_e/n_{crit} = .01$  to  $10^3$ , at  $n_e/n_{crit} = .75$ , and simulations using the inhibited thermal conductivity show that even  $\sigma_{RMS} \sim 0.001$  produces unacceptable filamentation, similar to the  $\sigma_{RMS} = 0.2$ ,  $\Gamma = 0$  case. This is a strong motivation to consider optical smoothing methods.

The simulation results are consistent with the theory summarized in Table 6.1. Integrating the predicted maximum spatial growth (minus the local absorption) rates along the propagation distance, the predicted filamentation length of  $\sim 7200\lambda_0$  is found. This compares with the observed value of about  $6500\lambda_0$ . This is somewhat remarkable given the simplicity of the model.

The width of these simulations is quite important in determining the correct filamentation levels. To illustrate, the same simulation was repeated while varying only the width, from  $100\lambda_0$  to  $1000\lambda_0$ . Only after extending the mesh size to at least  $500\lambda_0$  does the filamentation behavior converge (Fig. 6.6). This implies

that the fastest growing or dominant modes are larger than 250 laser wavelengths in size. The simulation mesh must also have many points in the transverse direction, since the filamenting light produces structure on the order  $\lambda_0$  and the mesh needs to resolve both this and the dominant modes.

These resolution considerations prevent us from performing proper time-dependent simulations of ISI in this plasma. An initial attempt was made using a simulation with a width of  $100\lambda_0$  and a numerical mesh of size  $128 \times 128$  (transverse) by 31 (axial), but it failed due to unresolvably high spatial frequencies that were forming in the beam (either due to filamentation or stochastic scattering of the light). The problem is both the inadequate mesh spacing in the propagation direction, and an inadequate simulation width in the transverse direction. Because of the extreme length of this plasma ( $2.5 \times 10^4\lambda_0$ ), the z-resolution is limited (by available computer memory) to  $\sim 10^3\lambda_0$ , so the propagation of filaments that are a few  $\lambda_0$  wide cannot be resolved. (This problem was exacerbated by starting with relatively small structure incident

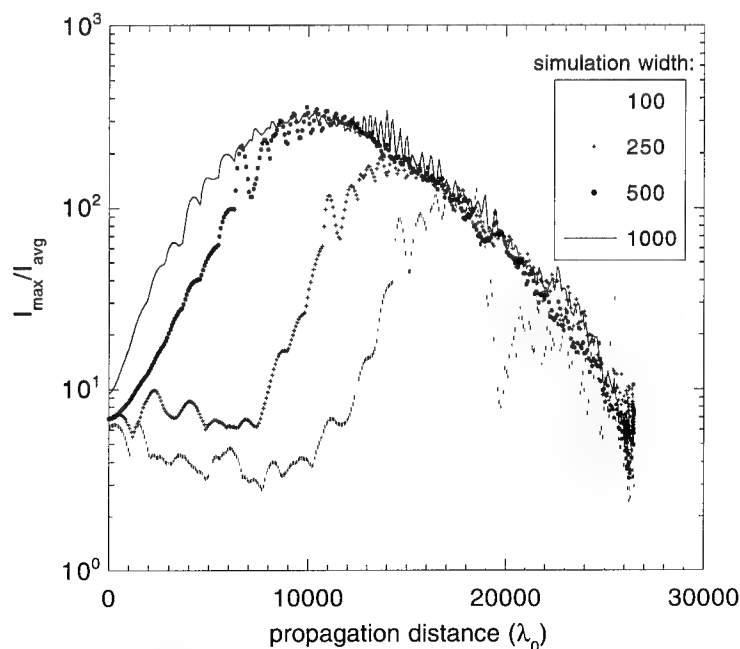


Fig. 6.6 — Increasing the size of the simulation mesh results in larger amounts of filamentation observed, until the mesh is at least  $500\lambda_0$  wide. All parameters are otherwise the same as in Fig. 6.5.

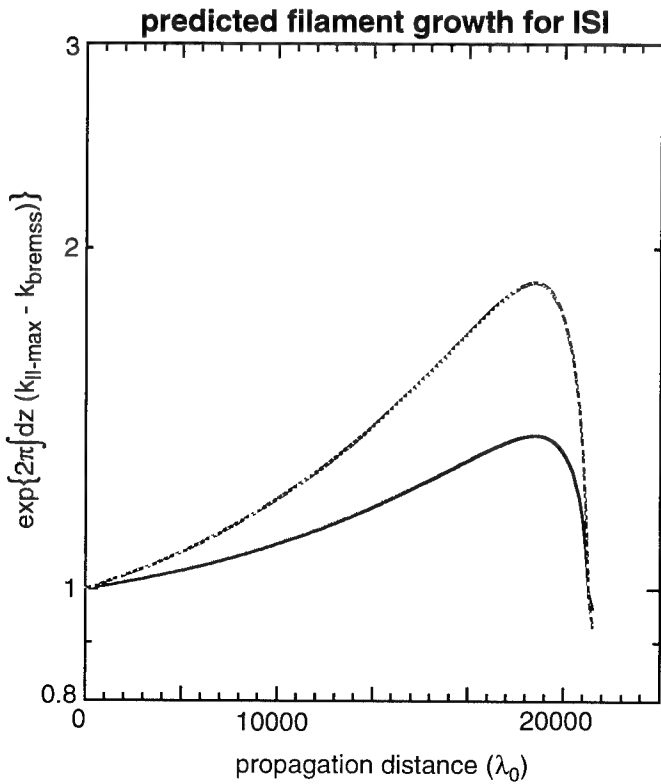
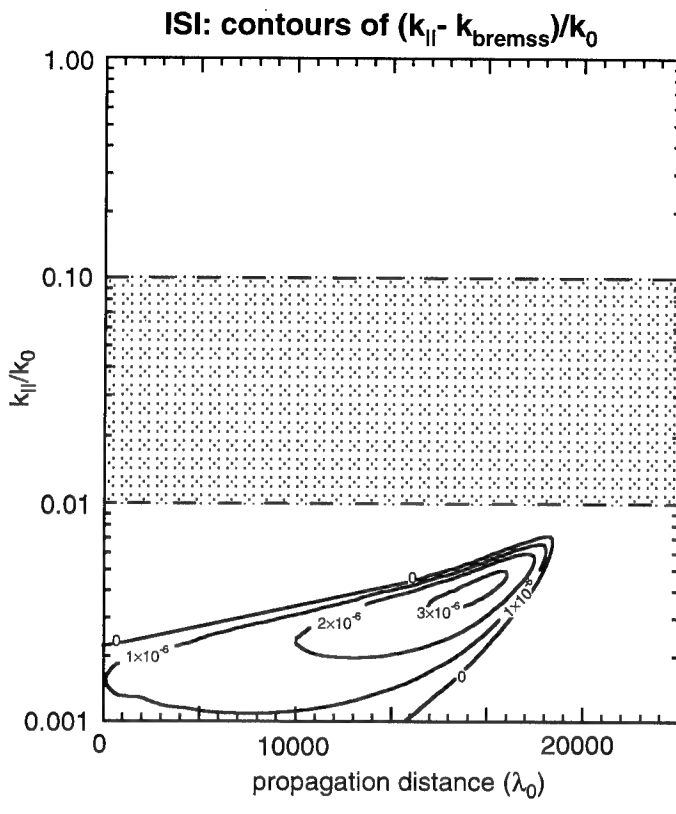


Fig. 6.7 — The predicted ISI filament growth in the inhomogeneous plasma used in Fig. 6.5. (a) Contours of spatial growth rates for the inhomogeneous plasma from Fig. 6.5, as a function of  $k_{\perp}$  and propagation distance. The horizontal dashed lines denote the limits of  $k_{\perp}$  produced by the incident laser and included in the initial simulation. Note that all the growing modes all lie outside of this boundary. (b) The integrated amplification of a mode constantly growing at the fastest spatial growth rate. The dotted line assumes growth occurring at twice the fastest spatial growth rate.

created by  $f/10$  optics; however, using  $f/40$  optics on the same mesh eventually produces the same result.) The transverse mesh spacing must be  $\sim \lambda_0$ , and given a  $128 \times 128$  transverse mesh, this limits the smallest perturbation allowed to be  $k_{\perp} \sim .01$ . Since theory predicts that the fastest growing modes are smaller, ( $\sim .002k_0$ ), the minimum simulation size needed is at least  $\sim 500 \times 500 \times 10^3$ , or about 500 times the current size. Calculational times increase by the same factor. This exceeds our present computational resources.

Lacking a full ISI filamentation simulation, we can estimate the expected growth by using the simple method benchmarked earlier, and demonstrated in the steady-state inhomogeneous case. Integrating the net growth of the fastest growing mode (accounting for absorption as before) we find relatively insignificant filamentation in the plasma when using ISI (Fig. 6.7). The sensitivity and uncertainty in the formula in the ISI case can be accounted for by assuming growth at twice the maximum growth rate; this also predicts less than an e-folding of growth. Thus, the simple formulas predict that ISI should smooth filamentation caused by nonlocal electron thermal transport in low- $Z$ , direct-drive ICF-scale targets.

## V. CONCLUSIONS

A simple and general model for the non-local thermal conduction has been incorporated into our 3d laser-plasma propagation code. A perturbation analysis is applied to this general model of nonlocal thermal conduction and simple forms are derived for the expected filamentation distances (Table 6.1). Simulations of both

generic and ISI-smoothed laser beams in simple homogeneous nonabsorbing plasmas were done under a wide variety of conditions, and the results are compared to the perturbation analysis, which agree with the scalings found.

Steady-state simulations of generic beams in a large reactor-scale KrF driven inhomogeneous, absorbing plasmas also are consistent with the perturbation model when the spatially integrated growth minus absorption was compared. However, because of computational constraints, we are unable to resolve simulations of ISI beams in this plasma. As a recourse, we use the perturbation formulas developed in the earlier simulations to predict the growth of ISI beams. These formulas predict little or no filamentation for ISI beams in these plasmas, despite the enhancements due to nonlocal thermal conductivities.

These results strongly suggest that optical smoothing of laser beams is necessary for large directly driven ICF targets.

## REFERENCES

- 6.1 A. J. Schmitt, *Phys. Fluids* **31**, 3079 (1988).
- 6.2 A. J. Schmitt, *Phys. Fluids B* **3**, 186 (1991).
- 6.3 E. M. Epperlein and R. W. Short, *Phys. Fluids B* **3**, 3092 (1991).
- 6.4 E. M. Epperlein, *Phys. Rev. Lett.* **65**, 2145 (1990).
- 6.5 H. A. Rose and D. F. DuBois, *Phys. Fluids B* **4**, 252 (1992).
- 6.6 H. A. Rose, D. F. DuBois and D. Russell, *Sov. J. Plasma Phys.* **16**, 537 (1990).

## Section 7

### SUPPRESSION OF PLASMA INSTABILITIES BY ISI: EXPERIMENTS

Andrew Mostovych  
*Laser Plasma Branch*  
*Plasma Physics Division*  
*Naval Research Laboratory*

Early experiments with high-intensity laser-plasma interactions in the ICF community demonstrated a rich variety of non-linear plasma instabilities. The levels of observed Stimulated Brillouin Scattering (SBS), Stimulated Raman Scattering (SRS),  $\omega/2$ ,  $3/2\omega$ ,  $2\omega$  harmonics, and hard X-rays indicated that these instabilities would be very severe under high-gain ICF conditions. SBS, SRS, Two Plasmon Decay (TPD), Ion-Plasmon Decay (IPD), Filamentation, and others would scatter a large fraction of the laser energy and would preclude low-isentropic compression of the ICF pellet as a result of hot-electron pre-heat.

With the advent of ISI,<sup>7.1</sup> it was discovered that the behavior of all observable laser-plasma instabilities was strongly modified by the ISI process. The under-dense plasma instabilities are always strongly suppressed. The instabilities operating near the critical density are suppressed for short-wavelength ISI illumination but showed signs of enhancement with ISI at longer wavelengths. In this paper we review the NRL ISI experiments and summarize the behavior of the different instabilities with ISI.

#### EXPERIMENTS

Laser-plasma interaction experiments were performed with two beams of the Pharos III Nd-glass laser, one with and one without ISI echelons as shown in Figs. 7.1 and 7.2. Both beams are plane polarized and have a 2-nsec FWHM pulse duration. For green experiments the  $1.054 \mu\text{m}$  beams were converted to  $0.527 \mu\text{m}$  with a set of harmonic crystals<sup>7.2</sup> placed in front of the ISI echelons. For most experiments the

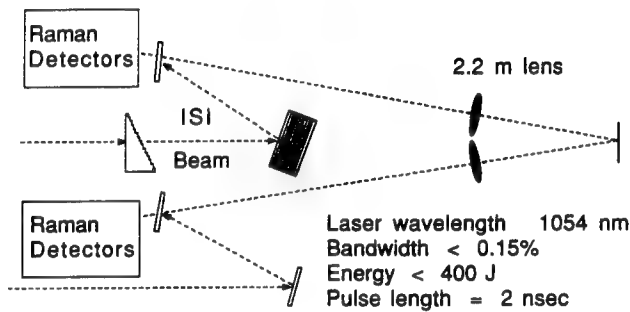


Fig. 7.1 — Experimental arrangement for the study of the effects of ISI on laser plasma instabilities. Raman detectors are shown behind the final turning mirrors before the target.

first echelon is transmissive, as in Fig. 7.1, even though a reflective first echelon was occasionally used. Each echelon assembly consists of about 25 strips, each of which introduce a finite optical delay (2 psec for the first assembly, 40 psec for the second). The echelons assemblies are perpendicular to each other, breaking the 20 cm diameter ISI beam into 350 beamlets, each  $0.95 \text{ cm} \times 0.75 \text{ cm}$ . Both beams are focused onto  $200 \mu\text{m}$  thick 2 mm wide plastic (CH) targets using 2.2 m focal length lenses. With a 2 psec minimum optical delay between beamlets the echelons stretch the duration of the ISI beam by approximately 700 psec. The beam energy, equivalent focal spot distribution, and the temporal envelope of each beam are obtained on every shot by incident beam diagnostics as in Fig. 7.2. The angle between beams is  $8^\circ$  and the target normal is midway between the two beams.

Typically the experiments alternated between the two beams and the laser coherence

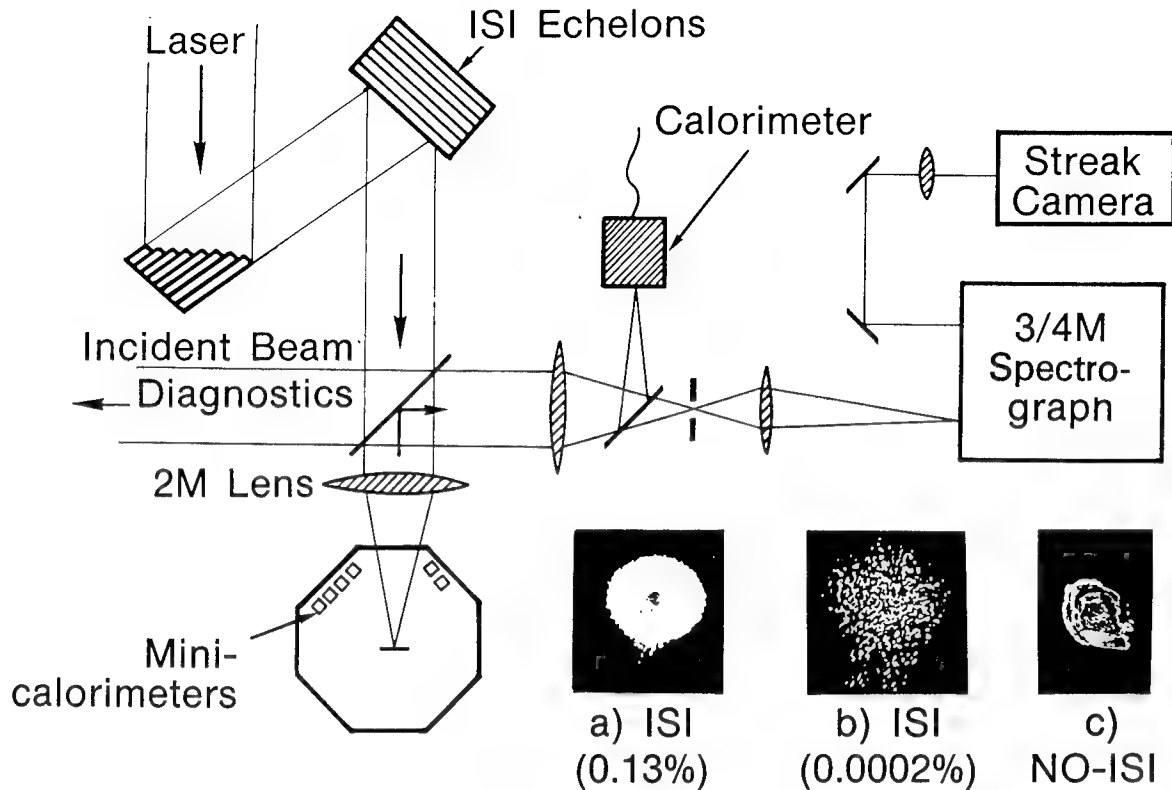


Fig. 7.2 — Schematic of experiment used to study SBS with ISI illumination. Typical focal-spot distributions are included: (a) echelons with broad bandwidth (0.13%); (b) echelons with narrow bandwidth (time-bandwidth-limit); and (c) standard beam, i.e., no echelons.

time was varied between  $\tau_c = 2$  nsec (time bandwidth limit) and  $\tau_c = 1$  psec ( $\Delta\omega/\omega = 0.0002\%$  to 0.3%). This resulted in very different time-averaged intensity distributions on target. Some examples of these intensity distributions are shown in Figs. 7.2 and 7.3. For the broadest laser bandwidths  $\Delta\omega/\omega = 0.3\%$  the laser coherence time ( $\tau_c = 1$  psec) is shorter than the minimum optical delay between beamlets. The interference pattern from the various beamlets changes every laser coherence time. Temporal averaging over the ensemble of statistically independent interference patterns produces a very smooth focal profile, Fig. 7.2a and Fig. 7.3a. For intermediate laser coherence times  $\tau_c = 8$  psec, only the beam strips from the second echelon are statistically independent. The resultant focal profile is smooth in only one dimension as in Fig. 7.3b. For the longest coherence times  $\tau_c = 2$  nsec there is no temporal averaging. All of the beamlets interfere

coherently to produce the high spatial-frequency multiply-peaked profile of Fig. 7.2b. This stationary focal profile is similar to the one obtained instantaneously with broad band (short coherence time) ISI. The ordinary beam focal profile, Fig. 7.3c, has hot spot intensity structure which extends by a factor of 2-3 above the average intensity. For the bandwidths used in these experiments there were no observable modifications to the ordinary beam focal profile with changes in the laser coherence time. Finally, all laser-coupling experiments were conducted with intensities of  $10^{13}$  to  $10^{14}$  W/cm<sup>2</sup>. The experiments were outfitted with diagnostics to measure the hard x-ray emissions of the plasma and the scattered or emitted light at the laser fundamental frequency  $\omega_0$  and at the  $1/2\omega_0$ ,  $3/2\omega_0$ ,  $2\omega_0$  harmonics. The density-profiles of the underdense plasma were measured with a 30-300 psec Raman-shifted laser-probe interferometer.<sup>7.3</sup>

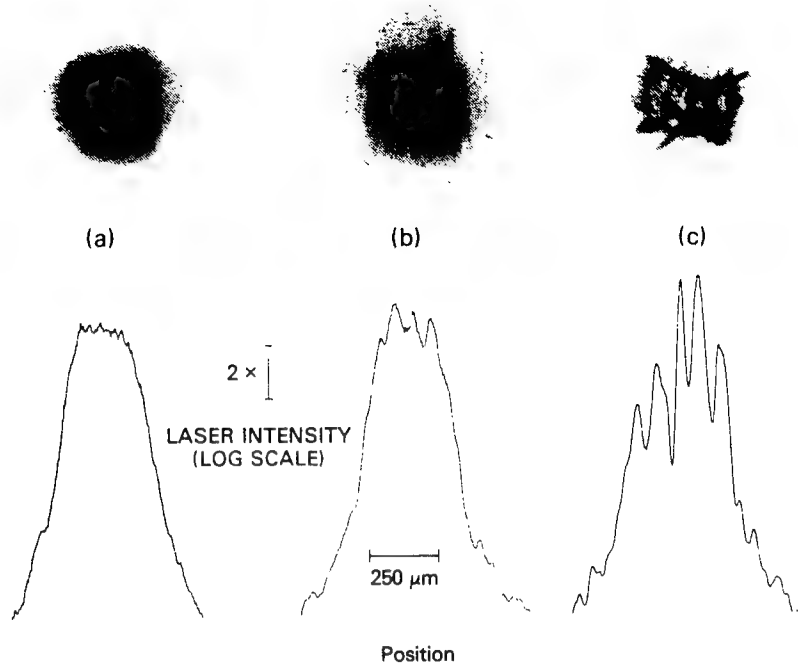


Fig. 7.3 — Photographic and film densitometry measurements of the focal distributions obtained (a) with the ISI echelons and broad laser bandwidth ( $\tau_c = 1$  psec); (b) with echelons and narrower laser bandwidth ( $\tau_c = 8$  psec); and (c) without echelons. Film grain is contributing to the small-amplitude nonuniformity observed in (a).

## SBS

The SBS instability in a laser-irradiated plasma involves the decay of the incident electromagnetic wave into an ion-acoustic wave and a scattered electromagnetic wave. SBS is potentially dangerous for laser fusion because at the high laser intensities needed for fusion it may be a significant loss mechanism.<sup>7,4</sup>

Brillouin scattering at the fundamental laser frequency  $\omega_0$  back through the main focusing lenses was measured on both beams<sup>7,5</sup> as in Fig. 7.2. On the beam line being fired the scattered light was direct backscatter into the collection cone of the lens whereas the alternate beamline always recorded the scattering at the specular reflection angle with respect to the target normal. The angular distribution of scattered light outside of the two lens cones was recorded with a set of mini-calorimeters located inside the target chamber. Whenever appreciable scattering was detected it was always highly peaked in the direction back through the lens of the active beamline and not at the specular reflection

angle. This angular distribution identified the scattered light as SBS.

The SBS time-integrated backscatter data for both green and red experiments are presented in Fig. 7.4. For the case with ISI echelons and medium to broad laser bandwidth the SBS backscatter is reduced by as much as an order of magnitude relative to a standard echelon-free beam and the levels of backscatter and specular reflection become comparable. By plotting the same data as a function peak intensity (Fig. 7.5) it is clear that this reduction is greater than would be expected if the hot spots in the non-ISI beam were smoothed over. Conversely, for the narrowband time-bandwidth-limit, the SBS backscatter fraction in the ISI echelon beam is about double that of the standard echelon-free unsmoothed beam. The higher peak intensities of the narrowband ISI beam produce more SBS but the basic intensity dependence is the same. The non-echelon and narrowband echelon data fall on the same curve (Fig. 7.5) of backscatter versus peak intensity. Finally, it is clear that since narrowband and broadband ISI have the

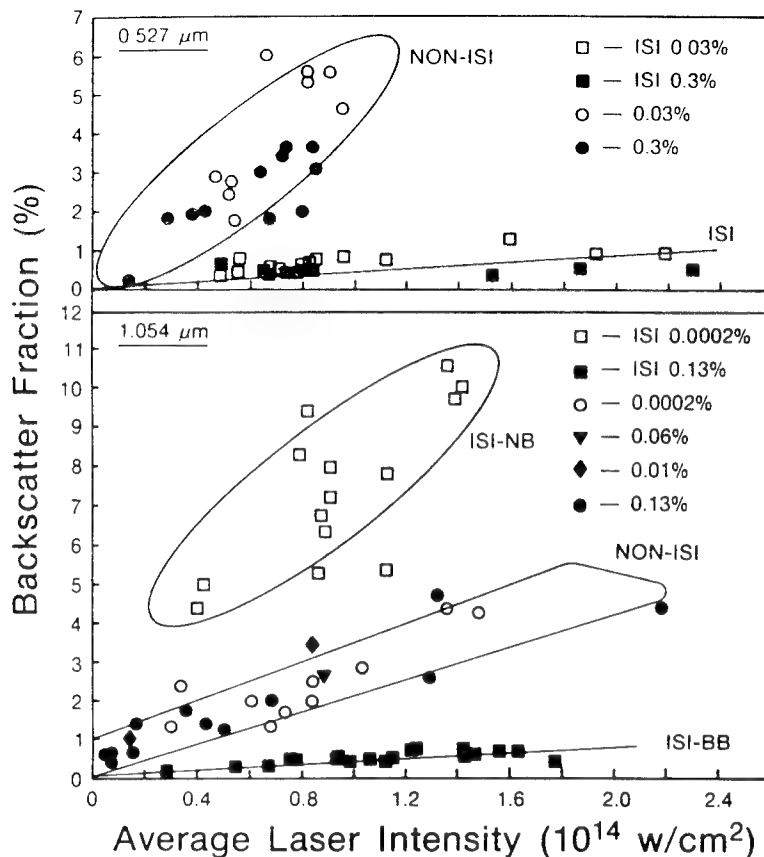


Fig. 7.4 — SBS backscatter fraction as a function of average laser intensity. Without the ISI echelons, bandwidth has no significant effect on the backscatter. With the echelons in place the backscatter is strongly suppressed for broad bandwidth ( $\Delta\omega/\omega \geq 0.015$ ) laser beams (ISI-BB) while for very narrow bandwidths (0.0002%) (ISI-NB) it is increased.

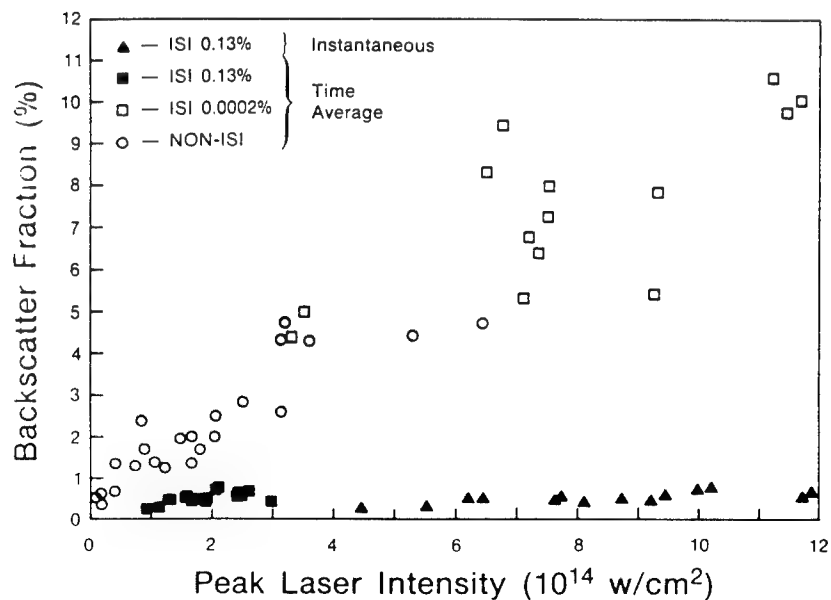


Fig. 7.5 — SBS backscatter as a function of peak time-averaged laser intensity. The ISI backscatter is lower even though the peak intensities are the same as for the non-ISI case. Backscatter with ISI echelons and broad bandwidth is much lower than the narrowband ISI case irrespective of the fact that the peak instantaneous intensities are the same.

same instantaneous intensity distributions but very different levels of SBS, the SBS instability is not responding on the time scale of the short to medium coherence times (1-8 psec).

For the standard non-echelon beam, changes in bandwidth over the full range available ( $\Delta\omega/\omega = 0.0002\%$  to  $0.3\%$ ) produces little or no reduction in backscatter. The largest reductions (factor of 2) were observed in some  $1.054\text{ }\mu\text{m}$  experiments with  $\Delta\omega/\omega = 0.3\%$ . Theoretical work<sup>7,6,7,7</sup> predicts that bandwidth will not be important unless  $\gamma/\Delta\omega \ll 1$ , where  $\gamma$  is the homogeneous growth rate. This is consistent with the data since  $\gamma/\Delta\omega$  is of order 1 or larger.

Time integrated and time resolved spectral measurements of the  $0.527\text{ }\mu\text{m}$  experiments show a large blue shift ( $4\text{-}5\text{\AA}$ ) for the non-ISI data and a no shift ( $\pm 1\text{\AA}$ ) for the medium to broadband ISI case (see Fig. 7.6). There is no observable change in the wavelength shift for the  $1.054\text{ }\mu\text{m}$  data with or without the ISI echelons. From the dispersion relations for ion-acoustic waves, the SBS k-matching conditions, and a two dimensional hydro-code calculation of the plasma conditions it is found that the blue-shifted  $0.527\text{ }\mu\text{m}$  non-ISI spectra originate [at  $(0.25\text{-}0.5)n_c$ ] where the plasma flow is supersonic. The neutral or slightly red-shifted ISI

spectra came from the subsonic regions close to the critical surface. For the  $1.054\text{ }\mu\text{m}$  data, the plasma flow is supersonic all the way up to the critical surface and the blue shifted spectra appear to originate close to the critical surface [ $(0.6\text{-}1)n_c$ ]. For the  $1.054\text{ }\mu\text{m}$  data there is no observable change in wavelength shift with or without the ISI echelons. The regions from which the blue shifted spectra originate coincide with the location of maximum gain as calculated from the convective gain model<sup>7,8</sup> for SBS. The fact that these shifts disappear with ISI at  $0.527\text{ }\mu\text{m}$  suggest that ISI quenches the SBS instability. Simple residual reflections from the critical surface could produce the very-weak unshifted ISI spectra. At  $1.054\text{ }\mu\text{m}$ , the SBS origination region is so close to the critical surface that a wavelength shift is not expected between SBS spectra and spectra from critical surface reflections.

Standard theoretical models<sup>7,9,7,10,7,11</sup> for SBS in inhomogeneous plasmas have difficulty explaining the measured results. The theory is based on either the slowly varying envelope ( $kC_s \gg \gamma$ ) or the quasimode approximation ( $kC_s \ll \gamma$ ). In this experiment,  $\gamma$  is of order  $kC_s$ . Calculations based on the quasimode model predict only about one e-folding of growth before saturation. For the slow-wave

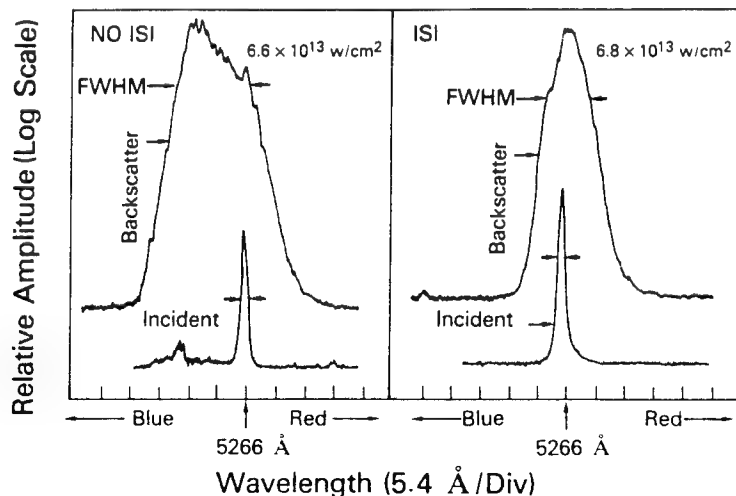


Fig. 7.6 — Sample time-integrated SBS backscatter spectra for the narrower-bandwidth case ( $t_c = 8\text{ psec}$ ). Without the ISI echelons the spectra are strongly shifted to the blue. This corresponds to SBS in the underdense plasma where the plasma flow is supersonic. With the ISI echelons the blue shift is replaced with little or no shift.

approximation, the total connective SBS gain is given by  $\exp(2\pi\gamma^2/K'V_1V_2)$ , where  $\gamma$  is the homogeneous growth rate,  $K'$  is the phase-mismatch wave number, and  $V_1$  and  $V_2$  are the ion-acoustic and scattered-light wave group velocities. For our experimental conditions SBS is predicted to grow convectively for about 1 psec and to saturate at a gain of 7 e-foldings. If the saturation time (1 psec) of the instability is shorter than a single laser coherence time then the instability should respond instantaneously to the intensity variations of the laser and ISI should not affect the instability. But we find that ISI is effective in quenching the SBS instability even when the laser coherence time is as long as 10 psec. Either the instability grows slower than predicted or some other process such as filamentation, which grows much more slowly, is dominating the interaction physics. In contrast to other instabilities such as SRS, the SBS instability has more than enough gain to produce the observed scattering levels without the need of invoking intensity enhancing processes such as filamentation. At this time, it is not known which process is responsible for the very effective quenching of SBS with ISI.

## SRS

The SRS instability in a laser-irradiated plasma involves the decay of the incident electromagnetic wave into an electron plasma wave and a scattered electromagnetic wave. The SRS instability is potentially dangerous to laser fusion because the excited electron plasma waves can accelerate electrons and produce unacceptable preheat of the fusion pellet. Experiments were conducted with 1.054  $\mu\text{m}$  and 0.527  $\mu\text{m}$  beams. SRS behaved similarly for both wavelengths and only the 1.054  $\mu\text{m}$  results are discussed in detail.

Raman backscatter in the 1350-1750 nm band [(1.3-1.7) $\lambda_0$ ] was measured with spectrally filtered detector arrays.<sup>7,12</sup> These arrays were located behind the final turning mirrors and they collected the light passing back through the final focusing lenses. The detectors had temporal resolution of 0.6 nsec and had sufficient sensitivity to detect thermal emission levels from the plasma. Figure 7.7 shows the peak Raman backscatter in the detection band for the case of broadband ISI ( $\tau_c = 2$  psec), narrowband ISI, and the ordinary beam with narrow bandwidth.

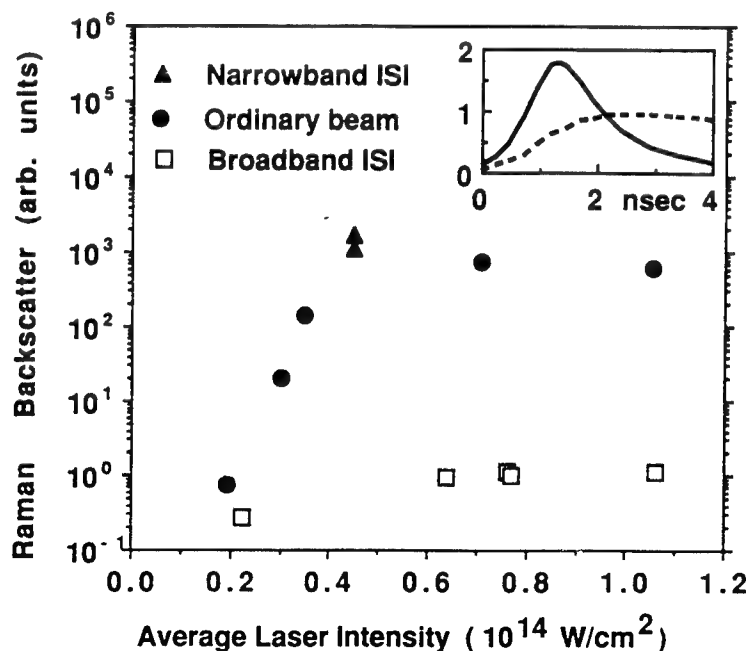


Fig. 7.7 — The peak Raman backscatter in the band 1350-1750 nm for the case of broadband ISI, narrowband ISI, and an ordinary laser beam with narrow bandwidth. Inset: Typical pulse shapes of the Raman emission with narrowband ISI (solid line) and broadband ISI (dashed line).

The emission with the ordinary beam and the narrowband ISI beam is orders of magnitude higher than that obtained with broadband ISI. Variations in the bandwidth had little effect on the emission with the ordinary beam. Typically, the Raman signal (Fig. 7.7 inset) was shorter than the laser pulse but for the broadband ISI case the detected emission was much longer than the laser pulse. This indicated that the backscatter with broadband ISI was dominated by thermal radiation from the laser-heated target. In fact, for experiments with small disc targets, matched in diameter to the FWHM of the focal profile and a  $0.527 \mu\text{m}$  laser, the measured emission was observed to be 60%-80% of that for an ideal blackbody with a temperature matching the plasma coronal temperature (1100-1330 eV). The Raman detectors are not spatially resolving so the disk targets were needed to measure accurately the emissions from only the region irradiated by the laser.

The threshold for turning on the Raman instability with the broadband ISI beam can be exceeded by focusing the broadband ISI beam into a preplasma produced by the ordinary laser beam. Figure 7.8 shows the emission near 1610 nm with the ISI beam, with and without the preplasma. The presence of the preplasma increases the Raman-band emission with ISI to almost the non-ISI levels, presumably due to a longer-scale-length plasma. The wave-number and frequency matching conditions for Raman backscatter indicate that the backscatter in this case originates near  $n = 0.1 n_c$ . Two-dimensional hydrocode calculations and interferometric measurements place the density scale length  $L = n/(\delta n/\delta z)$  in this region at approximately 0.065 cm. The convective gain of Raman backscatter in an inhomogeneous plasma with  $n < n_c/4$  is given by  $I_R = I_n \exp(G_o L I)$ , where  $G_o = 1.59 \times 10^{-13} \text{ cm/W}$  for a 1054 nm laser and  $n = 0.1 n_c$ , and  $I_n$  is the noise level from which the Raman instability grows.<sup>7,13</sup> For the time-averaged intensity of the ISI beam, the above formula predicts much less scattering than is observed with the combination of the ISI beam and a preplasma target. If, instead of reacting to the time-averaged intensity, the instability grows to convective saturation for each hot spot of the instantaneous intensity distribution, then the data

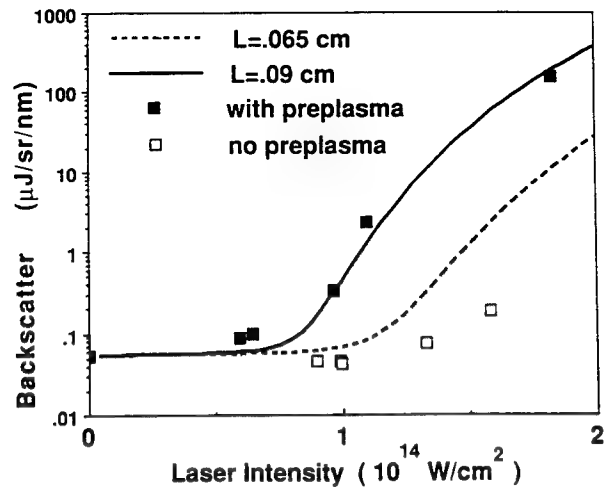


Fig. 7.8 — Raman backscatter near  $1.53\lambda_o$  with broadband ISI, but with and without a preplasma. The theoretical curves are calculated with Eq. (7.1). The data without the preplasma extend to somewhat higher laser intensity than in Fig. 7.7, and some measurable Raman backscatter appears above the background emission.

can be well fitted with the convective gain model.

The instantaneous intensity distribution at the target with ISI is accurately approximated by the probability distribution,  $P(I) = (1/I_o) \exp(-I/I_o)$ , provided that the intensity is not modified by filamentation. Integrating the convective gain over  $P(I)$  the Raman backscatter is given by:

$$I_R = I_n \int_0^{I_s} P(I) e^{G_o L I} dI + \alpha \int_{I_s}^{\infty} I P(I) dI. \quad (7.1)$$

$I_s$  is the incident intensity which satisfies  $\alpha I_s = I_n \exp(G_o L I_s)$  and  $\alpha$  is the saturated-reflectivity coefficient. The solid curve in Fig. 7.8 is the best fit of Eq. (7.1) to the preplasma data using  $L$  and  $\alpha$  as free parameters.  $I_n$  was taken as the blackbody emission into the cone of the focusing lens for a blackbody with coronal plasma temperature ( $T_e = 1200$  eV from computer simulations). The best fit occurred for  $L = 0.09$  cm and  $\alpha = 5 \times 10^{-6} \text{ nm}^{-1}$ . The dashed curve corresponds to the average  $L = 0.065$  cm obtained from the hydrocode, but uses the same  $\alpha$ . An increase or decrease in  $\alpha$  by several orders of magnitude does not significantly change the theoretical intensity threshold at which the

backscatter first emerges above the background emission. As a result it is not necessary to know  $\alpha$  precisely to predict the onset of Raman backscatter with Eq (7.1). The curves in Fig. 7.8 indicate that the onset of Raman backscatter with ISI is predicted well by a convective model that accounts for the instantaneous focal intensity pattern. A small discrepancy occurred in these experiments with a  $Li_0G_0$  product that is 30% lower than that predicted by Eq (7.1). This discrepancy may be the result of the uncertainties in the plasma scale length, uncertainties in the theoretical value of  $G_0$ , or due to weak filamentation of the ISI beam.

## TWO-PLASMON DECAY ( $3/2\omega_0$ )

The two-plasmon instability in a laser-irradiated plasma involves the decay of the incident electromagnetic wave, at the quarter-critical density, into two counter-propagating electron plasma waves each with a frequency approximately equal to  $\omega_0/2$ . Three-halves ( $3/2\omega_0$ ) harmonic emission occurs when the  $\omega_0/2$  plasma wave scatters an incident  $\omega_0$  photon in the vicinity of the quarter-critical surface. Similarly to SRS, the electron-plasma waves generated by two-plasmon decay can accelerate electrons to levels which would produce unacceptable pre-heat of fusion pellets.

Measurements of ( $3/2\omega_0$ ) emissions were made with three 6 cm focal-length fiber-optic collectors.<sup>7,14</sup> They were placed 50 cm from the target at  $0^\circ$ ,  $30^\circ$ , and  $50^\circ$  collection angles with respect to the target normal. The time-integrated ( $3/2\omega_0$ ) spectra, as in Fig. 7.9, showed the characteristic two-peak ( $3/2\omega_0$ ) signature of the two-plasmon decay instability. With the ISI echelons, significant reduction in overall levels of ( $3/2\omega_0$ ) emission are observed for broad bandwidths for both  $0.527 \mu m$  and  $1.054 \mu m$  irradiation. This is seen in individual spectra, Fig. 7.9, and in the total integrated emission of the ( $3/2\omega_0$ ) band, Fig. 7.10. In contrast to the SRS and SBS instabilities, substantial reduction in ( $3/2\omega_0$ ) emission only occurred at the broadest bandwidths. For SBS and SRS, reductions in emission were already observable at the intermediate bandwidths ( $\Delta\omega/\omega \sim 0.01\%-0.03\%$ ) where the echelons only provided smoothing in

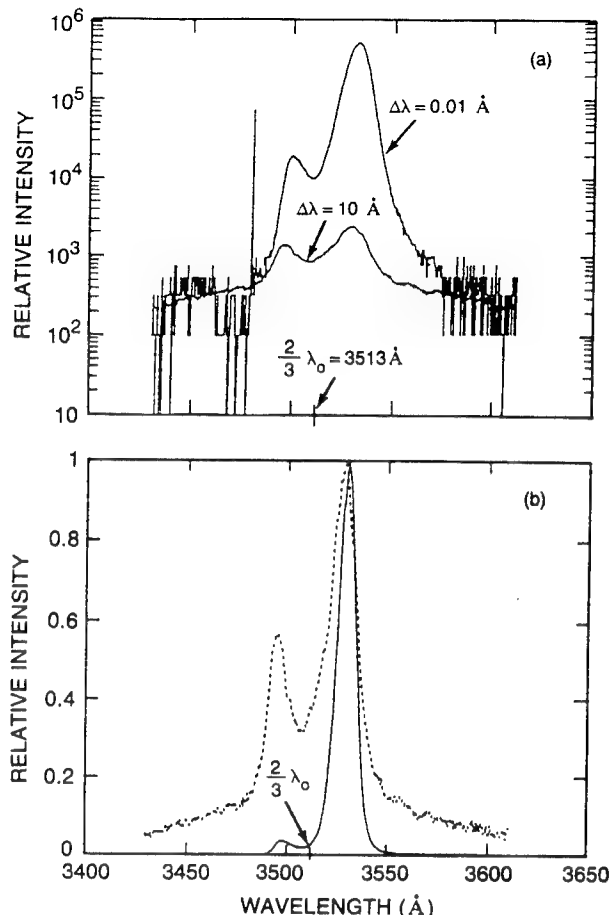


Fig. 7.9 — (a) Sample time-integrated spectra of the  $3\omega_0/2$  emission at the  $30^\circ$  observation angle for the two shots with ISI echelons. (b) same spectra but normalized to the maximum.

one dimension. This different behavior is displayed in a comparison of Raman and ( $3/2\omega_0$ ) emissions in Fig. 7.11. For an ordinary beam with no echelons, changes in the laser bandwidth had no effect on the ( $3/2\omega_0$ ) emissions.

Finally, concomitant time- and space-integrated hard x-ray measurements were made using an array of p-i-n diodes and scintillator/photomultiplier detectors with broadband k-edge filters. The hard x-ray signals were fit with bi-Maxwellian energy distributions to determine the hot electron component. Figure 7.12 shows, for the  $0.527 \mu m$  green experiments, the correlation between the x-ray data and the ( $3/2\omega_0$ ) data for the broad bandwidth and the intermediate bandwidth ISI-echelon beam. Broad bandwidth ISI is seen to reduce hard x-ray emission by almost two orders of magnitude. Since the

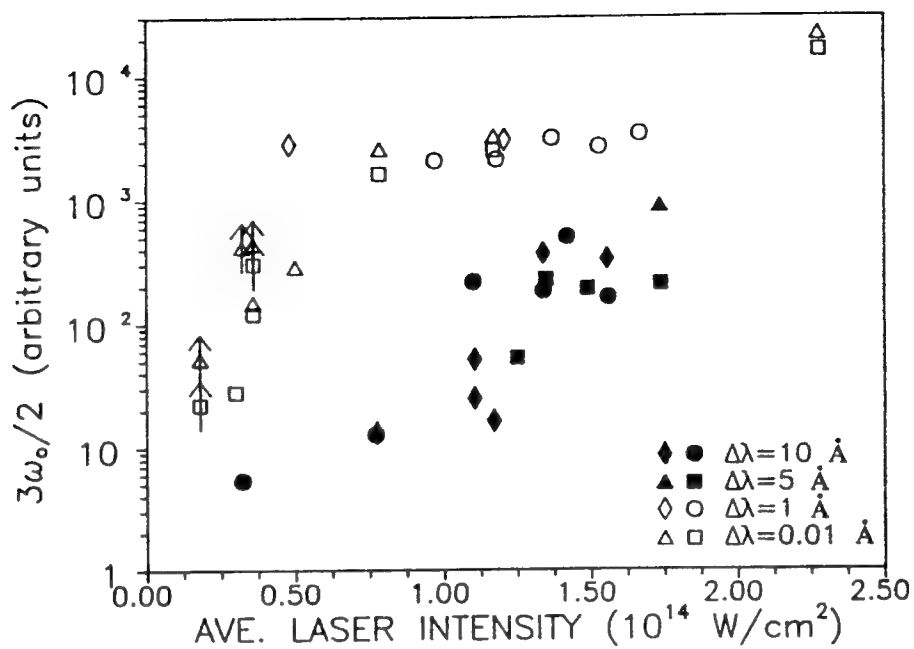


Fig. 7.10 — Time- and spectrally integrated  $3\omega_0/2$  signal for beam with ISI echelons at four bandwidths for two collection angles: circles and squares denote  $0^\circ$ , diamonds and triangles denote  $30^\circ$ .

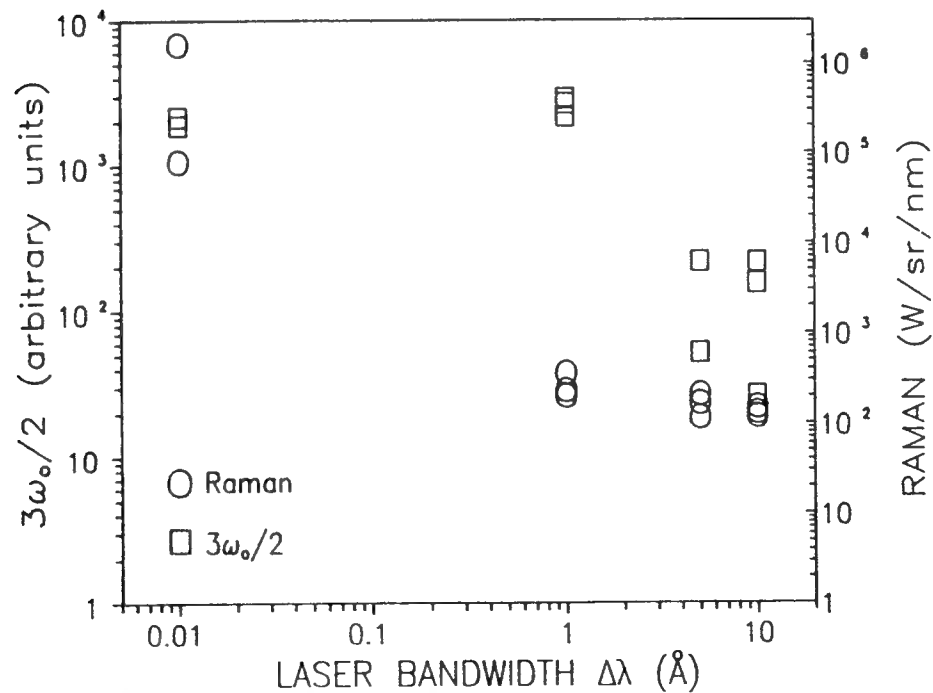


Fig. 7.11 — Comparison of Raman and  $3\omega_0/2$  signal levels at four bandwidths for an ensemble of shots with incident intensity between  $7.5 \times 10^{13} \text{ W/cm}^2$  and  $1.4 \times 10^{14} \text{ W/cm}^2$  showing significant reduction of Raman at narrow bandwidth compared with  $3\omega_0/2$ , which did not exhibit any substantial reduction in emission except at full laser bandwidth.

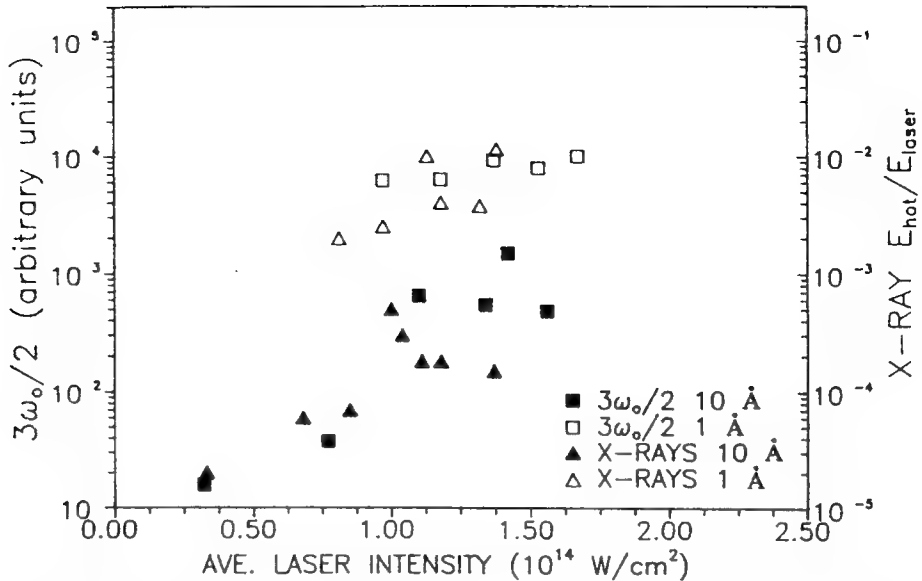


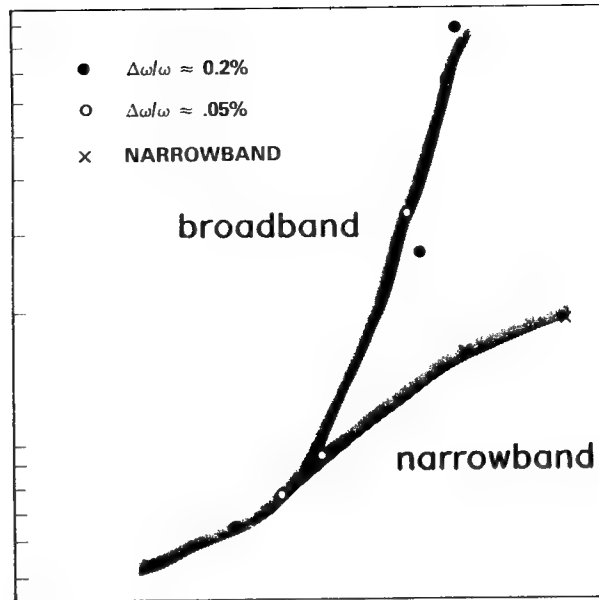
Fig. 7.12 — Correlation between time- and space integrated hard x-ray measurements (ratio of hot electron energy to the incident laser energy) and the  $50^\circ$  collection angle  $3\omega_0/2$  data at broad bandwidth and narrow bandwidth for the ISI-echelon beam.

x-rays are correlated with the  $(3/2\omega_0)$  emission and not the Raman emission it appears that the two-plasmon decay instability is responsible for the hot electrons observed in the green experiments. For the  $1.054 \mu\text{m}$  case the opposite is true. Hard x-rays increase with broader ISI bandwidths while  $(3/2\omega_0)$  emission is still quenched by the broad bandwidth. Apparently, the much lower absorption at  $1.054 \mu\text{m}$  permits substantial fractions of laser light to reach critical density and to excite critical density instabilities which are not quenched by ISI. This will be discussed in more detail in the next section.

#### ION-PLASMON DECAY, RESONANCE ABSORPTION AND $2\omega_0$ EMISSION

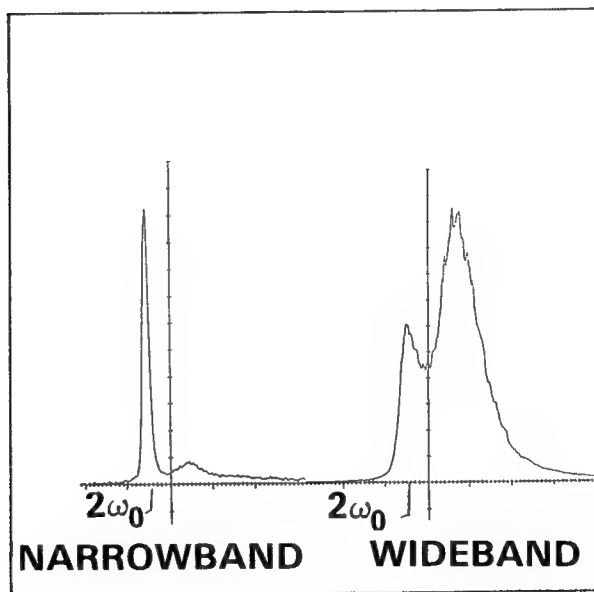
Both resonance absorption and ion-plasmon decay occur near or at the critical surface. They involve the decay of the electromagnetic wave into an electron-plasma wave or into an electron-plasma wave and an ion-acoustic wave. The scattering of the incident electromagnetic wave from an electron-plasma wave at critical density produces  $2\omega_0$  emission. These decay processes also produce hot electrons and may contribute to target preheat by hot electrons.

Arrays of detectors monitored the  $2\omega_0$  emission and the hard x-ray spectra. At  $1.054 \mu\text{m}$ , both the hard x-rays and the  $2\omega_0$  emission were observed to increase with bandwidth for ISI beams,<sup>7,15</sup> Fig. 7.13. As in the spectrum of Fig. 7.13b, the ion-plasmon component of the  $2\omega_0$  emission increased much more rapidly than the resonance absorption component. Since the broad bandwidths in this experiment are on the order of the ion-acoustic frequency it is presumed that increases in bandwidth increased the gain of the ion-plasmon decay instability by extending the range where the instability can operate with good energy and momentum matching. For experiments at  $0.527 \mu\text{m}$ , the deleterious effects seen with bandwidth increases at  $1.054 \mu\text{m}$  are reversed;<sup>7,16</sup> see Fig. 7.14. When ISI echelons are employed with broad bandwidth the hard x-ray intensity above 25 keV is reduced by at least 2 orders of magnitude to levels below the noise in the detector arrays. These measurements imply that the hot-electron temperature was reduced from about 20 keV without ISI to below 4 keV with ISI. In addition, the  $2\omega_0$  emissions were reduced by a factor of 50. As shown in Fig. 7.15, the shorter laser wavelength prevents light from reaching critical density and thereby suppresses any enhancements of hot electrons with bandwidth.



LASER ENERGY  
(JOULES)

(a)



(b)

Fig. 7.13 — (a) With  $1.054 \mu\text{m}$  illumination and ISI echelons bandwidth increases hard x-rays and (b)  $2\omega_0$  emission. The ion-plasmon component on the right increases more rapidly than the resonance absorption component on the left. The absolute amplitude of the spectra are normalized.

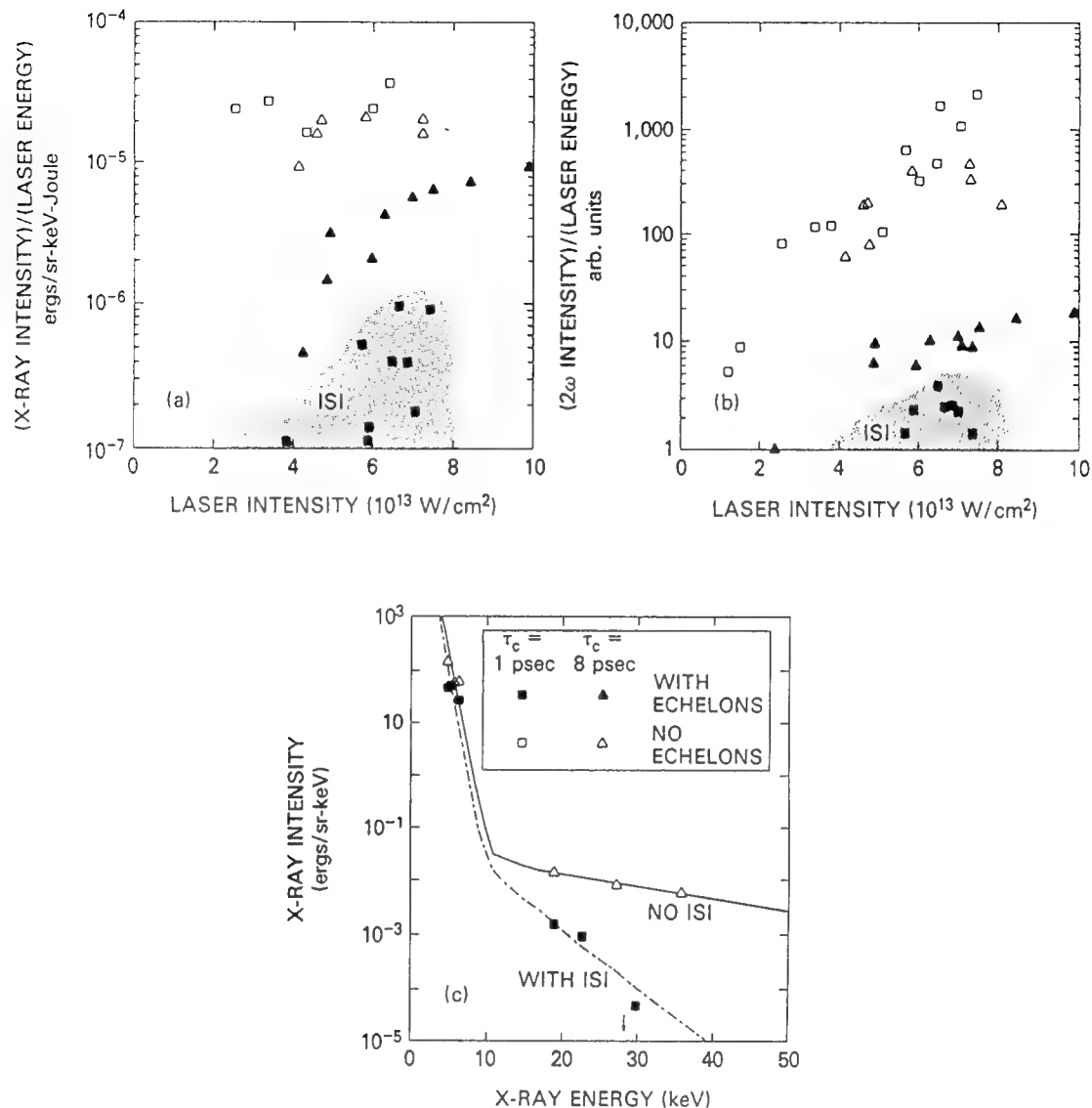


Fig. 7.14 — (a) X-ray emission near 25 keV as a function of laser intensity for  $0.527 \mu\text{m}$  illumination.  
 (b) second harmonic emission as a function of laser intensity. (c) Hard x-ray spectra with and without ISI for  $I \sim 7 \times 10^{13} \text{ W/cm}^2$ .

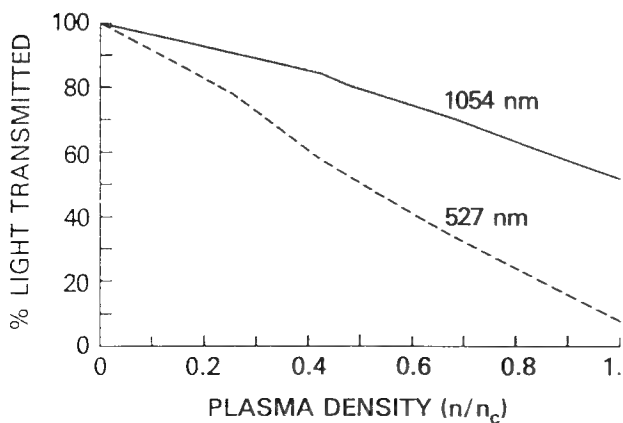


Fig. 7.15 — Calculated transmission of laser light through the blowoff plasma with a  $300 \mu\text{m}$  focal diameter and  $I \approx 10^{14} \text{ W/cm}^2$ . More light is transmitted to critical density with  $1.054 \mu\text{m}$  light than with  $0.527 \mu\text{m}$  light.

## CONCLUSIONS

For two laser beams with the same average intensity, one with broadband-ISI and one without ISI the levels of subcritical parametric instabilities was always found to be much lower for the ISI beam in the intensity range of  $10^{13}$  to  $10^{14}$  W/cm<sup>2</sup>. The parametric instabilities at critical density were not reduced by ISI if substantial laser intensities are found at the critical density as is the case for 1.054  $\mu$ m laser irradiation. However, the combination of short wavelength irradiation  $\lambda \leq 0.527$  and broad bandwidth ISI was found to be sufficient to control all subcritical and critical instabilities, and to reduce the hot-electron populations in plasmas irradiated in the  $10^{13}$  to  $10^{14}$  W/cm<sup>2</sup> intensity range of the experiments in this work.

The well-defined instantaneous and average intensity distributions of the ISI laser beams permitted meaningful comparisons of the measured instabilities with theoretical predictions. For the first time, the Raman instability was found to turn on at the thresholds predicted by the convective growth model of Raman in inhomogeneous plasmas. For SBS, the effectiveness of ISI in reducing backscatter was found to be much better than expected from theory. In fact, for all the parametric instabilities discussed in this work the theoretical growth time to saturation is shorter than the laser coherence time which is needed to make ISI effective. As a result, the reduction of these instabilities by ISI may be driven by reductions in laser filamentation which grows on time scales long compared to the laser coherence time.

## ACKNOWLEDGMENTS

This work was performed in collaboration with S. E. Bodner, J. H. Gardner, K. J. Kearney, R. H. Lehmberg, C. K. Manka, E. A. McLean, S. P. Obenschain, C. J. Pawley, A. J. Schmitt, and J. A. Stamper.

## REFERENCES

- 7.1 R. H. Lehmberg and S. P. Obenschain, Opt. Commun. **46**, 27 (1983).
- 7.2 M. S. Pronko, R. H. Lehmberg, S. Obenschain, C. J. Pawley, C. K. Manka, and E. Echart, IEEE J. Quantum Electron. **QE-26**, 337 (1990).
- 7.3 J. A. Stamper et al., in *Fast Electrical and Optical Measurements*, edited by J. E. Thompson and L. H. Luessen (Martinus, Nijhoff, Dordrecht, 1986), pp. 691-728.
- 7.4 B. H. Ripin, F. C. Young, J. A. Stamper, C. M. Armstrong, R. Decoste, E. A. McLean, and S. E. Bodner, Phys. Rev. Lett. **39**, 611 (1977).
- 7.5 A. N. Mostovych, S. P. Obenschain, J. H. Gardner, J. Grun, K. J. Kearney, C. K. Manka, E. A. McLean, and C. J. Pawley, Phys. Rev. Lett. **59**, 1193 (1987).
- 7.6 J. J. Thomson, W. K. Kruer, S. E. Bodner, and J. S. DeGroot, Phys. Fluids **17**, 849 (1974).
- 7.7 J. J. Thomson, Nucl. Fusion **15**, 237 (1975).
- 7.8 M. N. Rosenbluth, R. B. White, and C. S. Liu, Phys. Rev. Lett. **31**, 1190 (1973).
- 7.9 M. N. Rosenbluth, R. B. White, and C. S. Liu, Phys. Rev. Lett. **31**, 1190 (1973).
- 7.10 C. S. Liu, M. N. Rosenbluth, and R. B. White, Phys. Fluids **17**, 1211 (1974).
- 7.11 D. W. Forslund, J. M. Kindel, and E. L. Lindman, Phys. Fluids **18**, 1002 (1975).
- 7.12 S. P. Obenschain, C. J. Pawley, A. N. Mostovych, J. A. Stamper, J. H. Gardner, A. J. Schmitt, and S. E. Bodner, Phys. Rev. Lett. **62**, 768 (1989).
- 7.13 Kent Estabrook and W. L. Kruer, Phys. Rev. Lett. **53**, 465 (1984).
- 7.14 T. A. Peyser, C. K. Manka, S. P. Obenschain, and K. J. Kearney, Phys. Fluids **B3**, 1479 (1991).
- 7.15 S. P. Obenschain et al., in Thirteenth International Quantum Electronics conference: Digest of Technical Papers, J. Opt. Soc. Am. **B1**, No. 3 (1984).
- 7.16 S. P. Obenschain, J. Grun, M. J. Herbst, K. J. Kearney, C. K. Manka, E. A. McLean, A. N. Mostovych, J. A. Stamper, R. R. Whitlock, S. E. Bodner, J. H. Gardner, and R. H. Lehmberg, Phys. Rev. Lett. **56**, 2807 (1986).

## Section 8

### SUPPRESSION OF PARAMETRIC INSTABILITY BY ISI: THEORY

P.N. Guzdar  
*University of Maryland  
 College Park, MD*

The ISI beam smoothing technique for achieving uniformity of intensity on target was devised to prevent seeding of short scale Rayleigh Taylor instability of expanding laser plasmas. However, one of the most pleasant surprises of the experiments is the suppression of the parametric instabilities, like Raman, Brillouin, and Two Plasmon; see Section 7. This has recently motivated theoretical investigations on the role of beam smoothing techniques like ISI on parametric instabilities.

The ISI method requires the use of a laser with finite bandwidth. However the bandwidths are at best comparable to the homogeneous growth rates of the Raman or the reactive quasimode (i.e., the modified Brillouin when the acoustic frequency is very small compared to the conventional SBS growth). Thus an investigation of the effect of bandwidth on parametric instabilities in inhomogeneous plasmas with both large and small bandwidths (compared to the homogeneous growth,  $\gamma_0$ ) was undertaken. The specific instability considered was the convective Raman. It was found that in the large bandwidth case, the convective amplification was independent of the bandwidth. The effect of the bandwidth was two-fold. It reduced the growth rate  $\gamma$  during the amplification phase ( $\gamma \sim \gamma_0^2/\Delta\omega$ ). However it broadened the interaction region, such that the overall amplification was independent of bandwidth.<sup>8.1,8.2</sup> For the small bandwidth case, the amplification can be significantly enhanced over that obtained from the time averaged intensity. This is because the intensity variation caused by the small bandwidths leads to a significant enhancement in the scattered wave intensity since it has an exponential dependence on the pump intensity. This is a

statistical enhancement of the amplification. The effect is clearly seen by looking at the distribution function for the amplification factor. For a given realization of a pump intensity with a finite bandwidth we can define the amplification factor  $A_i$  as

$$\frac{I_S}{I_{S_0}} = \exp[2A_i], \quad (8.1)$$

where  $I_{S_0}$  is the initial intensity of the scattered wave and  $I_S$  the intensity after the wave has traversed the interaction region. The average scattered intensity over  $M$  realizations is

$$\begin{aligned} \langle \frac{I_S}{I_{S_0}} \rangle &= \frac{1}{M} \sum_{i=1}^M \exp[A_i] \\ &= \int dA P(A) \exp[A]. \end{aligned} \quad (8.2)$$

In Fig. 8.1 we show the probability distribution  $P(A)$  vs  $A$  for (a)  $\gamma_0/\Delta\omega \ll 1$ , (b)  $\gamma_0/\Delta\omega \sim 1$ , and (c)  $\gamma_0/\Delta\omega \gg 1$ , for  $\gamma_0^2 = 1$ . The most interesting feature is that for the small bandwidth cases,  $\gamma_0/\Delta\omega \leq 1$ , the distribution function has a significant tail compared to the large bandwidth case. This is because of the fact that there are realizations which sample large intensity during the amplification phase which is short compared to the correlation time  $\approx 2\pi/\Delta\omega$  and hence get strongly amplified. The scattered intensity would be further enhanced since the tail of the distribution weighted by  $\exp[A]$  contributes significantly to the average. Thus to get a reliable estimate of the scattered intensity a knowledge of the distribution of  $A$  is imperative.

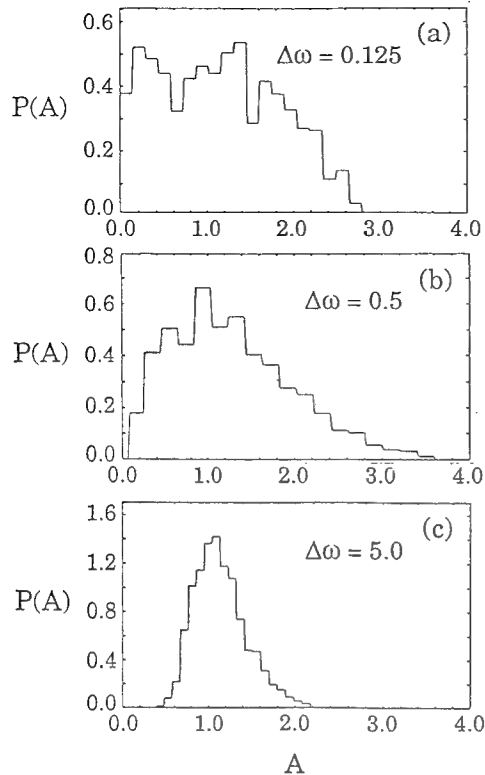


Fig. 8.1 — Probability distribution of the amplification factor for time averaged intensity  $\langle |\gamma_0^2| \rangle_T = 1$ : (a)  $\Delta\omega = 0.125$ ; (b)  $\Delta\omega = 0.5$ ; and (c)  $\Delta\omega = 5.0$ .

A two-dimensional [2d] study of the effect of ISI on the Convective Raman Instability has been completed. In this work, the incoherent pump wave propagating along the  $x$  direction, through an inhomogeneous plasma, excites a backscattered plasma wave and a forward propagating plasma wave. The structure of the pump in the transverse ( $y$ ) direction is a time varying, complicated speckle pattern. In Fig. 8.2 is shown the intensity of the scattered wave as a function of  $x$  and  $y$  for four different instants of time. The scattered light grows in the hot spots of the speckle pattern of the pump wave.

The pump wave keeps changing the location of its hot spot on the time scale of the correlation time, thereby producing a smoother time averaged intensity distribution. If the growth rate is less than the bandwidth, the excitation of the scattered wave, at the hot spot location, occurs for a short time. After the hot spots have migrated to a different location the growth of the scattered wave now has to be initiated in these new sites. This mitigates the dramatic growth of the scattered wave in the hot spots, had they been stationary and spatially correlated (which is what happens for very small

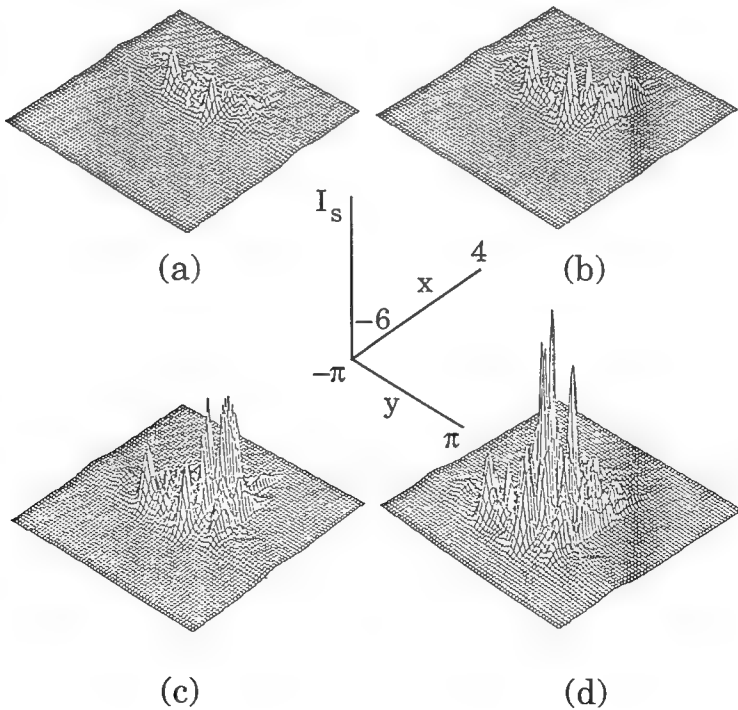


Fig. 8.2 — Intensity of backscattered wave as a function of  $x$  and  $y$  at four different instants of time with time increasing from (a) to (d).

bandwidths). The present study qualitatively captures the observed trends for Raman scattering. However, quantitatively the present model gives a much lower level of backscatter for the narrow bandwidth case compared to the observations. The limitations of the present model are that it is 2d and also that it does not account for the filamentation which channels the pump intensity into concentrated hot spots. In 2d the hot spots are typically  $\sqrt{N}$  larger in intensity than the average intensity. However in three-dimensions [3d] the intensity in the hot spots could be  $N$  times the average intensity. Also the existence of hot spots seeds the filamentation instability, which focuses the pump into narrow channels. The Raman amplification can be further enhanced in these channels. Thus a com-

bination of 3d effects as well as filamentation may resolve the present discrepancy. This will be studied in the future.

## ACKNOWLEDGEMENTS

My collaborators in this research are C.S. Liu of the University of Maryland and R.H. Lehmberg of the Naval Research Laboratory.

## REFERENCES

- 8.1 G. Laval, R. Pellat and D. Pesme, *Phys. Rev. Lett.*, **36**, 192 (1976).
- 8.2 P.N. Guzdar, C.S. Liu, and R.H. Lehmberg, *Phys. Fluids B*, **3**, 2882 (1991); *ibid* **5**, 910 (1993).

# **Laser Design Concept**

**53** **Nike Optical Design**  
*R. H. Lehmberg*

**57** **Nike Amplifier Staging**  
*S. P. Obenschain*

**61** **Analysis of Nike Image Quality**  
*T. Lehecka*

**65** **Scaling Laws for Nike Targets**  
*John H. Gardner*

## Section 9 NIKE OPTICAL DESIGN

R.H. Lehmberg  
*Laser Plasma Branch  
Plasma Physics Division  
Naval Research Laboratory*

The Nike laser is a 56 beam angularly-multiplexed system designed to produce flat-top focal profiles with a total energy of 3 kJ in 3-6 ns pulses. Forty four of the beams ( $\sim 2.2$  kJ) will overlap onto a planar foil target to ablatively accelerate it; the remaining 12 ( $\sim 800$  J) will be focused onto back- and side-lighters to produce X-ray illumination for plasma diagnostics. A schematic view of the optical train is shown in Fig. 9.1.

During the past year, an incoherent oscillator/front end system based on diffuse reflection was implemented to improve the reproducibility of the ISI object plane illumination.<sup>9.1</sup> This system, which is described in Sections 11 and 14, allows the routine production of very uniform focal profiles with spatial widths up to 100 times the diffraction limit (100 XDL), bandwidths  $\Delta\nu \sim 1$  THz, and temporal pulse shaping with a pulsewidth of 4 ns. Eventually, it will be split into two beam lines with independently adjustable ISI apertures and pulse shaping systems. The main line will provide 44 beams optimized for 3-4 nsec direct target illumination, while the second line will provide 12 beams of 5-6 nsec pulses optimized for diagnostic X-ray backlighting.

A single lens focuses the circular aperture  $F(x)$  at the object plane onto the Fourier transform plane, whose square aperture  $f(x)$  acts as the input pupil of the amplifier system. The beam from this pupil is expanded and relayed to a large aperture ( $4 \times 4 \text{ cm}^2$ ) discharge preamplifier. (The relay telescopes between these elements are not shown explicitly in Fig. 9.1.) A pair of neutral chromatic correction doublets, each consisting of a  $\text{MgF}_2$  convex lens and a

fused silica concave lens, can be placed at the input and output of this preamplifier when broader bandwidth operation is desired. The beam is then split and relayed into an array of three parallel large aperture discharge amplifiers identical to the one used in the preceding stage. (The fourth module of the array shown in Fig. 9.1 will be used to amplify the X-ray back-lighter beams.) Each of these modules, which are described in Section 15, has produced over 2 J in 15 nsec with very low distortion of the image profile. The output beams are split two-fold and differentially delayed by a stack of 8 folded image-relaying telescopes of unequal length and 2:1 magnification. An additional array of time delay mirrors again splits each of these beams to create 28 sequential beams, then feeds them to the  $4 \times 7$  input array of the angularly-multiplexed amplifier chain.

The angularly-multiplexed amplifier chain comprises two double-passed e-beam pumped stages, plus the associated transport optics. The diverging mirrors of the input array expand the 28 beams and overlap them at the concave rear mirror of the  $20 \times 20 \text{ cm}^2$  (driver stage) amplifier. This amplifier module is described in Section 17. Within the 120 nsec extraction time required for the sequential beams, it has produced 150 J with an input energy  $< 1$  J. At its output, a 50% beamsplitter creates an additional 28 beams, which will be delayed 120 nsec by a 1:1 off-axis reflecting telescope that images the beamsplitter onto an adjacent re-entrant mirror. The resulting 56 beams, which will extend over 240 nsec, will be overlapped at the concave rear mirror of the  $60 \times 60 \text{ cm}^2$  final amplifier by a single  $4 \times 14$  array of identical planar mirrors

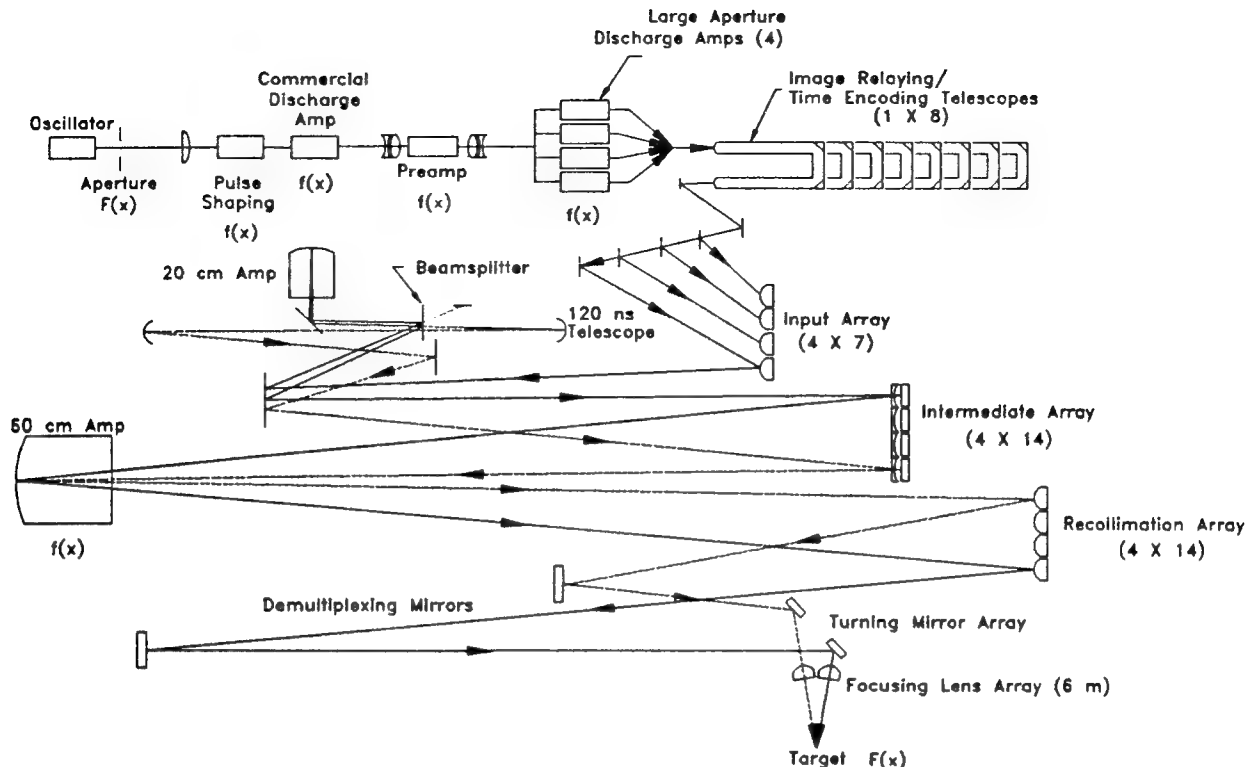


Fig. 9.1 — Schematic view of the Nike laser optical system, showing image locations of the object  $F(x)$  and optical Fourier  $f(x)$  planes.

and double-passed diverging lenses. The 60 cm amplifier, which is described in Section 18, is expected to provide up to 5 kJ laser output within 240 nsec.

A final  $4 \times 14$  array of diverging mirrors will recollimate the output beams with  $15 \times 15$   $\text{cm}^2$  widths, and direct them via the demultiplexing mirrors to the target chamber. The 44 (coincident) interaction beams will then be focused onto the planar target through a  $7 \times 7$  array of lenses (no lenses at the center or corners), while the remainder will serve as back-lighters. The back-lighter beams will come from the upper and lower rows at the recollimation array, where the shadowing losses in the final amplifier are large (12% to 22%). For the target interaction beams, these losses range from 0 to 19%.

Field angle divergences within the optical system are determined by the focusing lens array and the required spot size on target. Most target interaction experiments will require a spot diameter of  $600 \mu\text{m}$  in order to achieve the desired intensities ( $\sim 2 \times 10^{14} \text{ W/cm}^2$ ) with 3-4

nsec pulsewidths. The focal lengths were chosen to be 6 m, which will allow a reasonable depth of field around focus with the 2.2 m wide  $7 \times 7$  array. These conditions require a field angle divergence  $\Delta\theta_F = 100 \mu\text{rad}$ ; hence, the divergence scaled to the diffraction angle of the 15 cm beams will be  $\Delta\theta = \Delta\theta_F/(248 \text{ nm}/15 \text{ cm}) = 60 \text{ XDL}$ . The invariance of this quantity will determine the effective field angles in the entire optical system; e. g.,  $\Delta\theta_F = 25 \mu\text{rad}$  at the 60 cm amplifier.

The Nike optical design allows virtually complete compensation in each beam of all third order *systematic* phase aberrations (including a small amount of spherical aberration) over a 5 THz bandwidth.<sup>9,2</sup> Astigmatism and coma due to the off-axis optics will be compensated by tilting the lenses in the intermediate and focusing arrays, typically by angles less than  $3^\circ$ . Without this correction, the combined astigmatism and coma could be in excess of 15 XDL in some of the beams. The lens tilt angles need not be adjusted or maintained with high precision; spot diagrams show nearly complete compensa-

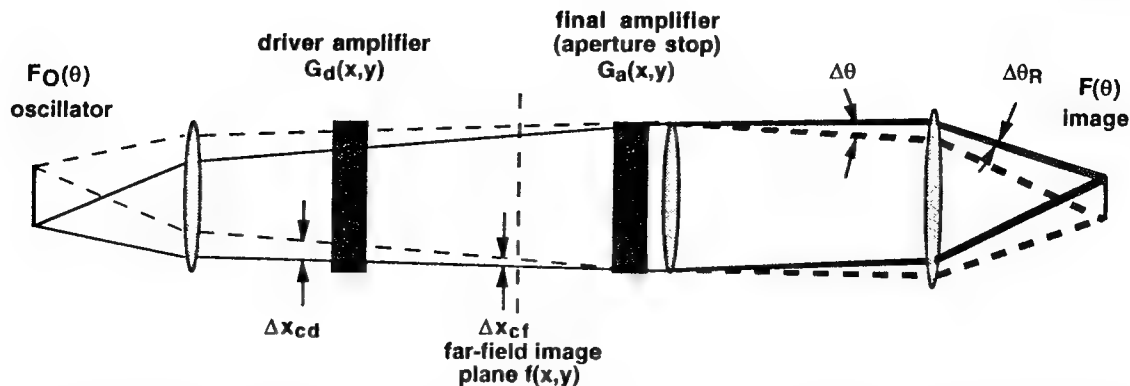


Fig. 9.2 — Illustration of image distortion: Amplifiers displaced from the far-field plane can partially imprint their gain nonuniformities, while beam divergence  $\Delta\theta_R$  from random phase nonuniformities can blur the image.

tion even for angular perturbations of 1 to 2 mrad.

As indicated in Fig. 9.1, the front end encoding telescopes are designed to image the Fourier (pupil) profile  $f(x)$  to the vicinity of the 60 cm amplifier, but not to the 20 cm amplifier. Imaging onto both stages would require the intermediate array to be replaced by either a pair of monolithic relay telescopes (resulting in excessive multiplexing angles at the 20 cm amplifier) or a cumbersome  $4 \times 14$  array of smaller telescopes and turning mirrors. This is unnecessary because the large beam sizes ensure that the two amplifiers will remain optically close to one another for all field angles of interest. With the 60 cm amplifier acting as the aperture stop of the system, and a 60 XDL angular divergence, the calculated chief ray displacement at the 20 cm stage remains within  $\pm 4$  mm. A 20% tilt in the gain profile of the 20 cm amplifier would then imprint only a 1% tilt onto the focal intensity profile.<sup>9,3</sup> The main penalty for this approach is a lower effective fill factor (65%) at the 20 cm stage. Although both

e-beam amplifiers are slightly overfilled in order to suppress ASE, the usable portion of the beams (i.e., the part that eventually clears the 60 cm amplifier aperture) must underfill the 20 cm stage to avoid focal spot distortion due to vignetting. This requirement is illustrated in Fig. 9.2.

## REFERENCES

- 9.1 A. V. Deniz, et. al., Proc. International Conf. on Lasers '93, STS Press (1994), p. 498.
- 9.2 R. H. Lehmberg and T. Lehecka, Proceedings of the IAEA Tech. Committe Meeting on Drivers for Inertial Confinement Fusion (Osaka, Japan, April, 1991).
- 9.3 R. H. Lehmberg, S. P. Obenschain, C. J. Pawley, M. S. Pronko, A. V. Deniz, and T. Lehecka, *Laser Coherence Control: Technology and Applications*. Proc. SPIE **1870**, 163 (1993), Edited by H. T. Powell and T. J. Kessler.

## Section 10

### NIKE AMPLIFIER STAGING

S. P. Obenschain  
*Laser Plasma Branch*  
*Plasma Physics Division*  
*Naval Research Laboratory*

In this section we will describe the amplifier system for Nike whereby output from the ISI oscillator system is amplified to high energy. The goal is to obtain sufficient laser energy on target for acceleration experiments ( $\sim 2.2$  kJ) and x-ray diagnostics ( $\sim 0.8$  kJ) while maintaining control of the laser pulse shape, the prepulse on target and the focal distribution. Here we will be treating the amplifiers as components of the Nike system. Detailed discussions of the individual amplifier design and performance will be provided in later sections.

KrF laser media has the properties of high gain, low saturation intensities (1 to 2 MW/cm<sup>2</sup>) and short excited state lifetimes (a few nsec). The short excited state lifetime and high gain lead to high levels of amplified spontaneous emission (ASE) if the lasing media is not nearly continuously loaded by extracting laser beams. The ASE is an energy loss, and if of sufficient level, could damage or alter the properties of targets prior to arrival of the intended interaction laser pulse. The short excited lifetime also means that the gain of the amplifier will closely mimic the pump for the excitation. We employ two laser-pumping technologies in the NIKE system. For the lower energy sections at the beginning of the amplifier chain, we employ discharge pumped amplifiers which provide gain pulses in the laser media of 15 to 30 nsec FWHM. We employ E-beam pumped amplifiers with 120 to 240 nsec gain durations to obtain high laser energy. The Nike design provides that the amplifiers are nearly continuously loaded by laser beams. This has the effect of suppressing ASE and minimizing the disturbances on pulse shape that a temporally varying

gain media would have. In this section we will discuss the amplifier staging including the design philosophy that led to the choices, and a summary of demonstrated performance and theoretical predictions. Section 16 deals with the status of our theoretical understanding of the KrF gain media and the predicted performance of the large Nike amplifiers.

#### FRONT END

Figure 10.1 shows the configuration of Nike from the ISI oscillator system through the discharged pumped amplifiers. The output from a multimode oscillator is used diffusely to illuminate the initial ISI aperture. See Section 14 for a discussion of the oscillator system. The Fourier transform plane from this ISI aperture is relayed into the center of the following discharge-pumped amplifiers. Because the energy from the diffusely illuminated aperture is too low (10's of nanojoules) to overcome ASE in the first amplifier with high contrast, the pulse shaping Pockels cell system is located after the first preamplifier. The temporal shape of the ISI beam is shortened from the nominal 20 nsec FWHM of the oscillator system via the Pockels cell. We plan to obtain a second beamline by splitting the output from the oscillator system and using a second Pockels cell system. The focal distribution on target for the two beamlines can be adjusted by placing apertures in the ISI object planes located within the relaying telescopes located between amplifiers. We thereby will have two beamlines with Nike which have independently variable pulse lengths and focal distributions. One beamline for example can be

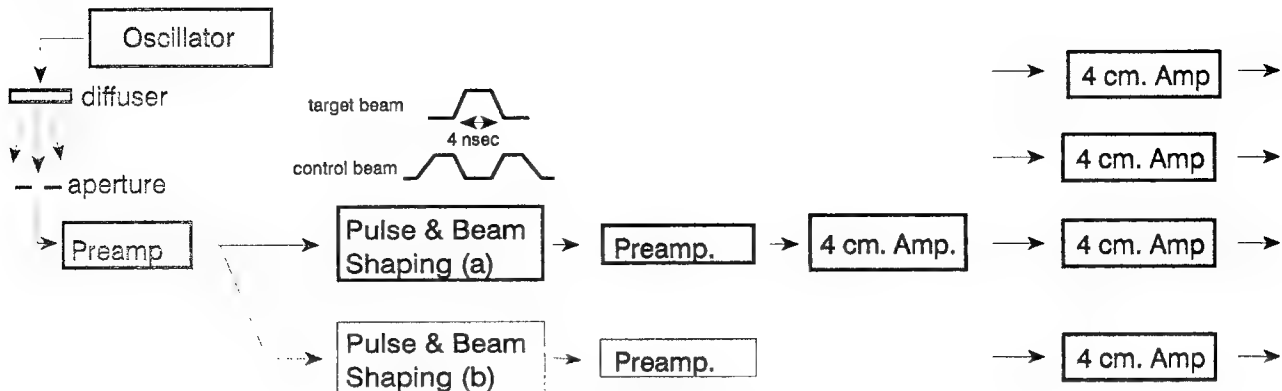


Fig. 10.1 — Staging of the Nike discharge-pumped amplifiers.

optimized for target acceleration while another is optimized for generating x-rays for backlighting.

The ISI oscillator-preamplifier and pulse shaping system provides a nominal few hundred microjoule 4 nsec pulse for the main target beam line. The main beam is first amplified by a 1 cm  $\times$  2 cm aperture commercial discharge amplifier followed by a 4 cm  $\times$  4 cm aperture amplifier developed at NRL. Finally the beam is split four ways and amplified by an array of four 4 cm  $\times$  4 cm aperture amplifiers. The alternate beamline when installed will utilize a single commercial preamplifier and a single 4 cm  $\times$  4 cm array module.

The discharge pumped amplifiers have gain pulse lengths of 15 to 30 nsec FWHM. This is advantageous for the planned pulse shapes for target acceleration that will likely include 5 to 10 nsec shaped prepulses before the main 4 nsec FWHM pulse. However, pulse distortion and unacceptable levels of ASE may result if the discharge amplifiers are not continuously loaded by an extracting beam. We obtain nearly continuous loading of the discharge-pumped amplifiers by means of a copropagating control beam. The control beam originates as the rejected beam from the first Pockels cell shutter. It is injected into the amplifier chain with its polarization rotated 90° with respect to the main beam and with a angle of a few milliradians with respect to the target beam. The control beam angle is arranged so that the control and target beams overlap in the center of the amplifiers. The timing of the two beams is arranged so that the

notch in the center of the control beam pulse is centered on the target beam. See Fig. 10.1. The series of relay telescopes used to relay the Fourier image in the optical train also cause the control and target beams to overlap in the following discharge pumped amplifiers. Since the originating oscillator pulse is as long as or longer than the amplifier gain pulse length, the amplifiers thereby see a nearly continuous extraction pulse. After the final discharge amplifier, the control beam is separated from the target beams by means of polarizers and spatial filtering. The final amplifiers have demonstrated more than 2 J output in 15 nsec FWHM pulses. We expect approximately 0.5 J output per array module for 4 nsec target beams or a total of 2.2 J total for the case of three 4 nsec target acceleration beams and a single 5 nsec duration backlighter beam. The optical configuration allows up to four additional array modules if additional energy is needed.

## **E-Beam Pumped Amplifiers**

The two high-energy amplifiers following the front end utilize double-sided E-beam pumping where the E-beam is guided by external axial magnetic fields. The first amplifier has a 20 cm square aperture and a nominal 120 nsec gain pulse while the second has a 60 cm square aperture and a 240 nsec nominal pulse length. The energy from these amplifiers is extracted by angularly multiplexed beams; 28 beams for the 20 cm aperture amplifier and 56 beams for the 60 cm amplifier. See Fig. 10.2. Both amplifiers

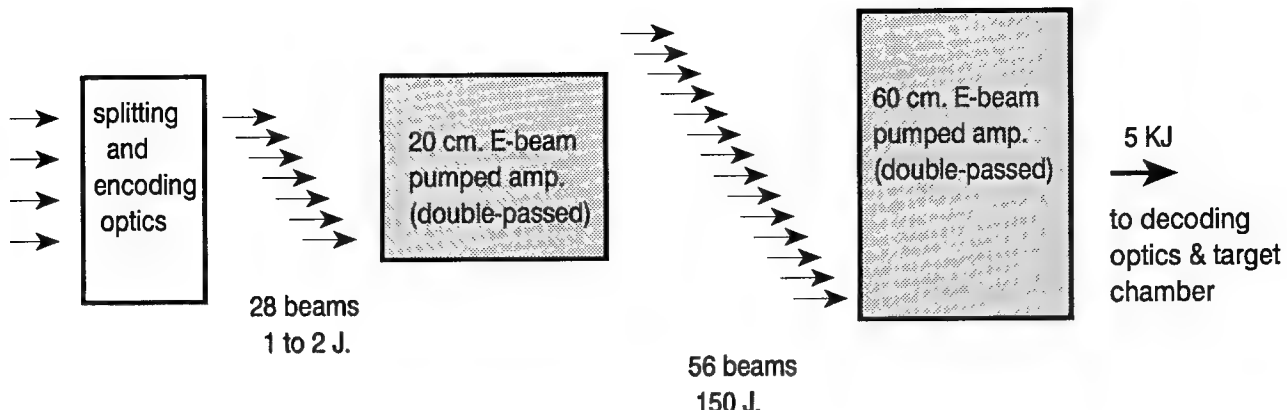


Fig. 10.2 — Staging of the Nike E-beam pumped amplifiers.

are double passed. The optical system includes a beam splitter near the input to the 20 cm amplifier that doubles the number of output beams from 28 to 56. This beam splitter introduces a factor of two loss between the front end and the 20 cm amplifier reducing the nominal 2 J output from the array amplifiers to 1 J. The baseline design for Nike calls for 130 J to 150 J output from the 20 cm. amplifier in 120 nsec with a 1 J input. We have obtained 120 J to 150 J output from the 20 cm amplifier with 1.4 J input and energies as high as 190 J output with higher input energies. It appears that the current system through the 20 cm amplifier will meet the energy requirements for Nike. However, we may elect to obtain more energy margin by increasing the number of array modules and/or

obtaining higher gain in the 20 cm amplifier by pushing the limits of its pulse power system.

The following 60 cm amplifier is under construction. The design calls for depositing 80 kJ of E-beam energy into the laser gas to obtain 5kJ of laser output. Calculations based on a kinetics model developed by M. McGeoch indicate that the design energy of the 20 cm amplifier provides a factor of two cushion for efficient extraction from the 60 cm amplifier. Figure 10.3 shows the expected output from the 60 as a function of input laser energy from the 20 cm amplifier. These calculations include the effects of ASE within the solid angle of the amplifier output windows and make use of kinetic predictions of gain and gain to loss ratios. These calculations are bracketed by

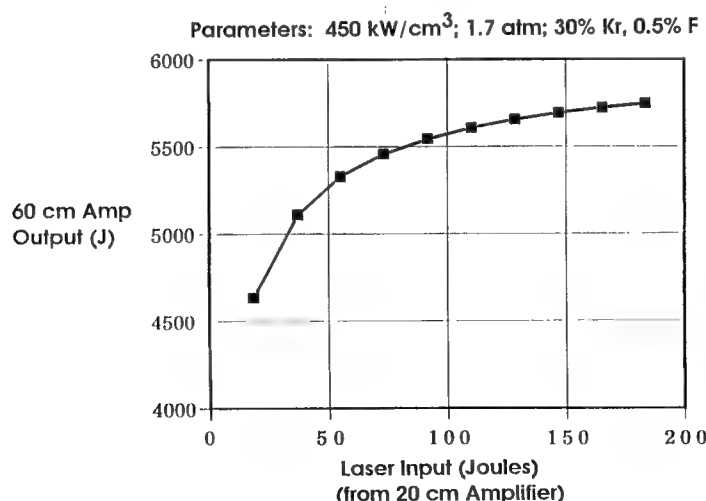


Fig. 10.3 — Kinetics code based calculation of the output from the 60 cm aperture amplifier as a function of input laser energy.

calculations conducted at Los Alamos and AVCO that predict 4 to 6 kJ output in 240 nsec. In order to obtain high energy with modest aperture the Nike 60 cm amplifier was designed to operate at high gain with relatively high saturation intensity ( $2 \text{ MW/cm}^2$ ). This will be achieved by the use of relatively high pumping rates ( $450 \text{ kW/cm}^2$ ) and high pressures (2 atm. for argon rich mixtures).

The uncertainty ( $\sim \pm 20\%$ ) in the predicted energy output from NIKE reflects the fact that the largest amplifier will utilize a parameter

regime of laser physics that is not heavily explored, and the lack of precise enough measurements of KrF kinetic parameters. Given the expected losses from amplifier to target, we would expect to have the 2.2 kJ available for target acceleration experiments (44 beams,  $2 \times 10^{14} \text{ W/cm}^2$  on  $600 \mu\text{m}$  focal diameters) with even the more pessimistic predictions. Some modest exploration of laser gas mixtures with the 60 cm amplifier should allow us significantly to exceed this goal.

## Section 11

### ANALYSIS OF NIKE IMAGE QUALITY

T. Lehecka  
*Science Applications International Corporation*

As of August 1993, approximately one-half of the final Nike laser system was operational and was undergoing beam uniformity testing. During the past year an ISI oscillator based on diffuse reflection was implemented to improve the reproducibility of the initial beam profile. This has allowed the routine production of very uniform focal profiles with spatial incoherence up to 100 times the diffraction limit (XDL). Details of this oscillator system are presented in Section 14. At present we are operating the laser up to and including the 20 cm amplifier to test the ISI concept, i.e. can we amplify the beam energy without significant distortion to the focal profile uniformity? The results of these experiments and the future plans for the system are discussed in this Section.

A block diagram of the experiments being performed is shown in Fig. 9.1 of Section 9. A spatially and temporally incoherent commercial KrF oscillator in the front end illuminates a Lambertian reflector. A small portion of the light from this reflection illuminates a circular aperture. The Fourier transform (diffraction plane) of this aperture is formed in the center of the first commercial discharge amplifier with a single lens. After amplification the Fourier image is relayed to a Pockels cell for temporal shaping of the pulse. The Fourier image is then relayed to a second commercial discharge amplifier.

The commercial discharge amplifiers have a tendency to impose a small ( $\sim 5\%$ ) linear tilt on the focussed beam. To overcome this difficulty, after the second amplifier the beam is split into two parts. One of these is focussed directly onto an aperture while the second is inverted in both the horizontal and vertical directions and then focussed onto the aperture. This aperture is the

object aperture for the rest of the system, which will be imaged onto the target. Superposition of the two beams should reduce the tilts below the desired 2% level. Results of this system will be discussed below.

A single lens again forms the Fourier transform of this aperture onto a square aperture which clips the beam to the appropriate dimensions for propagation through the remainder of the system. The size of the object and Fourier aperture, as well as the focal length of the lens between them, determine the beam divergence or number of times over the diffraction limit. For Nike experiments we plan to use focal spots in the range of 30-100 XDL, with a baseline of 60 XDL. The experiments described below were performed with 40 XDL beams.

The beam is expanded and the Fourier image relayed to a  $4 \times 4 \text{ cm}^2$  discharge amplifier (Section 15). After this amplifier the beam is split into four separate beams to begin the time multiplexing required for the electron beam pumped amplifiers (see discussions in Sections 14, 17 and 18). Two of these beams go directly to two  $4 \times 4 \text{ cm}^2$  discharge amplifiers while the other two are delayed by 64 nsec (via propagation delay) before going to another set of two  $4 \times 4 \text{ cm}^2$  discharge amplifiers. Telescopes in the beam paths relay the Fourier image from the preamplifier to this set of four discharge amplifiers.

After this set of four amplifiers, each of the beams is split in two and passed through an image relaying telescope. Each of these eight telescopes, in conjunction with the powered optics which direct the laser beams through the electron beam pumped amplifier stages, was designed to relay the Fourier image from the array of discharge amplifiers to the 60 cm

amplifier. These eight beams are then divided by beamsplitters into 28 beams. The temporal spacing for the first six beams (intended for backlighter use) is 5.33 nsec with 4 nsec spacing for the remaining 22 beams. This gives an effective pulse length of 120 nsec to drive the 20 cm amplifier.

It is important to note here that the 20 cm amplifier is not located at a Fourier image plane. However, because of the large beam sizes (and correspondingly small divergence angles) involved the optical distance from the 60 cm amplifier to the 20 cm amplifier is not large. The maximum deviation of extreme rays is calculated to be 1 cm in the 20 cm amplifier. If gain nonuniformities in this amplifier are less than 20% we would then expect less than a 1% ( $20\% \times 1\text{ cm}/20\text{ cm}$ ) tilt to be imposed on the beam. For this reason however, amplification in the 20 cm amplifier was thought to be one of the higher risk items in the Nike design, in terms of tilt, so we were particularly interested in obtaining focal profile data from this amplifier at the earliest possible date. The 60 cm amplifier lies closer to the Fourier plane, so we expect that any gain nonuniformities in that laser will have less of an effect on the focal spot uniformity.

When completed, the 28 beams emerging from the 20 cm amplifier will be split into 56 beams and then propagated to the 60 cm amplifier. At present we are directing these 28 beams to calorimeters, photodiodes and focal profile diagnostics.

A previous version of our oscillator has exceeded the beam uniformity requirements discussed above for a 60 XDL beam divergence. The present Lambertian reflector arrangement allows us to go to higher divergence while maintaining this beam uniformity. Later in this Section we will present results from amplification of this beam with the system described above. This data will show that we have successfully amplified the laser beam with insignificant distortion in the focal profile uniformity.

The main goal for the Nike laser is the production of uniform high intensity focal profiles for the acceleration of flat targets. Because we will be accelerating flat targets, we require a flat topped profile. The edges of this profile are

rounded by optical distortions (see Section 19), but this is, in fact, desirable for flat target accelerations because it helps reduce edge effects as discussed in Section 26. In our definition of beam uniformity we will therefore restrict our attention to the central region of the focal profile. The extent of the edge effects will be discussed below.

For this region of interest we assign three numbers to characterize the beam uniformity: peak to valley linear tilt; peak to valley first order curvature; and RMS deviation from a linear fit to the data. These numbers are obtained by performing a two dimensional linear and second order least squares fit to the appropriate region of interest. The maximum variation in the linear fit divided by the average value is defined as the tilt and the maximum deviation of the second order fit minus the linear fit divided by the average value is the first order curvature. The RMS error is simply the RMS deviation of the data from the linear fit divided by the average value. The goal for the Nike laser is: a tilt of less than 2% peak to valley; first order curvature less than 2% peak to valley; and less than 2% RMS deviation for each of the beams in the system. Overlapping multiple beams on target should reduce the RMS deviation even further.

The focal profile data described below were obtained in the following way. After amplification in the 20 cm amplifier, as described in the previous Section, one of the 28 beams is propagated through an aperture at a Fourier image plane. This aperture limited the beam to 40 times diffraction limited for these measurements. (Note that in the final system the 60 cm amplifier will act as the final Fourier image aperture.) This single beam is collimated to a 2.4 cm square size then focussed onto a CCD camera with an eleven meter focal length lens. This camera is a cooled, slow scan device capable of measuring RMS errors as low as 0.3%. The F# of the focussing lens is 458, resulting in an overall focal spot size of 4.5 mm for these 40 XDL beams. The residual speckle size is therefore  $4.5\text{ mm}/40(\text{XDL})$ , or  $113\text{ }\mu\text{m}$ , which is well resolved by the  $23\text{ }\mu\text{m}$  pixels of the CCD camera. The beam was attenuated by reflection from three uncoated flats (4% reflection per

surface) and propagation through a 95% and a 99% reflector. These attenuation methods have been routinely used in developing the Nike front end. A surface plot of the best focal profile obtained to date is shown in Fig. 11.1a, with horizontal and vertical cross-sections through the centroid of this profile in Fig. 11.1 b and c. Also shown in Figs. 11.1 b and c are the calculated focal profiles accounting for optical imperfections. They were calculated by taking the

interferograms available for the optics in the system and computer modelling the net effect of all the optics in the system to determine the point spread function (PSF). This PSF is then convolved with the initial aperture function. As is evident in the figure the model and data are in excellent agreement. Both the model and the data indicate that the optical system, described in the previous Section, is producing a seven times diffraction limited PSF at 248 nm.

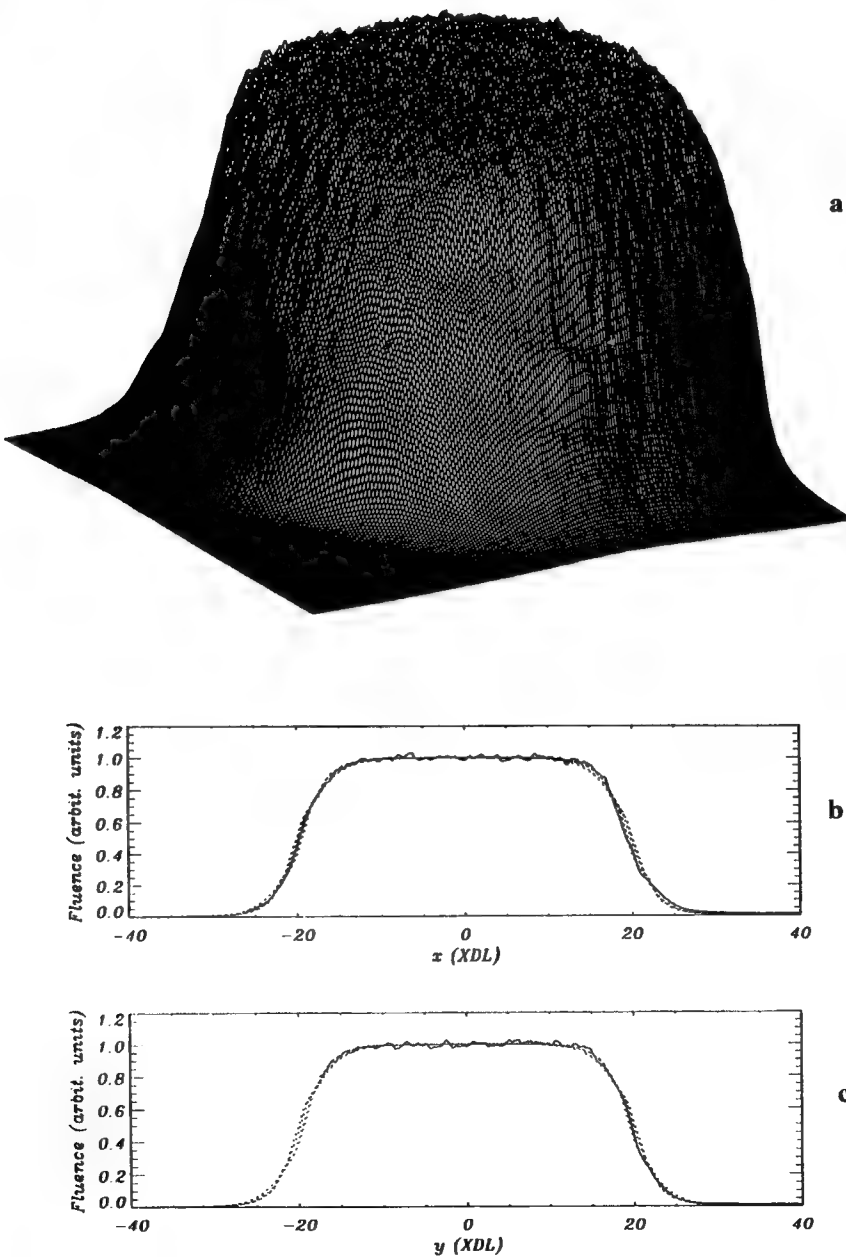


Fig. 11.1 — Focal profile after amplification in the Nike laser system up to and including the 20 cm amplifier. Solid lines are the measured profile cross sections, dashed lines are predicted profile for an ideal top hat convolved with a 7 XDL point spread function.

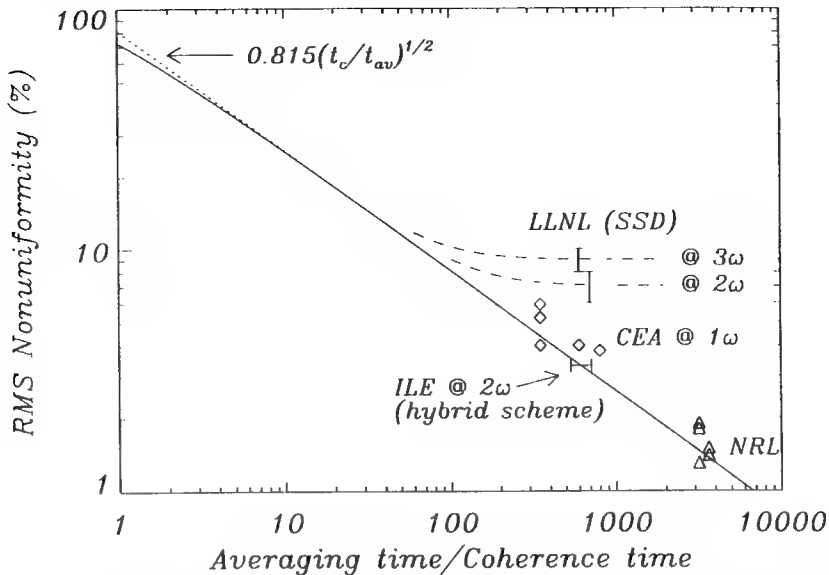


Fig. 11.2 — Comparison of beam smoothing experiments and theory.

The seven XDL PSF combined with the 40 XDL beam divergence yields a focal profile which should be uniform to less than 2% over the central 65% of the diameter. This is indeed the case for the focal profile shown in Fig. 11.1. The time averaged RMS nonuniformity for these four nanosecond FWHM pulses is measured to be 1.3% with a maximum linear tilt of 1.4%. The first order curvature is only 0.6%. These meet and exceed the Nike goals of 2% RMS deviation and 2% peak to valley tilt and curvature.

To compare this measured beam uniformity with theory the bandwidth of the laser after amplification was measured to be 0.8 THz FWHM, yielding a coherence time,  $\tau_c$ , of 1.25 psec. Using the formula discussed in Section 5,  $\Delta I_{RMS} = 0.815 \times (\tau_c/\tau_{pulse})^{1/2}$  and the measured pulse width of 4 nsec, an RMS deviation of 1.4% is predicted. This is in excellent agreement with the measurement of  $\Delta I_{RMS}$  of 1.3%. A plot of theoretically predicted beam uniformity along with data from this and other similar experiments is shown in Fig. 11.2. To the authors' knowledge, our measurements represent the highest degree of laser uniformity obtained at high energy to date.

As mentioned above these results are the best we have obtained to date (8/93) and this

level of uniformity was obtained on approximately 10% of the laser shots. They do, however, provide a proof of principle for the ISI concept on Nike. Typically we are obtaining tilts and curvatures of 5 to 6% from the front end and the 20 cm amplifier. At this time we believe the problem is in the front end. One of the commercial amplifiers has a severe degradation of the electrodes which is causing a highly nonuniform amplification. Because of the small beam size, and correspondingly large divergence, at this amplifier the ends of the amplifier are significantly removed from the Fourier plane. The focal profiles produced by this amplifier are not reliably meeting the Nike requirements. We are currently in the process of purchasing replacement components to repair this problem, which should improve the reproducibility of the front end.

#### ACKNOWLEDGEMENTS

The work described above was a collaborative effort with significant contributions from S.E. Bodner, A.V. Deniz, J. Hardgrove, R.H. Lehmburg, S.P. Obenschain, C.J. Pawley, and M.S. Pronko.

## Section 12

### SCALING LAWS FOR NIKE TARGETS

John H. Gardner

*Laboratory for Computational Physics and Fluid Dynamics  
Naval Research Laboratory  
Washington, DC*

There are a variety of parameters that can and will be varied, or held constant, for Nike laser-target experiments: laser power, laser intensity, target thickness, Rayleigh-Taylor e-folds, etc. This Section contains some simple analytic scaling laws that can be used to help design these experiments, and to help answer the question, "What if we varied ...." Comparison with more detailed hydrodynamic simulations shows that these simple scaling laws are surprisingly accurate — to a few percent.

For a constant laser intensity, the acceleration of the foil can be written:

$$\frac{d^2x}{dt^2} = \frac{P}{(m_0 - mt)}$$

where  $P$  is the ablation pressure and  $dm/dt$  is the mass ablation rate, assumed constant. The integral of this equation is contains a natural log function. However there is a rough approximation that works well for cases where approximately one-half of the mass is ablated (typical of direct drive experiments). We simply assume

$$x \approx C \left[ \frac{P}{m_0} \right] t^2$$

Analytically, the pressure  $P$  is usually derived to be proportional to  $I^{2/3}$ . However hydrodynamic computer simulations that better account for the details of the laser deposition are better fit by the relation

$$P = P_0 I^{0.8}$$

Substituting the equation for  $P$  into the equation for  $x$ , and normalizing  $C$  to the hydrodynamic simulations, one obtains

$$x = 880 \frac{I_{14}^{0.8} t_{ns}^2}{\rho_0 \Delta x_0}$$

where  $x$  and  $\Delta x_0$  are measured in microns,  $I$  is in units of  $10^{14} \text{ W/cm}^2$ ,  $t$  is in nsec, and  $\rho$  in gms/cc (set equal to 1 gm/cc for the remainder of this analysis). This formula can be useful for calculating the distance accelerated, which can then also be used to estimate the classical Rayleigh-Taylor e-folding.

A flat target can only be accelerated a limited distance before the edge effects destroy the flatness. The community only has limited knowledge on how far a flat foil can be accelerated before it loses its flat region. Our preliminary estimate is that the distance can be no more than the radius of the spot size radius  $R$ , defined by the relation  $W = I \pi R^2$ , where  $W$  is the laser power and  $I$  is the intensity in the center of the top-hat profile. If we place the restriction  $x = \alpha R$ , ( $\alpha \sim 1$ ), then the useful time duration of the experiment (the time for the foil to travel a distance equal to the spot size radius) is given by

$$t_{ns} = 0.8 \frac{(\alpha \Delta x_0)^{0.5} W_{TW}^{0.25}}{I_{14}^{0.65}}$$

For example, if the laser power  $W = 0.55$ , the intensity  $I = 2$ , and the target thickness  $\Delta x_0 = 80 \mu\text{m}$ , then the time to move the foil one radius is 3.9 nsec. Under this condition, that the

distance traveled equals the spot radius, one can easily derive

$$d(\mu m) = 564 \sqrt{\frac{W_{TW}}{I_{14}}}$$

Figure 12.1 plots  $t_{ns}$  versus  $\Delta x_0$  for  $x = R$ .  
 Figure 12.2 plots  $x$  versus  $\Delta x_0$  for a 4 nsec acceleration.

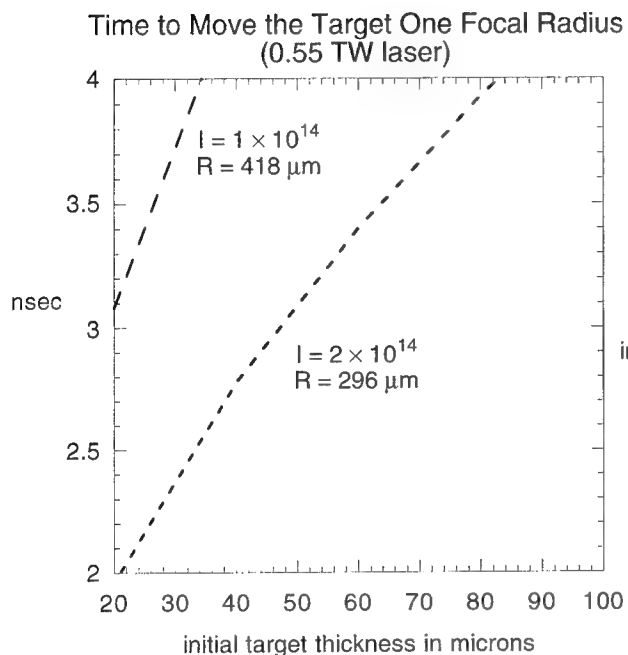


Fig. 12.1 — Two dimensional edge effects limit the distance and the useful time of acceleration of a foil target.

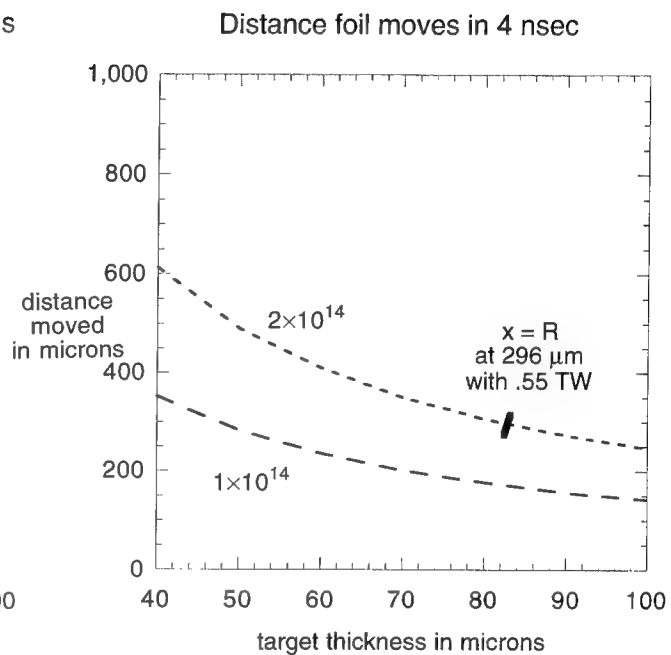


Fig. 12.2 — For a fixed laser intensity, the distance moved varies inversely with the initial target thickness. The maximum useful distance, with  $x = R$ , is indicated.

# **Nike Laser Facility and Progress**

**69      Floor Plan and Introduction**  
*S. P. Obenschain*

**71      The Oscillator and Pulse Slicing System**  
*A. V. Deniz*

**75      Large-Aperture Discharge-Pumped Laser Amplifier**  
*Mark S. Pronko*

**89      Amplifier Lasing Model**  
*M. W. McGeoch*

**113     20 cm Aperture Amplifier and Initial System Test**  
*C. J. Pawley*

**123     The 60 cm Amplifier**  
*J. D. Sethian*

**131     Propagation Bay**  
*T. Lehecka*

**135     Automated Beam Positioning System**  
*John Hardgrove*

**139     Nike Target Facility**  
*J. A. Stamper*

**147     Control System**  
*O. Barr*

## Section 13

### FLOOR PLAN AND INTRODUCTION

S. P. Obenschain  
*Laser Plasma Branch  
Plasma Physics Division  
Naval Research Laboratory*

In this section we briefly summarize the progress in development, installation and testing of the Nike laser system hardware by August of 1993. Details on the development of hardware for Nike are given in Sections 14 to 22. The amplifier system through the penultimate 20 cm aperture E-beam pumped amplifier had been installed and tested. Twenty-eight 4 nsec beams were angularly multiplexed through the 20 cm amplifier. The laser-gas cell and one of

two E-beam diodes for pumping the final 60 cm amplifier were completed. The remaining laser and target facility systems were in fabrication and completion of the facility scheduled for late 1994.

Figure 13.1 shows the Nike floor plan. The laser is contained in a 45 ft wide by 200 ft long enclosure while the target chamber will be housed in an adjacent 50 ft  $\times$  50 ft room. The long beam paths necessary for angular

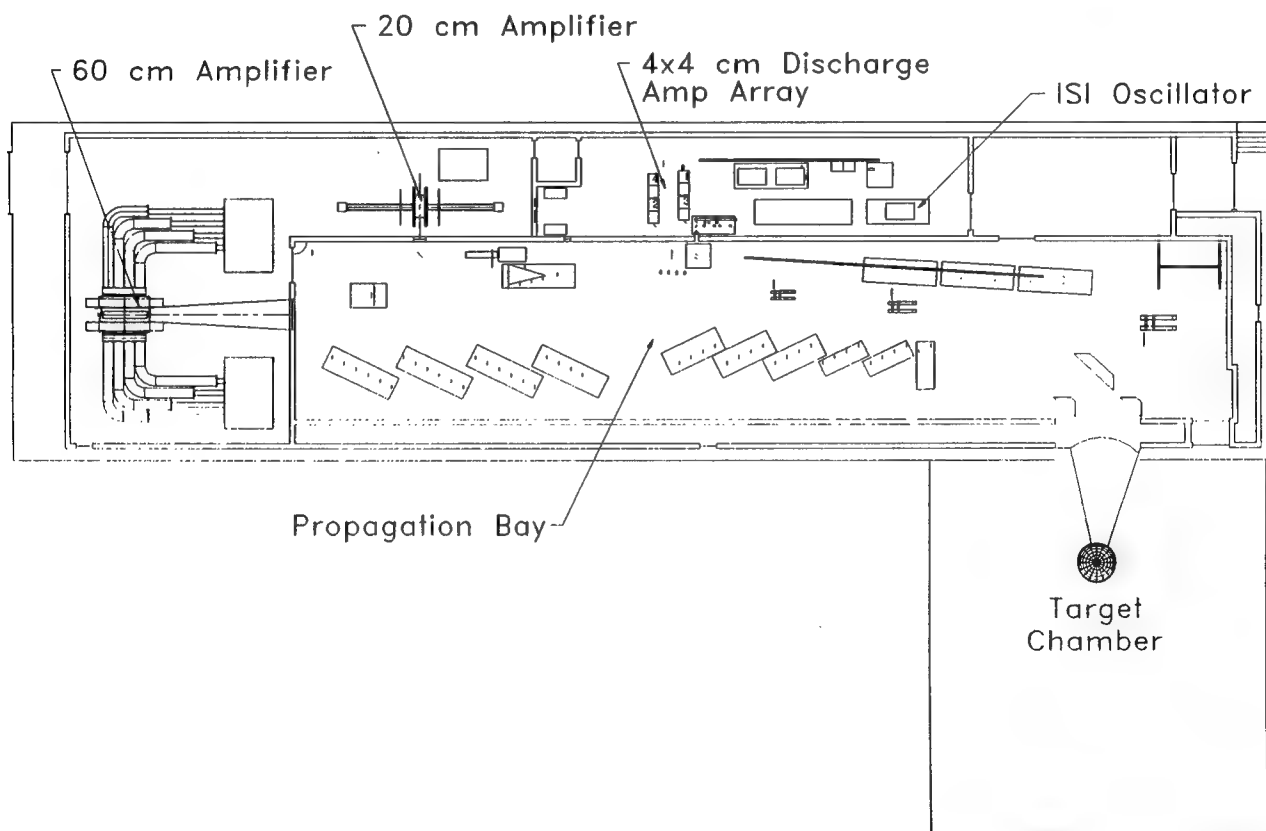


Fig. 13.1 — NIKE floor plan

multiplexing the two E beam amplifiers are enclosed in a double-walled structure called the propagation bay. (See Section 19.) The propagation bay has a specialized air conditioning system that provides a very quiescent atmosphere for the beam propagation. The oscillator discharge-pumped preamplifier system has reliably produced the flat-top highly uniform focal profiles desired for the facility. The 20 cm amplifier also produced the energy (120-150 J) required to extract energy from the following 60 cm aperture amplifier. The desired flat topped focal profiles have been demonstrated after amplification by the 20 cm amplifier, but the goal of <2% time-averaged nonuniformity was not obtained on most shots. Most shots with the 20 cm amplifier however did have good focal distributions ( $\leq 5\% \Delta I/I$ ) compared to earlier lasers. The main remaining goal for

the installed system through the 20 cm amplifier is to attain the 2% uniform focal profiles on a majority of shots. Tests on the 60 cm amplifier systems were well underway. The pulse-power system for the 60 cm amplifier demonstrated full voltage operation and the required E-beam deposition into the gas-cell (per diode) was achieved.

Other supporting systems and technology for Nike operation are also described in the following sections. A CCD camera system that can measure focal profiles with sub 1% resolution in intensity has been developed. A computerized beam alignment system has been developed that can automatically align the laser beams onto the mirror arrays in the propagation bay. An industrial based control system was adapted for control of the Nike laser amplifier and safety systems.

## Section 14

### THE OSCILLATOR AND PULSE SLICING SYSTEM

A. V. Deniz

*Science Applications International Corporation  
McLean, VA 22102*

#### ABSTRACT

We describe the Nike oscillator system which produces highly uniform flat-top focal distributions. With this system, time-integrated focal profiles with small long-scale-length non-uniformities are obtained. The nonuniformity was determined by performing a least-squares fit to a series of profiles, and calculating the deviation of each fit from a flat-top profile. The time-integrated uniformity meets the Nike requirements, and should be sufficient for high-gain direct-drive laser fusion.

#### I. DESCRIPTION

The Nike oscillator and pulse slicing system produces a 30 nsec linearly polarized beam, which includes the 4 nsec target beam that will illuminate the target. This target beam's polarization is orthogonal to the polarization of the rest of the beam (the control beam). The purpose of the control beam is to keep the discharge amplifier media loaded to minimize temporal pulse distortion of the target pulse. A

polarizer subsequently removes the control beam after it passes through the large-aperture discharge amplifier array so that only the target beam reaches the 20 cm Amplifier.

The flat profile is produced at the front end by illuminating the object aperture with the far-field of a diffuser, which is in turn illuminated by a 30 nsec pulse from a commercial broadband spatially multi-mode oscillator (Fig. 14.1). This illumination is ideal for Nike because each point of the object illuminates the subsequent Fourier plane (which is an image of the diffuser) with the same profile. The expected non-uniformity of the amplifiers (which are at or optically close to the Fourier plane) therefore has minimal effect on the image uniformity at the target. The energy from the diffuser is low ( $\sim 10$  nJ), but is enough to overcome the amplified spontaneous emission of the next amplifier.

The beam is amplified by a commercial amplifier. The target beam is produced by first linearly polarizing the beam, and then rotating the polarization by  $\pi/2$  for 4 nsec with a pockels cell at the fourier plane.

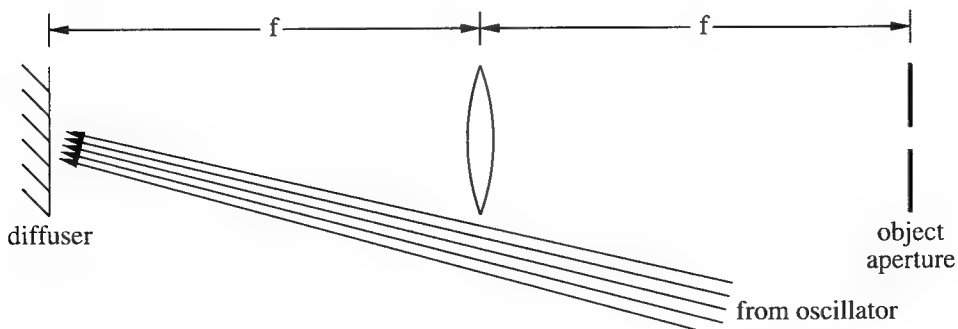


Fig. 14.1 — Illumination of the object aperture by the far-field of a reflective diffuser.

After passing through the second commercial amplifier, the target pulse's focal profile had a  $\sim 10\%$  tilt in the vertical direction, with  $\sim 5\%$  shot-to-shot variation. The tilts were caused by non-uniformities of the gain media of the commercial amplifiers. Both the tilt and variation were eliminated by splitting the beam into two beamlets, spatially inverting one beamlet, and recombining them.

## II. ANALYSIS

The focal profiles in this section are recorded after passing through the second commercial amplifier. They are then analyzed to determine the RMS uniformity and the long-scale-length variation (tilts). The following algorithm was used:

- (1) Determine the centroid  $(x_c, y_c)$  of the profile.
- (2) Find the edges of the flat region of the horizontal and vertical cross-sections through the centroid.
- (3) For the flat region of each cross-section:
  - (a) Perform a linear least-squares fit, and calculate the variation of the fit from a flat-top (tilt).
  - (b) Perform a quadratic least-squares fit, and calculate the mean-to-peak variation of the fit from a flat-top.
  - (c) Calculate the RMS deviation of the measured cross-section from the fits.

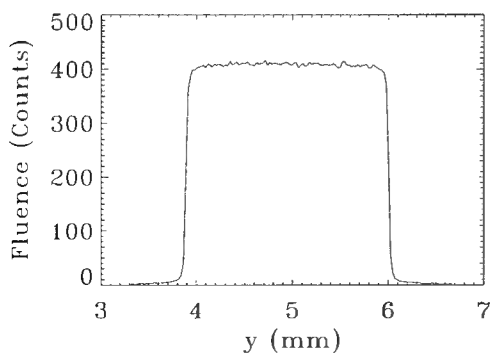


Fig. 14.2 — 80 XDL image of the object profile. The energy is  $\sim 10$  nJ, and the pulse length is  $\sim 30$  nsec.

The  $x$ -position of the centroid is determined by

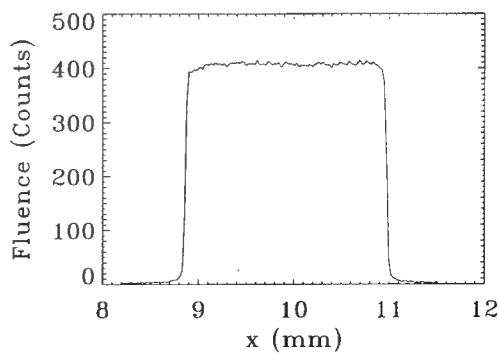
$$x_c = \frac{\sum_{i=1}^{N_p} x_i e_i}{\sum_{i=1}^{N_p} e_i}, \quad (14.1)$$

where  $x_i$  is the  $x$ -position of pixel  $i$ ,  $N_p$  is the number of pixels in the image,  $e_i$  is the signal at pixel  $i$ , and  $x_i$  is the  $x$ -position of pixel  $i$ . The calculation of the  $y$ -position of the centroid is analogous. The edges of the flat region of a cross-section are determined by the following algorithm:

- (1) Find the pixels  $l$  and  $r$  where the measured value of the cross-section is just greater than a specified fraction  $f_p$  of the maximum value.
- (2) The edges of the flat region are  $t$  pixels from  $l$  and  $r$  towards the center of the cross-section. For example, if  $l$  is the pixel on the left edge of the profile, and pixel numbers increase from left to right, the flat region is between pixels  $l + t$  and  $r - t$ , inclusive.

## III. PERFORMANCE

The object aperture is very uniformly illuminated by the far-field of a diffuser. Figure 14.2 shows the  $x$  and  $y$  cross-sections of the image of an 80 XDL test aperture. It is uniform, and has an RMS variation of 0.8% due



almost entirely to the noise in the CCD camera. The energy is on the order of 10 nJ.

After amplification by six orders of magnitude by the two commercial discharge lasers, the focal profile of the target beam has negligible tilt (Fig. 14.3), with an RMS variation again due almost entirely to the noise in the CCD

camera. The resulting target pulse has an energy of  $\sim 5$  mJ. This amplification with negligible distortion demonstrates the Nike system's ability to amplify profiles with high fidelity. The combined target and control beams are relayed to the first of two large aperture discharge amplifiers described in Section 15.

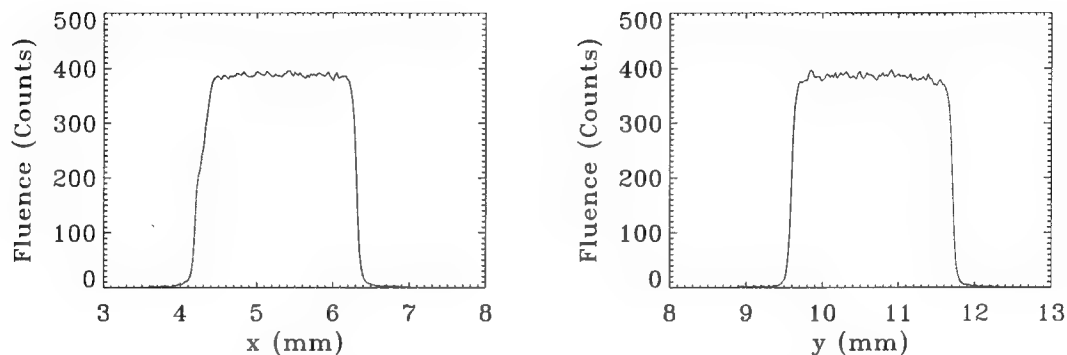


Fig. 14.3 — Images produced after two stages of amplification by commercial discharge lasers. The pulse length is  $\sim 4$  nsec, and the energy is  $\sim 5$  mJ.

## Section 15

### LARGE-APERTURE DISCHARGE-PUMPED LASER AMPLIFIER

Mark S. Pronko  
*Laser Plasma Branch*  
*Plasma Physics Division*  
*Naval Research Laboratory*

#### I. INTRODUCTION

High-pressure self-sustained electric discharge excitation is used extensively in excimer laser applications. These devices operate by producing a spatially uniform discharge in a high pressure gas mixture that is preionized by either UV or X radiation.<sup>15.1-15.13</sup> Typical commercially available high power discharge pumped lasers produce an output with a 30 ns long pulse duration and < 1 J in a 1 cm × 2 cm beam. The Nike system uses this type of laser for the oscillator and the first two stages of amplification, as discussed in Section 14. Additional higher peak power amplifier stages are required for efficient energy extraction from the first e-beam pumped amplifier. A large aperture x-ray preionized amplifier module was developed at NRL specifically for this application. The Nike design incorporates five of these modules, one is used as a pre-amplifier for an array of four modules operated in parallel (see Section 10 for a more detailed description of the Nike laser system design and performance).

Scaling these devices to larger aperture with higher output power is of particular interest for multiplexed laser fusion and short pulse amplification systems. However, the higher inductance intrinsic to an increase in aperture size limits the rate at which the electrical circuit can discharge current through the gas. This is a more stringent limitation in fluorine based excimer discharges since the discharge is stable for a shorter period of time than in other halogen gas mixes. Furthermore, nonuniform electric field distribution and the skin effect due to the discharge plasma

conductivity can affect gain uniformity. Several authors have discussed the requirements for maximizing power delivery to large aperture lasers;<sup>15.8,15.12-15.18</sup> the work presented here will emphasize a method for improving gain uniformity and its application to the Nike system.

The difficulties associated with obtaining uniform gain in large aperture discharge lasers have been observed previously.<sup>15.15,15.18</sup> In a uniformly preionized volume, the uniformity of the discharge current density is sensitive to the initial electric field distribution as well as the finite skin depth of the discharge plasma. In a typical arrangement where the electrode profile is predominately flat with some curvature at the edge, the field distribution can be enhanced near the electrode edge; this combined with the plasma skin depth can cause the current density to be higher along the edges of the discharge volume relative to the center. The net result is higher power deposition along the edges of the discharge volume resulting in a laser output profile similar to the one illustrated in Fig. 15.1. In some cases, a carefully selected electrode profile can compensate for these effects by providing a suitably adjusted initial electric field distribution. However, it is generally difficult to produce a uniform gain distribution with a square cross section using this method; typically the beam will have an aspect ratio (longest cross sectional dimension to the shortest) of two or three to one. Furthermore, simply adjusting the electrode profile is not always sufficient in lasers where the skin effect predominates. Large aperture devices are intrinsically susceptible to gain nonuniformity in this case since the

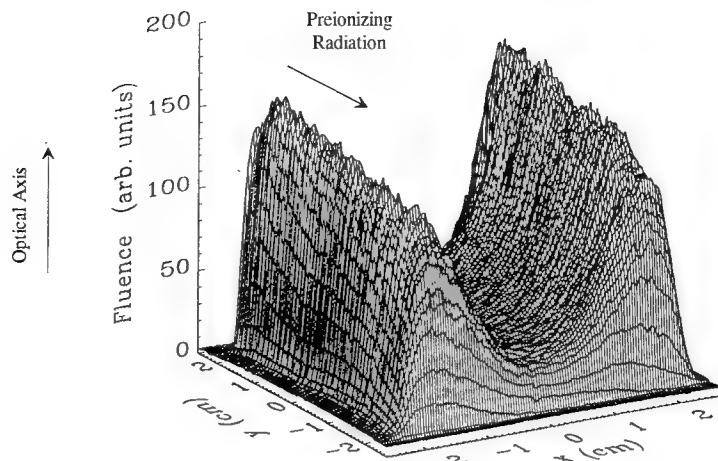


Fig. 15.1 — Time-integrated intensity profile of a uniformly preionized large aperture laser amplifier where electric field enhancement along the electrode edges and the skin effect limit the gain uniformity. The preionizing radiation enters the discharge volume through one of the laser electrodes.

discharge current duration can be short compared to the diffusion time of the current into the discharge volume.

Gain nonuniformity due to the effects described above can be controlled using the preionization distribution. It is well recognized that the extent of a discharge can be controlled by limiting the preionized volume.<sup>15,12,15,18-15,20</sup> This technique is used effectively in conventional lasers for controlling gain uniformity. Masking the preionization radiation in the high field region near electrode edges prevents discharge formation there; the resultant reduction in the transverse discharge dimension also minimizes the effect of the plasma skin depth. In both cases, the overall gain uniformity is improved. However, the resulting cross sectional aspect ratio of the output beam is typically greater than one, as was the case in the previous discussion. In some applications a square gain cross section (unity aspect ratio) is often most desirable (e.g., in laser fusion systems where the amplifier is part of a much larger optical system in which amplified spontaneous emission (ASE) from unloaded gain volume cannot be tolerated). A square beam simplifies the optical design since the aspect ratio remains constant throughout the system. In addition, it allows more efficient use of standard optical elements;

a rectangular beam requires larger diameter optical elements than a square beam of similar cross sectional area.

The results presented in this paper demonstrate a simple method for achieving a uniform gain profile with a square cross section in a large aperture laser. This is accomplished by shaping the preionization distribution using a combination of opaque and partially transmitting attenuators between an x-ray preionization source and the discharge. We describe the performance of a 4.25 cm  $\times$  4.25 cm clear aperture KrF laser amplifier which uses this novel, graded x-ray preionization technique. Since the source and attenuator materials are physically isolated from the harsh discharge environment, modifications to the attenuator configuration can be performed easily without disturbing the passivation of the laser, and the preionizer components do not contaminate the laser gas.

## II. EXPERIMENTAL DEVICE

The laser system (shown schematically in Figs. 15.2 and 15.3) consists of a discharge vessel, an array of peaking capacitors, an x-ray preionizer and two dc charged capacitor banks. An aluminum enclosure surrounds the components to allow the use of SF<sub>6</sub> for high voltage

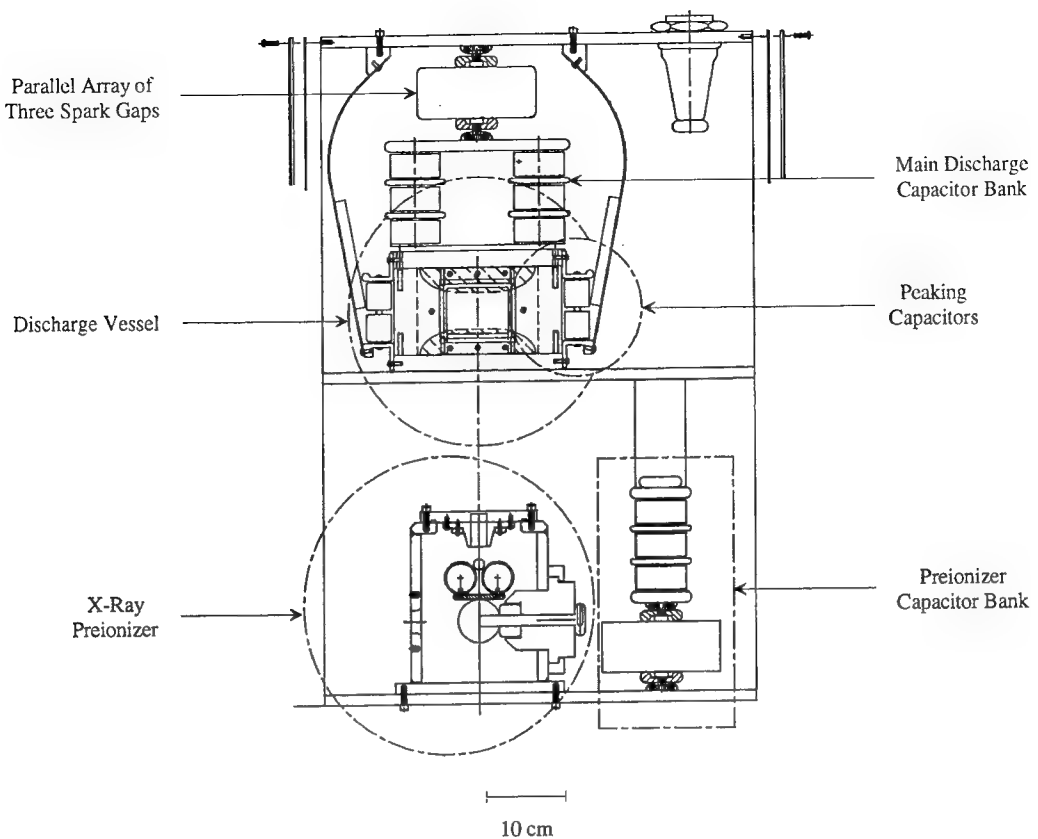


Fig. 15.2 — Cross sectional view of the laser amplifier.

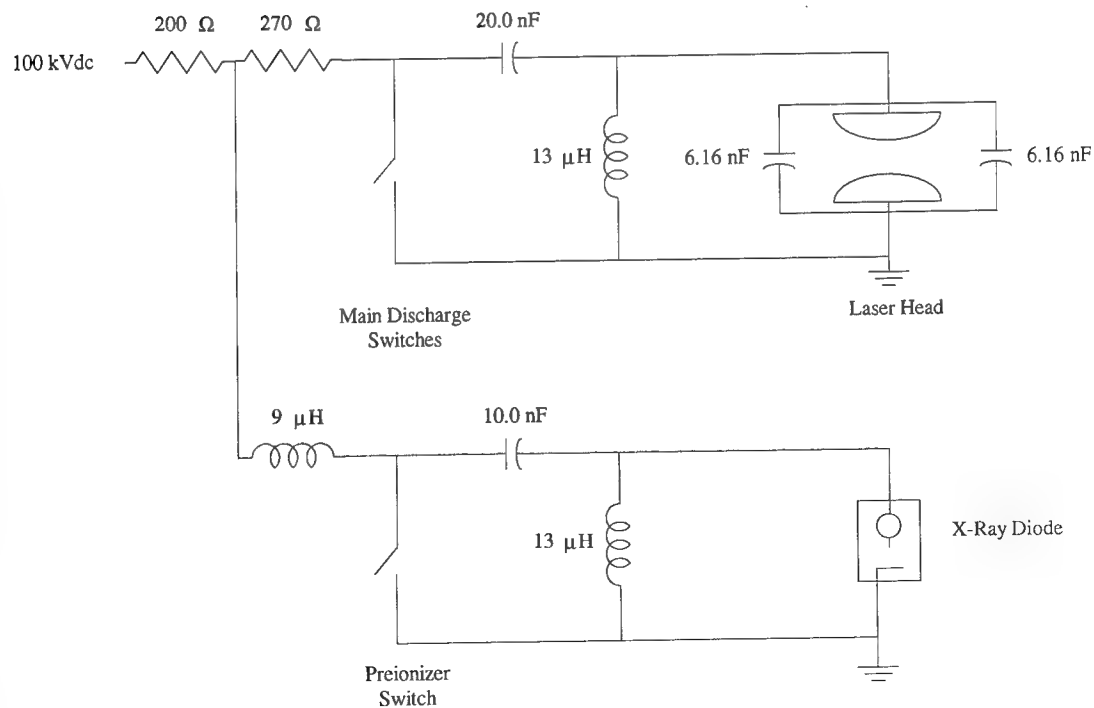


Fig. 15.3 — Equivalent electrical schematic of the laser amplifier. Trigger circuitry and bias resistors are omitted for clarity.

insulation and to provide electromagnetic shielding. The discharge vessel consists of a polyvinylideneflouride<sup>15,21</sup> body with aluminum electrodes separated by 4.25 cm. The amplifier has an active length of 80.0 cm with a clear aperture of 4.25 cm  $\times$  4.25 cm. The electrodes were originally designed using the method developed by Ernst<sup>15,22</sup> but were later modified to have a 4.0 cm wide central flat region. A 6.0 cm  $\times$  80.0 cm slot is milled into the back of one electrode to allow good transmission of the x rays into the laser cell. CaF windows (1.25 cm thick) are used to seal the vessel along the optical axis and are tilted at 11 degrees to suppress resonant feedback from the uncoated surfaces. Maximum output power was obtained with a laser gas pressure of 4.4 atm using a mixture of F<sub>2</sub>, Kr and Ne in the proportions 0.27/5.43/94.3, respectively. Less expensive helium buffered mixes were susceptible to arc formation and had lower output energy than the arc-free neon mixes. Large aperture, high pressure gas lasers are typically constrained to operate at a relatively low E/p (ratio of electric field to gas pressure); others have shown that for this operating condition better laser performance results with a neon buffer.<sup>15,8,15,10</sup>

Separate capacitor banks are used to store energy for the main discharge and the preionizer. Each bank is constructed similarly and consists of 2.0 nF strontium titinate ceramic capacitors. The main discharge and preionizer banks have total capacitances of 20.0 nF and 10.0 nF, respectively. The peaking capacitors located on either side of the discharge vessel are also strontium titinate and have a total capacitance of 12.32 nF (6.16 nF per side). Energy is transferred from the main discharge bank to the peaking capacitors using three UV-irradiated low-jitter spark gaps arranged in parallel. They are distributed along the length of the laser to reduce transit time effects caused by the high dielectric constant of the peaking capacitors. (A rail gap can be used in place of the discrete gaps; however, the uncertainty in the shot to shot variation of the number and distribution of arc channels could lead to variations in laser performance.) The voltage rises across the electrodes in  $\sim$  30 ns to  $\sim$  110 kV where the laser gas breaks down. Some voltage multiplication is

obtained due to an impedance mismatch between the main capacitor bank and the peaking array.

The x-ray preionizer is located 16 cm away from the discharge cell. It is a conventional forward scattered vacuum e-gun which uses a stainless steel screen anode and a carbon felt cold cathode emitter. X-rays are generated by thick target bremsstrahlung when transmitted electrons strike a 13 micron thick Ta foil target which is in contact with the output side of the anode screen. The emitter surface is supported by a 1.3 mm diameter brass rod and is 80 cm long. The A-K gap is set to 1.6 cm  $\pm$  0.25 mm over the length of the cathode. The expected maximum variation in the space charge limited diode current density is  $\pm$  3%. The diode is connected to the capacitor bank described above by a single UV irradiated spark gap identical to the ones used in the main discharge circuit. An impedance mismatch between the preionizer pulser and the diode allows the peak voltage to reach  $\sim$  80 kV for 50 ns producing x-rays with an effective energy of  $\sim$  55 keV. A dose of  $\sim$  100 mrad per shot was measured outside the discharge cell near the laser electrode using lithium fluoride thermoluminescent detectors. X-ray uniformity was measured at the diode output window using film. In as far as the developed film density is linear with exposure to x-ray wavelengths,<sup>15,23</sup> the x-ray flux is uniform to  $\sim$  5% along most of length of the diode with a gradual decrease in intensity near the ends.

### III. DISCHARGE UNIFORMITY

The compact design of the discharge circuit (comprised of the laser electrodes and the peaking capacitors) minimizes the circuit inductance in order to maximize the peak power delivered to the laser gas. For suitable conditions, this produces a fast rising current pulse for which the skin depth of the discharge plasma is comparable to the dimensions of the discharge volume. Qualitative evidence of the skin effect was observed early in the development of the laser. Initial operation was performed with an x-ray beam collimated at the laser electrodes to 4.0 cm  $\times$  80 cm. The resulting uniform preionization produced the output profile shown in Fig. 15.1. The laser electrodes were replaced

with a set which had a slightly more pronounced curvature along the axis. The curvature was sufficient to produce an electric field distribution on the electrode surface that was peaked along the axis and varied by a few percent over the central 5 cm width. The output profile was expected to follow the enhanced field along the laser axis. However, as the profile in Fig. 15.4 shows, the gain was increased along the axis but was still significantly stronger at the edge; this is consistent with a discharge dominated by the skin effect.

A rough estimate of the skin depth can be made using a measurement of the discharge current to calculate the lumped circuit resistance. A low inductance current shunt<sup>15,24</sup> in series with two pair of the peaking capacitors was used to measure the current pulse. A simplified schematic of the discharge circuit including the current shunt is shown in Fig. 15.5. The measured current waveform has a peak value of  $\sim 75$  kA and a half-cycle duration of  $\sim 18$  ns FWHM. The inductance of the laser head is estimated from its geometry to be  $\sim 12$  nH per

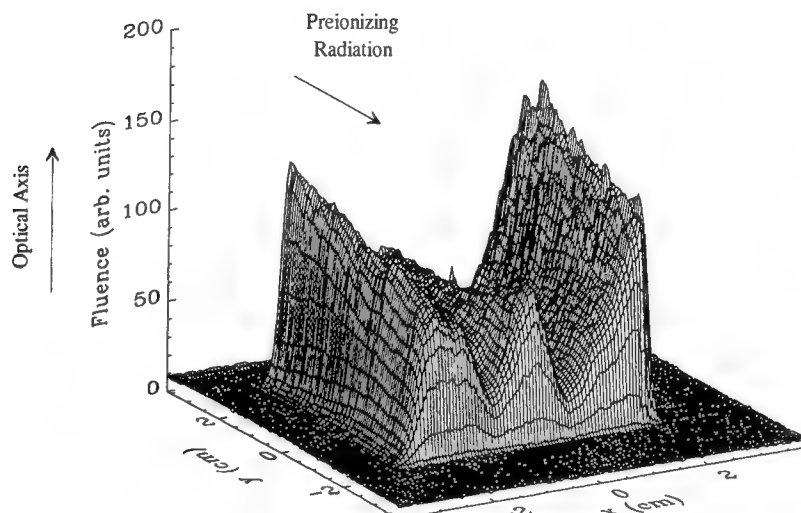


Fig. 15.4 — Output profile where the electric field is enhanced along the laser axis but dominated by the skin effect at the edge of the discharge volume.

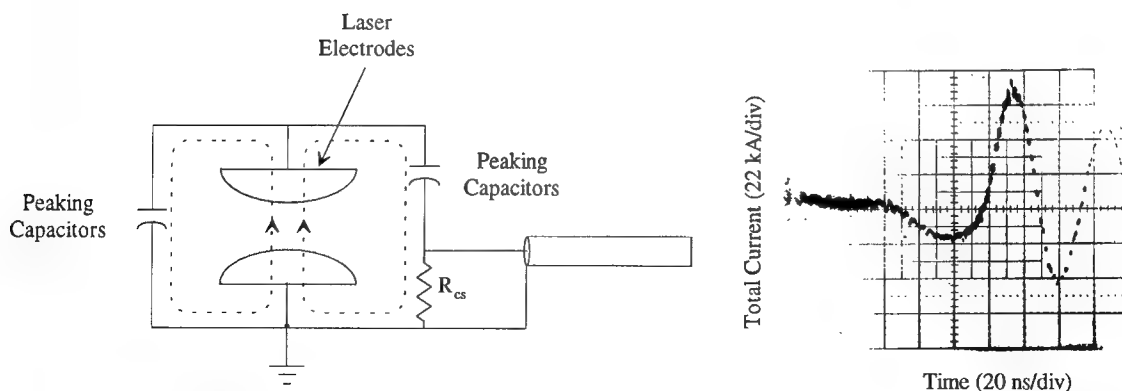


Fig. 15.5 — Cross section of the laser discharge circuit comprised of the peaking capacitors and the laser electrodes including the current shunt ( $R_{cs}$ ) used to measure the discharge current. The shunt is arranged in series with only two of the 28 peaking capacitors on one side. The current paths are indicated by the dotted lines. The initial negative polarity signal results from the pulse charging of the peaking capacitors before the laser breaks down.

half and agrees well with the measured period of oscillation. The most accurate method for calculating discharge resistance is to find the ratio of discharge voltage to current. The voltage can be inferred from the peaking capacitor voltage when corrected for the inductive voltage drop due to  $dI/dt$ . In our case, a poor signal to noise ratio severely limited the accuracy of our voltage measurement. An alternate method which is accurate enough for our purpose is to calculate the total circuit resistance from the damping observed on the current pulse. From Fig. 15.5, the damping is consistent with a resistance of  $\sim 0.1 \Omega$ ; it consists of the discharge resistance, contact resistance between circuit components and ohmic losses in the peaking capacitors. The latter two losses are estimated to account for up to 20% of the total resistance. Discharge parameter measurements performed on similar devices<sup>15.8,15.15,15.17,15.25-15.27</sup> qualitatively agree with this estimate.

To a first approximation, the weakly ionized plasma of a laser discharge can be modeled as a simple conductor where the conductivity is uniform throughout. The skin depth  $\delta$  for this case is<sup>15.28</sup>

$$\delta = \sqrt{\frac{2}{\omega \mu \sigma}} \quad (15.1)$$

where  $\omega$  is the frequency of oscillation and  $\mu$  is the permittivity. The conductivity,  $\sigma$ , relates the skin depth to the macroscopic discharge resistance through<sup>15.29</sup>

$$R = \frac{l}{\sigma S} \quad (15.2)$$

where  $R$  is the discharge resistance,  $l$  is the discharge electrode separation and  $S$  is the effective area of the discharge perpendicular to the direction of current flow. In general,  $S$  is a function of  $\delta$ ; but, if  $\delta$  is comparable to the discharge width, a good approximation for  $S$  is given by the product of discharge length and width. For this simple model, the skin depth of the laser discharge is calculated to be  $\sim 3$  cm using  $R = 0.08 \Omega$ ,  $\mu = \mu_0$  (the permittivity of free space),  $\omega$  corresponding to the current pulse in Fig. 15.5 and the discharge dimensions.

Given that laser gain is proportional to pump power, the skin depth calculation leads one to expect an output profile somewhat more uniform than measured (see Fig. 15.1). The discrepancy can be accounted for by considering spatial nonuniformity in both the discharge conductivity and the initial electric field distribution. In a realistic discharge plasma, the conductivity is a function of the electron density  $N_e$  and the electron mobility  $\mu_e$ <sup>15.30</sup>,

$$\sigma = -eN_e\mu_e \quad (15.3)$$

where  $e$  is the electronic charge. The mobility depends primarily on the electron collision frequency which is a function of both the gas composition and electron energy; it is assumed uniform throughout the volume once the discharge is established. The spatial variation of the electron density is much more sensitive to operating conditions. The initial magnitude and spatial uniformity is determined by the preionization source. When an electric field is applied, an avalanche process increases the electron density in a manner determined by the initial density distribution and the local electric field strength. The higher field strength present in the inter-electrode space before transition to a self-sustained discharge can amplify initial density nonuniformities. Additional nonuniformity determined by the details of the field distribution can also develop. In spite of these conditions, the avalanche process can quickly develop into a relatively arc-free discharge which is not necessarily spatially uniform.

Once the discharge is established, the effect of skin depth on the current density is complicated by the dependence of conductivity on plasma electron density. As a simple illustration, consider the case where the initial electron density is perfectly uniform; thus, the initial conductivity given by equation 15.3 is spatially uniform. (A uniform initial electric field distribution is also assumed.) As the current distribution develops, the skin effect causes more current to flow near the edges of the discharge resulting in higher electron density and correspondingly higher conductivity. Thus, for this simple example, the skin depth is

inversely related to the local current density resulting in an apparent skin depth that is smaller than predicted by equation 15.1.

In the next section we will show that suitable tailoring of the preionizing radiation flux is effective for controlling laser gain uniformity in the presence of the effects discussed above.

#### IV. LASER OUTPUT UNIFORMITY

The output energy of a rare gas halide laser has been shown to depend logarithmically on the initial preionization electron density.<sup>15,10,15,20</sup> The graded preionization technique applies this dependence to localized regions of the gain volume to improve the overall uniformity of the output. Electron density is reduced by attenuating the x-ray flux in regions of the discharge that would otherwise have higher gain. Implementation of this technique using a uniform x-ray source is relatively straightforward and is illustrated in Fig. 15.6. The x-ray attenuator is shown here as a discrete set of Pb and Al strips arranged in a staircase configuration. The maximum extent of the preionized region is defined by the Pb strips; the variable transmission of the additional Al strips attenuate the x rays from their maximum along the laser axis. An iterative process was used to

adjust the width and thickness of the individual Al strips for best results. The near field output profile (time integrated over the duration of the pulse) was measured with the arrangement shown in Fig. 15.7. The input beam had a peak  $I/I_{sat} \sim 0.1$ , an angular divergence of  $< 1$  milliradian and an intensity nonuniformity of  $\pm 20\%$  (peak to valley); the input beam also completely filled the geometric input aperture of the amplifier. The amplifier output was attenuated using first-surface reflections from uncoated high optical quality wedges and imaged onto a CCD camera. The profile presented in Fig. 15.1 shows the output of the amplifier when the volume is uniformly preionized (only the Pb strips used); spatial modulation greater than 60% is evident with the highest gain regions along the discharge volume edges. A significant improvement in the output uniformity (shown in Fig. 15.8) is achieved when the Al attenuator strips are added. The operating conditions (with the exception of the x-ray attenuator arrangement) were the same in both cases. It is clear from the two profiles that the Al attenuators increase the gain in the central region of the beam while decreasing it along the electrode edges. This is supported by the similar laser energy measured for both cases. It also suggests that a change in the preionization distribution does not have much of an effect on the

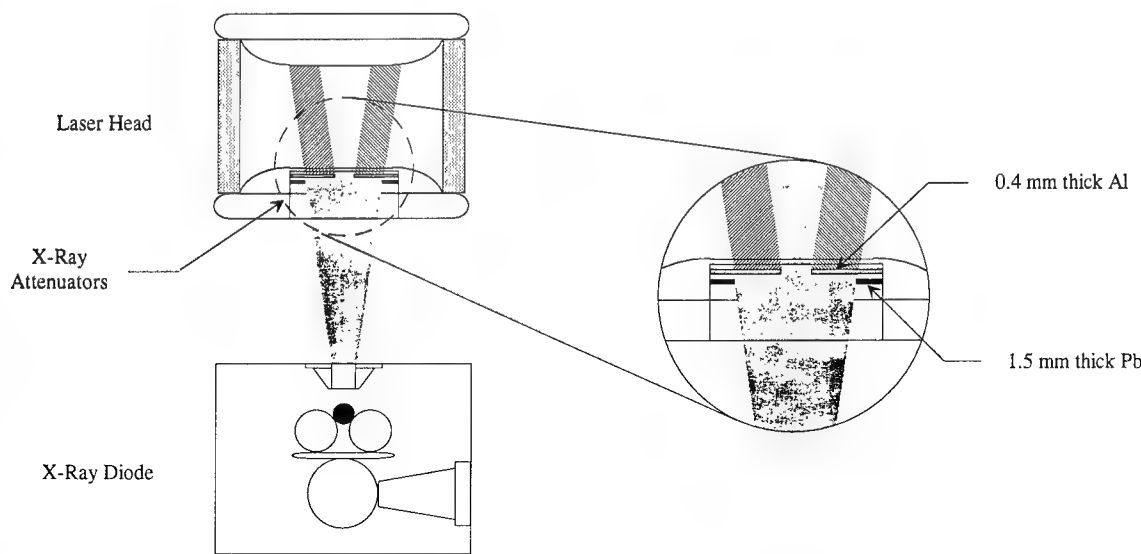


Fig. 15.6 — Schematic illustrating the graded preionization technique. The Al and Pb attenuators extend the length of the laser electrodes.

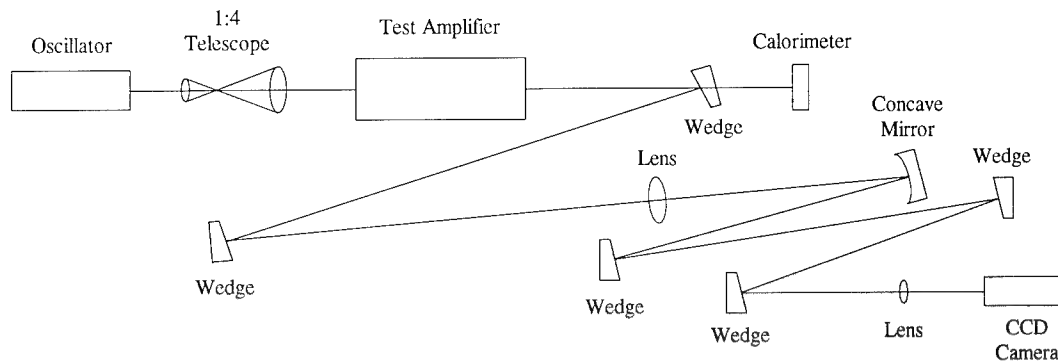


Fig. 15.7 — Experimental arrangement for measuring saturated laser amplifier gain uniformity. The output of the amplifier is attenuated by  $\sim 10^7$  using first surface reflections from uncoated optical wedges. The overall system magnification from the amplifier output to the CCD camera is  $\sim 0.1$ .

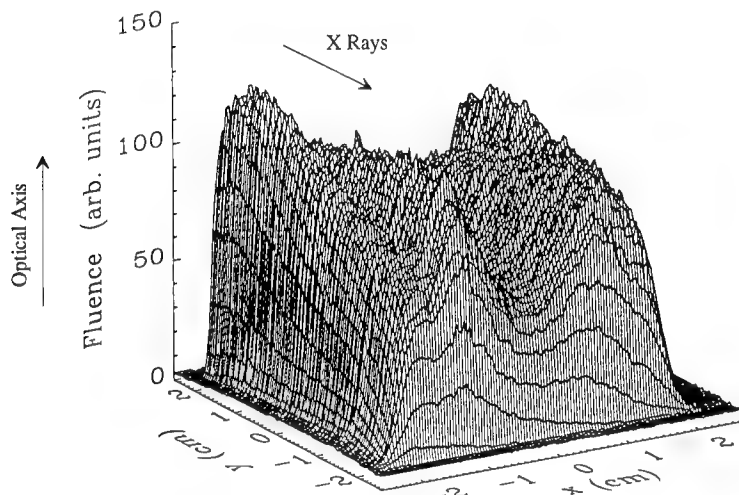


Fig. 15.8 — Output profile with graded preionization. The gap separation between the Al and Pb attenuators (illustrated in Fig. 15.6) are 2.3 cm and 4.0 cm, respectively.

total power delivered but changes its distribution in the volume.

A somewhat more uniform distribution was obtained by adding a short tapered Pb section to the attenuator arrangement as shown in Fig. 15.9a. In addition to grading the x-ray flux over the length of the laser, the higher gain region arising at the edge of the preionized volume is varied across the aperture along a short length of the device. The resulting output profile is shown in Fig. 15.9b. The effect of the tapered section is analogous to propagating off-axis through an amplifier which has a gain region with a large aspect.<sup>15.31</sup>

The initial preionization density has also been shown to have a weak effect on the temporal pulse width of the laser gain.<sup>15.20</sup> The change in the x-ray flux due to the Al grading attenuator is on the order of a few percent and, based on the results presented in reference 15.20, was not expected to have a significant effect. To verify this, spatially resolved temporal pulse shape measurements were made using the arrangement shown in Fig. 15.10. The laser output was divided into test and reference beams by a 50% reflecting beamsplitter; both of these beams were imaged onto the same silicon PIN diode.<sup>15.32</sup> The test beam propagated an addi-

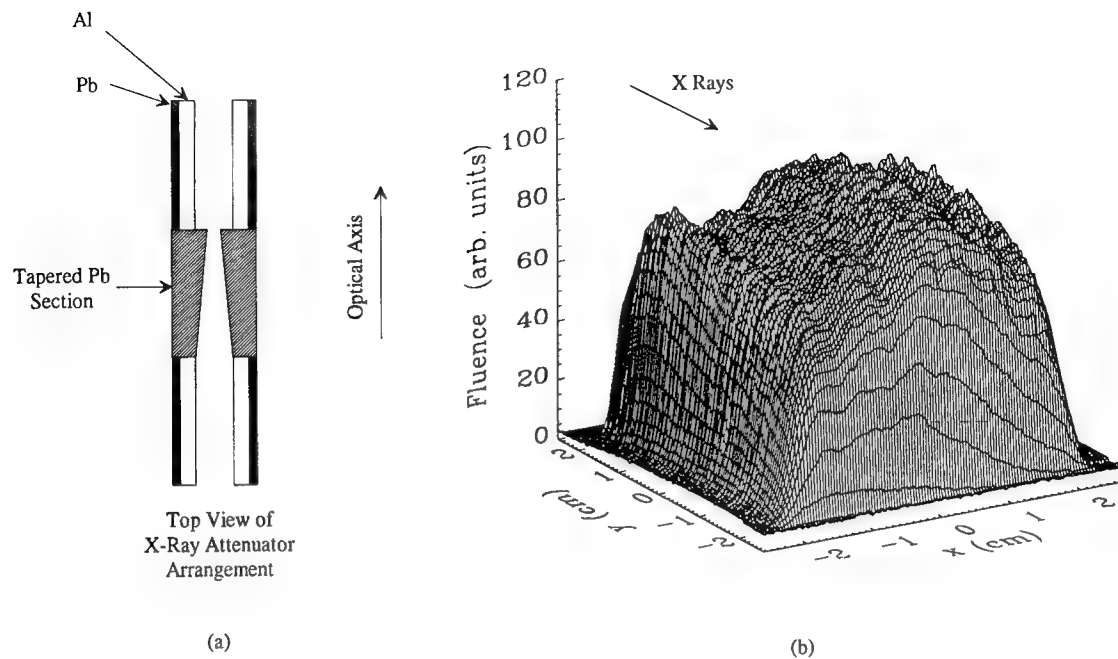


Fig. 15.9 — (a) X-ray attenuator configured with a tapered Pb section. The Al and Pb attenuators are the same as those used for the profile in Fig. 15.8. (b) Output profile where the tapered section was adjusted for best results.

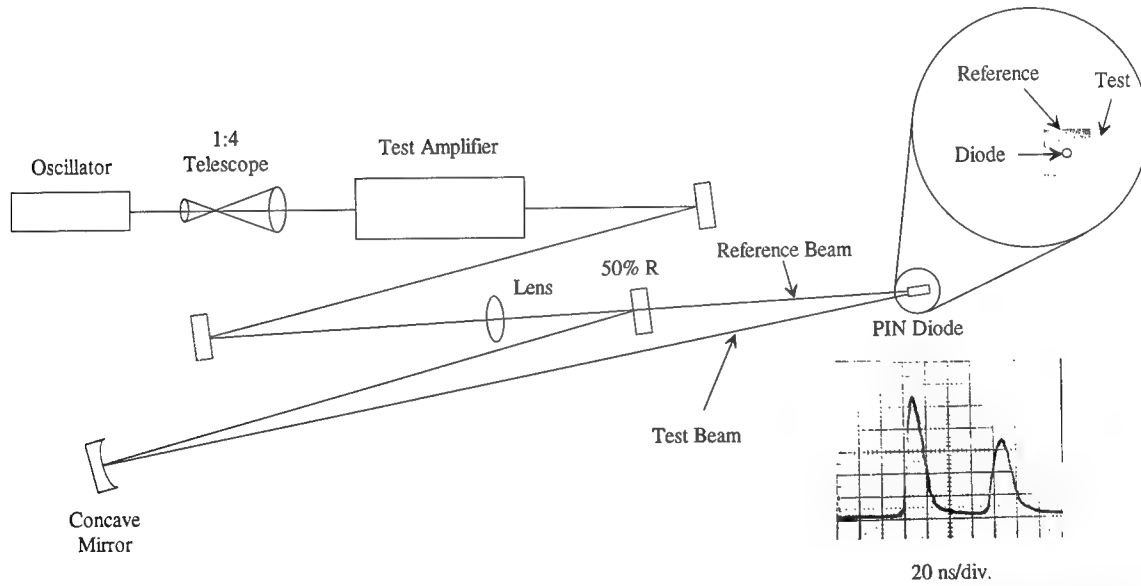


Fig. 15.10 — Arrangement used to measure the spatially resolved temporal pulse shape of the amplifier output.

tional 22.8 m so that there was good temporal separation of the two signals on the diode. The image of each beam at the diode was much larger than the  $< 1 \text{ mm}^2$  active area. Thus, only a small region of each beam was sampled. The reference beam was aligned so that the diode

sampled a region near the center. The alignment of the test beam was changed periodically to sample different regions of the beam. The data shown in Fig. 15.10 is typical for any location tested and shows similar pulse shapes and pulse widths that agree to within  $\pm 5\%$ .

## V. LASER PERFORMANCE

The performance of the device as a saturated amplifier was measured using the front end of the Nike. The diagnostic arrangement used to acquire the data presented here is shown in Fig. 15.11. Constraints imposed by the facilities optical system limit the beam size at the test amplifier to  $4 \times 4 \text{ cm}^2$ . With a 15 ns (FWHM) duration, 0.58 J input pulse ( $I/I_{sat} \sim 1.4$ ), a maximum energy of 2.7 J was measured with  $\pm 5\%$  shot to shot energy variation. Typical operation with a 0.1 J input pulse ( $I/I_{sat} \sim 0.25$ ) routinely produces 2.1 J at the output. A summary of operational conditions and performance achieved is presented in Table 15.1.

The measured input and output pulse shapes are shown in Fig. 15.12. The amplifier output energy versus normalized peak input intensity is plotted in Fig. 15.13 where the input was varied over two orders of magnitude. The curve fit was calculated numerically by integrating the equation<sup>15,33</sup>

$$\frac{dI}{dz} = (g - \alpha)I \quad (15.4)$$

where

$$g = g_0/(1 + I/I_{sat}), \quad (15.5)$$

$I$  is the amplifier output intensity,  $I_{sat}$  is the gain saturation intensity,  $g_0$  is the small signal gain and  $\alpha$  is the nonsaturable loss. Both  $g_0$  and  $\alpha$  are assumed uniform throughout the volume. The input pulse was modeled using the pulse shape shown in Fig. 15.12a; the gain pulse was modeled as a half sinusoid with a 15 ns FWHM duration. ASE was modeled as a lumped input intensity; its effects are appreciable only for  $I/I_{sat} < 0.1$ . The total output energy was calculated by integrating the output intensity over the amplifier aperture with the assumption that the output intensity profile is uniform. The best fit to the measured data occur for an average  $g_0 L = 8$ ,  $g_0/\alpha = 10$  and  $I_{sat} = 2 \text{ MW/cm}^2$ .

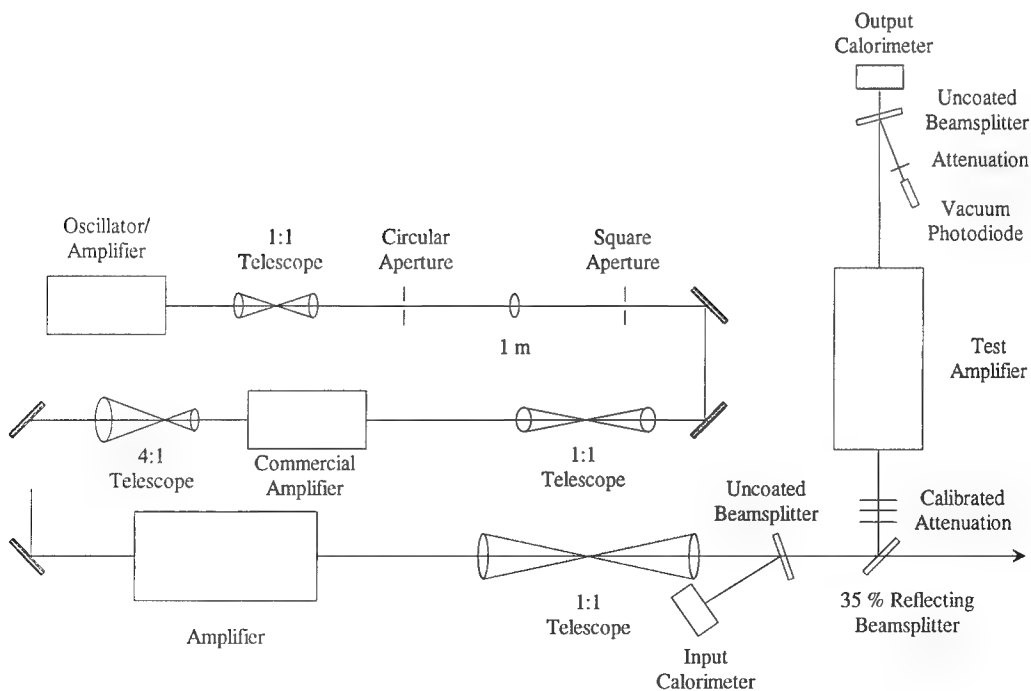


Fig. 15.11 — Arrangement used to measure the performance of the laser as an amplifier. Light from the oscillator illuminates the square aperture which is image relayed into each of the amplifiers. The final two amplifiers in the arrangement are identical modules.

Table 15.1 — Discharge Amplifier Characteristics

Output Energy (4.0 cm square beam, $I_{in}/I_{sat} \sim 1.4$ )	2.7 J
Pulse Duration	15 ns FWHM
Timing Jitter	$\pm 2$ ns
Gain Length	80 cm
Maximum Clear Aperture	4.25 cm $\times$ 4.25 cm
Gas Pressure	4.4 atm
% Partial Pressure F <sub>2</sub> /Kr/Ne	0.27/5.43/94.3
Nominal Charge Voltage	100 kV
Nominal X-ray Diode Operating Voltage	80 kV
Diode Output Dose	100 mrad/shot

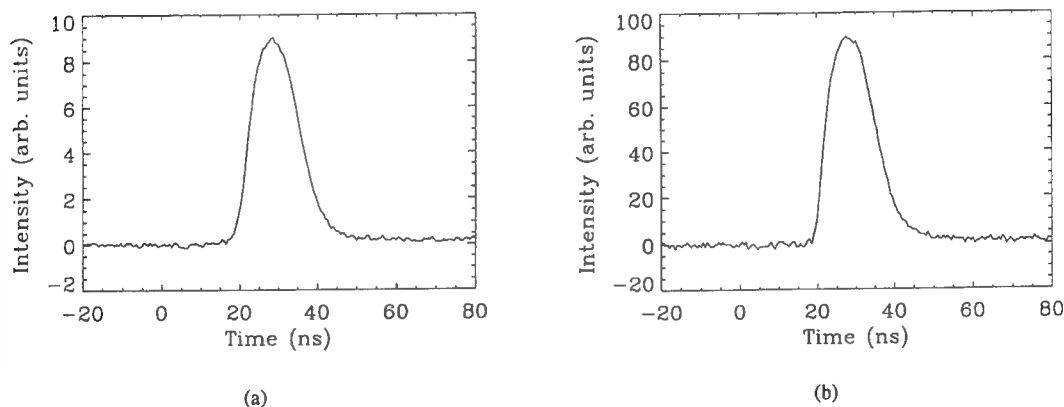
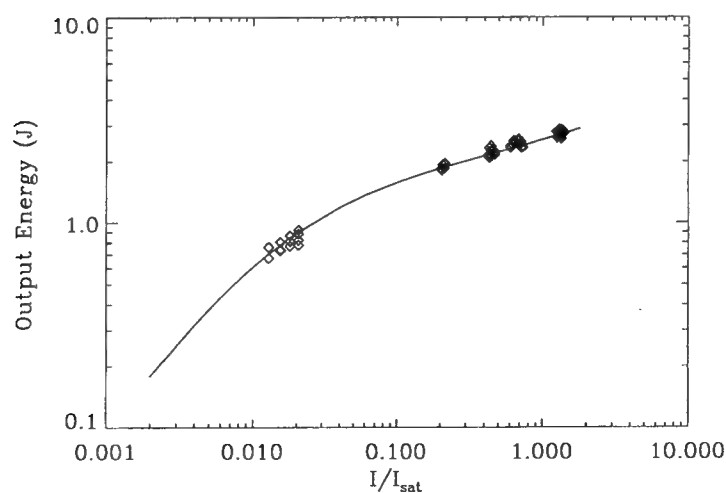


Fig. 15.12 — Temporal pulse shapes of the amplifier (a) input and (b) output.

Fig. 15.13 — Amplifier output energy vs normalized peak input intensity for a 4.0 cm  $\times$  4.0 cm input beam. The curve fit assumes  $g_0L = 8$ ,  $g_0/a = 10$  and  $I_{sat} = 2.0$  MW/cm<sup>2</sup>.

## VI. SUMMARY

We have demonstrated the performance of a large aperture (4.25 cm  $\times$  4.25 cm) KrF amplifier which exhibits the required performance for efficient energy extraction from the next stage of amplification in the Nike system. We have shown that gain nonuniformity which results from discharge plasma skin depth and electrostatic field nonuniformity can easily be controlled by grading the volumetric preionization of the laser gas. The observed performance is consistent with redistribution of the discharge current. The measurements performed for the investigation focused on laser operation near saturation and may underestimate the actual gain nonuniformity present. Further investigation is required to determine performance in the small signal regime. Nevertheless, the technique produces uniform, square output profiles from large aperture discharge amplifiers using relatively simple technology. This ability allows efficient amplification of unity aspect ratio beams, thus improving utilization of the gain volume and ancillary optical components.

## ACKNOWLEDGMENTS

The author thanks Malcolm McGeoch and Warren Webster for their collaboration in the design and construction of the laser system, Alban Deniz for help with the profile diagnostic, Robert Lehmberg and Stephen Obenschain for comments on the manuscript. I am especially indebted to Julius Goldhar for the many useful discussions we had throughout the investigation. This work was supported by the U. S. Department of Energy.

## REFERENCES

- 15.1. R. Burnham, F. X. Powell, and N. Djeu, *Appl. Phys. Lett.*, **29**, 30, (1976).
- 15.2. C. P. Wang, *Appl. Phys. Lett.*, **29**, 103, (1976).
- 15.3. R. S. Taylor, W. J. Sarjeant, A. J. Alcock and K. E. Leopold, *Optics Comm.*, **25**, 231, (1978).
- 15.4. R. C. Sze and P. B. Scott, *Rev. Sci. Instrum.*, **49**, 772, (1978).
- 15.5. S. Sumida, M. Obara and T. Fujioka, *Appl. Phys. Lett.*, **33**, 913, (1978).
- 15.6. S. Watanabe, T. Sato and H. Kashiwagi, *IEEE J. Quantum Electron.*, **QE-15**, 322, (1979).
- 15.7. R. C. Sze, *IEEE J. Quantum Electron.*, **QE-15**, 1338, (1979).
- 15.8. S. Watanabe and A. Endoh, *Appl. Phys. Lett.*, **41**, 799, (1982).
- 15.9. K. Midorikawa, M. Obara and T. Fujioka, *IEEE J. Quantum Electron.*, **QE-20**, 198, (1984).
- 15.10. M. Steyer and H. Voges, *Appl. Phys. B*, **42**, 155, (1987).
- 15.11. S. C. Lin and J. Levatter, *Appl. Phys. Lett.*, **34**, 505, (1979).
- 15.12. H. Mizoguchi, A. Endoh, J. Jethwa, B. Racz and F. P. Schafer, *Appl. Phys. B*, **52**, 195, (1991).
- 15.13. W. J. Sarjeant, A. J. Alcock and K. E. Leopold, *IEEE J. Quantum Electron.*, **QE-14**, 177, (1978).
- 15.14. R. Nodomi, Y. Oeda, K. Sajiki, S. Nakajima, M. Watanabe and S. Watanabe, *IEEE J. Quantum Electron.*, **QE-27**, 441, (1991).
- 15.15. L. F. Champagne, A. J. Dudas and N. W. Harris, *J. Appl. Phys.*, **62**, 1576, (1987).
- 15.16. H.-J. Cirkel, R. Baumgartl, W. Bette, V. Bruckner, D. Friede, U. Kempfer, R. Muller, M. Schmutzler, *Proc. SPIE*, **1023**, 38, (1988).
- 15.17. M. Steyer, K. A. Stankov, H. Mizoguchi, B. Ouyang and F. Schafer, *Appl. Phys. B*, **49**, 331, (1989).
- 15.18. M. Steyer, O. Bin, K. A. Stankov, G. Szabo, H. Mizoguchi and F. P. Schafer, *Proc. SPIE*, **1023**, 75, (1988).
- 15.19. L. J. Denes and L. E. Kline, *Appl. Phys. Lett.*, **30**, 197, (1977).
- 15.20. S. Sumida, K. Kunitomo, M. Kaburagi, M. Obara and T. Fujioka, *J. Appl. Phys.*, **52**, 2682, (1981).
- 15.21. Trade name: Kynar
- 15.22. G. J. Ernst, *Optics Comm.*, **47**, 47, (1983).
- 15.23. C. E. K. Mees, *The Theory of the Photographic Process*, (The Macmillan Company, New York, 1954).

---

- 15.24. T&M Research Products Inc.  
Albuquerque, NM, Model # W-1-025-  
FC, risetime < 1 ns.
- 15.25. M. R. Osborne, P. W. Smith and M.  
H. R. Hutchinson, Optics Comm., **52**,  
415, (1985).
- 15.26. H.-J. Cirkel, W. Bette, D. Friede, R.  
Muller, Proc. SPIE, **735**, 50, (1987).
- 15.27. S. Watanabe, A. J. Alcock, K. E. Leop-  
old and R. S. Taylor, Appl. Phys. Lett.,  
**38**, 3, (1981).
- 15.28. W. K. H. Panofsky and M. Phillips,  
*Classical Electricity and Magnetism*,
- 15.29. Ibid. 28.
- 15.30. E. H. Holt and R. E. Haskell,  
*Foundations of Plasma Dynamics*, (The  
Macmillan Company, New York, 1965).
- 15.31. S. Szatmari and P. Simon, Optics Com-  
m., **98**, 181, (1993).
- 15.32. Motorola MRD-500 modified for UV  
sensitivity.
- 15.33. A. E. Siegman, *Lasers*, (University  
Science Books, Mill Valley, 1986).

## Section 16

### AMPLIFIER LASING MODEL

M. W. McGeoch  
*PLEX Corporation*

#### Abstract

A KrF kinetics model which considers far fewer species and rates than other published models is developed for use in amplifier calculations. The model includes all the major kinetic processes which have been identified as important in prior work, but makes use of a generalised rare gas atom to represent either argon or krypton processes, particularly relating to molecular ion formation and recombination, and does not explicitly consider intermediate steps when a sequence of reactions goes to completion in much less than 0.5 nsec. The model output of small signal gain, saturable and non-saturable absorptions and saturation intensity has been fine-tuned, by the variation of a limited set of rates and cross sections within their probable range, to represent accurately a very wide range of data from different laboratories and experimental situations.

A new amplifier code is developed and compared with data. Novel features of the code include the explicit consideration of krypton fluoride kinetics at each plane in the amplifier, and the fully time-dependent inclusion of amplified spontaneous emission (ASE) with angular and spectral resolution. The new code is successful in giving an exact quantitative description of a number of different experiments performed on the Nike 20 cm amplifier. A number of different versions of the code allow different issues such as the ASE distribution or shaped pulse propagation to be studied. The code runs in times as short as 1 minute on a 486 class personal computer.

#### 16.1.1 DESCRIPTION OF MODEL.

Several detailed krypton fluoride kinetics codes have been written in order to gain predictive power for the design of new lasers and amplifiers [16.1], [16.2], [16.3], [16.4]. Generally these codes consider from 40 to 80 kinetic processes and more than 20 species, and they are run separately from the amplifier calculation to provide the small signal gain, saturation intensity and absorption losses as a function of time. Ideally an amplifier calculation follows the kinetics locally at each point in space, to allow for transient effects in extraction and the time-dependent effects of amplified spontaneous emission. However, with such large systems of equations the combined calculation becomes a major computational exercise. The aim of this work is to create the simplest kinetic description of the krypton fluoride amplifier that still retains predictive power. A set of 20 processes has been found sufficient to give a very good description of all the published gain, loss and saturation data. Only nine variable species need to be followed, including the photon flux.

The most important innovation has been to consider a generalised rare gas atom, named G, to represent either Ar or Kr. It is necessary to follow the complexing of ions into dimer ions mainly to model the electron density, because electron quenching of KrF\* is a significant process, particularly at higher pump rates, and attachment is a significant fluorine loss mechanism. A generalised dimer ion absorption can be used, but there appears to be a large

difference between Ar\* and Kr\* absorptions, which necessitates a weighted absorption cross section for G\*.

The set of rates, listed below with notes, was arrived at by a process of iteration in which the different data sources in turn were matched. The compact kinetics segment was run for 100 nsec without lasing to generate a set of gain, loss and saturation parameters. Also calculated were the KrF\* formation efficiency and the fluorescence efficiency.

Integration of the equations was performed using the explicit two-step time centered algorithm. Because sub-nanosecond kinetic rates were not explicitly considered (the product was assumed to be formed directly, see notes below) the integration step could be as large as 0.5 nsec for typical cases. When using the kinetics segment within an amplifier calculation it should be noted that the simulation of gain recovery on times much shorter than 0.5 nsec may not be quite accurate, if the Kr partial pressure is less than 0.1 atmosphere.

The model does not at present consider internal energy transfer between the B and C states of KrF\*, which occurs in 60 psec, nor does it include vibrational relaxation within the KrF manifold. The latter effect would be evident at mixture densities below 1 atmosphere and on timescales shorter than 1 nsec.

The data sources matched by this code are listed in references [16.5], [16.6], [16.7], [16.8], and [16.9]. They refer, with some minor exceptions, to greater than one atmosphere mixture pressure and measurement times longer than 1 nsec.

### 16.1.2 DESCRIPTION OF RATES FOR COMPACT KINETICS SEGMENT.

In this kinetics segment the letter G denotes a generalised rare gas atom, either Kr or Ar or both. In order to model the electron density, which is important for KrF\* quenching, the formation of  $G_2^+$  and its recombination with electrons must be followed. The pumping electron beam is assumed to create one  $G^+$  ion and one electron with each 26eV(Ar) or 24eV(Kr) deposited and 0.35 G\* excited atoms for each electron ion pair. The processes in this simplified model and the underlying assumptions are listed below. The starting point for the rates was the list of Mandl et al. (1984) [16.6]. Rates that were varied from this set are marked by an asterisk. Binary rate constants are in the units of  $\text{cm}^3 \text{ sec}^{-1}$  and ternary constants are in  $\text{cm}^6 \text{ sec}^{-1}$ . Absorptions and stimulated emission are in  $\text{cm}^2$  and radiative rates are in  $\text{sec}^{-1}$ .

$$1. \quad \text{Sources:} \quad \text{ions wp/wav} \quad (16-1)$$

$$\text{metastables } 0.35\text{wp/wav}$$

where wp is the specific pump power and

wav =  $(26*\text{Ar} + 24*\text{Kr})*1.6\text{e-19}/(\text{Ar} + \text{Kr})$  is the averaged energy per ion pair.

$$2. \quad k2 = 2 \times 10^{-6} \quad G^+ + F^- \rightarrow KrF^* \quad (16-2)$$

$$\begin{array}{lll} \text{represents} & Ar^+ + F^- + G \rightarrow ArF^* + G & 2 \times 10^{-6} \\ & Kr^+ + F^- + G \rightarrow KrF^* + G & 2 \times 10^{-6} \end{array}$$

$$\begin{array}{lll} \text{note} & ArF^* + Kr \rightarrow KrF^* + Ar & 6 \times 10^{-10} \end{array}$$

goes at  $1.6 \times 10^9 \text{ sec}^{-1}$  for 0.1 Amag. Kr.

$$3. \quad k3 = 2.5 \times 10^{-31} \quad G^+ + 2G \rightarrow G_2^+ + G \quad (16-3)$$

$$\begin{array}{lll} \text{represents} & Kr^+ + Kr + G \rightarrow Kr_2^+ + G & 2.5 \times 10^{-31} \\ & Kr^+ + Ar + G \rightarrow ArKr^+ + G & 1 \times 10^{-31} \end{array}$$

$$\begin{array}{lll} \text{note} & Ar^+ + Ar + G \rightarrow Ar_2^+ + G & 2.3 \times 10^{-31} \\ \text{then} & Ar_2^+ + Kr \rightarrow Kr^+ + 2Ar & 7.8 \times 10^{-10} \end{array}$$

goes at  $2.1 \times 10^9 \text{ sec}^{-1}$  for 0.1 Amag. Kr.

4.\*  $k_4 = 5 \times 10^{-8}$   $G_2^+ + e^- \rightarrow G^* + G$  (16-4)

represents  $Kr_2^+ + e^- \rightarrow Kr^* + Kr$   $1.9 \times 10^{-7}$   
 $Ar_2^+ + e^- \rightarrow Ar^* + Ar$   $6.5 \times 10^{-8}$   
 $ArKr^+ + e^- \rightarrow Kr^* + Ar$   $1 \times 10^{-7}$  est.

5.  $k_5 = 7.2 \times 10^{-10}$   $G^* + F_2 \rightarrow KrF^* + F$  (16-5)

represents  $Kr^* + F_2 \rightarrow KrF^* + F$   $7.2 \times 10^{-10}$   
 $Ar^* + F_2 \rightarrow ArF^* + F$   $7.5 \times 10^{-10}$   
note  $ArF^* + Kr \rightarrow KrF^* + Ar$   $6 \times 10^{-10}$   
goes at  $1.6 \times 10^9$  sec $^{-1}$  at 0.1 Amag. Kr.

6.\*  $k_6 = 2 \times 10^{-9}$   $F_2 + e^- \rightarrow F^- + F$  (16-6)  
(reduced from AVCO value of  $4.5 \times 10^{-9}$ )

7.  $k_7 = 1 \times 10^{-6}$   $G_2^+ + F^- \rightarrow KrF^*$  (16-7)

7a  $k_{7a} = 1 \times 10^{-6}$   $G_2^+ + F^- \rightarrow Kr_2F^*$  (16-7a)

represents  $Ar_2^+ + F^- + G \rightarrow ArF^* + G$   $2 \times 10^{-6}$   
(followed by)  $ArF^* + Kr \rightarrow KrF^* + Ar$   $6 \times 10^{-10}$   
 $Kr_2^+ + F^- + G \rightarrow KrF^* + G$   $2 \times 10^{-6}$   
 $Kr_2^+ + F^- + G \rightarrow Kr_2F^* + G$   $2 \times 10^{-6}$   
 $ArKr^+ + F^- + G \rightarrow KrF^* + G$   $2 \times 10^{-6}$   
 $ArKr^+ + F^- + G \rightarrow ArKrF^* + G$   $2 \times 10^{-6}$   
(followed by)  $ArKrF^* + Kr \rightarrow Kr_2F^* + Ar$   $5 \times 10^{-10}$   
going at  $1.3 \times 10^9$  sec $^{-1}$  for 0.1 Amag. Kr.)

8.  $k_8 = 8 \times 10^{-10}$   $KrF^* + F_2 \rightarrow Kr + 3F$  (16-8)

9.\*  $k_9 = 3 \times 10^{-7}$   $KrF^* + e^- \rightarrow Kr + F + e^-$  (16-9)  
(increased from AVCO value of  $1.8 \times 10^{-7}$ )

10.\*  $k_{10} = 2 \times 10^{-31}$   $KrF^* + Kr + G \rightarrow Kr_2F^* + G$  (16-10)  
(reduced from AVCO value of  $6.7 \times 10^{-31}$ , but closer to theory [10]).

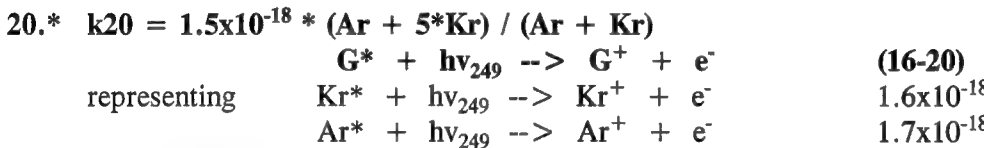
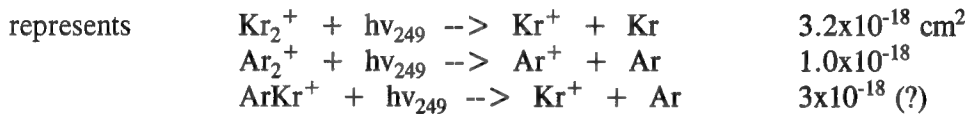
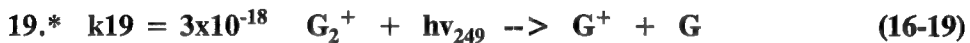
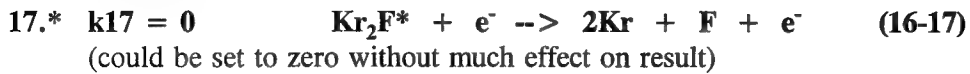
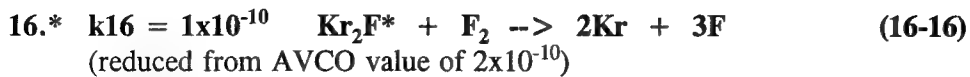
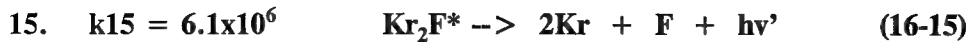
11.  $k_{11} = 8 \times 10^{-32}$   $KrF^* + Ar + G \rightarrow Kr_2F^* + G$  (16-11)

note that this goes via  $ArKrF^*$  and then  
 $ArKrF^* + Kr \rightarrow Kr_2F^* + Ar$   $5 \times 10^{-10}$   
going at  $1.3 \times 10^9$  sec $^{-1}$  for 0.1 Amag. Kr.)

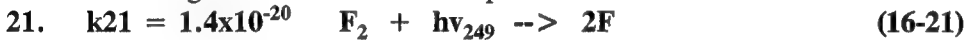
12.  $k_{12} = 2.6 \times 10^{-16}$   $KrF^* + hv_{249} \rightarrow Kr + F + 2hv_{249}$  (16-12)

13.  $k_{13} = 1.54 \times 10^8$   $KrF^* \rightarrow Kr + F + hv_{249}$  (16-13)

14.\*  $k_{14} = 1.6 \times 10^{-18}$   $Kr_2F^* + hv_{249} \rightarrow 2Kr + F$  (16-14)  
(ref. 11)



Note large increase in  $Kr^*$  absorption to  $7.5 \times 10^{-18}$  is needed.



List of Variables :  $G^+$      $G^*$      $e^-$      $F_2$      $F^-$      $G_2^+$      $KrF^*$      $Kr_2F^*$      $hv_{249}$   
Significant absorbers     $G^*$      $F^-$      $F_2$      $G_2^+$      $Kr_2F^*$

### 16.2.1 FIT TO EXPERIMENTAL DATA

Fitting data and comments on each of these sources will now be given in turn:-

Reference 16.5 "Measurements of Gain and Absorption Saturation in an Electron-Beam-Pumped KrF Amplifier", D. C. Thompson, R. Fedosejevs, A. A. Offenberger, J. P. Santiago, and H. R. Manjunath, IEEE J. Quant. Electron., 25, 2161 (1989).

This work is a very careful and detailed measurement at a fairly high pump rate. The absorptions were measured off-line on either side of 248.5nm.

Conditions:- **1.13 MW cm<sup>-3</sup> 1.51 Amag. 6% Kr 0.3% F<sub>2</sub>**

Parameter (% cm <sup>-1</sup> )	Expt.	Code
$g_0$	<b><math>11.5 \pm 0.5</math></b>	<b>11.4</b>
$\alpha_0$	<b><math>1.58 \pm 0.10</math></b>	<b>1.78</b>
$\alpha_s$	$0.50 \pm 0.34$	0.562
$\alpha_{ns}$	$1.09 \pm 0.36$	1.22

In addition to their measurement these authors give a thorough literature survey plotted in their Fig. 13. The present code was run for standard conditions close to those of most of the data :- **1.5 Amag. 6% Kr 0.3% F<sub>2</sub>** with the results:-

Specific Pump Power (MW cm <sup>-3</sup> )						
	0.1	0.2	0.5	1.0	1.5	2.0
$g_0$ (% cm <sup>-1</sup> )	1.69	3.20	6.78	10.7	13.3	15.4
$\alpha_0$	0.389	0.547	0.971	1.62	2.22	2.80
$\alpha_s$	0.074	0.143	0.313	0.515	0.662	0.779
$\alpha_{ns}$	0.315	0.404	0.658	1.10	1.56	2.02
$\Phi_s$ (MW cm <sup>-2</sup> )	1.28	1.37	1.64	2.11	2.56	2.98
$\eta_{FORM}$ (%)	21.6	21.9	22.3	22.5	22.7	22.9
$\eta_{FLUOR}$	8.0	7.6	6.4	5.1	4.2	3.6

These representative points are plotted (as X's) on their Fig. 13, see Fig. 16-1. Throughout the range the agreement is excellent. (The results of a 1989 LANL code are shown as lines in their Fig. 13).

**Reference. 16.6 "KrF Laser Kinetics Studies", A. Mandl, D. Klimek and J. H. Parks, J. Appl. Phys., 55, 3940 (1984).**

This work represents probably the most careful fluorescence efficiency measurements made on KrF and its range of pump intensities brackets those used in the Nike system. The measurements span a density range between 0.5 and 2 Amag. giving the data particular sensitivity to the rate for  $\text{KrF}^* + \text{Ar} + \text{G} \rightarrow \text{etc}$ . We found that the original Avco value for this rate  $8 \times 10^{-32} \text{ cm}^6 \text{ sec}^{-1}$  gave the best fit. At 1 and 2 Amag. the fluorescence efficiency is matched to within the experimental error, but at 0.5 Amag. the code is higher than experiment. Being at 4% Kr this data does not depend strongly on the rate for  $\text{KrF}^* + \text{Kr} + \text{G} \rightarrow \text{etc}$ .

Conditions	Fluorescence Efficiency	
	Expt.	Code
<b>0.2 MW cm<sup>-3</sup></b>	<b>7.8%</b>	<b>9.8%</b>
<b>0.5 Amag 4%Kr 0.3% F<sub>2</sub></b>		
<b>0.4 MW cm<sup>-3</sup></b>	<b>7.3%</b>	<b>7.8%</b>
<b>1.0 Amag 4%Kr 0.3% F<sub>2</sub></b>		
<b>0.8 MW cm<sup>-3</sup></b>	<b>5.4%</b>	<b>4.8%</b>
<b>2.0 Amag 4%Kr 0.3% F<sub>2</sub></b>		

**Reference. 16.7 "Experimental Support for KrF Laser Modeling" Final report from Spectra Technology, 19 July 1989, submitted to LANL under contract 9-X65-W1478-1.**

The Spectra Technology study appears to be the only detailed work on the absorption and gain at high krypton fraction. The measurements are in the Nike pump intensity regime. Their results turn out to be difficult to "square away" with the kinetics assumptions that have been adopted to explain

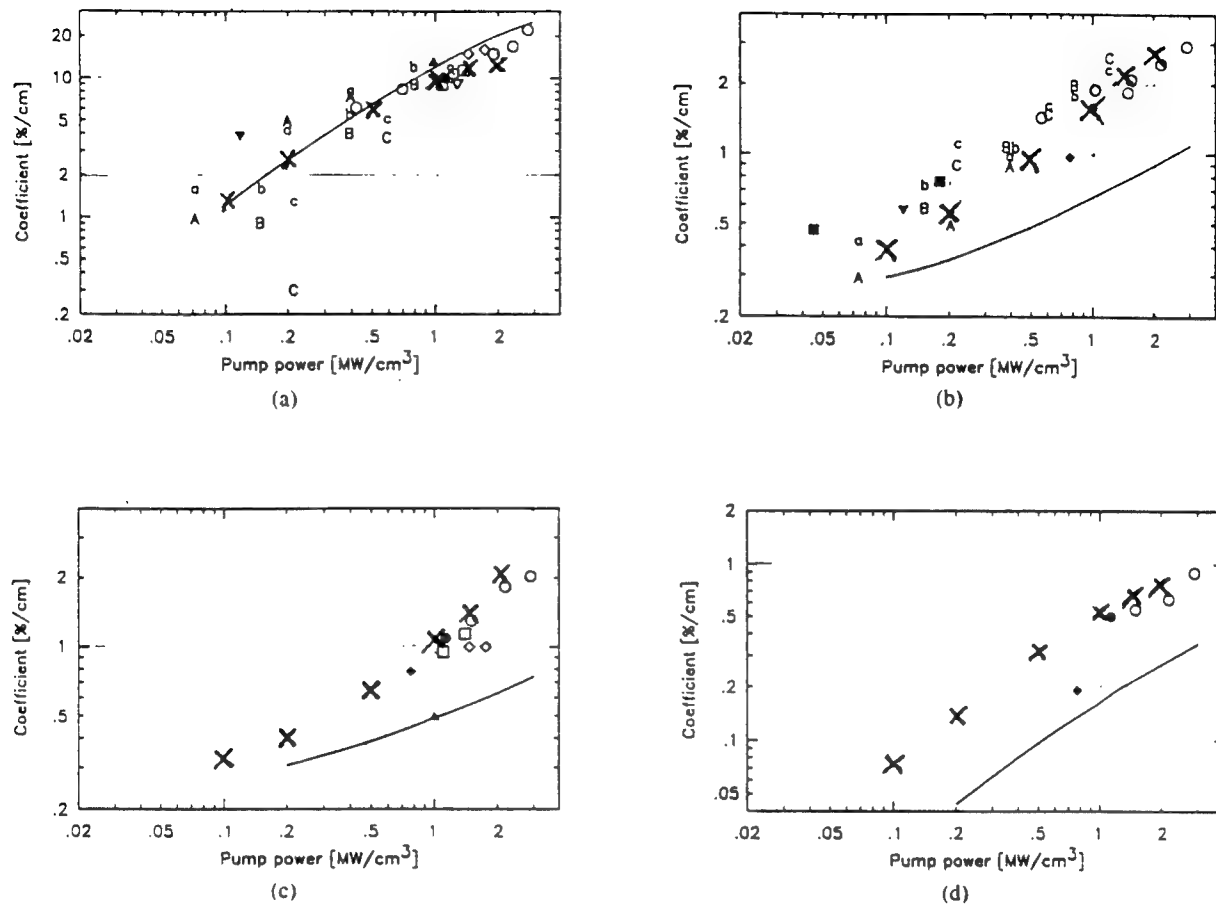


Fig. 13. Comparison of experimental and predicted values of small-signal net gain (a), small-signal absorption (b), nonsaturable absorption (c), and saturable absorption (d) versus pump power. The solid lines are the model predictions. The gas mixes for the various experiments are shown below (in torr).

Reference	$F_2/Kr/Ar$
■ [7]	7/137/2140
◊ [11]	3/97/900
○ [12]	4/125/1370
□ [13]	4.5/76/1440
□ [6]	4/83/1310
A [14]	4.5/30/730
a [14]	1.5/30/730
B [14]	9/60/1450
b [14]	3/60/1450
C [14]	13.5/90/2180
△ [14]	4.5/90/2180
▽ [15]	2.5/40/960
● [16]	3/38/720
▲ [17]	3/76/1240
This work	4/80/1240

Fig. 16-1 — Comparison of simplified code to data compilation of Thompson et al. Crosses show predictions for standard conditions of 1.5 Amag., 6% Kr, 0.3%  $F_2$ . Data is for a range of conditions. Lines are 1989 version of LANL code.

low krypton cases. In particular, the absorption at high krypton fraction is much higher, and we have been able to model this by assuming that Kr\*\* (or Kr\*) is the responsible species. Another major difference is that the gain is higher. Part of this is explained by the higher formation efficiency, but this is not enough. It was found necessary to decrease the (quenching) rate for KrF\* + Kr + G  $\rightarrow$  etc. from its usually assumed value of  $6.5 \times 10^{-31} \text{ cm}^6 \text{ sec}^{-1}$  to  $2 \times 10^{-31} \text{ cm}^6 \text{ sec}^{-1}$ . This is in any case a more believable value [16.10].

Even with these changes, it was only possible to fit the gain for the highest krypton case (99.6%). The code still underpredicted the gain for the intermediate krypton case (14.5%). However, the code gain prediction is accurate for the slightly lower krypton case (8.5%) of Edwards et al. (below) so this 14.5% Kr data may be anomalous. Possibly the deposition was higher than estimated. The comparison figures are:-

a) **350kW cm<sup>-3</sup> 99.6%Kr 0.875 Amag. 0.42% F<sub>2</sub>**

	Expt.	Code
$g_0$ (% cm <sup>-1</sup> )	<b>6.39</b>	<b>5.98</b>
$\alpha_0$	<b>1.11</b>	<b>1.08</b>
$\alpha_s$	<b>0.35</b>	<b>0.238</b>
$\alpha_{ns}$	<b>0.85</b>	<b>0.839</b>
$\Phi_s$ (MW cm <sup>-2</sup> )	<b><math>1.4 \pm 0.1</math></b>	<b>1.48</b>
$\eta_{FORM}$ (%)	<b>27</b>	<b>25.3</b>

b) **350 kW cm<sup>-3</sup> 1.32 Amag. 14.5% Kr 0.28% F<sub>2</sub>**

	Expt.	Code
$g_0$ ( % cm <sup>-1</sup> )	<b>7.23</b>	<b>5.38</b>
$\alpha_0$	<b>0.79</b>	<b>0.791</b>
$\alpha_s$	<b>0.2</b>	<b>0.232</b>
$\alpha_{ns}$	<b>0.55</b>	<b>0.559</b>
$\Phi_s$	<b><math>1.1 \pm 0.1</math></b>	<b>1.47</b>
$\eta_{FORM}$ (%)	<b>22.4</b>	<b>22.5</b>

**Reference. 16.8 "Scalability of High Power KrF Laser Systems", K. Ueda, A Sasaki, H. Yoneda and H. Takuma, Workshop on KrF Laser Technology, Santa Fe (1989).**

The Ueda et al. data is a wide-ranging measurement of the gain and absorption in extraction conditions, giving one of the best estimates of the saturation flux. In general the code agrees well with saturation fluxes and gains, but predicts higher absorptions than Ueda. A possible explanation is that the absorption coefficient is not very well determined by the fit to data, because there are not many points in the saturation regime, and the experimental accuracy required is very high. This is the difficulty with on-line estimates of the absorption. The code predictions for a range of pump powers in the Ueda et al. mix are as follows:-

Conditions: **1.76 Amag. 6% Kr 0.284% F<sub>2</sub>**  
**Specific Pump Power (MW cm<sup>-3</sup>)**

	<b>0.1</b>	<b>0.2</b>	<b>0.5</b>	<b>1.0</b>	<b>1.5</b>	<b>2.0</b>
$g_0$ (% cm <sup>-1</sup> )	<b>1.44</b>	<b>2.78</b>	<b>6.15</b>	<b>10.1</b>	<b>12.9</b>	<b>15.1</b>
$\alpha_0$	<b>0.423</b>	<b>0.586</b>	<b>1.03</b>	<b>1.70</b>	<b>2.33</b>	<b>2.94</b>
$\alpha_s$	<b>0.080</b>	<b>0.157</b>	<b>0.359</b>	<b>0.620</b>	<b>0.819</b>	<b>0.981</b>
$\alpha_{ns}$	<b>0.343</b>	<b>0.429</b>	<b>0.668</b>	<b>1.08</b>	<b>1.51</b>	<b>1.96</b>
$\Phi_s$ (MW cm <sup>-2</sup> )	<b>1.48</b>	<b>1.55</b>	<b>1.78</b>	<b>2.19</b>	<b>2.60</b>	<b>2.98</b>
$\eta_{FORM}(\%)$	<b>21.3</b>	<b>21.6</b>	<b>21.9</b>	<b>22.2</b>	<b>22.4</b>	<b>22.5</b>
$\eta_{FLUOR}(\%)$	<b>6.82</b>	<b>6.59</b>	<b>5.83</b>	<b>4.80</b>	<b>4.08</b>	<b>3.57</b>

These points are plotted as X's on two of Ueda's Figures, shown as our Figs. 16-2 and 16-3. Their  $\alpha$  corresponds to our  $\alpha_{ns}$ . The predicted gain comes out a little higher than the measured gain. One possible reason is that if ASE was a factor, it would lead to the suppression of the measured gain at low intensities.

**Reference 16.9 "Absorption and Gain Measurements in the KrF Laser Medium at High Pump Rate", C. B. Edwards, F. O'Neill and M. J. Shaw, Appl. Phys. Lett. 38, 843, 1981.**

There is also reasonable agreement with some high pump rate data from Edwards et al. Their conditions were:-

**1.5 MW cm<sup>-3</sup> 1.8 Amag. 8.3% Kr 0.27% F<sub>2</sub>**

Parameter	Expt.	Code
$g_0 - \alpha_0$ (% cm <sup>-1</sup> )	<b>11</b>	<b>11.4</b>
$\alpha_0$	<b>2</b>	<b>2.8</b>
$\alpha_s$	<b>0.6</b>	<b>0.77</b>
$\alpha_{ns}$	<b>1.4</b>	<b>2.0</b>

### 16.2.2 REMARKS ON COMPARISON WITH EXPERIMENT

In conclusion, the compact kinetics code can be made to fit a broad range of current data within the errors of the experiments, with only two exceptions: (a) The 14.5% krypton gain data from Spectra Technology, and (b) the absorption data of Ueda et al. Even in case (a) the absorption data are accurately modeled, while in case (b) the gain and saturation data are well described. In each of these cases the new code errs on the conservative side, by underpredicting the gain in case (a), and by overpredicting the absorption in case (b).

### 16.3.1 EFFECT OF KRYPTON FRACTION IN MIXTURE.

The new code has been written specifically to allow, for the first time, the coupling of an amplifier propagation routine with a kinetics routine. This will be discussed in Section 16.4 below. In the present section some general kinetics predictions on the effect of mixture variation are given. The specific pump power that is achieved in the 20cm amplifier is 480kW cm<sup>-3</sup>, as measured and predicted by deposition codes. We are interested in the likely effect of substituting krypton for argon while keeping constant the electron stopping power of the mixture. This involves substituting one krypton atom in the mix for every two argon atoms (calculations indicate 1.8 to 2 as a range). Figure 16-4 shows the calculated output energy of the 20cm amplifier as a function of fluorine concentration

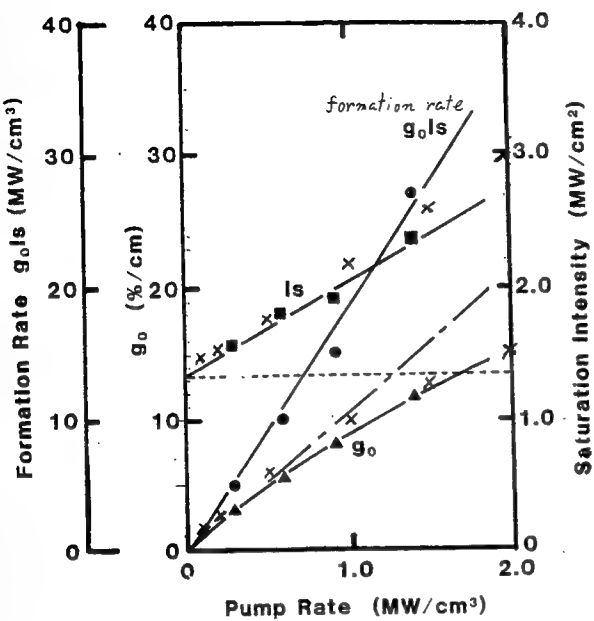


Fig. 16-2 — Comparison of gain and saturation intensity from simple code (crosses) with measurements of Ueda et al.

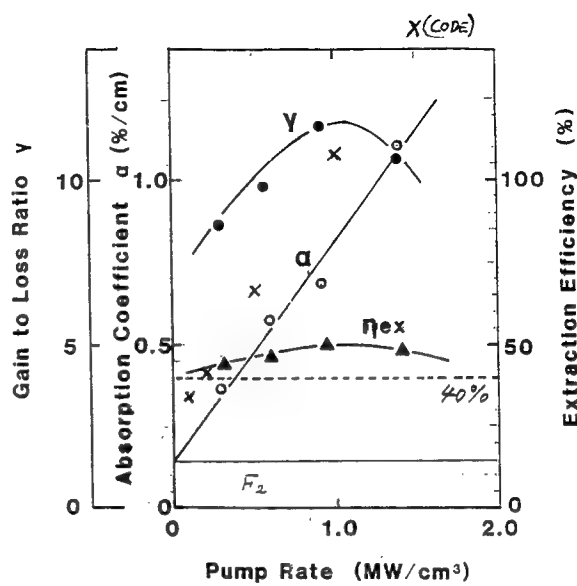


Fig. 16-3 — Comparison of absorption (nonsat) with measurements of Ueda et al. derived at saturating intensities.

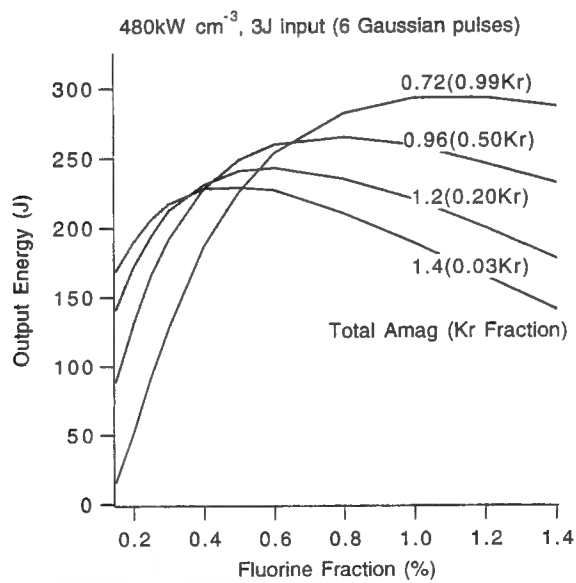


Fig. 16-4 — Code predictions for the 20cm amplifier at constant deposited power of  $480\text{ kW cm}^{-3}$ . ASE loss not included.

for a range of krypton fractions between 3% and 99%. This calculation used the input pulse train of some recent experiments, consisting of a six pulse chain of Gaussian pulses (in space and time). Noteworthy is the prediction that the highest output should be obtained at 99% krypton, using a higher than normal fluorine fraction. This result is due to the higher formation efficiency of krypton mixes combined with their higher gain (at high fluorine fraction). In practice, at constant electron beam current density off the cathode the increasing albedo of krypton rich mixtures will modify the curves. The albedo rises from about 14% with pure argon to 20% with pure krypton, so that the same electron beam deposits about 6% less energy.

### 16.3.2 REDUCTION OF 'NONSATURABLE ABSORPTIONS' AT HIGH FLUX

Even the so-called nonsaturable absorption should be reduced by the passage of sufficient KrF laser intensity. In the 60cm amplifier (Section 18) the outgoing flux approaches  $5\text{MWcm}^{-2}$  and it is calculated to reduce the nonsaturable absorption by about 10%. The KrF code can be easily modified to look at this effect. For a typical case of  $450\text{kWcm}^{-3}$ , 1.5Amag., 47%Kr and 0.5%F<sub>2</sub>, the application of increasing flux leads to a reduction of  $\alpha_{ns}$  as follows:-

Flux $\text{MWcm}^{-2}$	$g_0$ % cm <sup>-1</sup>	$\alpha_0$ % cm <sup>-1</sup>	$\alpha_s$ % cm <sup>-1</sup>	$\alpha_{ns}$ % cm <sup>-1</sup>	$\phi_s$ $\text{MW cm}^{-2}$
0	5.61	.986	.297	.690	1.86
0.5	4.41	.908	.225	.684	1.87
1.0	3.64	.857	.197	.678	1.87
2.0	2.69	.791	.124	.667	1.88
4.0	1.77	.719	.072	.647	1.89
8.0	1.05	.649	.035	.615	1.91
16	.579	.581	.014	.568	1.94
32	.306	.513	.005	.508	2.00

### 16.3.3 FLUORESCENCE LOSS FOR 20cm AMPLIFIER DEPOSITION

At the approximately 300kV voltage X-ray losses are small (< 1%) and the principal loss is via KrF fluorescence. There is also a component of Kr<sub>2</sub>F fluorescence, but according to the code, it accounts for only 15% of the fluorescence power. The combined KrF + Kr<sub>2</sub>F fluorescence efficiency is calculated from the code. The wavelength of the Kr<sub>2</sub>F emission was assumed to be 400nm ( $5 \times 10^{-19}\text{J}$ ).

The combined fluorescence loss is around 8% for typical 20cm conditions, see following table of fluorescence losses (%):-

kW cm <sup>-3</sup>	F <sub>2</sub> Fraction	Total Pressure (Amag.)			
		.72	.96	1.2	1.4
400	0.003	8.6	8.9	8.8	8.7
	0.006	9.9	9.3	8.5	7.9
480	0.003	7.8	8.3	8.4	8.3
	0.006	9.4	8.9	8.3	7.8
560	0.003	7.3	7.8	8.0	7.9
	0.006	8.9	8.6	8.1	7.6

The other potential source of loss is radiation from  $\text{Kr}_2^*$ . The lifetimes of the  $\text{Kr}_2^*$  species range from 100nsec to 1 $\mu$ sec so they are strongly quenched by collisions with  $\text{F}_2$  before they can radiate. For example, at  $2 \times 10^{17}$  cm $^{-3}$  of  $\text{F}_2$  with a quenching rate constant of  $5 \times 10^{-10}$  the quenching goes at  $10^8$  sec $^{-1}$ , so radiation from  $\text{Kr}_2^*$  is at most 10% effective. The  $\text{Kr}_2^*$  formation efficiency is probably less than 20% in these conditions, so at most 2% of the radiation goes via  $\text{Kr}_2^*$ .

In summary, to assume 8% - 10% radiation loss will be reasonably accurate.

#### 16.4. ASE TREATMENT

It is necessary to follow the propagation of amplified spontaneous emission (ASE) from point to point within the amplifier, in order to correctly account for the effects on the ASE of the coherent pulses that are being amplified. For example, when a non-overlapping train of pulses is being amplified, inversion builds up in the time gap between the pulses and co-propagating ASE is preferentially amplified. An example of this is quoted later and compared to experimental data from the Nike 20cm device. Also, in order to predict the effects of ASE propagation beyond the amplifier, the ASE intensity must be carried as a function of angle. In this respect, most other work has not kept angle information, summing instead at a selected point all the ASE contributions from other parts of the amplifier, over all angles. An example of this approach is ref. [16.12] in which the ASE is calculated only at points within the amplifier (time-dependence is lost because the result is reached by multiple iterations). Other treatments [16.13],[16.14] propagate ASE along with the amplified pulse, keeping time dependence, but again lose angle information by summing over solid angles to obtain the ASE at any plane in the amplifier. Earlier treatments of ASE are all steady state solutions. The model of Hunter and Hunter [16.15] is one-dimensional with an analytic accounting for the frequency spectrum. Lowenthal et al. [16.16] employ a steady state three-dimensional treatment in cylindrical geometry and include the frequency spread and mirror reflections. Sasaki et al [16.17] consider

reflections off cylindrical side walls, but do not consider the frequency spread. Leland [16.18] considers a three-dimensional array of cubical cells with diffuse reflection from side walls, mirror reflection and frequency spread. This solution iterates to steady state. The approaches of references [16.12] and [16.18] are suitable for low aspect ratio gain volumes and the amplification of single pulses. The present model is better adapted to high aspect gain volumes.

There are different possibilities for the angle coding of ASE. We chose an approach which in principle allowed separate treatment in the orthogonal directions that are inclined to the foil and the amplifier ceiling, respectively. In practice, we did not differentiate between these directions, and obtained a good comparison with present data. It is possible that in the future more refined comparisons will require separate treatment in each direction, which can easily be incorporated.

The amplifier geometry for which this code is designed has typically a length-to width (aspect) ratio of 4 and is operated in double pass. The greatest gain is experienced by rays propagating at the smaller angles to the axis. We take this into account by defining a fractal distribution of ASE propagation angles, with geometrically increasing angular resolution towards the axis. At first we consider a general pair of angles  $\{\alpha, \beta\}$  in the x and y directions from propagation direction z, as illustrated in Fig. 16-5. To fix ideas consider that the x direction is perpendicular to the foil. It is assumed that the amplifier is divided into segments separated by an axial propagation distance h and that the amplifier has a square cross section of side d. A square of ASE originating at one segment propagates to the neighbouring segment at angles  $\{\alpha, \beta\}$  encountering reflections at the walls. The spatial position that would be reached if the square had not been reflected is shown as a dashed square in Fig. 16-5. The actual position reached by the reflected rays is shown shaded. Specular reflection is assumed. The displacements without a reflection would be  $h \tan \alpha$  and  $h \tan \beta$  in the x and y directions. Considering reflection coefficients  $R_x(\alpha)$  and  $R_y(\beta)$  respectively, the

## TREATMENT OF REFLECTIONS

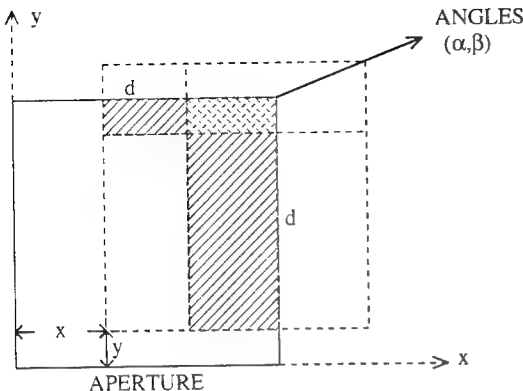


Fig. 16.5 — ASE propagation in z-direction (out of page) between segment planes

overall transmission after propagating the distance  $h$  is estimated from the areas defined in Fig. 16-5 as:-

$$T = \frac{(d - x)(d - y)}{d^2} + \frac{x(d - y)R_x}{d^2} + \frac{y(d - x)R_y}{d^2} + o(R_x R_y) \quad 16-22$$

Setting  $\gamma = h/d$  and taking  $\alpha = \beta$  (considering the same angular resolution in each transverse direction) the transmission simplifies to

$$T_\alpha = (1 - \gamma \tan \alpha)^2 + \gamma \tan \alpha (1 - \gamma \tan \alpha) (R_x + R_y) \quad 16-23$$

where the term of order  $R_x R_y$  has been neglected (this corresponds to two reflections during propagation between segments, shown as the heavily shaded area in Fig. 16-5). This expression depends only on the sum of the x- and y- direction reflectivities, and not separately on them.

A geometrically decreasing series of angles  $\alpha = \pi/2^{m+1}$ ,  $m = 1, 2, 3, \dots$ , is defined in Fig. 16-6. The angle  $\alpha$  defines orthogonal planes subtending a solid angle of  $\alpha \cdot \sin \alpha$  in the octant drawn. As a check, setting  $\alpha = \pi/2$  yields the whole octant solid angle of  $\pi/2$ . We have defined solid angles bounded by the planes at

angles  $\alpha$  and  $2\alpha$ , giving a largest angle  $\alpha$  of  $\pi/4$  and a solid angle increment of  $2\alpha \cdot \sin 2\alpha - \alpha \cdot \sin \alpha$ . The sequence of angles is ended at a core ray angle  $\alpha_c$  which satisfies the criterion  $4\alpha_c < d/2L$  where  $L$  is the length of the amplifier. It can be shown that the index corresponding to the core ray is

$$m > \frac{\log \left[ \frac{8L\pi}{d} \right]}{\log 2} - 1 \quad 16-24$$

In tests which included more ray angles than given by this criterion, the ASE results were unchanged.

Finally, the propagation between segment planes of ASE waves (coded by angle  $\alpha$ ) was modeled by the expression:

$$I_\alpha^{n+1} = T_\alpha I_\alpha^n e^{\bar{g}h} + \frac{FhN^*}{\tau} (2\alpha \sin 2\alpha - \alpha \sin \alpha) \quad 16-25$$

where  $N^*$  = KrF\* density (from local kinetics)  
 $I_\alpha$  = photon flux of ASE ray in solid angle defined by  $\alpha$   
 $g$  = spatially averaged gain between segments  $n$  and  $n+1$   
 $\tau$  = spontaneous emission lifetime  
 $F$  = fraction of spontaneous emission in central Gaussian  
 $T_\alpha$  = transmission as defined above  
 $h$  = separation of planes.

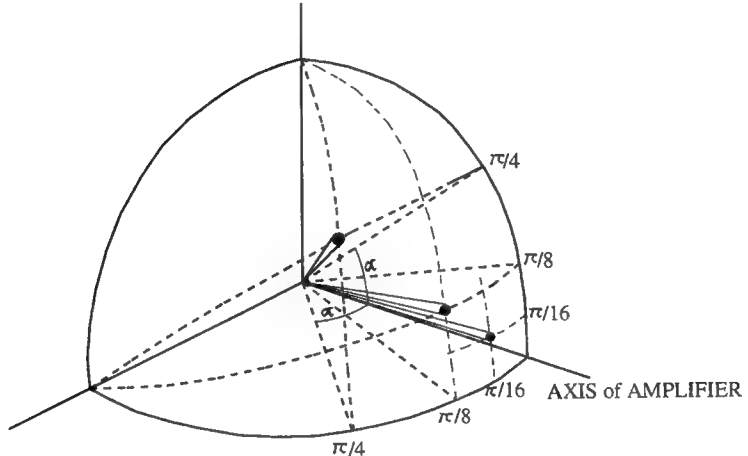
The second term represents the spontaneous emission per unit cross section due to fluorescence in the space of length  $h$  between segments. Because the spontaneous emission spectrum of KrF is not symmetrical, but has a low wing to short wavelength of line center, the (total) fluorescence power estimated from the kinetics does not all contribute to the central Gaussian part of the spectrum. From gain measurements [16.5] it appears that there is net loss on the short wavelength wing, and hence it does not make any contribution to ASE. The central portion of the spectrum contains

## DEFINITION OF SOLID ANGLES FOR ASE

Angles  $\alpha$  of defining surfaces to axis are:-

$$\alpha = \frac{\pi}{2^{m+1}}$$

$$m = 1, 2, 3, \dots, \text{INT} \left( \frac{\log \left[ \frac{8L\pi}{d} \right]}{\log 2} \right)$$



Solid angle increment per quadrant is

$$\Omega_{\alpha(m)} - \Omega_{\alpha(m+1)} = 2\alpha \sin 2\alpha - \alpha \sin \alpha,$$

except core ray which has  $\Omega_c = 2\alpha \sin 2\alpha$ .

Fig. 16.6 — Definition of the geometric progression of solid angles for ASE.

approximately 0.84 of the spontaneous emission power [16.5], which is accounted for in our ASE calculation by the introduction of factor F. The central part of the spectral line is approximately symmetrical, so the ASE calculation only considers a half line, divided into ten spectral segments. This would correspond to a resolution of 20 segments over the whole line.

## 16.5 INTEGRATION ALGORITHM.

The integration method is described with reference to Fig. 16-7B. The time and space steps are related by  $h = c \cdot \Delta t$  where  $c$  is the velocity of light. A separate set of kinetics variables (listed above) is carried at each segment plane. The kinetic populations are advanced by the explicit two step algorithm. Using the derivatives at the time labelled

"populations" in Fig. 16-7B the kinetic variables are advanced by a half time step. The derivatives are re-calculated and then these time-centered derivatives are used to advance a full step from "populations" to "new populations". The photon fluxes are propagated from the times labelled "s" (which denotes stored values) to the times labelled "i" (intermediate values) using the spatially and temporally averaged gain g which is computed from the KrF\* and absorber densities. The "intermediate" fluxes are averaged with the "stored" fluxes at a given segment plane to provide time-centered photon terms to drive the first half time step of the populations. The intermediate fluxes alone are used to drive the full time step of the populations. They then become the stored fluxes for use in the next time step. This algorithm derives the maximum benefit from time and space centering, and is very stable for time

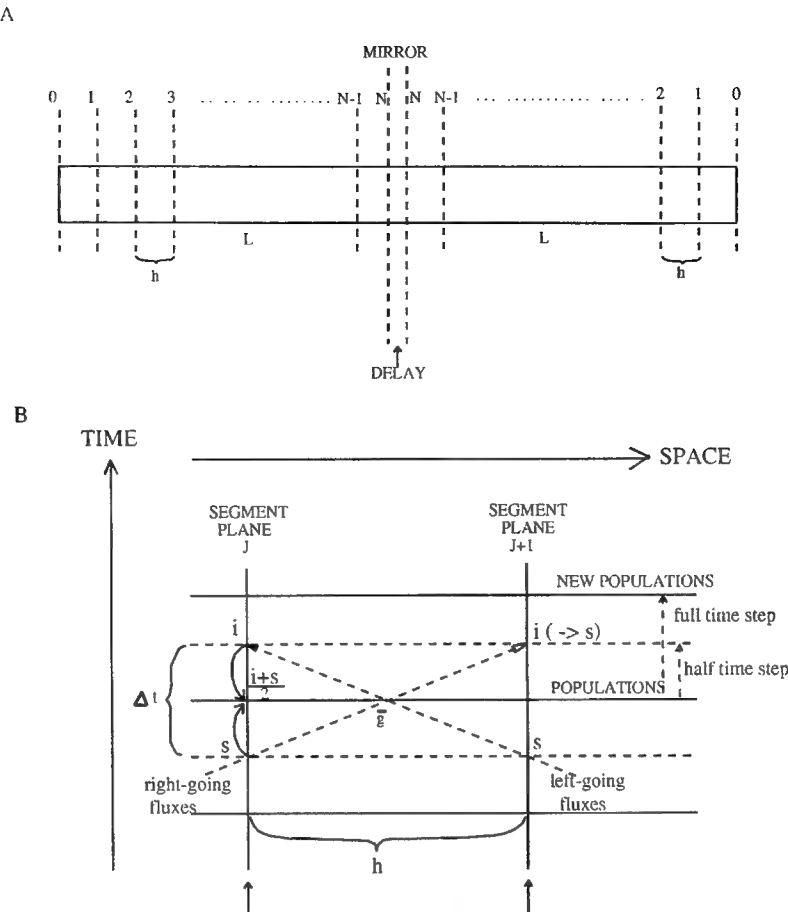


Fig. 16-7A — Division of the amplifier into segments, shown unfolded, but superimposed in the calculation. B. Integration method.

steps shorter than 0.5 nsec, the time scale of the fastest kinetic processes considered. The only other circumstance that requires shorter time steps for stability concerns cases where the amplified pulse has built up to such intensity that the KrF\* population is depressed in times less than 0.5 nsec. This generally is not the case for Nike conditions, but would become relevant for the amplification of intense picosecond pulses. The run versions of the program provided with this report have  $h = 8$  cm, corresponding to  $\Delta t = 0.27$  nsec. Figure 16-8 shows the effect of varying the segment length between 10cm and 2.8cm. There is convergence below a segment separation of about 5cm. However, in the interest of computing speed a separation of 8cm can be used with little error, and if more accurate results are required the segment length can always be reduced.

The shortcoming of this ASE calculation is that all ASE rays are assumed to propagate at the same speed axially down the amplifier. This is actually a fair assumption, as the most intense ASE rays are close to axial. However, errors will be observed in the case of isolated pulses of subnanosecond duration propagating down the amplifier, due to an exaggerated ASE suppression coincident with the pulse. The overall "static" gain suppression due to ASE will still be accurate however, and this is the largest effect of ASE.

#### 16.6 COMPARISON WITH NIKE 20cm DEVICE DATA

The most interesting comparison is with the data for a set of six pulses of FWHM 16 nsec, separated by 25 nsec. The strong fluctuations in

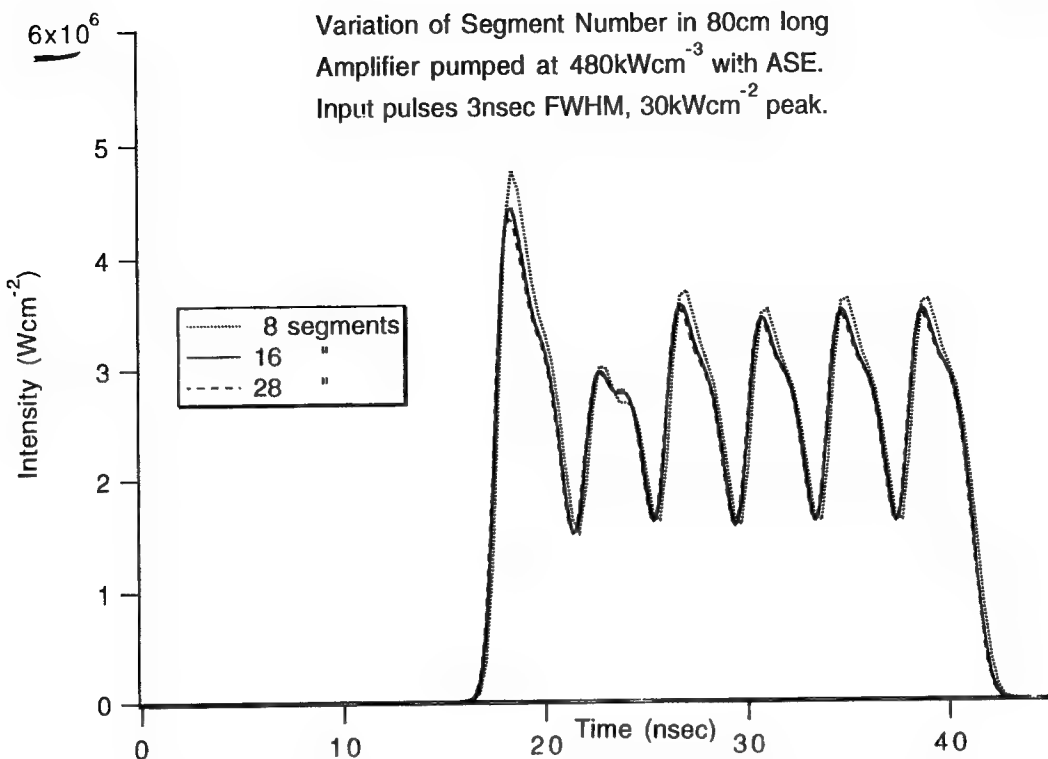


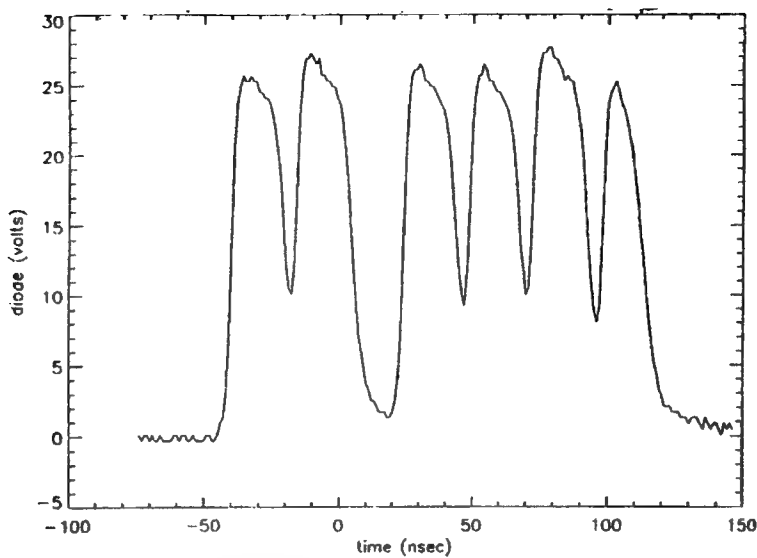
Fig. 16-8 — Test of convergence as segment length (and time step) are decreased.

coherent drive intensity, due to the separation of the pulses, provided a good test of the time-dependent kinetic treatment. Figure 16-9 shows the observed output intensity for the six pulse train at two input intensities (the separation between pulses two and three was 35 nsec, rather than 25 nsec). The input pulses were best represented by a "supergaussian" curve of exponent 3. Calculated input and output waveforms are shown in Fig. 16-10. There is good agreement with experiment in pulse shape and amplitude. The peculiar saturation effect at the peak of the output pulses is simulated quite accurately. The shape of this saturation is very sensitive to the delay between the amplifier medium and the end mirror. For this simulation the most accurate estimate of the delay was used. The output train energy also agrees with measurement to within the experimental accuracy of 10%, as discussed below.

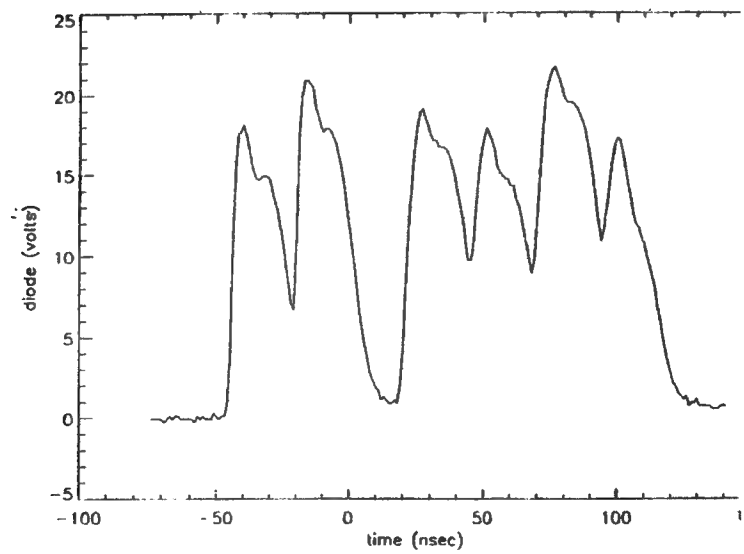
A second case involved a higher pump power on the 20cm device together with a consecutive train of 28 pulses of 4 nsec duration. The simulated output is shown in Fig. 16-11.

The strong effect of ASE gain suppression is shown by turning the ASE "off", when a strong overshoot occurs on the leading edge of the pulse. The experimental and simulated energies for the 6- and 28- pulse cases are shown in Fig. 16-12. Agreement is within experimental error, with the code possibly underpredicting the output. Considering that the experimental measurement of deposition was used in the simulation, and that this is a difficult measurement, and that the theory contains no adjustable parameters, the agreement is extraordinarily good. The kinetic code itself was anchored to a broad cross section of data from different experiments around the world, which did not include data from the 20cm device itself, so the most probable explanation of the agreement is that both the ASE code and the experiment are accurate.

For an estimate of the considerable effect of ASE in these 20 cm device experiments we show the energy predictions in the absence of ASE in Fig. 16-13. When saturating fluxes are present the ASE loss is 16%, but when the input energy is only 0.3J the ASE loss is 50%.



**300 mJ IN, 70 J OUT**



**3 J IN, 180 J OUT**

Fig. 16-9 — Data for 6-pulse train from NIKE 20cm amplifier.

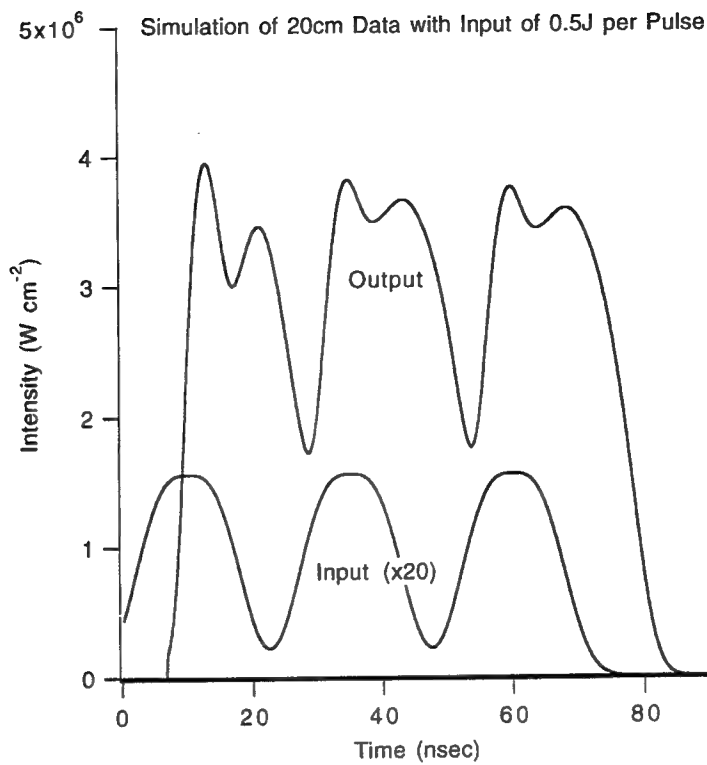


Fig. 16-10 — Calculated waveforms for 6-pulse experiment on 20cm amplifier.

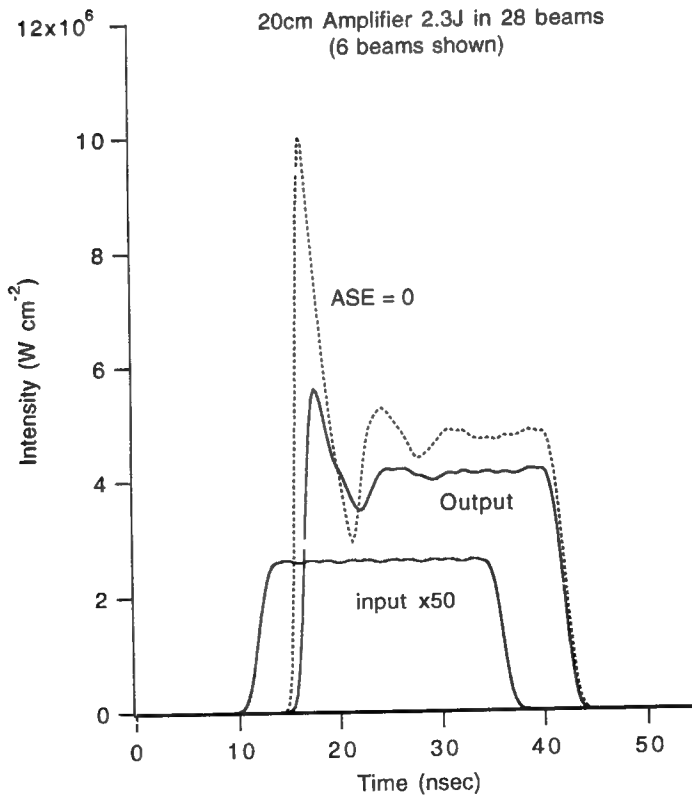


Fig. 16-11 — Calculated waveforms for a train of 4nsec pulses. 20cm device pumped at  $575 \text{ kW cm}^{-3}$ .

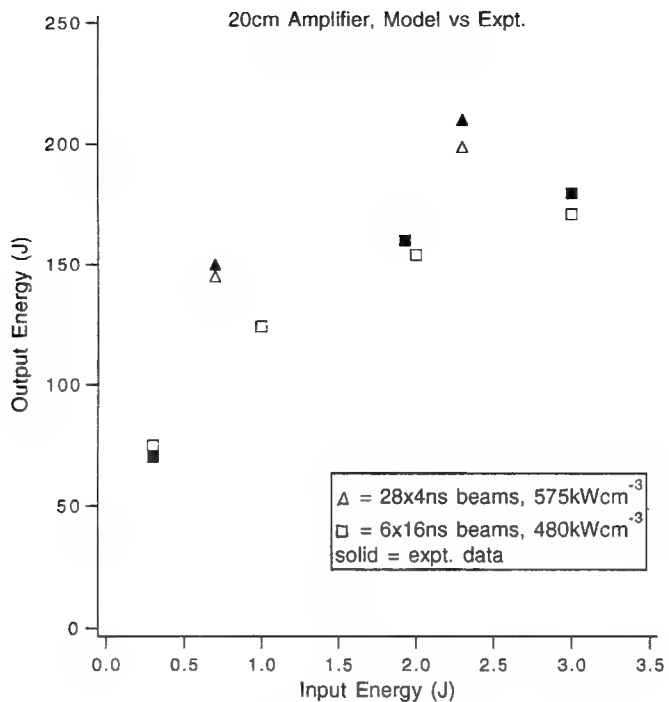


Fig. 16-12 — Experimental and calculated output versus input energies on the 20cm amplifier.

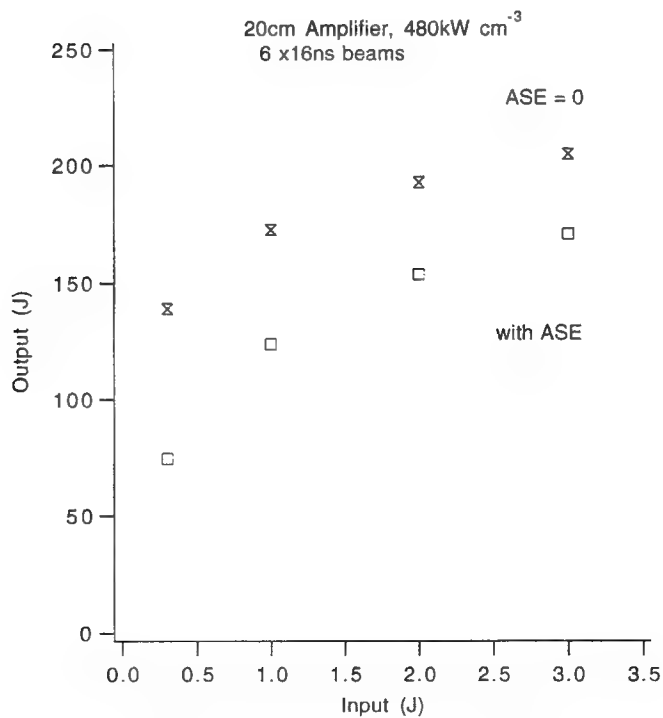


Fig. 16-13 — Effect of "turning off" ASE for 6x16 nsec beams on 20cm amplifier.

The off-axis ASE exiting from the 20cm device was recorded, at an angle of  $15^\circ$  (Fig. 16-14), for the 6 pulse train described above. The same circumstances were modeled, looking at ASE in the ray associated with the angle  $\pi/16$  ( $11.25^\circ$ ), as shown in Fig. 16-15. The same strong fluctuations in ASE were seen in the experiment and the simulation. If anything, the simulation showed more ASE suppression by the coherent beams than was observed experimentally. The difference was not due to the slight angle mismatch between experiment and simulation. There are two possible explanations for the difference. One is that there was some background light at wavelengths other than 249nm incident on the (unfiltered) photodiode and that this component was not suppressed. The other is that the code underestimates ASE. Stronger ASE leads to less suppression by a given coherent flux. This could be resolved by quantitative, filtered ASE measurements at some future opportunity.

## 16.7 PREDICTIONS FOR NIKE 60cm DEVICE.

In order to treat angularly multiplexed beams a special version of the ASE code was made which treated one single pulse separately, among a chain of otherwise identical pulses. This allowed the study of specially shaped pulses with temporal overlap. To preserve the input pulse shape through the 20cm followed by the 60cm amplifiers it was necessary to have the full width at half maximum of the shaped pulse equal to the separation between pulses in the train. The gain was then suppressed all through the train to an approximately equal extent, and distortion did not occur. Figure 16.16 shows the preservation of a 1% "foot" through both Nike amplifiers in spite of its overlap with neighboring pulses spaced by the multiplexing delay of 4 nsec. Figure 16.17 shows preservation of an exponentially rising pulse with an accuracy of 5%. The use of rapidly modulated pulses could be of interest, so a  $(1 - \cos^2\omega t)$  waveform was propagated, again with good fidelity (Fig. 16.18). Although the 0.25 nsec structure in this waveform is much shorter than the 4 nsec interpulse spacing, the gain depletion on any

one cycle of modulation is relatively small, so there is an averaging effect which reduces the distortion. Lastly, in Fig. 16.19 an exponentially rising pulse with a "spike" is also shown to propagate without much distortion, the only remarkable effect being the dip at the pulse peak due to the co-propagation of the spike of a neighboring pulse in the multiplexed train. In conclusion, the many useful pulse shapes that can be generated in the Nike laser will give great experimental flexibility.

The effect of foil + wall reflectivity on the 60cm device output energy is illustrated in Fig. 16-20. In fact, for this calculation a rather high pump rate of  $450\text{ kW cm}^{-3}$  was used, so the 60cm energies are overstated. The loss of output with increasing foil and / or ceiling reflectivity is possibly less dramatic than would be expected. For example, if each reflectivity was 0.5, their sum would be 1.0 and only a 13% reduction is predicted. However, this calculation assumes that there is absolutely no feedback from reflections outside the amplifier, and even small amounts of feedback can lead to parasitic oscillations. Furthermore, glancing reflections of the coherent beams themselves can cause cross-talk between the multiplexed channels, with bad results.

Lastly, the effect of an output window reflectivity was simulated. At first the reflected beam was allowed to propagate straight back along the amplifier axis, but an oscillation very rapidly built up. It was then postulated that the reflected beam experienced the same transmission between segments as one of the ASE rays at an appropriate angle, and further that the residual reflected beam was dumped at the mirror end. Typical results are shown in Fig. 16-21, assuming a window tilt of  $10^\circ$  and considering an input pulse train of  $8 \times 4\text{ nsec}$  pulses. The output is not immediately depressed by the reflected beam, but the effect develops on the propagation time. The systematic variation of window reflectivity up to an (uncoated) value of 8% (Fig. 16-22) showed that a total output drop of 15% was possible. This was composed of a loss of 8% due to the exit pass itself, 5% due to losses to the amplified reflected beam and 2% attributable to the reduction in input intensity.

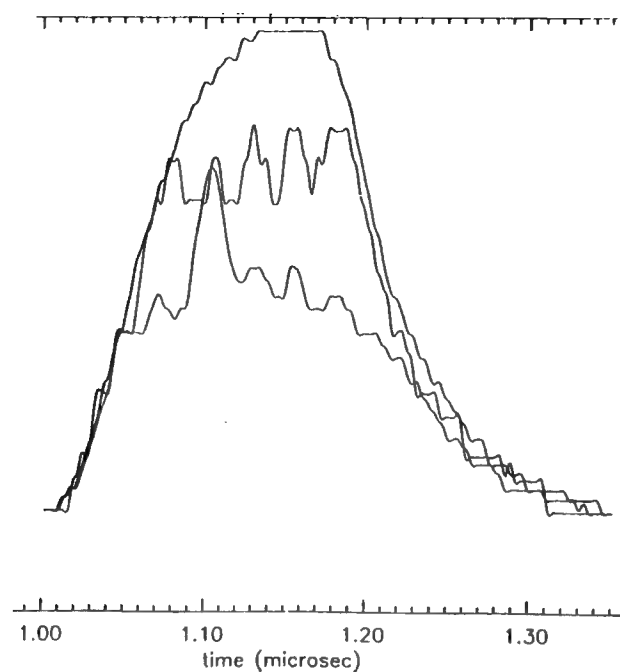


Fig. 16-14 — Experimental measurement of 15° off-axis ASE on 20cm device. Top, no input, middle 0.3J input, bottom 3J input.

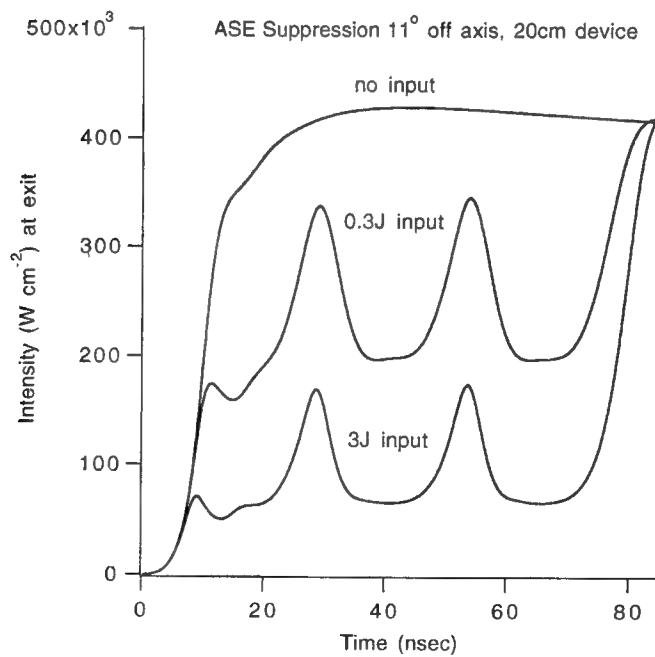


Fig. 16-15 — Calculated off-axis ASE suppression for conditions of data in Fig. 16-14.

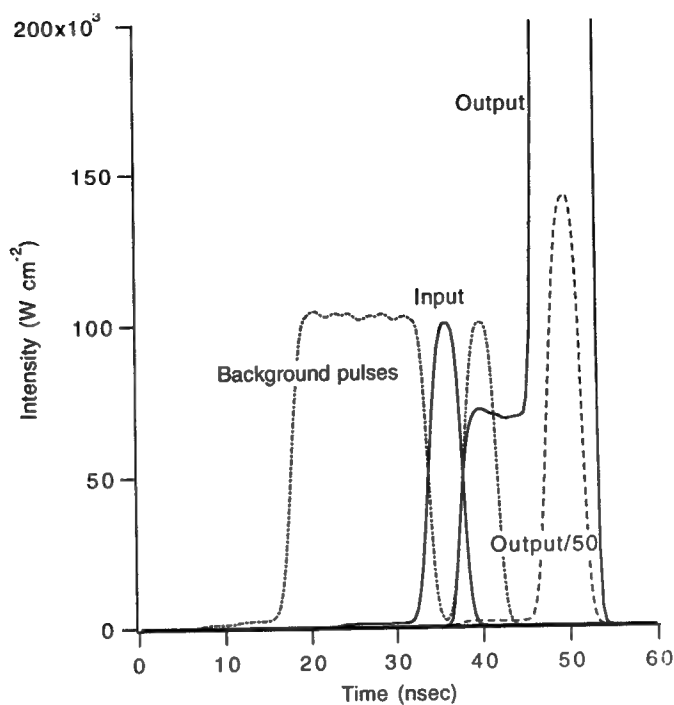


Fig. 16-16 — Simulation of a chain of 4 nsec pulses with a 10 nsec "foot" at the 1% level.

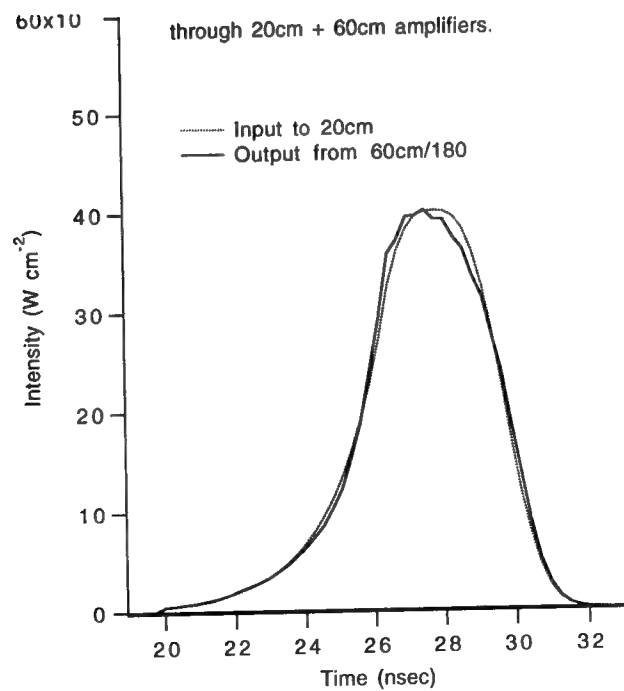


Fig. 16-17 — Propagation of an exponentially rising pulse of 4nsec overall duration

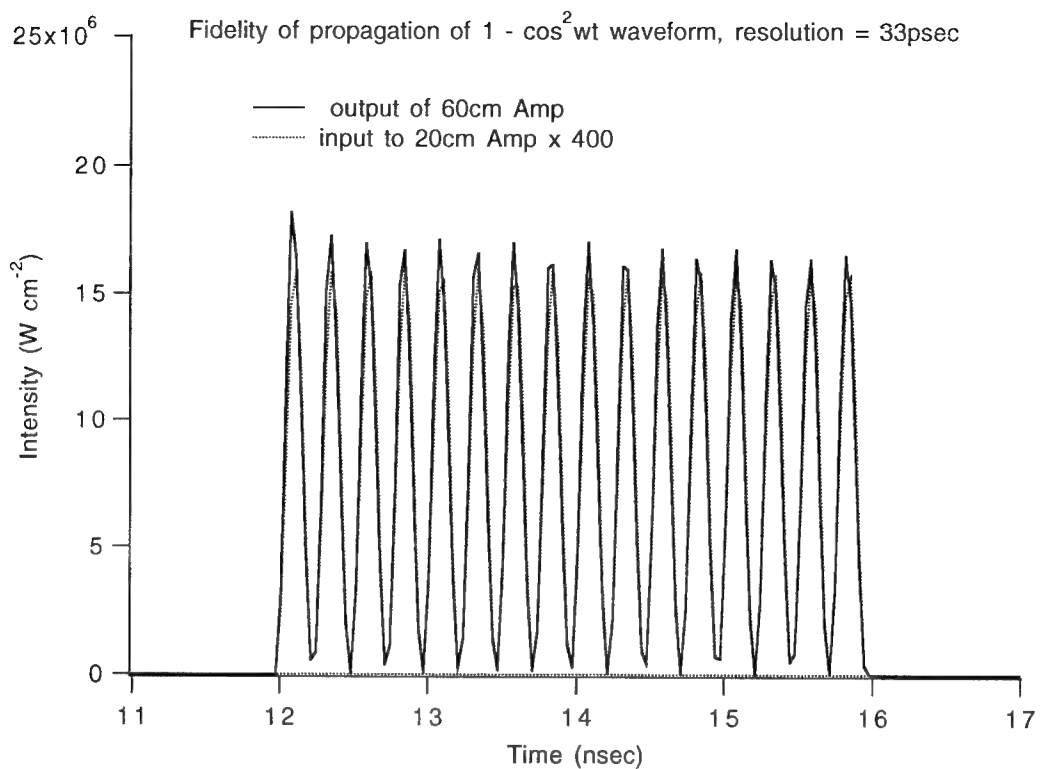


Fig. 16-18 — Propagation of a 100% modulated train of 250 psec pulses.

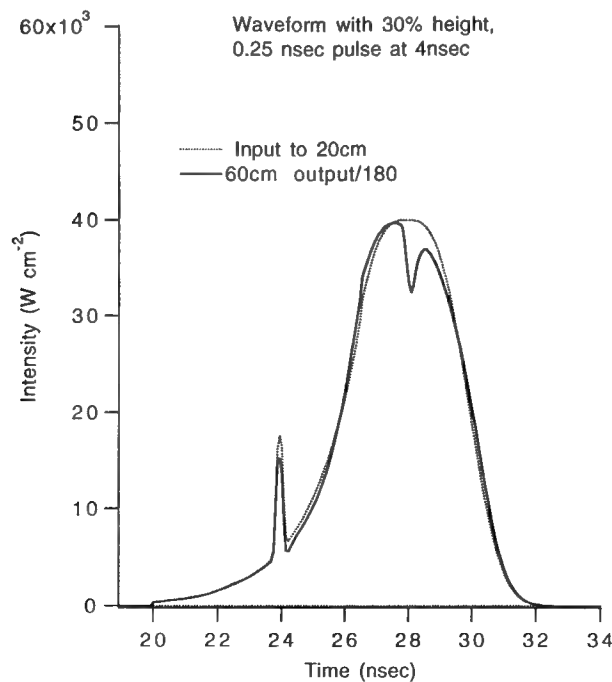


Fig. 16-19 — Propagation of an exponentially rising pulse with 250 psec spike on foot.

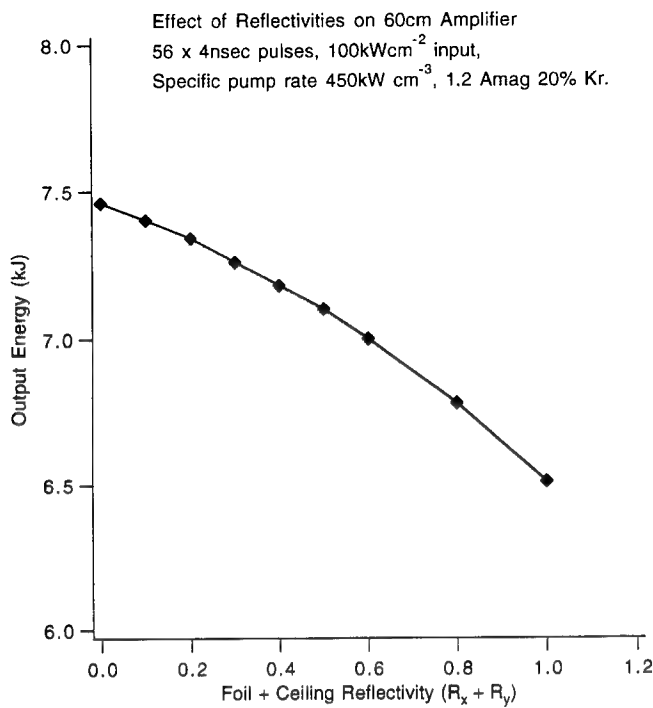


Fig. 16-20 — Variation of the output energy with the parameter  $R_x + R_y$ , the sum of foil and ceiling reflectivities.

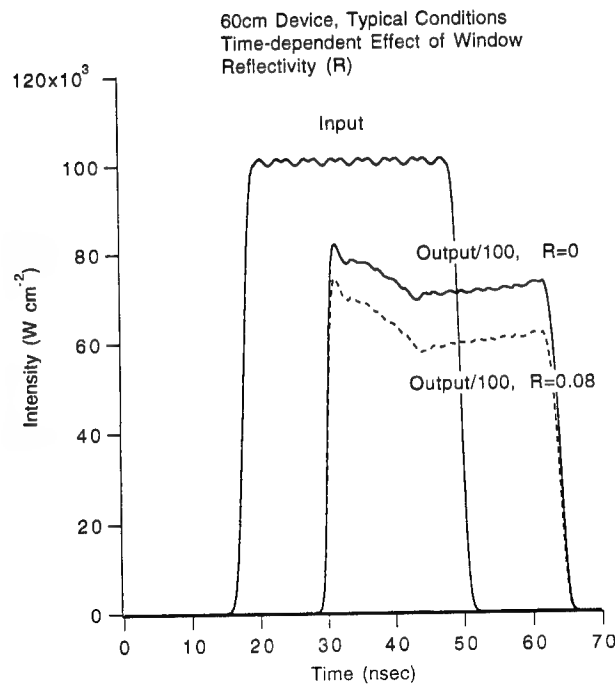


Fig. 16-21 — Simulation of effect of 8% reflectivity on window tilted at 10°.

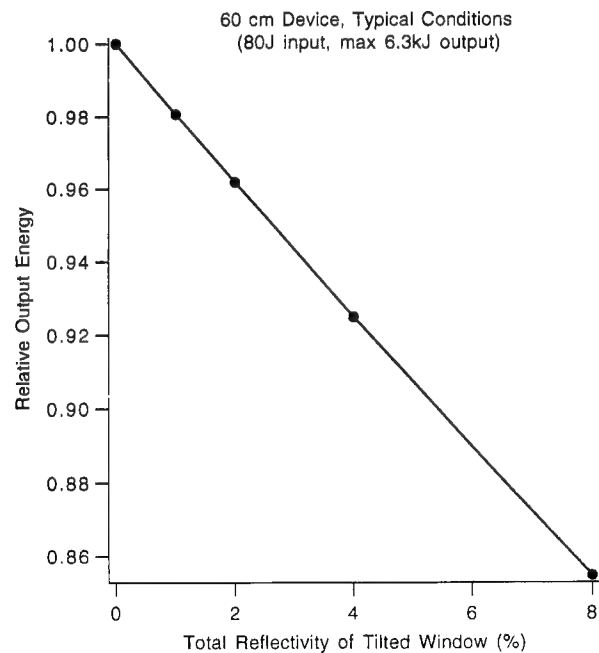


Fig. 16-22 — Loss to 60cm output energy as a function of assumed window reflectivity.

## REFERENCES

1. M. Rokni, J. A. Mangano, J. H. Jacob and J. C. Hsia, *IEEE J. Quantum Electron.* **QE-14**, 464 (1978).
2. T. H. Johnson and A. M. Hunter II, *J. Appl. Phys.* **51**, 2406 (1980).
3. LANL code. (D. Hanson, Los Alamos National Laboratory).
4. F. Kannari, M. Obara and T. Fujioka, *J. Appl. Phys.* **57**, 4309 (1985).
5. D. C. Thompson, R. Fedosejevs, A. A. Offenberger, J. P. Santiago and H. R. Manjunath, *IEEE J. Quant. Electron.*, **25**, 2161 (1989).
6. A. Mandl, D. Klimek and J. H. Parks, *J. Appl. Phys.*, **55**, 3940 (1984).
7. "Experimental Support for KrF Laser Modeling" Final report from Spectra Technology, 19 July 1989, submitted to LANL under contract 9-X65-W1478-1.
8. K. Ueda, A. Sasaki, H. Yoneda and H. Takuma, Workshop on KrF Laser Technology, Santa Fe (1989).
9. C. B. Edwards, F. O'Neill and M. J. Shaw, *Appl. Phys. Lett.* **38**, 843, 1981.
10. V. H. Shui and C. Duzy, *Appl. Phys. Lett.* **36**, 135 (1980).
11. D. B. Geohegan and J. G. Eden, *J. Chem. Phys.* **89**, 3410 (1988).
12. I. Okuda and M. J. Shaw, *Appl. Phys.* **B54**, 506 (1992).
13. E. C. Harvey, C. J. Hooker, M. H. Key, A. K. Kidd, J. M. D. Lister, M. J. Shaw and W. T. Leland, *J. Appl. Phys.* **70**, 5238 (1991).
14. D. E. Klimek (private communication).
15. A. M. Hunter and R. O. Hunter, *IEEE JQE* **QE-17**, 1879 (1981).
16. D. D. Lowenthal and J. M. Eggleston *IEEE JQE* **QE-22**, 1165 (1986).
17. A. Sasaki, K. Ueda, H. Takuma and K. Kasuya, *J. Appl. Phys.* **65**, 231 (1989).
18. W. T. Leland (unpublished).

## Section 17

### 20 CM APERTURE AMPLIFIER AND INITIAL SYSTEM TEST

C.J. Pawley

*Laser Plasma Branch  
Plasma Physics Division  
Naval Research Laboratory*

The 20 cm amplifier is an electron beam pumped KrF amplifier with a 20 cm × 20 cm square aperture. It is designed to amplify the 1-2 J output from the discharge array to approximately 150 J to drive the last amplifier stage, the 60 cm amplifier.

The design of the first electron beam amplifier was driven by the unique requirements for the optical system in Nike and incorporating that information to the existing technology base for KrF amplifiers. The design information from the Rapier amplifiers at Lawrence Livermore<sup>17.1</sup> and the Aurora laser at Los Alamos,<sup>17.2</sup> the Sprite laser at Rutherford (U.K.),<sup>17.3</sup> the Ashura laser at Electrotechnical Institute<sup>17.4</sup> and the Siden laser at the Institute for Laser Science UEC<sup>17.5</sup> (Japan) were gathered and studied in order to maximize the performance of this amplifier. The 20 cm amplifier began construction in 1989 and underwent testing and modification in 1990 and 1991. The experience gained in this time was used to help guide the design of the 60 cm amplifier, identify various improvements in efficiency and reliability, and build our data base on KrF laser kinetics and performance. In late 1991 the 20 cm amplifier was modified for higher reliability and moved to the Nike facility. New tests were performed in the Nike facility to document the reliability of the pulse power and electron beam diodes, and to measure the laser characteristics for this amplifier. In order to perform laser tests, the entire Nike system had to be integrated together through the 20 cm amplifier.

The first section will cover the basic parameters of the 20 cm pulse power and electron diode performance. The second section will

present some of the system integration effort and laser amplifier test results.

#### THE 20 CM PULSE POWER AND ELECTRON BEAM

Figure 17.1 shows the location of the 20 cm amplifier on the southeast corner of the propagation bay in the wing of the amplifier bay. Both the 20 and 60 cm (see Section 18) amplifiers are sealed from the propagation bay to keep oil vapors and other gases from being in the light propagation path. Sealed tunnels (not shown) connect the output windows of the large amplifiers to the propagation bay. Figure 17.2 shows the basic components of the pulse power system. An eight stage Marx bank provides the initial energy for the pulse power. Each stage of the Marx can be charged up to 100 kV to give an erected voltage of 800 kV and 16 kilojoules of energy minus switch and inductance losses. To extend Marx bank capacitor life and reduce strain on other high voltage components, the system is routinely fired with an 80 or 85 kV charge per stage. The output of the Marx bank is split by two inductors which charges two water pulse forming lines. The inductors are adjusted so that when the Marx is erected, both water lines reach peak charge simultaneously. The water lines are matched and the total capacitance of the two water lines is the same as the Marx bank, resulting in 93% of the erected Marx energy being transferred to the water lines. Figure 17.3 shows a cutaway view of the laser triggered gap, electron diode, and the laser cell. At peak charge on the water lines, laser triggered spark gaps on the output end of the

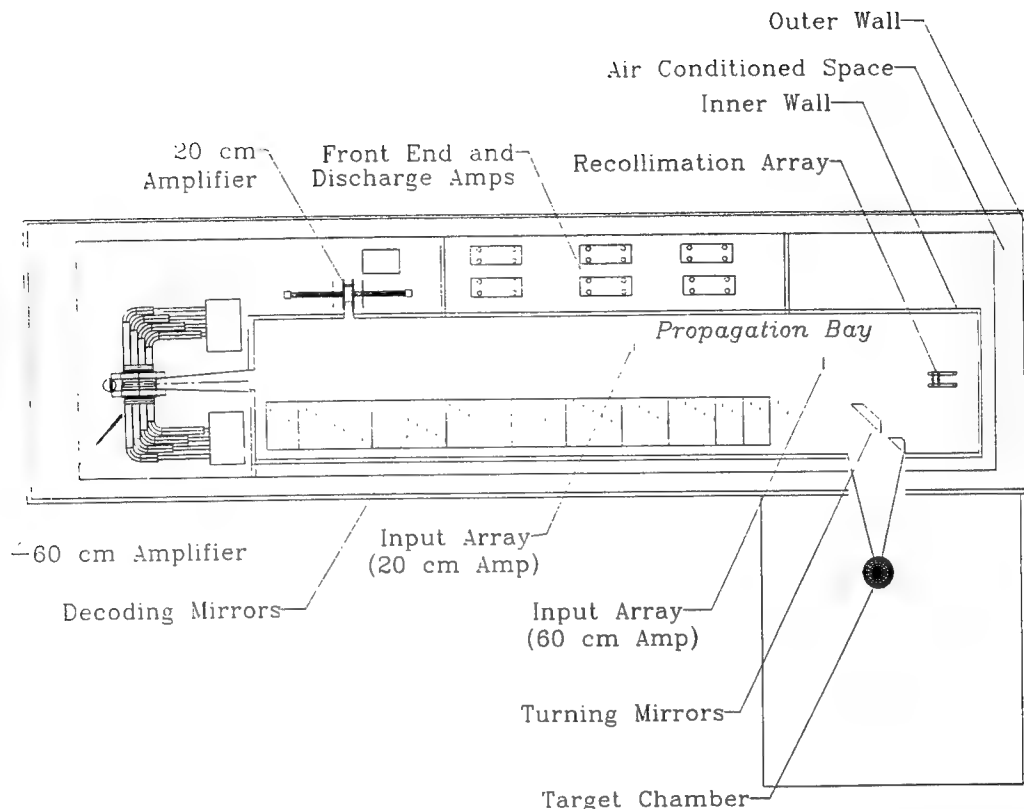


Fig. 17.1 — A simplified view of the Nike facility. The large room which is the propagation bay contains only optics. The amplifier room is on a separate air system to avoid contaminating either the propagation bay or the oscillator and control rooms.

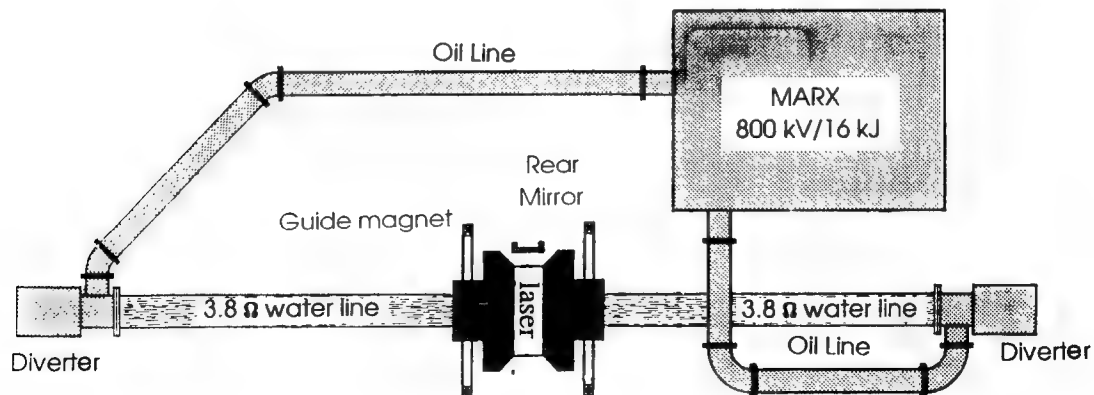


Fig. 17.2 — The 20 cm amplifier. Diverters protect the system in case of misfire.

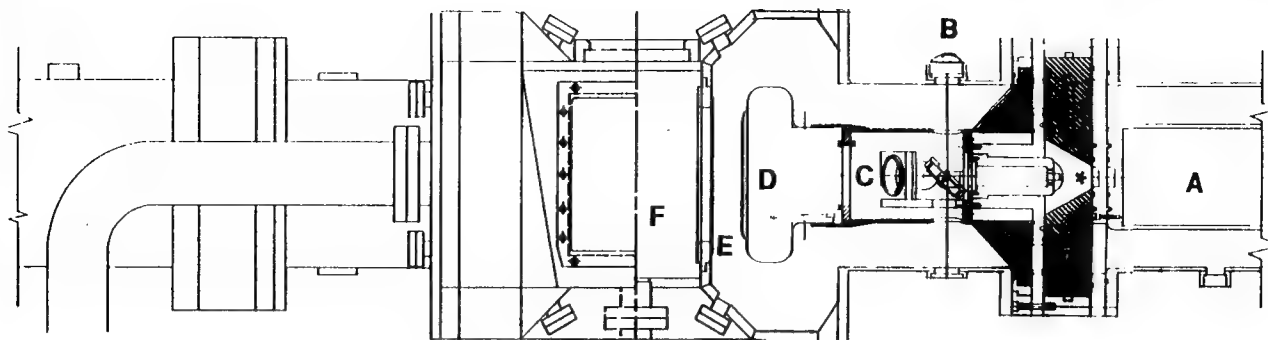


Fig. 17.3 — Close up front view of the electron diodes and laser cell. Right hand side is a cutaway view. The water line is A, trigger laser light enters through lens B reflects off of a  $45^\circ$  mirror and focuses at \*, C is the cathode stalk and D is the cathode shell and emitter. E is the anode screen, hibachi and gas foil, and F is the laser cell.

water lines are fired, closing the connection between the water lines and the electron diode cathodes. The electron diode is a matched load to the water line to maximize energy efficiency and to give a flat topped voltage pulse 180 nsec long (full width half maximum). For a 80 kV charge on the Marx capacitors, the voltage pulse on the diodes is 290 kV delivering 75 kA of beam current. Typical diode current and voltage waveforms are shown in Fig. 17.4. The system jitter for firing the electron diodes is  $\pm 5$  nsec and the current and voltage time histories are extremely reproducible even over periods as long as 1 year. The pulse power system has not required any repairs in 2 years and has been operating with over 99% reliability.

The diode creates an electron beam 21 cm high and 80 cm long that is directed into the laser cell. There is an electron diode on the east and west side of the laser cell, so the electron beams are counterpropagating into laser gas. The electron beams pump the laser gas mix which causes the lasing action. Extensive effort was placed on the electron diode design as most of the important improvements in KrF lasers occurs there.<sup>17,6</sup> Research was conducted to solve problems with vacuum insulators, stray electron currents, and electron beam uniformity. One of the most important factors is the transfer efficiency of the electron beam from the diode into the laser gas. Electron diodes require vacuum pressures on the order of  $1 \times 10^{-4}$  torr or less to work. The laser gas should be 1000 torr (19 psia) to absorb the electrons efficiently in

one pass from one side of the cell to the other. This requires a thin foil that can hold the gas pressure against vacuum but through which electrons can pass easily. The 20 cm amplifier uses 0.002 inch thick (50  $\mu\text{m}$ ) Kapton plastic to separate the gas from the vacuum. The Kapton does not have the mechanical strength to support the pressure force of the entire area of the electron beam aperture. To provide the required mechanical strength a grill like foil support structure (see Fig. 17.5) was made using vertical steel bars .42 cm thick, 1.5 cm deep, spaced 4.2 cm apart to span the 24 cm high by 84 cm wide aperture for the electron beam. The aperture is larger than the electron beam in either dimension, allowing the entire beam to pump the gas.

A uniform ground plane for the accelerating electric field in the electron diode is supplied by an anode screen fitted over the foil support structure on the diode side (opposite side from the foil). The electron beam suffers losses before reaching the laser gas due to electrons being blocked by the anode wires and support bars. The total transmission loss in the 20 cm just due to these elements is 5% for the anode screen and 15% for the support structure. The 50  $\mu\text{m}$  Kapton has the same areal mass as 1 cm of 1100 torr of 20% krypton 80% argon gas, and therefore will backscatter the same fraction of electrons and have similar energy absorption per pass. As electrons enter the foil and gas, some will backscatter toward the cathode and be intercepted by the foil supports or the anode.

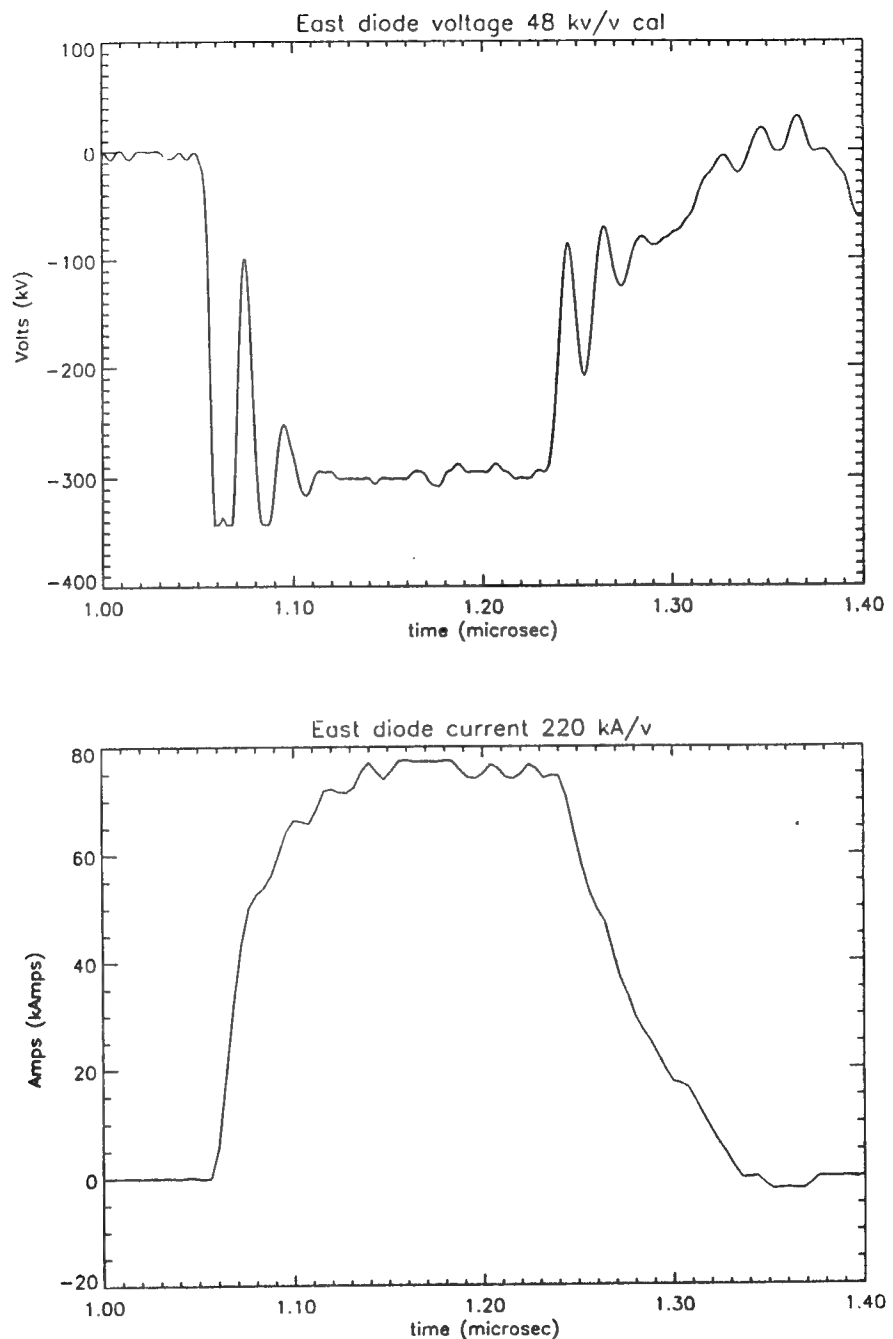


Fig. 17.4 — The diode voltage at the vacuum insulator and the diode current through the cathode stalk. The flat portion of the pulse is 135 nsec long.

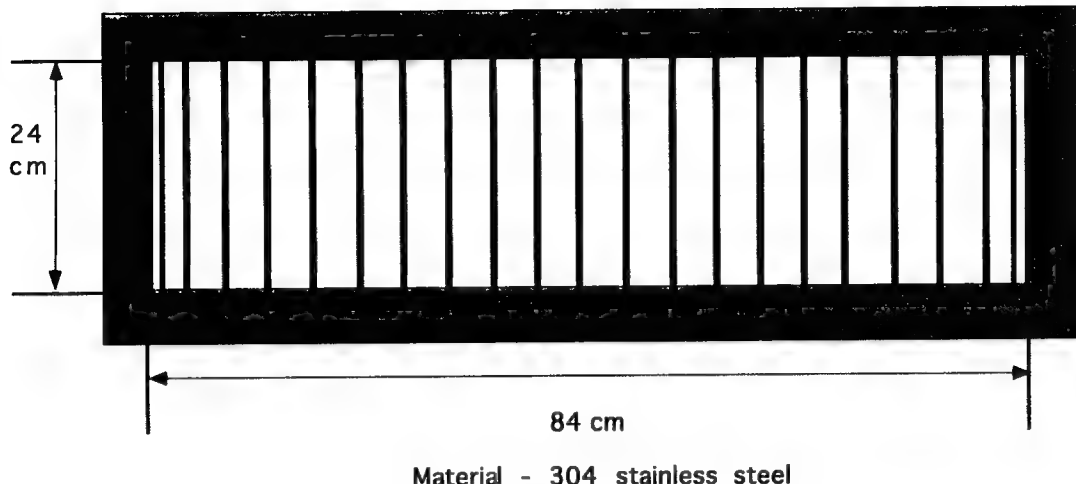


Fig. 17.5 — Beam view of the foil support structure.

Those which do not get intercepted will reflect from the cathode potential and go back into the gas. Electrons will reflex in and out of the gas as well as reflex inside the gas due to repeated scattering losing energy continually. The best hope for calculating the energy deposition is by the use of Monte Carlo codes. Monte Carlo codes track single electron trajectories of a large number of electrons to predict the average energy deposited in the laser gas as a function of position. Simulations which were run for the 20 cm amplifier found the total energy deposited into the gas will be on the order of 45% of the beam energy reaching the Kapton with the remainder being absorbed either by the laser walls, the support structure or in the Kapton foils.<sup>17.7</sup> Using the average measured values of the diode voltage and current and multiplying first by .8 and then by .45, then by 2 for both electron beams, the energy deposited into the laser gas should be 3.5 kJ.

Experience in other electron beam lasers has resulted in energy transfer efficiencies worse than the simple estimate given above. In order to check this and other important characteristics of the electron beam a series of experiments were performed. Using a 7.7 cm  $\times$  7.7 cm Faraday cup the average transmission of the electron beam into the gas (including gas backscattering losses) was measured over 10 different places in the electron beam. An average current of 21 amps/cm<sup>2</sup>  $\pm$  10% was found over the 21 cm  $\times$  80 cm beam. The uniformity

was in agreement with a single shot diagnostic that uses a GAF densitometry media<sup>17.8</sup> which gives an image of the electron beam intensity in the laser cell very close to the hibachi. Repeated measurements with improved anode screens gave 25 A/cm<sup>2</sup> approximately 1 cm into the gas. The amount of energy absorbed by the laser gas is estimated by correcting pressure rise measurements for fluorescence losses. This gives 4 kilojoules, which is higher than predicted. Further improvement in energy transfer efficiency will require more exotic support and foil structures.

The velvet type cathode used in the 20 cm diodes has a low closure velocity, which is indicated by the flat top current and voltage time histories. The 135 nsec flat top portion of the diode pulse will be used to amplify the laser pulses, which should result in good laser beam balance with no spatial variation from one laser beam to the next. Additionally the velvet cathode when used with a smooth anode screen gives no small scale structure in the electron beam profile which could damage the foil or give anomalous results by distorting the amplified laser beam. The cathode structure was designed so that the electron beam profile was flat over the entire aperture with less than a 10% variation, i.e. no high intensity edges or center. Profiles of the electron beam which had been taken with the aforementioned GAF dosimetry media show good uniformity with no high intensity edges or spots. All measurements of

the laser pumping profile across the aperture of the laser and the electron beam uniformity has met the requirements for the Nike system. More complete data should be available in 1994.

## INITIAL SYSTEM INTEGRATION AND TESTS

In order to test adequately the 20 cm amplifier, the complete Nike system was required to be integrated together through the 20 cm amplifier. To achieve this goal the 20 cm amplifier is operated by remote control in the Nike control room (upper right hand corner of Fig. 17.1). Fiber optically coupled PLC links operated by a 486 base computer operate all the required safety interlocks to avoid personnel exposure to X-rays generated by the 20 or 60 cm amplifier, exposure to the ultraviolet laser light or accidental release of fluorine gas. This same system performs routine checks on the 20 cm, turns on the power supplies for the Marx bank and the guide magnetic field, charges the Marx and sets the system for firing when the charge voltage is reached. This control system is described in more detail in Section 22.

The trigger system is centralized in the control room to limit system jitter. The triggers are sent out by fiber optic links to avoid feedback to the pulsers. Pulse power data is taken by digitizing oscilloscopes which send data back to a central computer disk via GPIB fiber optic links. Data from the oscillator room showing the laser pulse time history and images from the CCD cameras are also stored with calorimetric data of the output energy of the 20 cm amplifier. The data can then be analyzed by a number of different computers or sent to other labs. The combination of the central control system, central triggering, and central data acquisition allows close coordination of the entire facility and is responsible for virtually all of the data shown.

Initial tests to extract laser energy out of the 20 cm amplifier were started before the complete optical system components were available. Therefore the system was set up with test optics which were available from the 1990 experimental arrangements. This allowed us to send six beams through the 20 cm amplifier. These

beams did not optically relay the focal profile and so no focal profile measurements were made at this time. The 30 nsec FWHM oscillator pulse was fed directly into the discharge amplifiers. The shorter gain pulse of the  $4 \times 4$  discharge results in the laser beam having a half sine pulse 16 nsec FWHM (see Sections 14 and 15). The multiplexing table was set up to separate the beams by 25 nsec (except between the 2nd and 3rd beam there is a 35 nsec gap). Figure 17.6 shows the input and output pulse chains to the 20 cm amplifier. These initial results showed the output from the 20 cm amplifier were sufficient for the system requirements. The remaining optics to complete the Nike system through the 20 cm amplifier were then installed. The front end was completed to include the pulse slicing and control beams to give a 4 nsec pulse (see Section 10). The control beam was separated from the main beam by polarizers and spatial filters were added in between the  $4 \times 4$  large aperture discharge amplifiers output and the input array to the 20 cm amplifier to eliminate window reflections. 75% of the energy which passed through the spatial filters passed through the aperture of the 20 cm amplifier (the 20 cm amplifier is slightly overfilled by the input beams). Twenty-eight beams were sent into the amplifier and the output beams were bounced off of the lower set of mirrors on the intermediate (60 cm feed) array. There are only 28 beams here because the beam splitter/delay telescope that will be installed on the output of the 20 cm amplifier to give 56 beams will not be installed until testing of the 60 cm amplifier as a laser amplifier is in progress. Apart from this difference, these beams are exactly as they will be when used to drive targets. The output beams reflected off of the intermediate array are not expanded to fill the 60 cm, but instead are directed into calorimeters, photodiodes, and CCD cameras so that energy, time histories, and focal profile data can be obtained from any beam (see Fig. 17.7). The results in terms of energy input (measured at the spatial filters) to energy output (measured by calorimeters after the intermediate array) is plotted in Fig. 16.12, Section 16. These results are compared with a simplified kinetic code result in order to predict what improvements

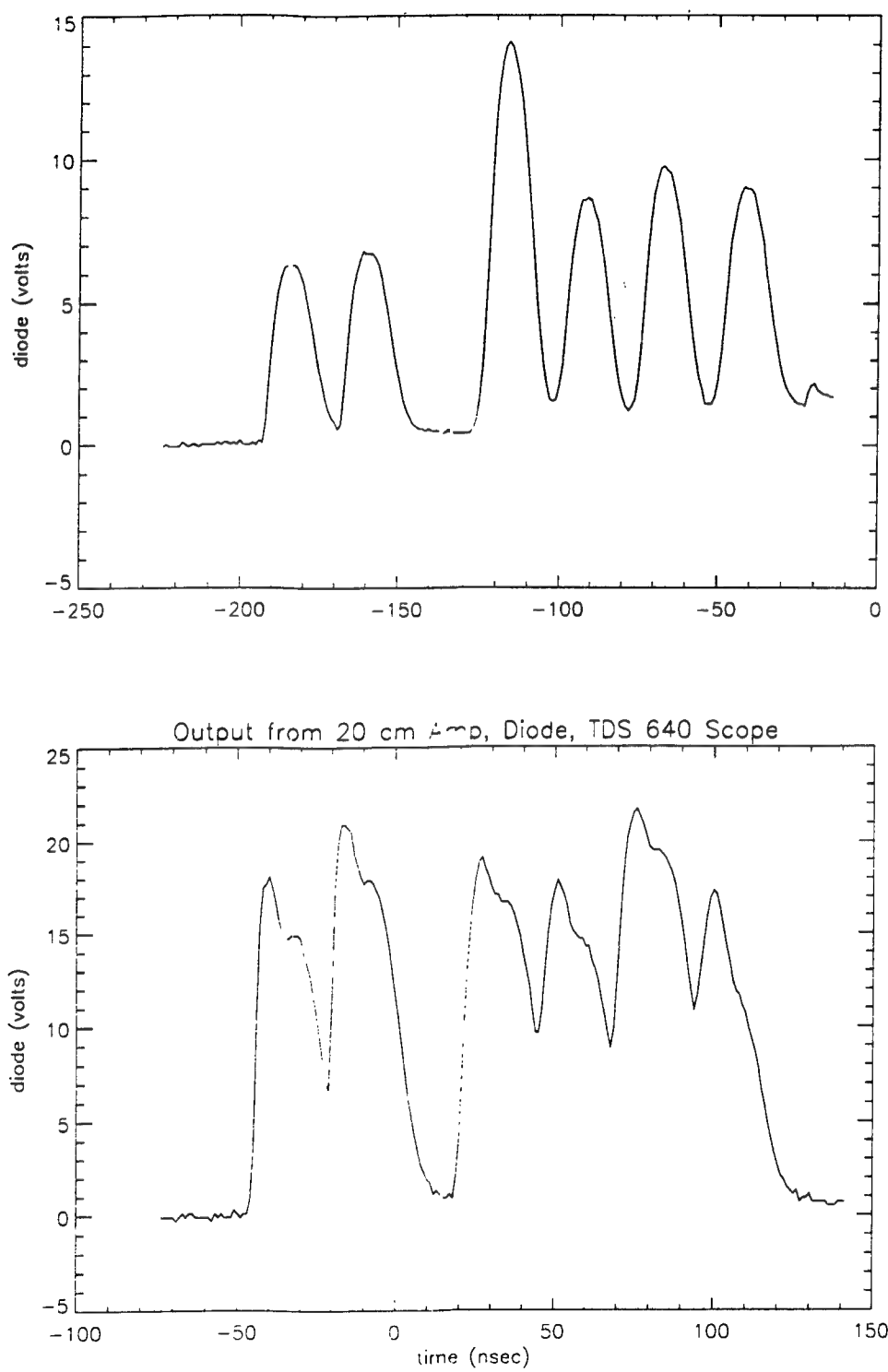


Fig. 17.6 — Input and output pulse trains through the 20 cm amplifier.

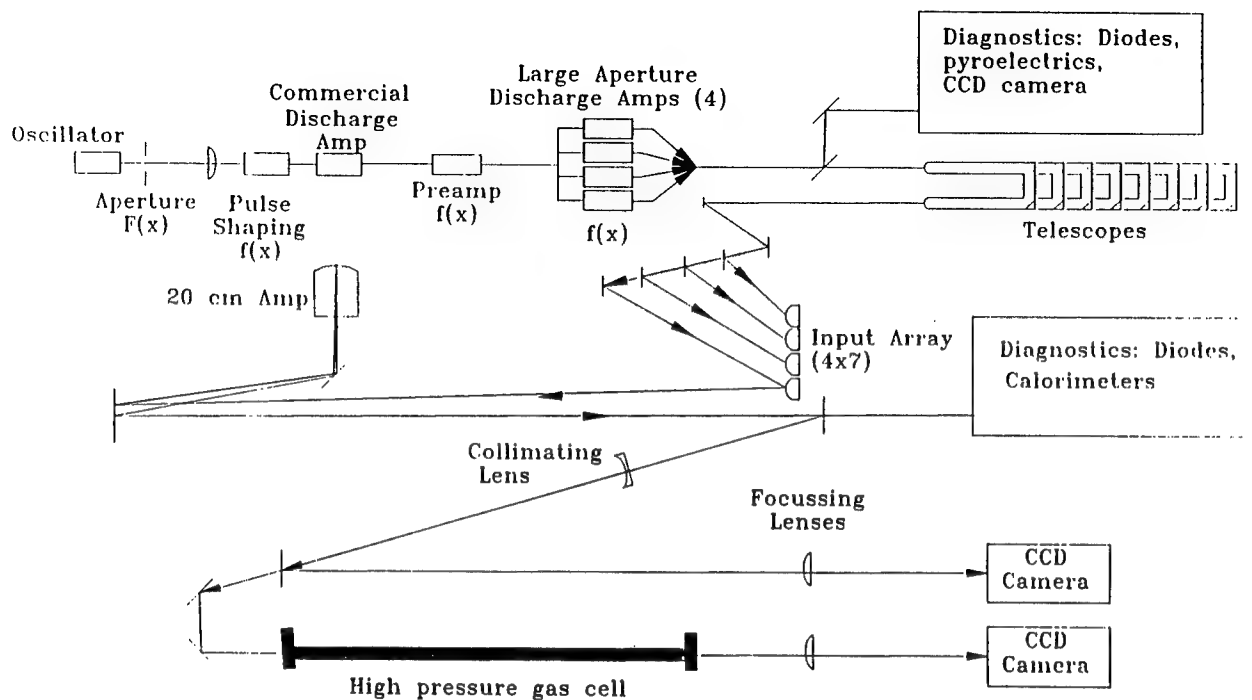


Fig. 17.7 — The current experimental setup to measure the energy and profiles of the output beams from the 20 cm amplifier

can be obtained in the performance of the 20 cm amplifier and obtain a reasonable test case for predicting the output of the 60 cm amplifier based on the design pumping power and laser mix. This code is described in more detail in Section 16 along with additional data obtained from the system. The code predictions are in excellent agreement with the data. This code will be more thoroughly tested for various laser gas mixes, fluorine burn up, and ASE predictions.

Figure 17.7 shows the setup for the focal profile measurement described in Section 11 which showed that the Nike requirement can be met. There is also additional setup for a pressure tube to measure nonlinear optical index and absorption in air and other gases. Spectrometers are also set up to measure any bandwidth narrowing due to amplification. As work progresses, these additional diagnostics will be used to examine all aspects of the Nike operation.

## SUMMARY

System performance has been to expectations with no outstanding difficulties encountered. The 20 cm amplifier has the required uniformity for beam amplification and appears to have the required output energy. More detailed analysis and improvements in reproducibility will be examined with an eye to completing the system as a routine target shooting device. Improvements in service lifetime and operating conditions will be examined.

This work was performed with the help of T. Lehecka and A. Deniz of Science Applications International Corporation.

## REFERENCES

17.1 L. G. Schlitt, *4th Annual IEEE Int. Pulsed Power Conf.*, (1983).

17.2 L. A. Rosocha, K. B. Reipe, *Fusion Technology*, Vol. 11, No. 3, 576, (1987).

17.3 I.N. Ross, M.J. Shaw, C.J. Hooker, M.H. Key, E.C. Harvey, J.M.D. Lister, J.E. Andrew, G. J. Hirst, and P. A. Rodgers, *Optical Communications* **78**, 263, (1990).

17.4 Y. Owadano, I. Okuda, M. Tanimoto, Y. Matsumoto, T. Kasai, M. Yano, *Fusion Technology*, Vol. 11, No. 3, 486, (1987).

17.5 K. Ueda and H. Takuma *Conf. on Lasers and Electro-Optics Tech Digest*, 7, 40 (1989).

17.6 C. J. Pawley, J.D. Sethian, S.P. Obenschain, S. J. Czuchlewski, *9th Int. Conf. on High Power Particle Beams, (Beams92)*, Vol III, 1912, (1992).

17.7 W. T. Leland and D. Hanson, codes at LANL, (1991).

17.8 W.L. McLaughlin, C. Yun-Dong, C.G. Soares, A. Miller, G. Van Dyk, D.F. Lewis, *Nuclear Inst. and Methods in Physics Research A*302 165 (1991).

## Section 18 THE 60 CM AMPLIFIER

J.D. Sethian

*Laser Plasma Branch  
Plasma Physics Division  
Naval Research Laboratory*

### INTRODUCTION

The 60 cm amplifier, shown in Fig. 18.1, is the final and largest amplifier in the Nike laser. It is a double-sided electron beam pumped system whose goal is to produce a 240 nsec pulse of laser light with an energy of at least 5000 Joules. The input laser energy is

150 Joules produced by the 20 cm amplifier. In order to achieve the required gain, the electron beams must deposit 80 kJ (40 kJ per beam) into the gas. This corresponds to a power density of around .45 MW/cc. Figure 18.2 shows the predicted gain of the 60 cm amplifier as a function of the input energy from the 20 cm amplifier.

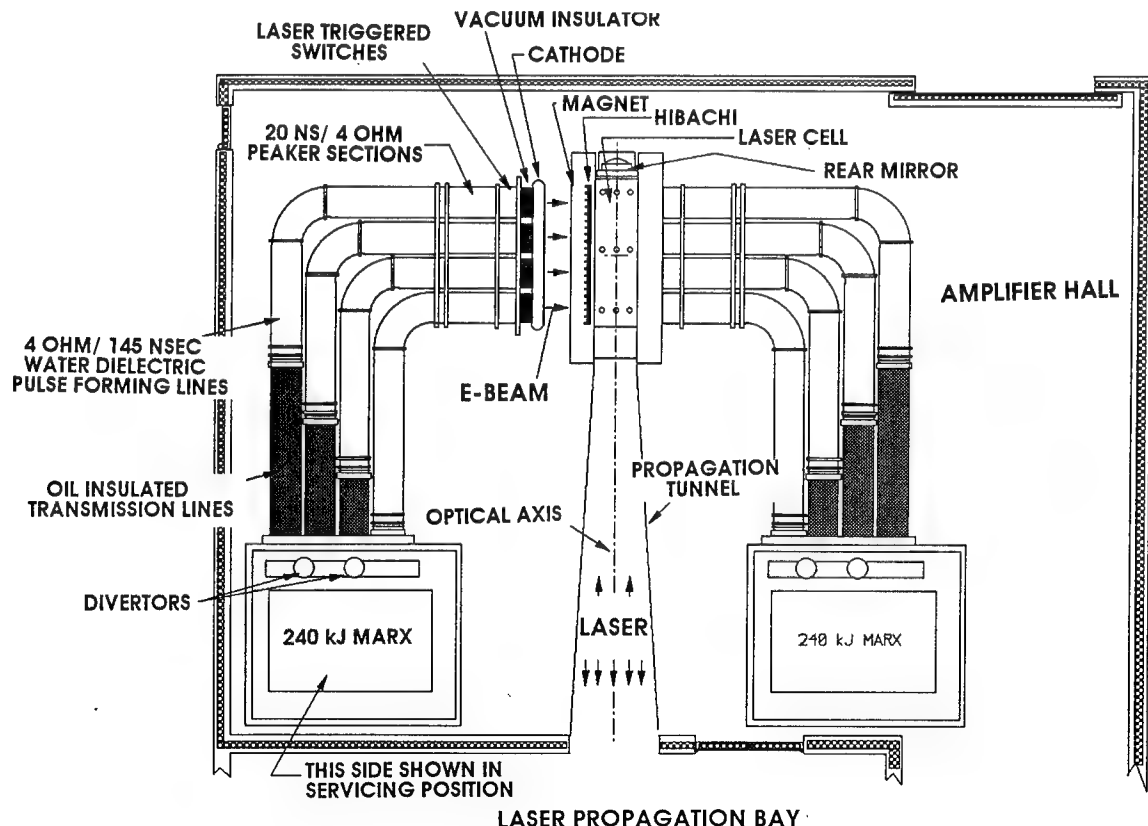


Fig. 18.1 — The Nike 60 cm amplifier. The left half of the system (north side) has been rolled back for servicing.

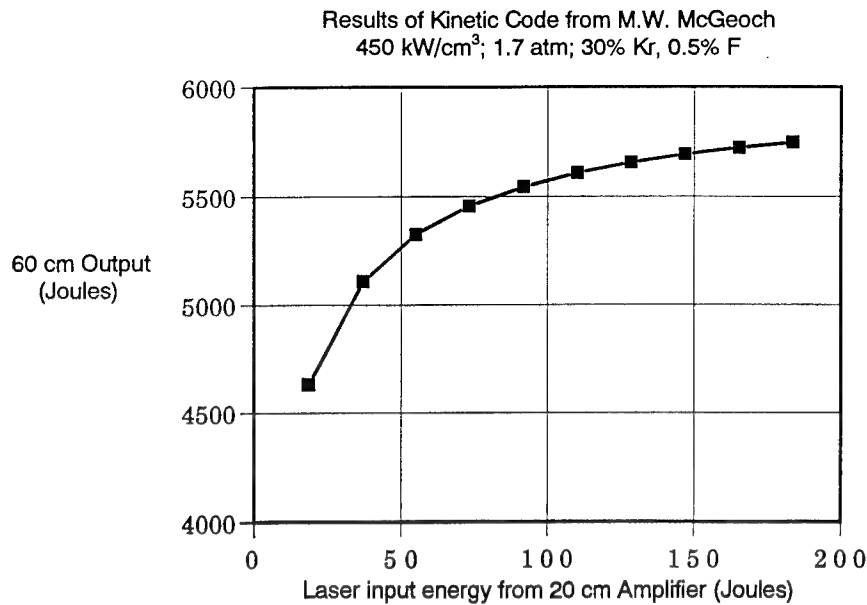


Fig. 18.2 — Simulations of the predicted laser output from the 60 cm amplifier.

The 60 cm amplifier was built using the experience gained with the 20 cm amplifier which is now a fully operational and reliable component of the Nike laser. Details of the 60 cm Amplifier can be found in the Fact Sheet in Table 18-1, in the open literature,<sup>18.1,18.2</sup> and in the 1992 DOE Nike Review.<sup>18.3</sup> Significant progress has been made in the development of the 60cm amplifier since the date of that review. Both sides have been fully assembled, the pulsed power has been fully tested on one side, and the preliminary E-beam tests show that both the energy deposition and uniformity requirements can be met.

## DESCRIPTION OF THE 60 CM AMPLIFIER

The 60 cm amplifier is based on the well-established Marx/pulseline/output switch/z stack insulator/field emission cathode architecture. Although using established technologies, the amplifier does have several novel features, including: radial diaphragm laser triggered switches; a relatively low inductance (and hence fast rise time) large field-emission cathode; and, a relatively high transparency hibachi (foil support) structure.

**Marx:** The Marx generators follow the well-proven ANTARES<sup>18.4</sup> low inductance arrangement. The Marxes have 24 half stages (i.e. 12 switches) with each half stage composed of two 2.8  $\mu$ F @60 kV capacitors. Maximum charge voltage is 60 kV/half stage, with an erected voltage of 1330 kV. As oil vapor is highly absorbent at the KrF laser wavelength of 248 nm, the Marx oil tanks have been completely sealed.

**Oil Transmission Lines:** Each Marx is connected to four separate oil transmission lines that contain electrically identical 2 $\Omega$  resistor/1.2  $\mu$ H inductor networks. The oil transmission lines vary in length to compensate for the 90° bends in the water dielectric pulselines. These networks electrically isolate the pulselines from each other, and prevent all the lines from discharging into one if a fault develops.

**Water Dielectric Pulse Forming Lines:** Each of the four coaxial pulse forming lines consists of two sections; a 145 nsec long, 5 $\Omega$  impedance main section followed by a 20 nsec long, 4  $\Omega$  peaker section. The peaker gives an initial higher voltage increase to the leading edge of the pulse in order to reduce the voltage rise time. In order to fit the amplifier into the available space, the pulse forming lines are bent

Table 18.1 — 60 cm Amplifier Fact Sheet

<b>MARX</b>	Capacitor type	2.8 $\mu$ F @ 60 kV	<b>RESISTOR</b>	
Caps/half stage/Marx	2		Value	100 $\Omega$
Number of half stage/Marx	24			
Number of switches/Marx	12			
Total # caps/Marx	96			
Maximum operating charge voltage	55 kV	<b>INSULATOR</b>		
Stored energy/Marx	203 kJ	Number of Insulator rings/line	7	
Erected capacitance	.233 $\mu$ F	Field on each ring	59-72 kV/cm	
Erected voltage	1320 kV	Uniformity	$\pm 13\%$	
Marx Inductance	4.45 $\mu$ H	Total Insulator area (all eight lines)	$2.2 \times 10^2$ cm <sup>2</sup>	
Marx Resistance	284 m $\Omega$	Breakdown probability	53% - 69%	
Maximum discharge current/Marx	200 kA	SF6 insulation	75 psi	
Nom discharge current (4 lines)/Marx	190 kA	Breakdown probability	60%	
Charge time (1/4 cycle)	2.1 $\mu$ sec	Max field in SF6	210 kV/cm	
Switches fire	1.9 $\mu$ sec			
Divertors fire	2.2 $\mu$ sec			
Clamp resistance	4.5 $\Omega$			
<b>OIL LINES</b>				
Resistance (external at manifold)	2 $\Omega$	<b>DIODE</b>		
Inductance	1.2 $\mu$ H	Peak voltage	$671 \pm 30$ kV	
<b>PULSELINES</b>		Current (one side)	540 kA	
Total line length (ns)	165 nsec	Cathode area	204 cm x 64 cm	
Total line length (ft)	18.14 ft (553 cm)	Aperture cathode	200 cm x 60 cm	
Peaker Line length	20 nsec	Cathode current density (one side)	40-45 A/cm <sup>2</sup>	
Main line impedance	5 $\Omega$	Gap	5 cm	
Peaker line impedance	4 $\Omega$	Nominal Impedance	1.25 $\Omega$	
Main Capacitance (one line)	33 nF	High Impedance (for stability)	1.5 $\Omega$	
Peaker Capacitance (one line)	5 nF	Low impedance (for deposition)	1.0 $\Omega$	
Total Capacitance (38 nF x 4)	.152 mF	Peak power (55 kV)	387 GW	
Peak volts	1.50 MV	Pulse length (flat top, $\Delta V < \pm 5\%$ )	253 ns	
Stored energy (one side)	171 kJ	Cathode stress (Non-emitting areas)	70 kV/cm	
Peak field/inner	170 kV/cm	Cathode stress (in corners, 4% of area)	102 kV/cm	
Peak field/outer	76 kV/cm	Field at emitter surface	140 kV/cm	
Total area/inner	$1.67 \times 10^3$ cm <sup>2</sup>	Emitter material	Velvet (probably)	
Total area/outer	$3.45 \times 10^3$ cm <sup>2</sup>			
Breakdown prob/main (normal op)	62% (both sides)	<b>MAGNETIC FIELD</b>		
Breakdown prob/peaker (normal op)	65% (both sides)	Strength	3-4 kG	
Breakdown prob/main (divertor only)	71% (both sides)	Risetime	10 seconds	
Breakdown prob/peaker (div only)	89% (both sides)	Pulse duration	30 seconds	
<b>DIVERTORS</b>				
Number	2/Marx	<b>TRANSMISSION FOIL</b>		
Operating pressure	60 psia max	Anode	Screen (for now)	
Resistance (external)	3 $\Omega$	Laser Cell/Diode vacuum	3 mil Kapton	
<b>SWITCHES</b>		Hibachi Rib Depth	4 cm	
Current	134 kA	Hibachi spacing	who knows	
Charge transfer	.05 Coul			
Gap	4 cm			
Maximum electric field	390 kV/cm	<b>LASER</b>		
Maximum operating pressure	100 psia	Cell Volume	$60 \times 60 \times 200$ cm <sup>3</sup>	
Breakdown probability	65%	Quartz end window thickness	5 cm	
Laser energy /switch	20 mJ @ 266 nm	Cell Fill pressure	30 psi max	
Laser power	5 GW/cm <sup>2</sup>	Pressure jump	8 psi	
Inductance	100 nH	Laser pulse length	240 nsec	
Diaphragm material	Nylon	Deposit power, two sides; 80 kJ/240 ns	.50 MW/cm	
Field on diaphragm	85 kV/cm			
		<b>ENERGY ACCOUNTING</b>		
		Marx Energy	203 kJ	
		Line Energy	171 kJ	
		Diode 671 kV x 540 kA x 253 nsec =	92 kJ	
		Transmitted into gas (total, 253 nsec)	46 kJ	
		Deposited into gas (240 nsec)	40 kJ	
		laser (6.25% efficiency)	2.50 kJ	
		for two sides	5.00 kJ	

through  $90^\circ$ . While creating a few mechanical complications, the electrical effects of these bends are negligible. Both numerical simulations with a three dimensional (3d) transmission line code and simple experiments with a scale model show that the bends neither degrade the output pulse risetime, nor compromise the electrical strength of the system.<sup>18,5</sup>

Main Output Switches: Each pulseline is terminated with its own output switch shown in Fig. 18.3. The switches are SF<sub>6</sub>-insulated and consist of two radial nylon diaphragms that each have a single quasi-spherical electrode in the center. The output side of the switch is held at ground by a  $100\ \Omega$  radial water resistor. Each switch is triggered with a laser pulse of about 11 mJ @ 266 nm that is generated by a frequency quadrupled Nd:YAG laser and focused to a power density of about  $5\ \text{GW}/\text{cm}^2$ . The total inductance of each switch is about 100 nH.

Vacuum Insulator: The power is fed from each switch through a conventional z-stack insulator to a common cathode. Calculations show that the insulator is operating at about 69% of breakdown of one segment. The entire insulator stack is designed to be assembled on the bench where it can be tested for vacuum integrity and electrical stress before installation.

Diode: The cathode shell is electropolished and the average field kept below 70 kV/cm, both of which should prevent emission of parasitic currents to the wall. The emission surface itself is made from velveteen following experience learned from the 20 cm amplifier. The edge of the emitter is fully radiused and extends 2 cm beyond the edge of the anode aperture. This blocks the intense beam halo that is emitted from the edge of the cathode from entering the hibachi; those electrons would have high angle trajectories and be poorly transmitted, thus compromising foil lifetime.

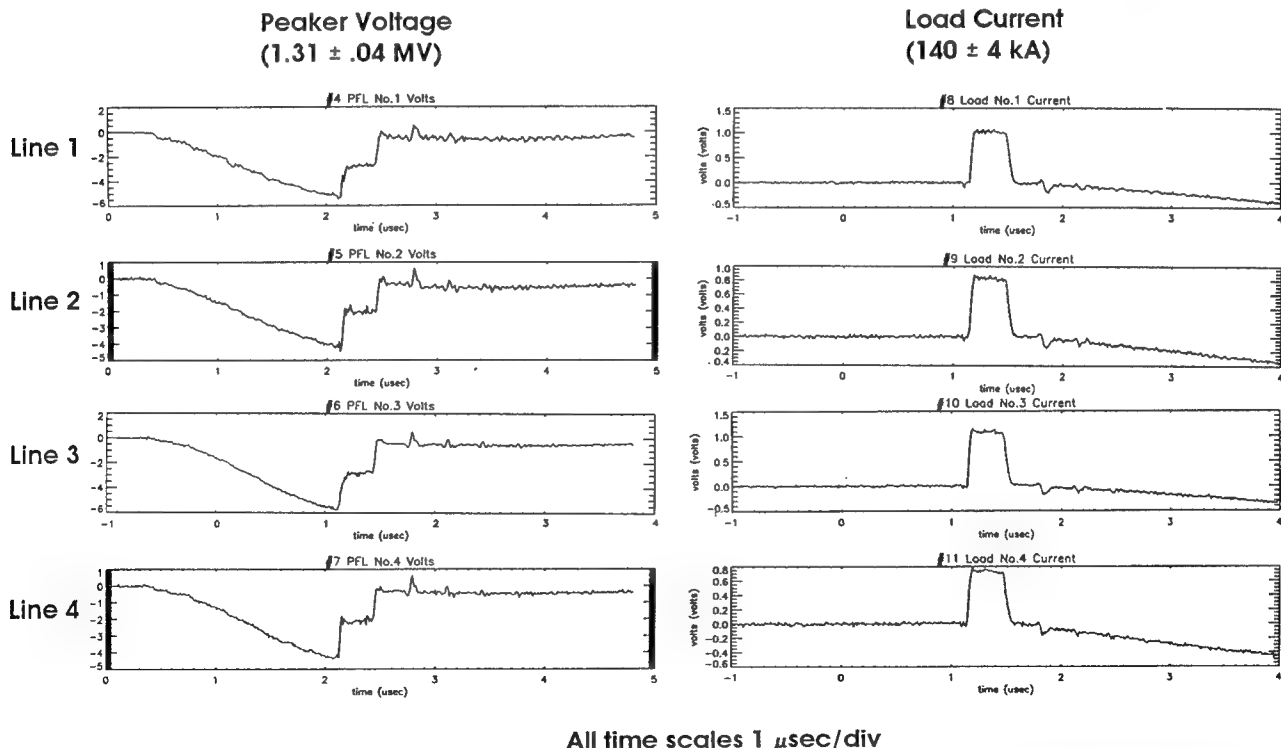


Fig. 18.3 — Peaker Voltage (left column) and Load Current (right column) for all four lines fired simultaneously, but driving their own fixed resistive loads. The charging voltage was 55 kV, or 110% full charge. The current waveforms are nearly identical and exhibit the flat pulse required by the laser.

We have designed the amplifier so the diode impedance and power can be varied according to the requirements of the electron beam or laser kinetics. In the baseline mode, the diode impedance is  $1.25 \Omega$  and the total electron beam power from each of the two sides is 330 GW at 650 kV. If we need to pump the amplifier harder, we have the option of operating at higher charge voltages to increase the diode power to 390 GW (670 kV). If, on the other hand, the laser kinetics call for increased beam current, then we can lower the diode impedance to  $1.0 \Omega$  to maintain 330 GW at 650 kV, but at a higher current. Finally, we can raise the diode impedance if it is required to stabilize the electron beam.

Transmission foil: The electron beam is passed through an anode screen, past the "hibachi" structure ribs, and through a Kapton foil into the laser cell. The beam is guided by a 4.0 kG magnetic field. The hibachi ribs are of a new design and composed of a high strength nickel-based alloy which allows them to be relatively thin for a hibachi of this size. They are also mounted vertically. These two features should increase the transmission efficiency. Our calculations show that with this design (a .0076 cm thick Kapton foil, and an anode grid with 78% transmission) 51% of the beam will be transmitted into the gas. The actual efficiency will probably be about 5-10% less due to gas backscatter.

The Laser Cell: The laser cell and diode boxes are a single large monolithic unit constructed of stainless steel with 5 cm thick quartz windows at either end. Both windows are mounted in non-parallel planes and neither are perpendicular to the cell axis, in order to prevent parasitic buildup of ASE. The cell is designed to operate at pressure of up to two atmospheres, with an overpressure jump of up to 0.7 atmospheres.

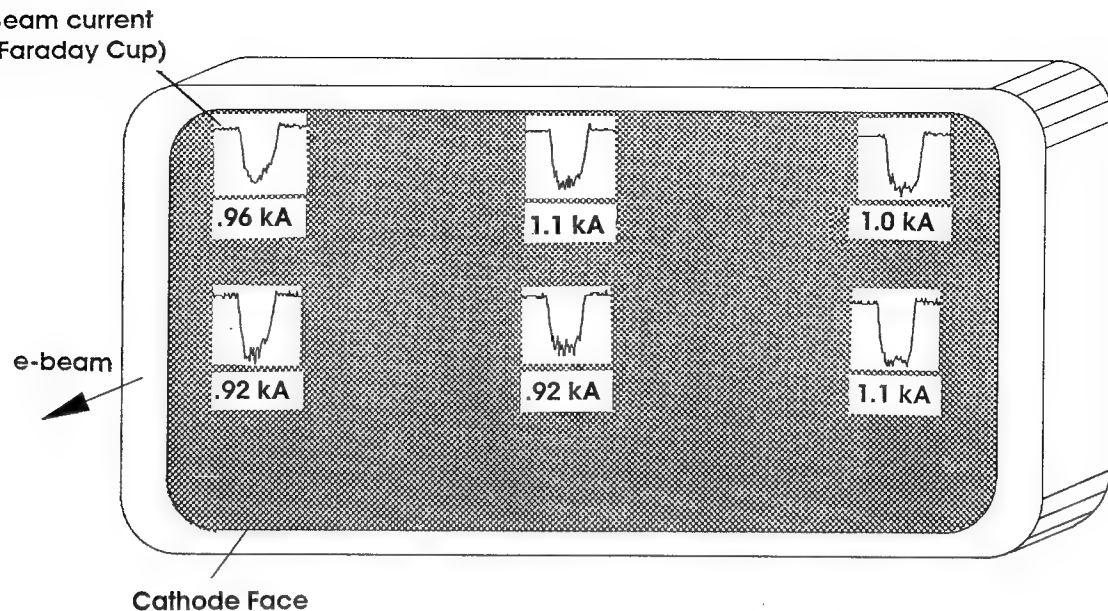
Divertors: The pulselines operate at about 65% of the maximum allowable electrical stress, and hence should be fairly immune to breakdown. However if the main switches fail to fire and the system is subjected to a full "ringing cycle" (i.e. energy oscillates between Marx and pulselines), the maximum electrical stress on the lines will be exceeded, and the pulselines will

in all probability break down. To prevent such an undesirable event from occurring, we have incorporated two SF<sub>6</sub>-insulated divertor switches that discharge the pulselines safely into a  $3 \Omega$  resistive load. These switches are copies of the successful Rimfire design developed at Sandia<sup>18,6</sup> and are triggered 400 nsec after the main switches are supposed to fire by a timing circuit that derives its initiation signal from the erected Marx. Thus the divertors are triggered independent of whether the Marx is triggered or prefires. While the divertor circuit is fully operational, we have yet to require its services as the output switches have never failed to fire in over 350 shots.

## STATUS

As of August 1993 the north side (the left hand side in Fig. 18.1) of the amplifier has been constructed and the first experiments to inject the electron beam into the gas have begun. The south side has been assembled and is awaiting the results of tests on the north. Figure 18.3 shows the voltage in the peaker sections and current through the switches of the north side operated at 110% normal operating voltage. This corresponds to the "high power mode." Each line was fired simultaneously, but each was connected to its own independent 5 ohm resistive load. The voltage on all four lines was  $1.3 \pm 0.04$  MV, and the current through each load  $140 \pm 4$  kA, which attests to the balance of the system. As can be seen, all four lines are switched out with a jitter of a few nsec, and all four current pulses have the flat output waveform required for uniform electron beam pumping of the laser cell.

The first tests of firing the electron beam into the laser cell are equally encouraging: Fig. 18.4 shows the current measured in the laser cell with a Faraday Cup array located across the 60 cm  $\times$  200 cm cathode. In these tests, the electron beam was produced by the north side of the 60 cm amplifier and injected into both the laser cell and the empty south side diode. The target volume was filled with 15 psi argon. The current injected into the cell across the 200 cm  $\times$  60 cm cathode varies by less than 10% throughout the 240 nsec portion of the



Transmission efficiency from cathode stalk to laser cell is 54%

Fig. 18.4 — Beam current in the laser cell as measured with a Faraday Cup array. The array consists of three sensors equally spaced in the horizontal (long) dimension of the cathode, which is then moved to two different vertical positions to acquire the data shown. The array is located in the laser cell, 8.0 cm from the Hibachi Foil. The beam current has sufficient temporal and spatial uniformity and reproducibility for the Nike requirements.

current pulse that will be used to amplify the laser beam. By comparing the current through all four switches with that measured in the cell, we can get an idea of the transmission efficiency of the foil support structure: Our calculations show that about  $54 \pm 4\%$  of the current through the switches is transmitted into the cell, which is in good agreement with the calculated figure of 51% quoted above. The beam is macroscopically stable over the range of guide fields between 2-4 kG.

Figure 18.5 shows the energy deposited in the laser cell as a function of Marx charging voltage. Here, 50 kV corresponds to full charge, or an electron beam energy of about 670 kV. The deposited beam energy was measured with two pressure rise diagnostics, a Baratron and a Piezo crystal, and corroborated with electrical measurements comparing the stored energy of the pulselines and the transmission efficiency. Note that a single side can deposit up to 45 kJ into the gas. These measurements are a bit optimistic, as we operate at a low enough cell pressure and stop the beam

over a long enough distance so scattering of electrons back through the hibachi foil (i.e. "backscattering") is not an issue. However the measured deposition does exceed our design requirements and gives us optimism that the electron beams can deposit the required energy in just the cell itself. We fully anticipate the 60 cm amplifier will be ready for routine operation by late spring/early summer of 1994.

#### ACKNOWLEDGMENTS

The author would like to acknowledge the contributions of W.D. Webster of East Coast Engineering; K.A. Gerber, D. Hardesty, S.P. Obenschain, C.J. Pawley, and V. Serlin of NRL; O.C. Barr of Pharos Technical Enterprises; T. Lehecka, and A. Mangassarian of SAIC; I. D. Smith, P.A. Corcoran and R.G. Altes of Pulsed Sciences, Inc; M.W. McGeoch of PLEX Corporation, and R.L. Morse, J. Sawyer, D. W. Williams and J. Peterson of Commonwealth Technologies, Inc.

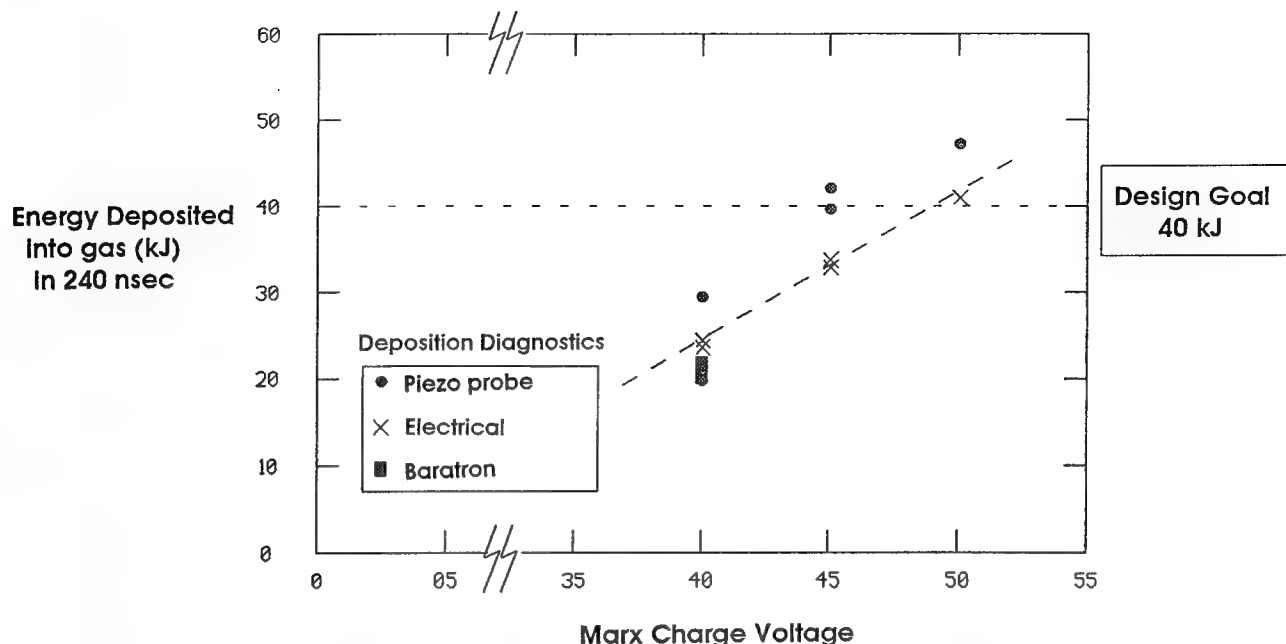


Fig. 18.5 — Energy deposited into the laser cell as measured by three different diagnostics. At 50 kV charge the beam exceeds the 40 kJ design goal. The data assumes that 10% of the energy is lost to radiation, that 28% is lost to the Faraday Cup array (based on geometrical considerations) and only counts the energy deposited in 240 nsec, the length of the input laser beam.

## REFERENCES

- 18.1 P.A. Corcoran, I.D. Smith, R.G. Altes, M.J. Christensen, B.D. Chugg, M.W. McGeoch, J.D. Sethian, S.P. Obenschain and R. L. Morse, Proceedings of The Eight IEEE Pulsed Power Conference, San Diego, Ca, p. 934, (June, 1991).
- 18.2 J. D. Sethian, S. P. Obenschain, C. J. Pawley, I.D. Smith, P.A. Corcoran, R.A. Altes, and M.W. McGeoch, Proceedings of The Eight IEEE Pulsed Power Conference, Albuquerque, NM, (June, 1994).
- 18.3 1992 DOE Nike Report, (August, 1992).
- 18.4 K.B. Riepe et al, Proceedings of The Second IEEE Pulsed Power Conference, Albuquerque, N.M. p. 254 (June 1979).
- 18.5 J.D. Sethian and P.A. Corcoran, Rev. Sci. Instrum. 63, 1 (1992).
- 18.6 B.N. Turman and D.R. Humphreys, Proceedings of The Sixth IEEE Pulsed Power Conference, Arlington, Va. p. 347, (June, 1987).

## Section 19 PROPAGATION BAY

T. Lehecka  
*Science Applications International Corporation*

As discussed in Section 9 the optical design for Nike is complete. The Nike propagation bay is designed to house the majority of the optical components of the Nike laser system in a sealed, temperature and humidity controlled environment. Areas of concern for this portion of the laser include; low optical and air turbulence distortion of the beam to maintain an acceptable point spread function (PSF), vibration levels compatible with achieving our goal of  $\pm 5 \mu\text{Rad}$  pointing stability on target, and an adequately clean environment to minimize atmospheric absorption of the 248 nm light. All of

these points have been addressed in tests of the propagation bay and results of these tests are discussed in this Section.

Figure 19.1 shows the floor plan of Nike as it will be when completed. The optical system fabrication is complete through the 20 cm amplifier. This includes the image relaying optics and angular multiplexing optics to provide 28 beams to drive the 20 cm amplifier stage. Results of beam uniformity and energy produced by this portion of the laser were presented in Section 11.

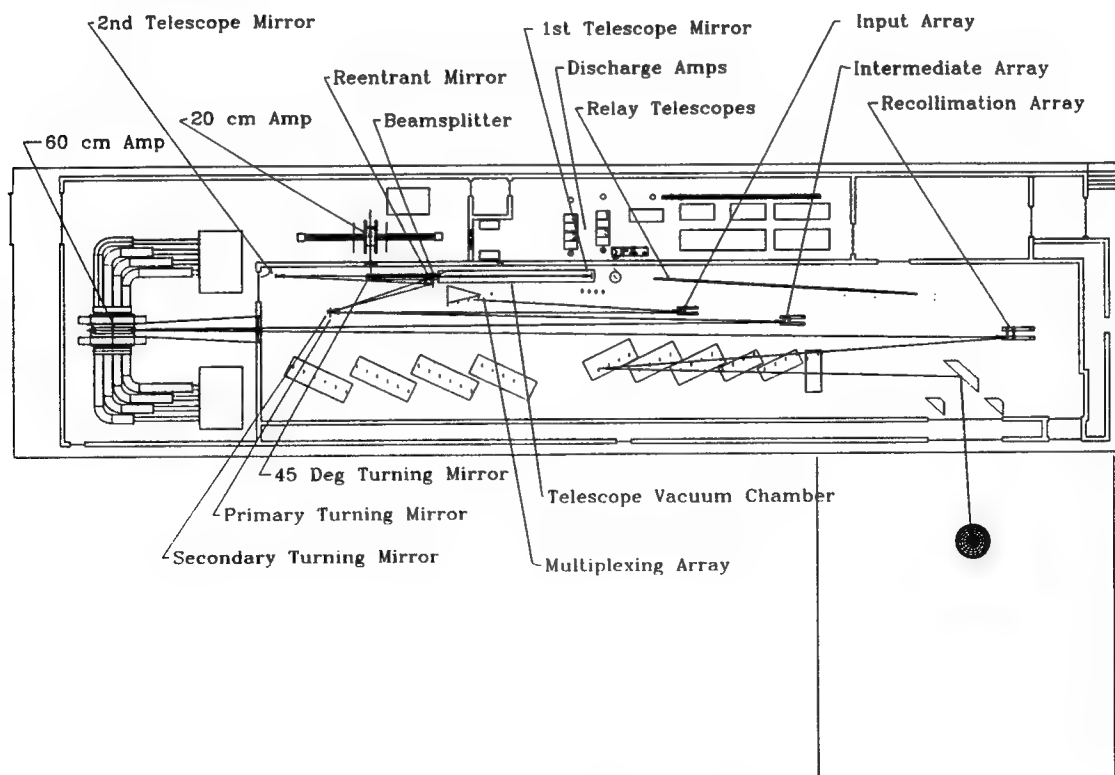


Fig. 19.1 — Floor plan for the Nike laser.

The structures to hold the optics and mounts for the 56 mirror/lens pairs between the 20 cm and the 60 cm amplifier and the structure to house optics and mounts after the 60 cm amplifier is also in place. These components were designed and built by Los Alamos National Laboratory. In addition, the demultiplexing structure is in place and a design for the final turning array structure, completed by Los Alamos, is ready for fabrication.

Tests of optical and atmospheric distortion have been performed in three ways: optical interferometry; optical star tests over long propagation paths; and measurement of optical performance through the actual optical system in place at 248 nm. The optical (633 nm) tests demonstrated that a diffraction limited beam could be propagated over 80 meter distances with less than  $\lambda/4$  peak to valley wavefront distortion and negligible distortion to the Airy pattern at focus.

Results of the more important test, system performance at 248 nm are shown in Fig. 19.2. For this the Nike front end was used to produce a 60 times diffraction limited (XDL) beam at low energy which was propagated through the optical system. A CCD camera was set up after the 20 cm amplifier to measure the resulting focal profile. A cross section of the resulting profile is shown by the solid line in Fig. 19.2. Also shown are calculated profiles using the available optical surface information and calculating the expected PSF due to the optical imperfections. This resulted in a PSF of 7 XDL. This PSF is then convolved with an ideal top

profile and the results are shown as the dashed lines in Fig. 19.2. As is evident the predicted 7 XDL performance is a very good fit to the data. Also, as discussed in Section 11, the amplifiers do not alter this level of optical performance.

In order to predict the optical performance of the entire Nike system, the expected wavefront distortion due to the optics not yet in place was included in the PSF calculations. (There are 11 optical surfaces required to deliver the beams from the present system to target whereas 55 surfaces are included in the system as it is so we expect the model to be an accurate predictor of performance.) The result was a predicted PSF of 10 XDL. This is only slightly larger than the 9 XDL performance predicted in the initial Nike designs and is acceptable for the planned experiments.

As mentioned previously, we have a desired target pointing stability of  $\pm 5 \mu\text{Rad}$ . This would correspond to 5% of the focal spot diameter on target. An error budget for individual mirror stability consistent with this is given in Table 19.1. The total pointing stability is calculated by,

$$\Delta\Theta_{\text{Total}} = \sqrt{\sum_k \left( \frac{\Delta\Theta_k}{D_f/D_k} \right)^2}$$

Where  $\Delta\theta$  is the angular pointing stability,  $D_f$  is the final beam footprint (15 cm), and  $D_k$  is the beam footprint at the optic in question. Ignoring

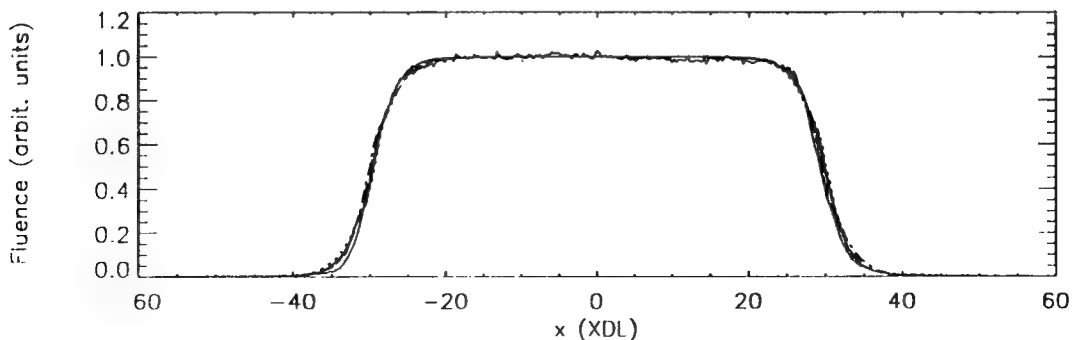


Fig. 19.2 — Focal profile measurement demonstrating 7 XDL optical performance. Solid line is a cross section of the profile generated by the oscillator propagated through the existing optical system (see text). Dashed lines are calculated profiles for an ideal top hat convolved with a 7 XDL point spread function.

Table 19.1

Location	Stability ( $\mu$ Rad)	Beam Footprint (cm)
Multiplexing Array (3 mirrors for each beam)	2	6.0
Input Array	2	6.0
20 cm Amp Mirror	2	15.7
Intermediate Array	2	8.85
Recollimation Array	2	15.0
Demultiplexing Array	3	15.0
Final Turning Array	3	15.0

the mirror at the rear of the 60 cm amplifier (for reasons discussed below) one can see that an RMS stability of 2 to 3  $\mu$ Rad is required of individual mirrors in Nike. Both short term (1 to 2 minutes) and long term (20 minutes) tests of the floor and various structures in Nike have been performed. This was accomplished by propagating a HeNe laser beam through the propagation bay and reflecting from a mirror on the structure under test. The beam is then focussed onto a CCD camera and a series of centroid measurements of the focal spot recorded. Results of one such test, in this case the tallest structure in the demultiplexing array, is shown in Fig. 19.3. As one can see all of the 100 points fall within a circle of radius 2  $\mu$ Rad. This is within the error budget of 3  $\mu$ Rad RMS for this structure.

The mirror at the rear of the 60 cm amplifier is treated separately for two reasons. First the effect of instability of this mirror is to move all of the beams on the target. This is not a severe problem for the oversized flat targets to be used in Nike experiments. Second, we are developing a 'real-time' alignment system for this mirror. This system will be able to reduce low frequency (1-2 Hz) drifts of the mirror and may be able to reduce vibrations up to 15 Hz. Prototype tests of this system are currently being planned.

The final concern to be addressed in this Section is atmospheric absorption in the propagation bay. It is well known that ozone, hydrogen sulfide, and various hydrocarbons absorb

strongly at 248 nm. For this reason we have included HEPA and carbon filtering in the air handling system in the Nike propagation bay. An error budget of 10% atmospheric absorption between the 60 cm amplifier and the target have been included in the Nike design. Initial measurements of absorption at 248 nm were made in the propagation bay before any filtering was in place. These measurements indicate that between 10 and 17% of the energy should be absorbed for the Nike beam paths, which range from 100 to 150 meters. The experimental arrangement used for these tests tended to overestimate the actual absorption and improved measurements in filtered air are planned. We expect that these two improvements will result in lower atmospheric absorption, at or below the error budget level.

One of the remaining issues is nonlinear distortion of the beams by high intensity propagation through air. We are planning to investigate this for conditions similar to those expected on Nike by propagating small high intensity beams produced by the 20 cm amplifier through a high pressure gas cell. This should give us a B-integral ( $n_2 \int I dl$ ) in the range expected for Nike, i.e. 0.2-0.35.

In summary, construction of the optomechanical structures in the Nike propagation bay is nearing completion. Optics to propagate 28 beams through the 20 cm amplifier are in place. Orders for the remaining optics will be placed in Fiscal year 1994. Tests of the propagation

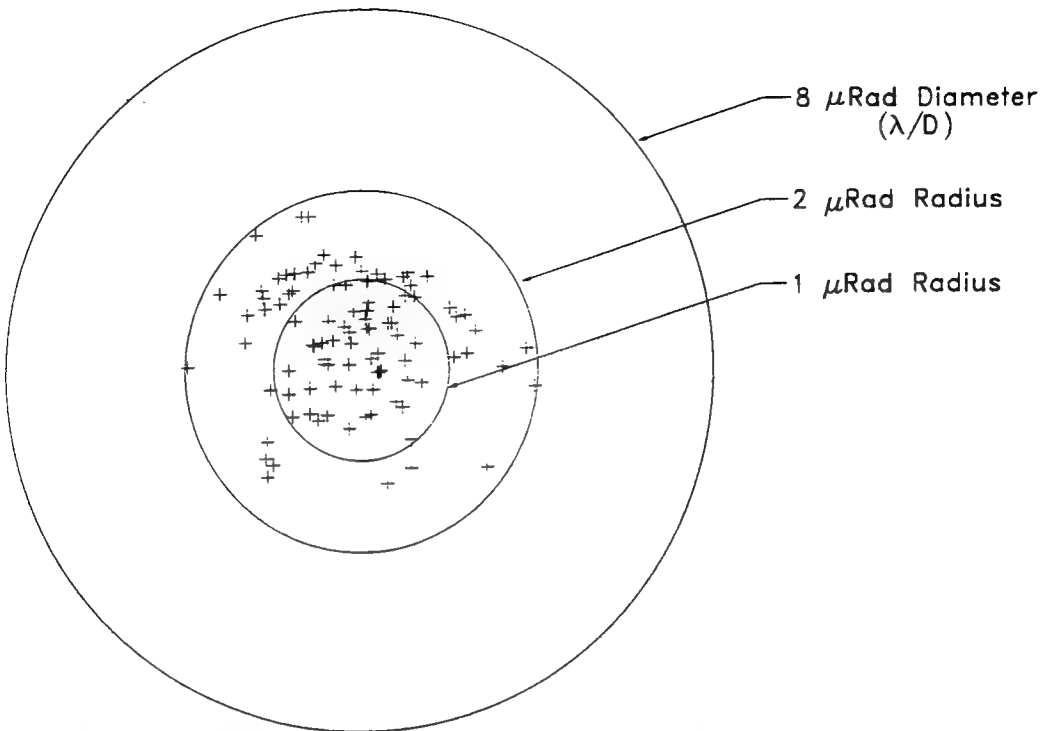


Fig. 19.3 — Measurement of long term pointing stability of one of the demultiplexing structures. Crosses indicate the instantaneous beam centroid. One hundred measurements were made over a 20 minute period. All of the points lie within a circle defined by a 2  $\mu$ Rad radius. The 8  $\mu$ Rad diameter diffraction limited spot size is shown for reference.

bay have demonstrated a point spread function of 7 times diffraction limited through 55 optical components at 248 nm with an expected total system performance of 10 XDL (66 components). Vibration levels are consistent with  $\pm 5 \mu$ Rad point stability on target. Initial tests of atmospheric absorption show no disastrous effects with improved conditions expected in the final system. Experiments to determine the

effects of nonlinear distortion are planned for the near future.

#### ACKNOWLEDGEMENTS

The work presented above was a collaborative effort with significant contributions from R.H. Lehmberg and S.P. Obenschain.

## Section 20

### AUTOMATED BEAM POSITIONING SYSTEM

John Hardgrove  
*Science Applications International Corporation*  
*McLean, VA*

Angularly multiplexed KrF laser systems involve the alignment of large numbers of optical components. The Nike laser system consists of approximately 350 mirrors, 50 lenses and 128 shutters which constitute a complete automated beam positioning system from discharge amplifiers to target.

In the propagation bay, atmospheric and thermal stability is necessary to achieve Nike's high quality beam profiles. Limited personnel entry is necessary and access will be especially restricted if an inert gas atmosphere is required in the propagation bay. Specifications placed on the beam positioning systems in the propagation bay include low heat generation, small overall size and low cost per axis. Commercial products could not meet these specifications. For these reasons, NRL has successfully developed a remote beam positioning system capable of controlling all of the optical components and associated shutters in the Nike propagation bay.

The alignment process begins with commercial CCD cameras and image processing software that monitors the beam positions at various points in the system. Individual mirror positions are then adjusted with custom designed linear actuators and the associated driver software and electronic hardware. The system is IBM PC compatible and has demonstrated the ability to simultaneously align an array of 28 mirrors in approximately 10 seconds. This capability will allow remote alignment of the Nike optical system in less than fifteen minutes.

Figure 20.1 shows the positions of the mirror arrays in the Nike propagation bay. The multiplexing and 20 cm input arrays each have 28 mirrors that need to be adjusted in the X and

Y axes. During 1993, a prototype of the alignment system was in use on both the multiplexing and 20 cm input arrays. The alignment system was tested and debugged as mirrors were aligned to set up experiments on the Nike system. Experience gained during this year, using the alignment, system allowed us to enhance the design of the motor driver cards, the linear actuators and the control software, which improved the reliability and performance of the system. This next generation design will be installed on the entire Nike system in 1994.

The Nike beam positioning system (Fig. 20.2) places a motor control box at the base of each array. This control box communicates over a fiber optic communication link to the mirror position control computer, located in the control room. This computer, through a combination of custom and commercial software, can track the position of each of the laser beams. With the current position identified and desired position previously set, the software instructs the appropriate motor driver cards to move the specified linear actuators the correct distance.

The development of the Nike beam positioning system started with the selection of a suitable linear actuator. Several motor types and controllers were evaluated. Stepper motors using a full step mode of operation were determined to best serve our needs.

Commercial linear actuators employing stepper motors cost more than \$1,000 each. An internal study was conducted and a prototype was developed that reduced the cost per actuator to approximately \$350 per unit (in quantities over 100). The Nike linear actuator incorporates a commercial stepper motor into a commercial

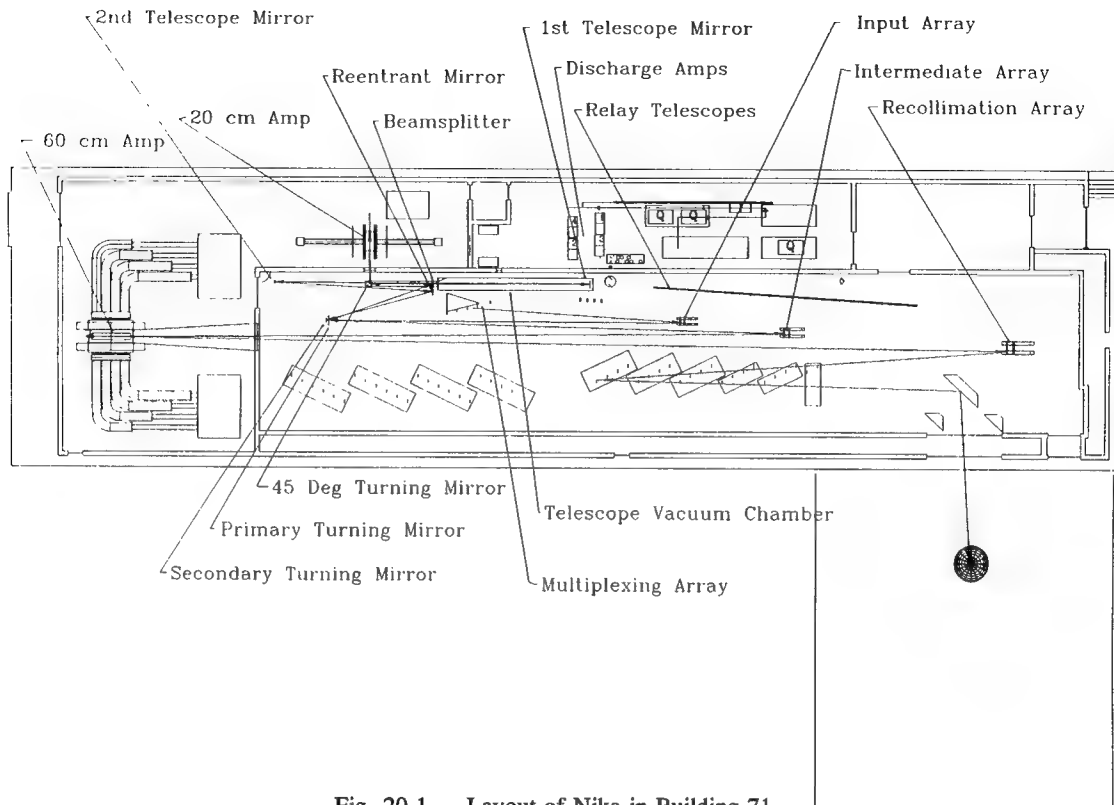


Fig. 20.1 — Layout of Nike in Building 71.

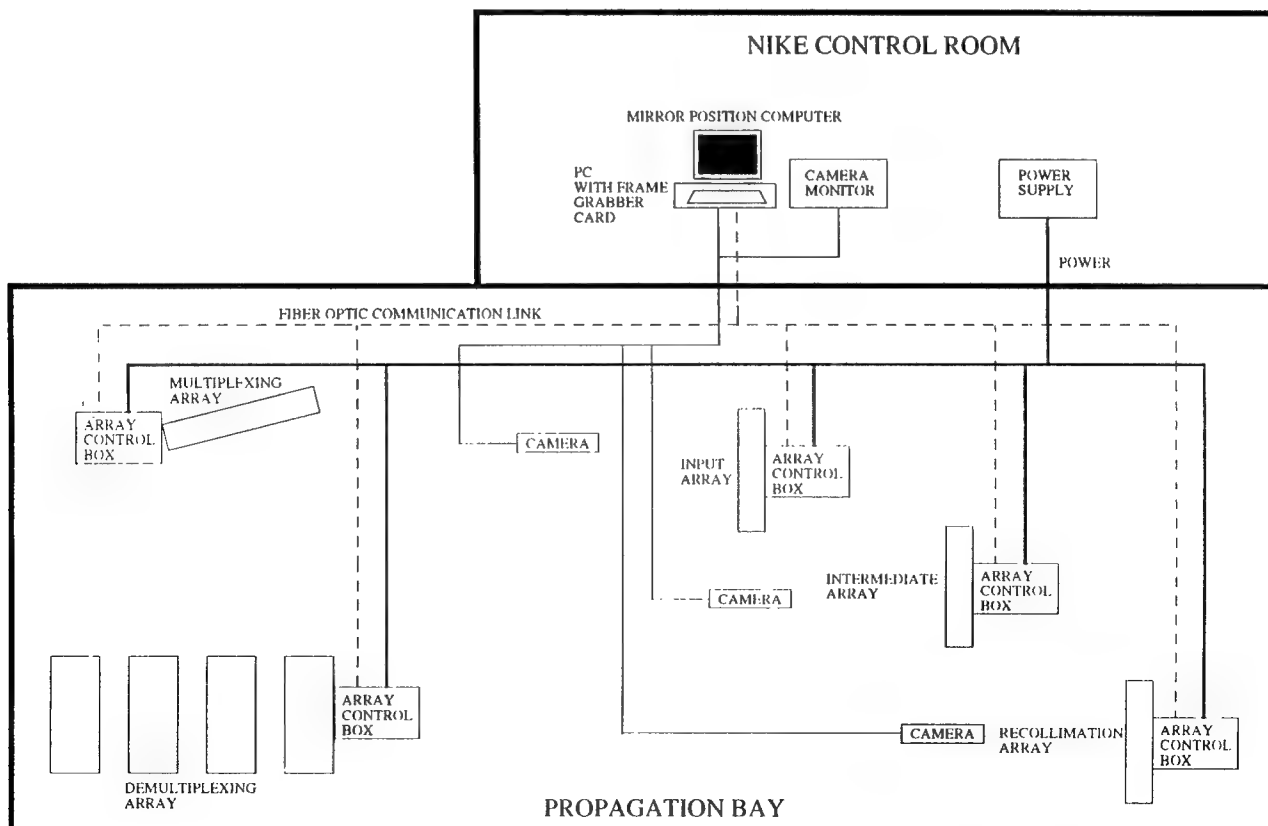


Fig. 20.2 — The Nike mirror alignment system.

gearhead. This motorized gearhead is then attached to a custom fabricated rotational to linear adapter section.

The position control box, mentioned earlier, contains one microprocessor card which provides the communication link between the Nike control room computer and the motor driver cards. Each motor driver card contains eight stepper motor drivers. System requirements on heat generation, size and cost per axis required NRL to develop its own motor driver card. Using a standard commercial card cage, up to 20 of these cards can be placed in a single card cage. This will allow up to 160 motors to be driven from a single card cage.

The Nike mirror position software provides a user-friendly interface through a series of

pop-up menus that helps visualize the current status of each mirror in the selected array. The user, after selecting an array to adjust, will see a graphical representation of the array's mirrors on the PC screen (Fig. 20.3).

Automated movement is achieved by using a commercial imaging card and CCD cameras that image the arrays. The user after selecting the KrF image command will capture the next KrF pulsed laser image. The commercial software then identifies each beam, calculates the centroid and updates the beam position file. The Nike position control software compares the current X and Y positions of the beams to the desired position to calculate the amount of linear adjustment required to move the beams to their proper position. The linear distance is then

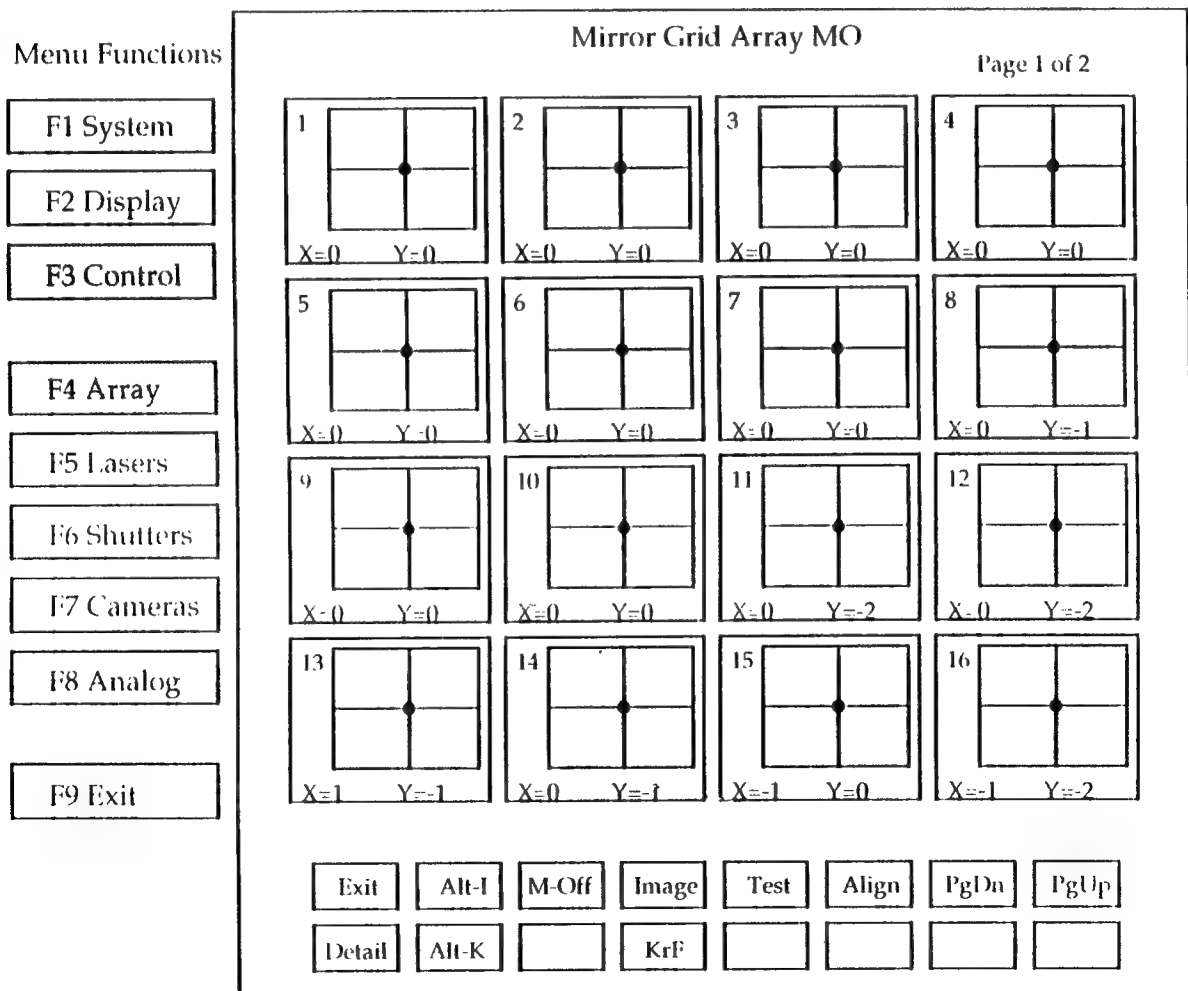


Fig. 20.3 — The Nike alignment software main menu.

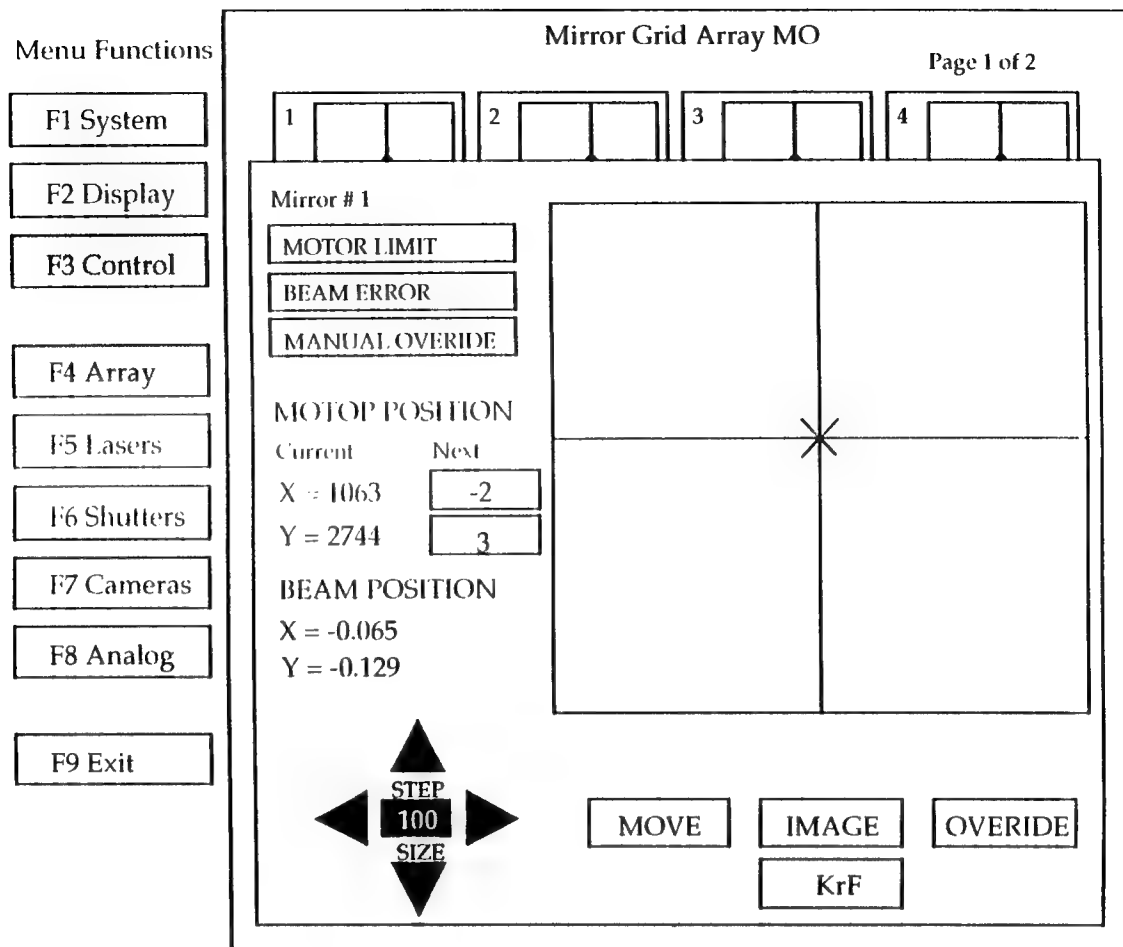


Fig. 20.4 — The Nike alignment software individual mirror menu.

converted into the correct number of motor steps. The user instructs the software to implement this position change by selecting the **Align** command. The Nike position control software transmits a string of commands to the local array processor located at the array. These commands instruct the appropriate counters and latches on the motor driver cards to move the stepper motors the required amount, thus re-aligning all the mirrors in the selected array.

Individual mirrors are moved manually by selecting the desired mirror with either the key-

board or the mouse. A new screen appears (Fig. 20.4) which displays additional information about that individual mirrors status. The user at this time can select the direction and amount that mirror needs to be moved.

After working with the automated beam positioning system for over a year we feel that we have developed a viable and cost effective method of controlling large numbers of optical components from a remote source.

## Section 21

### NIKE TARGET FACILITY

J. A. Stamper  
*Laser Plasma Branch*  
*Plasma Physics Division*  
*Naval Research Laboratory*

The Nike Target Facility has been designed to study the critical physics issues of direct-drive ICF using an ISI-smoothed laser beam. The Rayleigh-Taylor (RT) instability in the dense accelerated target material is of particular interest. The target facility thus includes the target chamber, lenses for focusing the main (target ablative accelerating) laser beams and backlighter (for X-ray sources) laser beams, and diagnostics for these beams. It also includes a variety of target interaction diagnostics, a shielded room for electrical signals, a room for data analysis, and various spaces for diagnostic development and storage.

The design of the target facility structures has been a joint effort by the LANL and NRL Nike teams. NRL was responsible for the conceptual design of the target chamber/snouts, the lens arrays and the beam and target interaction diagnostic concepts. The LANL design group has designed the chamber/snout, lens arrays and

turning arrays. They have also solved the difficult three-dimensional problem of finding ray paths for all 56 beams so that they end up at the right place at the right time.

The location of the target facility is illustrated in Fig. 21.1. The target facility is located at the northwest end of the propagation bay. As more of the laser is completed, more emphasis will shift to this "North West Territory". The target facility is housed in a 58(N-S) foot by 56(E-W) foot space. This space is separated from the rest of the parent building (# 71) by its own inner walls and ceiling and will have its own HVAC systems. It is connected to but sealed from the Nike propagation bay through an interface region, to be described later.

The connection between the laser and target facility is illustrated in the scaled drawing of Fig. 21.2. This shows how the 56 Nike laser beams are directed into the target chamber. The main laser beams, used for ablative acceleration

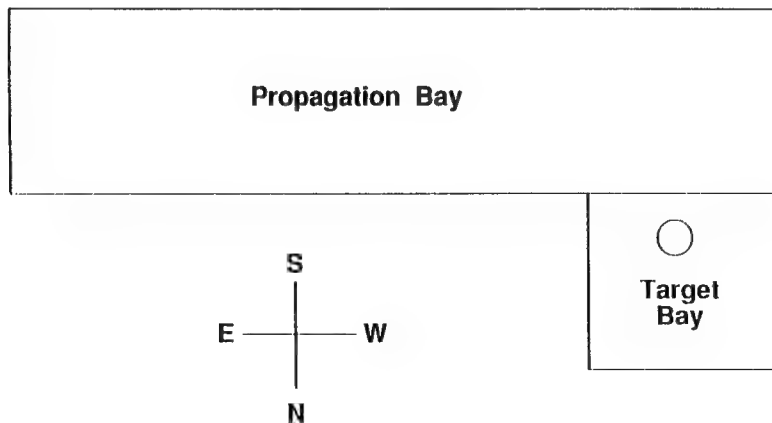


Fig. 21.1 — The NIKE target bay is located at the northwest end of the Nike laser propagation bay.

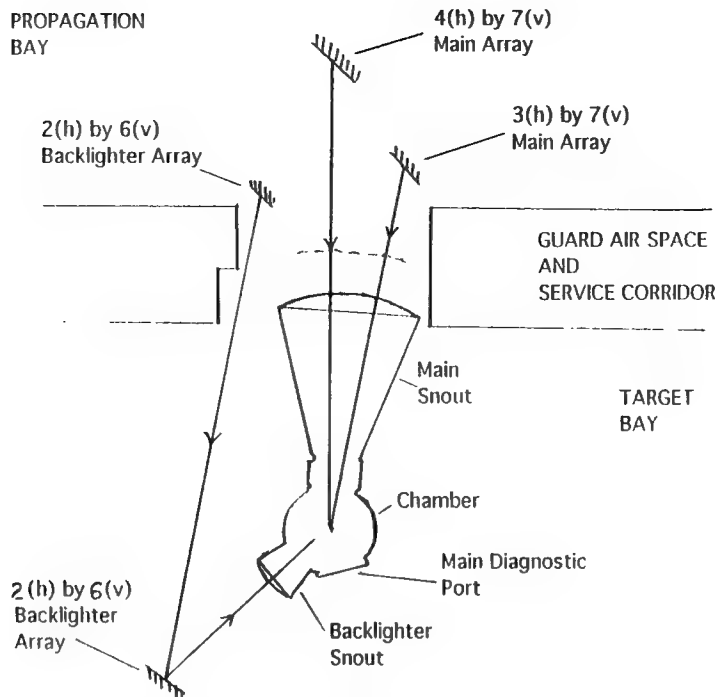


Fig. 21.2 — Arrays of turning mirrors direct the 44 main beams and 12 backlighter beams into the the target chamber.

of the target, use the two main turning arrays. One of these arrays has 4 columns (horizontally spaced) of mirrors, with each column having up to 7 mirrors (vertically spaced), and is called the 4-column turning array. Similarly, there is a 3-column main turning array. Taken together, the two main turning arrays direct a 7 by 7 square array of square beams toward the chamber. These can accommodate up to 48 main laser beams since the center position is reserved for diagnostics. The initial studies will use 44 main beams and 12 backlighter beams, which are used to produce X-ray sources for diagnostics. The 12 backlighter beams are directed from the propagation bay to the target bay by the propagation bay backlighter array. The backlighter beams are then directed toward the chamber by the target bay backlighter array.

The main laser beams pass through the main lens array (6 m from the target), through windows on the main snout, and into the snout and the LMI (laser-matter-interaction) chamber. The backlighter beams pass through the backlighter lens array (3 m from the target), through windows on the backlighter snout, and into the LMI chamber. The square cross sections of all Nike beams are retained from the 60 cm ampli-

fier up to the lens arrays at the target chamber. However, at the focus of each lens, the defining circular aperture (which is located at the output of the oscillator) has been imaged onto the target and a beam of circular cross section is obtained. The lenses have Fourier-transformed the incident transverse angular spectrum to recover (at focus) the circular transverse spatial variation. Before discussing the main lens array and its effect on the composite focus, a brief description is given of the target facility layout and interface region.

The target facility layout is shown in Fig. 21.3. The target chamber/snouts is located at the south end of the space. The axis from chamber center through the main snout is tilted 3.5 degrees to the west and is horizontal at a height of 8.2 feet above the finished floor. The surrounding target bay will accommodate a variety of structures including the backlighter turning array and support structures for working around the chamber. It will be serviced by an overhead bridge crane. A shielded room, located to the east, will be used for controlling the laser-target interaction shots and for electronic equipment to receive and analyze the fast electrical signals. Facilities for analyzing and storing laser-target

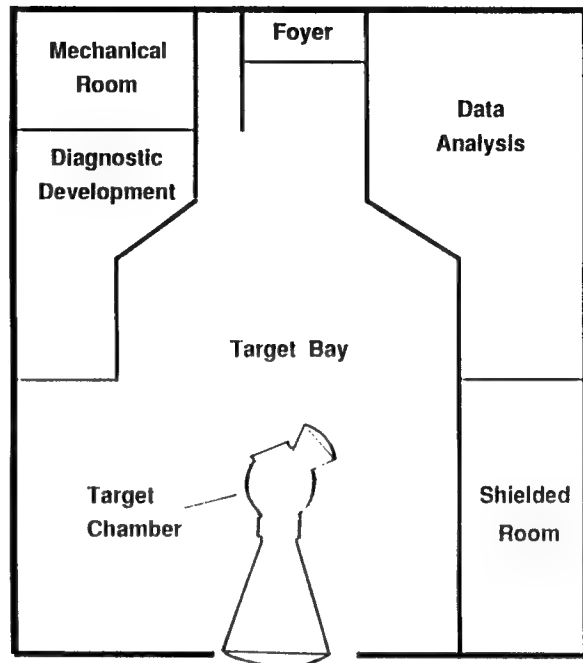


Fig. 21.3 — Layout of the target facility.

interaction data, including computers, are located in the data analysis area north of the shielded room. A diagnostic development area on the west side will be used for developing new diagnostics. A probing laser beam will diagnose the lower density regions, using interferometry, shadowgraphy, and Faraday rotation. The large mechanical vacuum pump for evacuating the chamber/snouts is located in the mechanical

room. The areas on both sides of the north end of the target bay have a second level which will be used for storage. The second level of the mechanical room is used for HVAC equipment.

The interface region between the propagation bay and target bay is shown in Fig. 21.4. The 48-beam main lens array is the dominant structure in this space. The interface wall must seal around the main snout since the windows

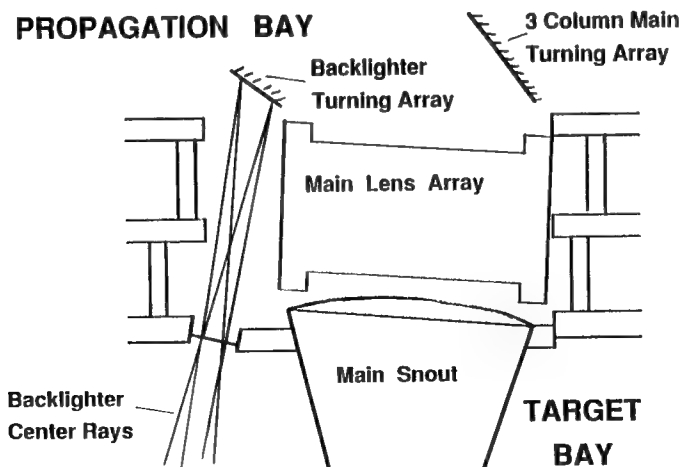


Fig. 21.4 — Interface region between the laser propagation bay and target bay. The seal includes a wall enclosing the main snout and a panel of windows for the backlighter beams.

are only 1 meter from the lenses. In addition, windows must be provided for the 12 back-lighter laser beams as they come into the target bay. These windows are located in a window panel east of the main snout. The main lens array support structure is about 14 feet tall by 12 feet wide.

The 48 lenses of the main lens array are arranged as a 7 by 7 square array with the center position open (used for diagnostics). The 6 meter focal length chosen for lenses in the array represents a compromise between the needs for high laser intensity (for large acceleration), a large focal diameter (to reduce edge effects) and large focal depth (for uniform acceleration). For shorter focal lengths, the individual beam intensities are higher but the beam-to-beam convergence angles are greater, thus reducing the composite focal depth. For studies of the Rayleigh-Taylor instability, one would like nearly-uniform acceleration over a distance of one focal radius.

A 36-cm center-to-center (horizontally or vertically) lens spacing was chosen for the array in order to allow a minimum space between windows (5 m from focus) on the snout. The composite focal waist with this large (F/2.6) focusing array was estimated by assuming a top-hat profile for each of the 48 beams and repre-

senting the beams as circular cylinders whose axes intersect at the prescribed focal length. The individual beam focal variations could be ignored because of the large focal depth (F/32) of the individual beams. The individual beam profiles are rounded - as discussed elsewhere in this report. Nevertheless, the top-hat model reasonably describes the overall effect of the 48-lens array on the focal depth of the composite focus. The composite intensity at a particular axial position in the focal region was obtained for each transverse position, by adding the intensities for the elliptical beam projections onto a plane normal to the array axis at that axial position.

The composite focal spot of 48 top-hat beams is shown in Fig. 21.5 at half an individual beam radius from focus. This axial position corresponds to the required total focal depth of one focal radius. One can see the deviations from a flat beam profile at the edges, where discrete top-hat profiles are encountered. The shaded region in the sketch at the upper left of Fig. 21.6 illustrates where uniform acceleration is needed. The plot shows how the laser energy within the flat part of the composite profile varies with lens focal length. The calculation indicates that, for the 6 m focal length lenses, about 80 percent of the energy is within the

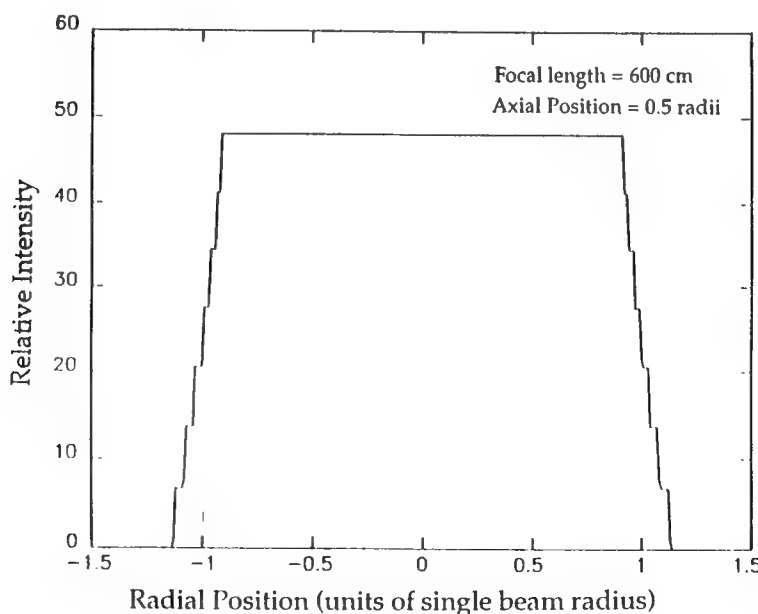
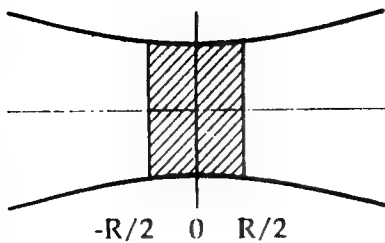


Fig. 21.5 — Calculated composite focal distribution for 48 top-hat beams.



- Need uniform acceleration for a distance of one target radius

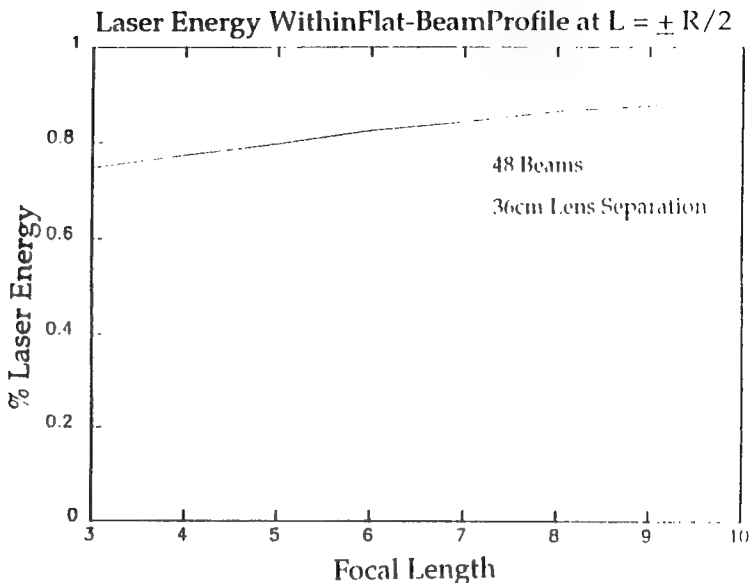


Fig. 21.6 — Upper left : Region (shaded) within the composite focus where uniform acceleration is needed. Lower right : Variation with lens focal length of the fraction of laser energy within the flat part of the composite focus.

flatter, central part of the composite focus - over the required acceleration distance of one focal radius.

The layout of the LMI chamber, main snout, backlighter snout, side-on and large diagnostic ports are shown in Fig. 21.7. The 44 main laser beams (entering through the main snout, at the right) ablatively accelerate the target. The 12 backlighter beams (entering through the backlighter snout, at the upper left) provide X-ray sources for face-on and side-on Rayleigh-Taylor diagnostics. The large diagnostic port (at the lower left) permits a choice of angles for the face-on RT diagnostics. The collar section between the chamber and main snout contains the vacuum pumping ports (chamber side) and the main gate valve (snout side).

In addition to the target interaction diagnostics (carried out in the LMI chamber), a number of diagnostics are planned to characterize the laser beams that enter the chamber. As illustrated in Fig. 21.8, using the reflections from tilted

beam snout windows seemed a natural way to introduce calorimeters (measuring energy) and photodiodes (measuring temporal pulse shape). However, it is difficult, with the final design of the main turning arrays, to find room to install the calorimeters. Another approach which we are considering (as shown at the bottom) uses partially transmitting demultiplexing mirrors.

The equivalent focal plane diagnostic, illustrated in Fig. 21.9, places even more stringent requirements on the demultiplexing mirrors used. The mirror substrates must be of very high homogeneity, and the added expense limits the number of mirrors which can be used for this diagnostic. However, these mirrors can be switched between different beams, so that the focal-diagnostic beam set can be varied. A transmissive beam attenuator is illustrated in the figure, but a less expensive method is to use a series of reflections off of uncoated silica flats. This is practical because of the large focal length of the main focusing lenses.

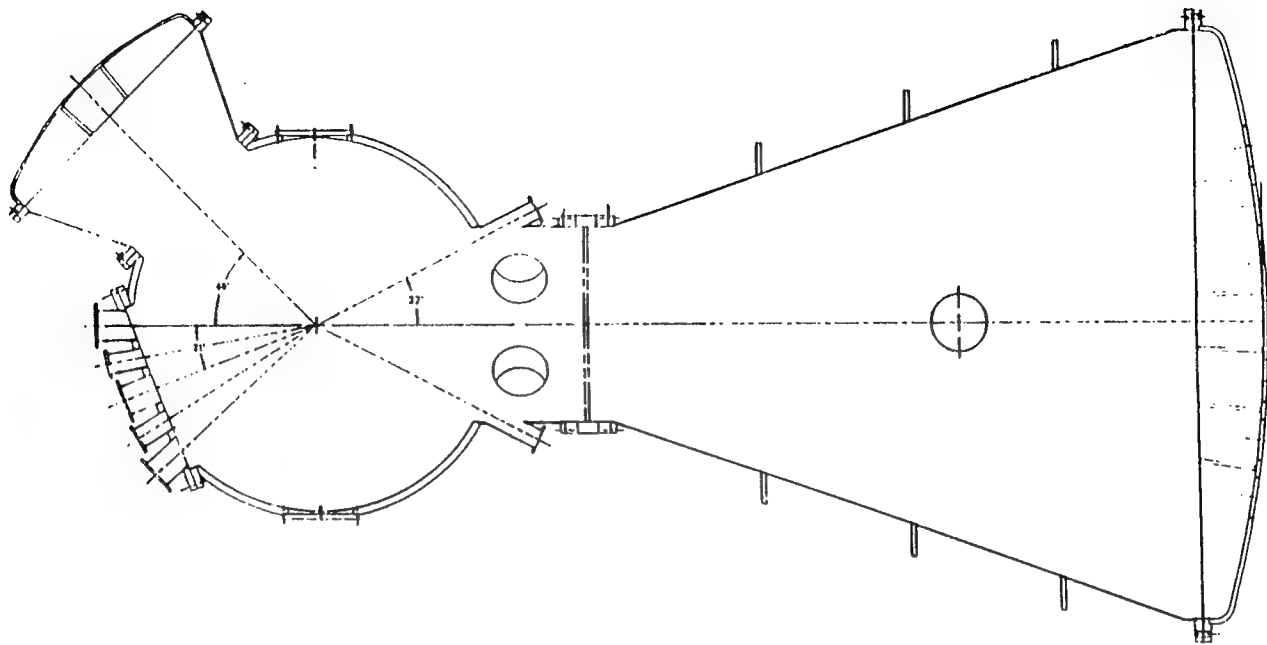
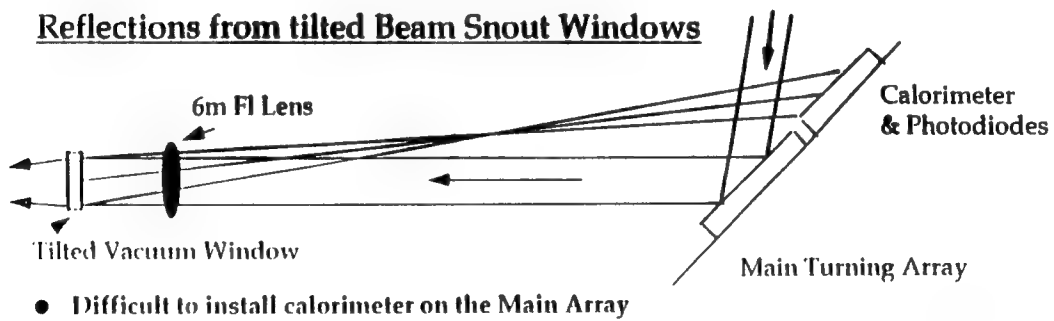


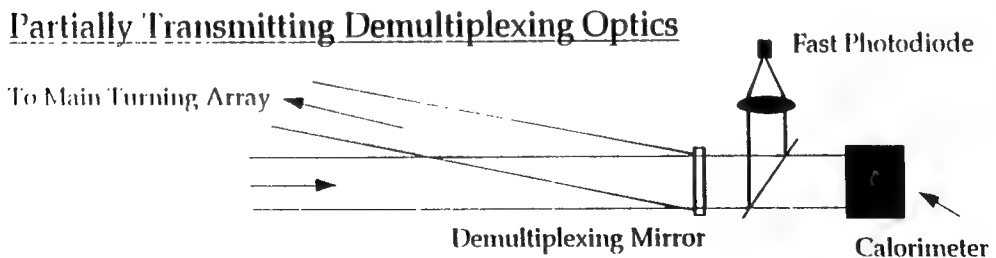
Fig. 21.7 — Layout of the target chamber (2 m diameter sphere at left), main-beam snout (tip at 5 m from chamber center), backscatterer snout (upper left), and main-diagnostic port (lower left).

#### Reflections from tilted Beam Snout Windows



- Difficult to install calorimeter on the Main Array

#### Partially Transmitting Demultiplexing Optics



- Cost of partially transmitting mirrors may be too high

Fig. 21.8 — Laser beam energy and time history diagnostics may include: (upper) reflections from tilted beam snout windows and (lower) partially transmitting demultiplexing windows.

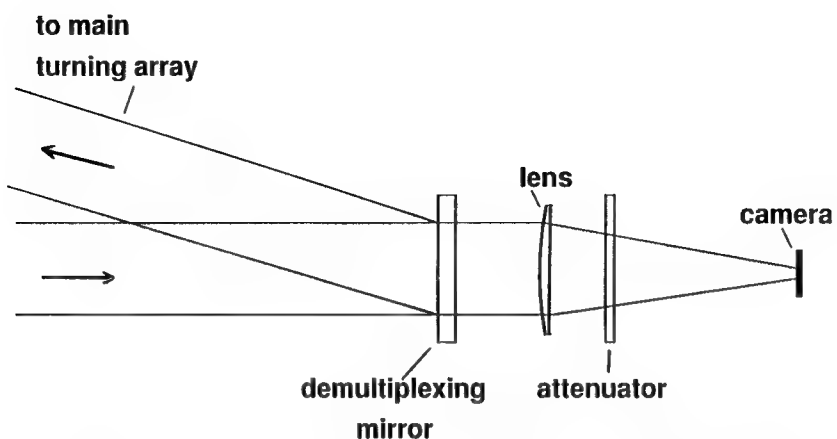


Fig. 21.9 — Equivalent-focal-plane diagnostics will require high-quality substrates for selected demultiplexing mirrors.

## Section 22

### CONTROL SYSTEM

O. Barr  
Pharos Technical Enterprises  
Livermore, CA

#### I. INTRODUCTION

The Nike control system implements the following functions:

- laser amplifier charging and monitoring
- charge-cycle data logging for maintenance support
- initiation of shot sequences
- facility-wide laser and high-voltage interlocking
- support for maintenance functions.

It does not perform tasks related to optical alignment, fast data acquisition, or firing sequencing. However, it interfaces with these functions as follows:

- It provides the master firing pulse to the slow and fast timing system, initiating each shot firing sequence.
- It prepares a charge-cycle summary file for transfer to the data acquisition system for archival with other shot data.
- It is planned to interface with the optical alignment system to assure the alignment, diagnostic, and amplifier configurations are compatible to reduce the risk of damage to diagnostic hardware.

#### II. PROCESSORS AND SYSTEM STRUCTURE

The Nike facility control system utilizes commercial industrial hardware and software extensively, minimizing the project investment in custom circuits and programming. This entails some trade-offs in performance, but with costs and schedule commensurate with the Nike project. The hardware is a distributed system implemented in five low-cost processors optimized for their function. This will expand to seven when the target chamber is added. The system is easily extensible to dozens of specialized processors with minimal difficulty. Fig. 22.1 shows an overview of the Nike control system.

##### A. PROCESSORS

The processors and their functions are as follows:

A) All critical logic executes in a programmable logic controller (PLC) in the Nike control room. The processor selected is a Modicon 984-485 with 8 kilobytes of user memory. The processor and its operating system are reliable and self-checking.

B) Inputs to and outputs from the PLC located in the oscillator room and the amplifier hall are fiber-optically coupled to the PLC via a Modicon S908 master-slave data network. Local interface control within the

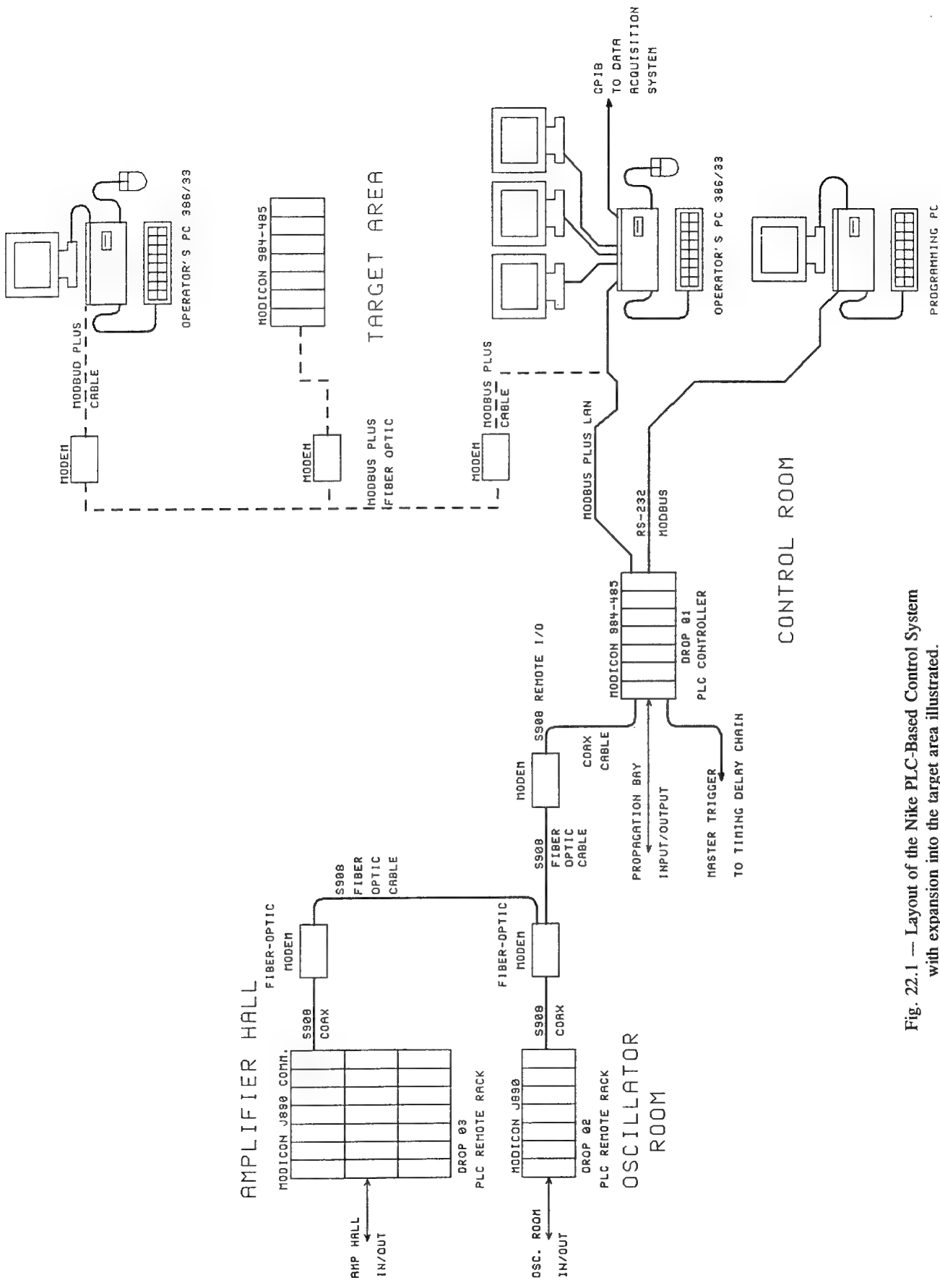


Fig. 22.1 — Layout of the Nike PLC-Based Control System with expansion into the target area illustrated.

isolated rooms is provided by two Modicon J890 remote I/O processors. The basic Modicon S908 is a cabled, highly noise-immune, self-checking, long distance, RF data system. In Nike we convert it to fiber-optics for high-voltage safety reasons using Modicon-certified, 3-M EO-Tech modems.

C) Operator inputs to the PLC and displays are provided by an IBM-compatible clone 386/33-MHz PC with three VGA displays and mouse and keyboard input. The PC and PLC swap data blocks via a dedicated peer-to-peer high-speed LAN implemented with a protocol called Modbus-Plus and a Modicon SA-85 interface card in the PC. In the Nike system all data swaps are initiated by the PC software, although the system is not limited to this mode. Modbus-Plus is very Ether-Net like. The operator's PC also has two-way communication with the data acquisition system via a GPIB link and with a printer via its Centronics printer port.

D) A second IBM-compatible PC is used for system debugging and PLC programming. It communicates with the PLC via a RS-232 link using a PLC-dictated protocol called Modbus.

Expansion into the target area can be implemented by extension of either the S908 data channel or the Modbus Plus peer-to-peer LAN. We have chosen to use the latter, as illustrated. This choice provides more flexibility in the system and avoids becoming bottle-necked by the memory limitations of the 984-485 PLC.

## B. PLC SELECTION BASIS

The PLC-based system was selected after reviewing the PLC-based personnel-safety system at the CEBAF accelerator facility in Hampton, Virginia. CEBAF's installation is implemented with fully redundant processors and communications channels, a feature not carried over to Nike. The advantages of the PLC-based system include the following:

- Processor operating system in ROM, un-touchable by user program
- User program in non-volatile RAM, safe through transients and shutdowns
- Hardware and software self-check every few tens of milliseconds
- Defined-state shutdown
- Fully IEEE- and UL-compliant interfaces for insulation and transient withstand
- Full ground isolation via relays or optical couplers included
- High level of noise immunity
- Flexible system structure with no practical expansion limits
- Fully differential, optical isolated analog input/output
- Ease of installation and wiring
- Very simple or no interface circuits required for control interfaces to Nike equipment
- Minimization of total system installed cost including hardware, software, special interfaces, and programming

The disadvantages of the PLC approach include the following:

- Very limited program memory per processor (less than 7 kilobytes)
- No fast response (35 milliseconds typical, 300 milliseconds worst case)
- Extremely limited calculational capability
- A unique programming language (Ladder Logic)
- Limited communications capabilities

PLCs were developed to replace hardware relay logic in the operation of cement plants. Their application rapidly spread to chemical plants, which is apparent in Modicon's specification of the S908 communications link as "limited" to only 5,000 feet between the PLC and its most distant I/O point (15,000 feet optional). In the past several years their usage has spread rapidly through the industrial process control world.

### III. SOFTWARE

The software consists of the following three components.

#### A. PLC LOGIC

The executing PLC logic is in an internal language, Ladder Logic. It was developed by Modicon to allow programmable controllers to look like hardware relay logic, which is what they replaced. Ladder Logic is almost universally used in PLC applications although it is unpopular with computer programmers who must deal with PLCs.

#### B. OPERATOR'S INTERFACE PROGRAM

The Nike operator's interface is implemented in U.S. Data's Factory Link running on a 386/33-MHz PC clone with three VGA monitors, mouse, and keyboard.

#### C. PLC PROGRAMMING ENVIRONMENT

Programming and debugging the PLC is normally user transparent. It is done on a second IBM-PC clone connected to the PLC with an RS-232 link. For programming the PLC we selected Taylor Industrial Software's Ladder Logic Development System.

A distinct advantage of this programming environment is that the PLC logic can be programmed on-the-fly. That is, since the PLC executes its logic sequentially and communicates between logic cycles, logic changes become effect within a few tens of milliseconds after being entered in the programmer's interface in

the PC. The PLC does not have to be stopped, reloaded, or rebooted to effect most logic changes. Since the Taylor environment represents the PLC logic in the form the PLC executes, no program compilation or linking steps are required. The PLC supports temporary programmer disabling of selected hardware functions for test purposes.

**NOTE**—The PLC must be stopped in order to change its hardware configuration, such as adding additional I/O modules or racks. It must also be stopped if a saved version of its program is to be down-loaded to it from the PC's hard disk. Facility down-time for configuration changes or program version changes is typically less than two minutes and occur about once or twice per month. All program documentation, archival, verification, and backup functions are performed off-line and/or with interference with PLC logic execution.

The Modicon PLC and Taylor programming environments include hardware and software locks to protect the running program from inadvertent modification. Also included is support for monitoring disabled functions and programmer over-rides of hardware status.

### IV. DATA FLOW

Data flow is illustrated in Fig. 22.2. In general, the operator enters set-points, initiates actions, and views status displays. The operator's PC and the Factory Link data base provide the communication between the operator and the PLC, and archive charge-cycle data. The PLC monitors facility parameters, executes control logic, incorporates down-loaded set-points, acknowledges and reacts to command inputs, and formats status information for the operator.

### V. COMMUNICATION INTERFACES

#### A. PLC I/O

Communication internal to the PLC system is between the processor in the control room and its remote I/O racks in the Oscillator and amplifier rooms. This is implemented in a

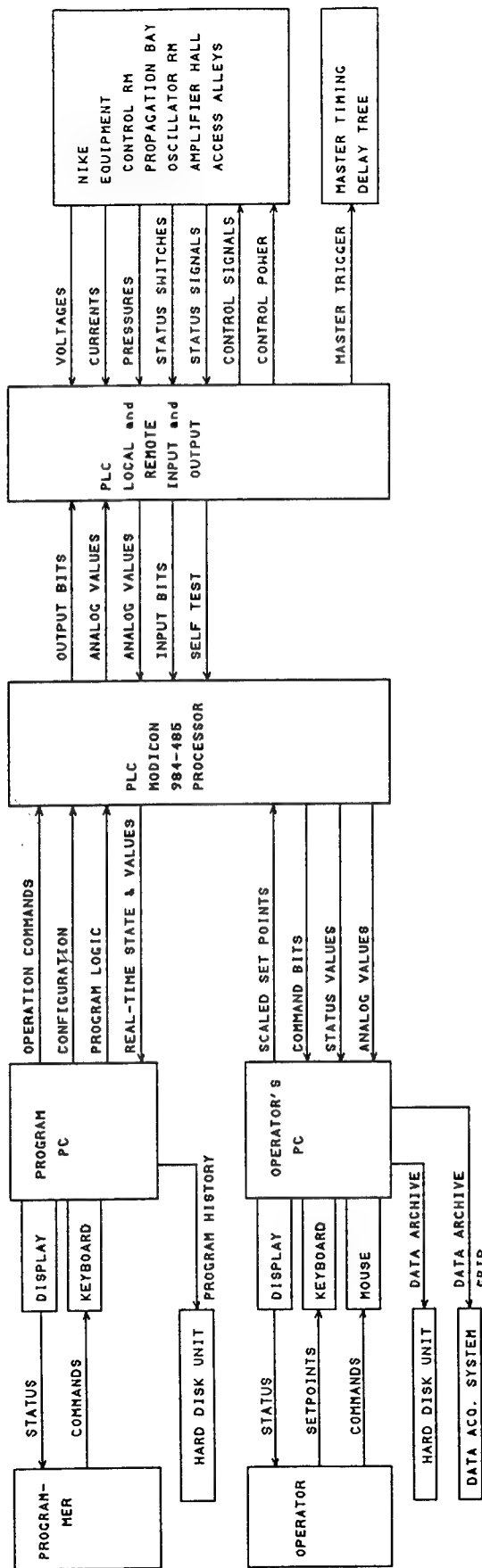


Fig. 22.2 — Conceptual Nike Control System data flow.

Modicon S908 remote I/O data link. The S908 link uses bi-directional communications over 75-ohm coaxial cable between the 984-485 processor (where the logic executes) and J890 remote communications processors (one per remote room). The remote racks of I/O are referred to as "Drops" in PLC-speak, so the PLC has three drops: 01 in the Control Room, 02 in the Oscillator Room, and 03 in the Amplifier Hall. Each drop has one or more card cages (called "racks") and each rack has seven slots for module installation.

At Nike we replace the bi-directional 75-ohm coaxial cable with two uni-directional fiber optic cables. This reduces electromagnetic interference pickup and re-radiation between rooms and provides protection from high voltage ground fault propagation. The S908 to fiber optic transitions are handled with 3-M EO-Tech modems approved by Modicon for such applications.

The existing S908 link could be extended to the target area in a future expansion. This would require all logic to run in the control room PLC, which is reaching its memory limit. Thus, we will not implement the target area expansion this way.

The Modicon 984-series PLCs support fully redundant S908 data channels with either single processors or redundant processors. The Nike installation does not utilize redundant hardware.

## B. OPERATOR-TO-PLC COMMUNICATION

The operator's interface runs as an independent program on a 386/33-MHz IBM PC clone. This program communicates with the PLC via a high speed (about 1.5 megabits per second) peer-to-peer data link called Modbus Plus. Modbus Plus is very Ether-Net like. The PC interface is implemented with a Modicon SA-85 card and US Data's software driver. Although the Modbus Plus link is peer-to-peer, Nike uses it in a master-slave configuration in which the PC is master and the PLC is slave. That is, all communications is initiated by the PC with either a write to the PLC's memory or a request for data. The PLC then responds with either an acknowledgment or with a write to the PC of

the requested data. The operator's PC is address 01 and the control room PLC is address 02.

This data channel will be extended to the target area and expanded to four attached processors, with an additional PLC and PC added in the target area. Both control PCs will be able to obtain data from either PLC for operator interaction and display status updating. The two PLCs will swap blocks of memory to keep their logic synchronized.

Modbus Plus is implemented on shielded, balanced, two-wire cable. The extension of the Modbus Plus link to the target area will use fiber optics. As with the S908 channel, Modicon-approved, 3-M EO-Tech fiber-optic modems will be used.

## C. PLC PROGRAMMING LINK

The programming PC communicates with the PLC over an RS-232 channel using a PLC-dictated protocol called "Modbus." Modbus is a master-slave protocol with the PC as the master and the PLC as the slave. As with Nike's implementation of Modbus Plus, all communication is initiated by the PC software with the PLC acknowledging receipt of data or responding with the requested data packet. This channel is in use only when the PLC program is being modified or the PLC operation is being monitored.

The PLC provides bi-directional Modbus to Modbus Plus translation. Nike does not use this communications path.

## D. DATA ACQUISITION

The operator's PC is able to pass a formatted data file to the data acquisition system for archival with the shot records. This file may assist in troubleshooting system malfunctions, although it is not anticipated to be a high-value file. The file size is about 50 kilobytes. The data transfer path is a GPIB link with the data acquisition work station acting as bus master. A program on the Control System PC formats the file and transmits it on request from the data acquisition system. A copy of the Factory Link archive file is maintained on the PS's hard disk drive.

# **Planned Laser-Target Experiments**

**155      Planned Target Experiments and Diagnostics**

*S. P. Obenschain*

**165      Nike Target Modeling**

*John H. Gardner*

**177      Targets for Nike**

*J. D. Sethian*

## Section 23

### PLANNED TARGET EXPERIMENTS AND DIAGNOSTICS

S. P. Obenschain  
*Laser Plasma Branch*  
*Plasma Physics Division*  
*Naval Research Laboratory*

#### INTRODUCTION

The primary goal of the Nike laser-target experiments is demonstration of the highly uniform laser-ablative acceleration required for pellet fusion while maintaining low enough target preheat for high gain. The Nike experiments will utilize laser-accelerated planar targets to simulate the initial stages of a pellet implosion. A good portion of the most challenging technical issues facing direct-drive fusion occurs during these initial stages of the implosion. Acquisition of a detailed understanding of hydrodynamic instabilities and the effects of various control mechanisms on the overall laser-target interaction is likely to be necessary for laser fusion. Planar targets can serve an important role in this effort because of the good diagnostic access. Planar targets also have the advantage that they require relatively modest laser energy to reach fusion-like parameter regimes. These advantages have been recognized for some time and there has been extensive use of planar targets by NRL and other ICF laboratories for studies of laser-ablative acceleration and laser plasma interactions. The Nike baseline experiments will involve accelerating 600  $\mu\text{m}$  diameter, 4 to 8  $\text{mg}/\text{cm}^2$  targets using laser intensities near  $2 \times 10^{14} \text{ W}/\text{cm}^2$ . The intensity and mass per unit area are less than but close to the operating regime envisioned for high-gain targets. Simulations predict that Nike targets will undergo acceleration over sufficiently long distances that Rayleigh-Taylor (RT) instability will grow to large amplitudes unless means are found to inhibit the instability. We

will explore means for controlling the RT instability that is seeded by initial target imperfections and by the imprint of residual laser nonuniformity. We do not expect to encounter serious parametric laser-plasma instabilities with the ISI smoothed Nike beams at the few  $\times 10^{14} \text{ W}/\text{cm}^2$  planned for the acceleration experiments. See Sections 7 and 8. However, the facility will have the capability to conduct laser-plasma experiments at much higher intensity ( $> 10^{15} \text{ W}/\text{cm}^2$ ), where instabilities may occur, by concentrating the laser energy into smaller focal diameters.

#### LASER-TARGET EXPERIMENTS

Figure 23.1 shows the target facility for Nike. Forty-four laser beams will overlap onto targets to obtain the nominal  $2 \times 10^{14} \text{ W}/\text{cm}^2$  for ablative acceleration experiments. We chose a small enough cone angle for the converging beams ( $20^\circ$ ) so that targets can be accelerated over distances of half the focal diameter (300  $\mu\text{m}$  for 600  $\mu\text{m}$  focal diameter) without appreciable loss of illumination uniformity. We will use the remaining 12 beams to generate x-rays for backlighting and sidelighting of the accelerated targets. These diagnostic beams will have pulse lengths and focal profiles that are independently adjustable from that of the target-acceleration beams. The delay between the acceleration beams and diagnostic beams will be variable by about  $\pm 10$  nsec by adjusting the demultiplexing delay paths in the twelve backlighter beams. The backlighter beams will provide about  $5 \times 10^{13} \text{ W}/\text{cm}^2$  in 5 nsec pulses

## NIKE Target Chamber

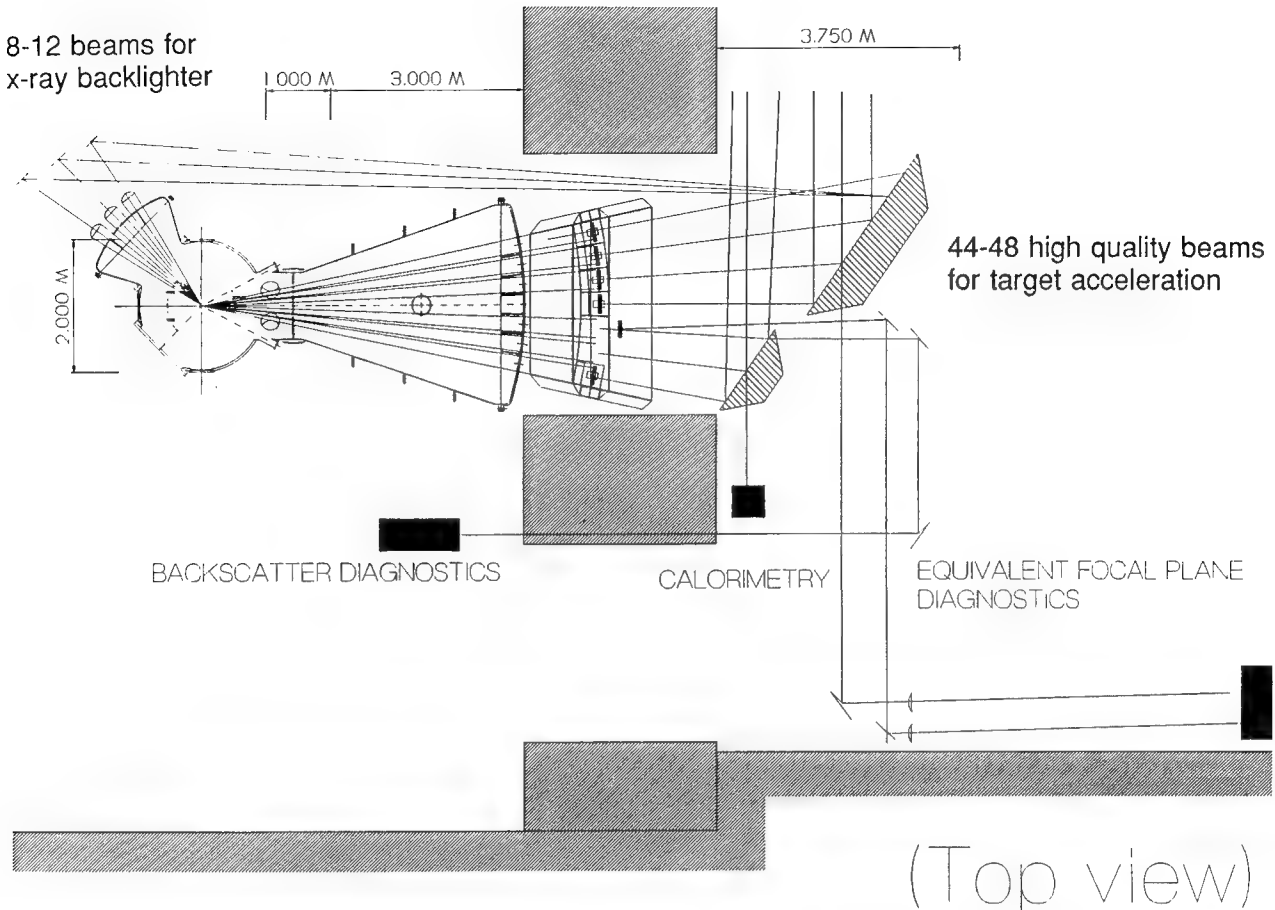


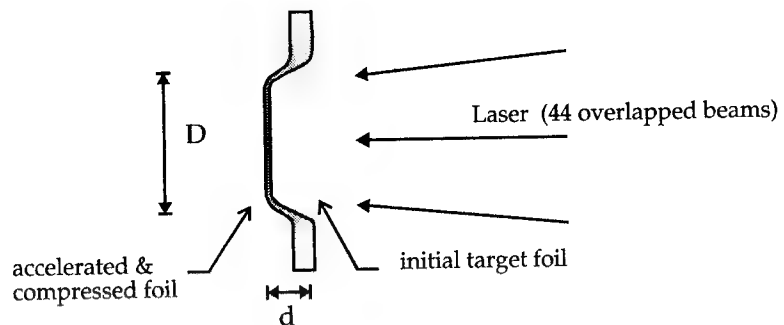
Fig. 23.1 — The overlap of 44 to 48 Nike ISI beams will provide the intensity for target acceleration experiments. Eight to 12 beams will be available for illuminating x-ray sources for diagnostics.

when illuminating extended-source backlighter targets (600  $\mu\text{m}$  diameter). The diagnostic beams will be able to generate much higher intensities if necessary by using short pulses and tighter overlapped foci. Intensities above  $10^{15} \text{ W/cm}^2$  should be easy to attain.

Figure 23.2 shows the arrangement for Nike target acceleration experiments. The overlapped focus of the 44 accelerating beams will illuminate a foil target whose lateral dimensions are larger than the laser focus. These oversize targets will isolate the rear surface from spurious heating from the hot laser-produced plasma on the front surface. Calculations indicate that this isolation can be destroyed if one uses top-hat shaped focal profiles that "cookie-cutter" out the accelerated portion of the target. We plan to use focal profiles that have gentle

enough slopes on the perimeter (50 to 100  $\mu\text{m}$  gradient lengths) so that the foil near the edges of the accelerated target "stretches" but does not break during most of the acceleration. We should be able to accelerate such targets over axial distances of about half the focal diameter (300  $\mu\text{m}$  for 600  $\mu\text{m}$  focal diameters) without severe complication from edge effects.

The parameters and materials of the target foil will vary with the experiment. Thick targets ( $> 10 \text{ mg/cm}^2$ ) that do not accelerate far enough for appreciable Rayleigh-Taylor (RT) growth will be used to measure the ablation pressure uniformity produced by the ISI smoothed beams. Use of thinner targets (3 to 6  $\text{mg/cm}^2$ ) will allow study of the complicating effects of RT instability. The simplest targets will consist of pure plastic (CH) foils. Future targets will



$D > 2d$  to obtain "planar" acceleration

target parameters	laser parameters
3 to 12 mg/cm <sup>2</sup> areal density	$I = 1$ to $3 \times 10^{14}$ W/cm <sup>2</sup>
distance accelerated (d) = 0.1 to 0.3 mm	focal diameter (D) = 0.5 to 0.8 mm
final velocity 100 to 200 km/sec	$E = 2.2$ kJ in 4 nsec

Fig. 23.2—Setup for target acceleration experiments.

include a layer of frozen deuterium on the rear surface of a plastic ablator to simulate more closely the fueled-pellet configuration. We will use various dopants in the targets to modify the x-ray preheat of the ablator. The use of such targets offer one avenue for controlling laser printing and Rayleigh-Taylor growth. Finally, we plan to use various specialized targets (such as double-foils and layered targets) as diagnostic aids.

The baseline experiments call for the aforementioned 600  $\mu$ m focal diameter and  $\sim 2 \times 10^{14}$  W/cm<sup>2</sup> intensities. The facility will have the flexibility to explore other parameter regimes. We should be able to double the focal spot size while maintaining good focal quality. This will allow studies of larger diameter targets (1.2 mm) accelerated over longer distances ( $>0.3$  mm), at the expense that the targets will be thinner and the laser intensity lower ( $\sim 5 \times 10^{13}$  W/cm<sup>2</sup>). Use of shorter than 4 nsec laser pulses (2 to 3 nsec) may allow target acceleration studies at intensities well above  $2 \times 10^{14}$  w/cm<sup>2</sup>. However, use of such short pulses in the NIKE optical train poses some challenges in controlling pulse shape and amplified spontaneous emission. See Sections 10 and 16.

The experimental program calls for accelerating targets with less than 2% ablation pres-

sure nonuniformity and with acceptable levels of Rayleigh-Taylor growth and payload preheat. In the following sections we will discuss the diagnostics techniques for studying target acceleration and verifying achievement of this goal.

## TARGET DIAGNOSTICS—UNIFORM ABLATION PRESSURE

Prior to beginning any extensive experimental campaign to measure the pressure uniformity, the intensity uniformity of the overlapped beams will be characterized and the 2% or better time-averaged intensity uniformity achieved. The intensity uniformity of the overlapped beams will be measured for dedicated laser shots within the target chamber to establish that the laser has the desired capability. (See Section 21.) In addition the focal distributions of sample individual beams will be monitored during the target shots.

The ablation pressure uniformity obtained with the NIKE laser beams will be determined by observing spatial variations in the acceleration of targets. We plan to use the double-foil technique as a primary diagnostic for measuring the velocity uniformity of the accelerated targets. This technique involves placing a second (impact) foil parallel to and a few tens to a few

hundred microns behind the laser accelerated foil. The impact of the laser accelerated foil shock heats the impact foil. Nonuniformities in the impact are monitored by streak-camera measurements of the light emitted as the shock emerges from the rear surface of the impact foil. See Fig. 23.3(a). This technique has been used in experiments at NRL and elsewhere.<sup>23.1, 23.2, 23.3, 23.4</sup> Figure 23.3(b) shows sample measurements conducted at NRL where a planar target ( $0.65 \text{ mg/cm}^2 \text{ CH}$ ) was accelerated to 160 km per second by a 3 nsec  $1.05 \mu\text{m}$  glass laser beam with focal intensities near  $10^{13} \text{ W/cm}^2$ . Here the velocity uniformity was determined at different times during the acceleration by varying the distance between the target and impact foil. Figure 23.4 shows similar use of the diagnostic for conditions closer (thicker targets, higher intensity) to those of the Nike experiments. Here  $4 \text{ mg/cm}^2$  pyrolytic graphite (carbon) targets were ablatively accelerated at intensities near  $10^{14} \text{ W/cm}^2$  using the LLNL Shiva laser facility. These earlier experiments demonstrated the capability of the double-foil

technique to measure velocity (ablation pressure) nonuniformity as small as 3 to 4%. At the time this was adequate resolution to measure the ablation-pressure nonuniformity produced by existing, non-smoothed lasers. No attempt was therefore made to push the resolution limits of the diagnostic in these experiments.

Since the focal nonuniformity with Nike is expected to be small, we will need to obtain better resolution (1 to 2%) than previously demonstrated with the double-foil technique. For target accelerations over 2 to 4 nsec, resolutions in impact times of about 20 to 40 psec are needed for resolving 1% velocity uniformity. This is well within the temporal resolution of optical streak cameras. One-dimensional hydrocode simulations (see Section 24) indicate that 1% pressure nonuniformities can be resolved under Nike target conditions with the double-foil technique. Figure 23.5 shows a simulation result where a  $12 \text{ mg/cm}^2 \text{ CH}$  target is accelerated by a  $2 \times 10^{14} \text{ W/cm}^2$  248 nm laser and collides with a  $1 \text{ mg/cm}^2 \text{ CH}$  target. The first foil is thick to shield the impact

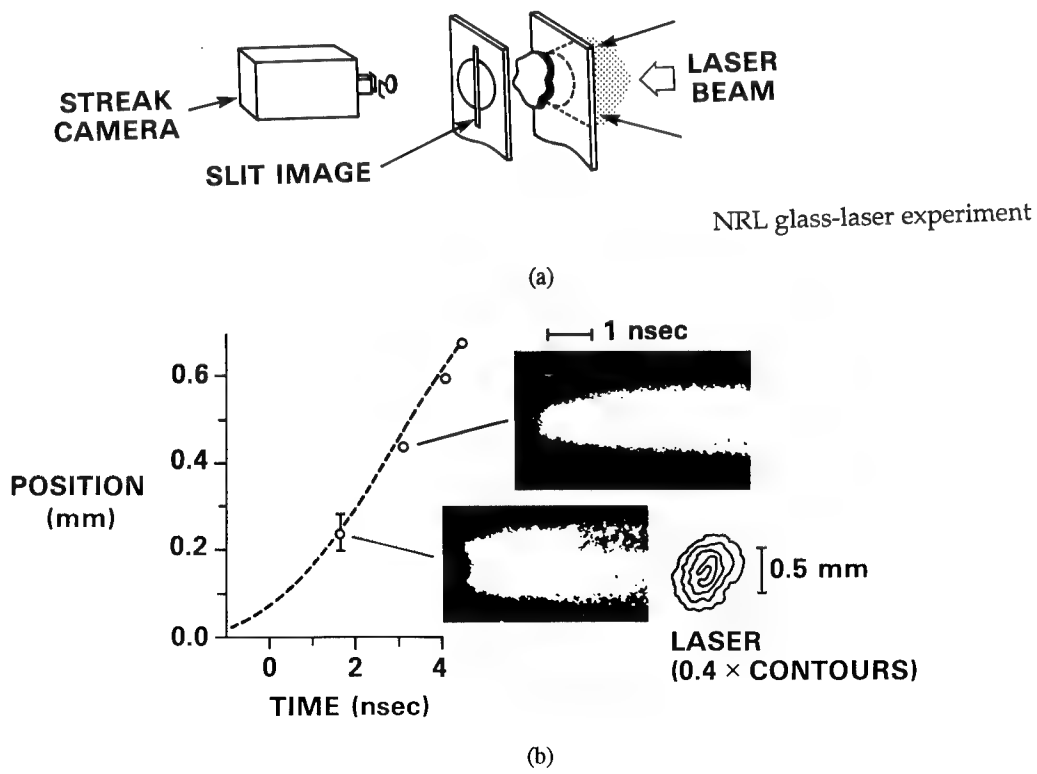


Fig. 23.3 — (a) The double-foil diagnostic technique. (b) Double-foil measurements using the NRL glass laser.

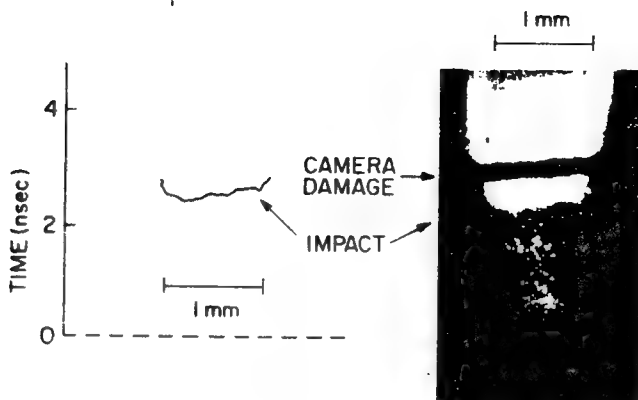


Fig. 23.4 — Double foil measurements from the joint LLNL/NRL experiments using the Shiva laser.

conditions:

**Thick target foil (shields 2nd foil)**

**Thin impact foil (fast shock transit)**

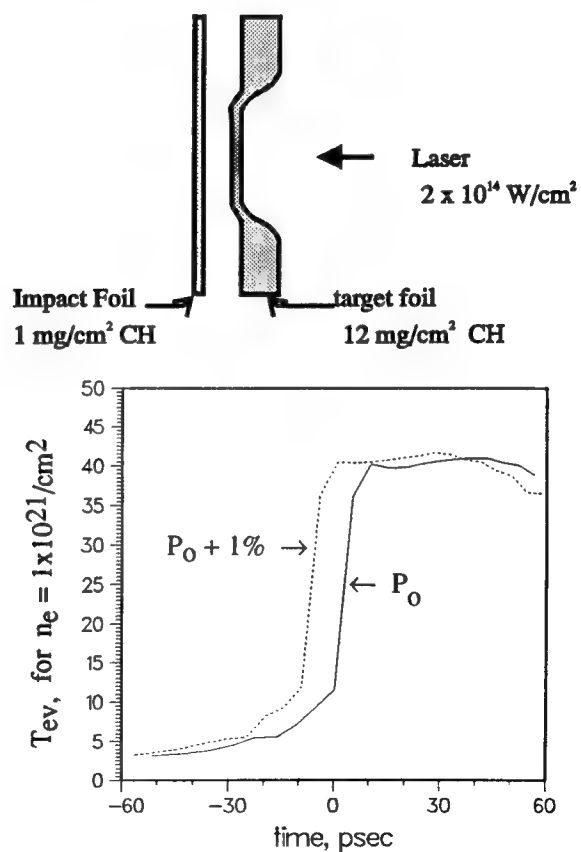


Fig. 23.5 — Simulation of the collision of a Nike target with an impact foil.

foil from x-rays produced by the ablation plasma. The second foil is chosen thin in order to obtain a short shock transit time. The simulation shows the change in shock break out time from the impact foil when the pressure on the first foil is changed by 1%. The shock break out produces a fast enough rise time in impact foil temperature to allow resolution of a 1% ablation-pressure variation. We expect that the double-foil technique will easily provide sufficient spatial resolution to detect first order (tilts) and second order (concavity/convexity) in the accelerated target velocity profile. Two-dimensional simulations are in progress to examine the limits of the spatial resolution of this technique for measuring pressure nonuniformity.

Figure 23.6 illustrates other diagnostics that complement the double-foil technique. Side-on x-radiography provides a time resolved profile of the accelerated target. Figure 23.7 shows a sample result obtained with the NRL glass laser facility where an x-ray flash produced by a short pulse laser on Al captured an accelerated target just before impact on a second foil.<sup>23,5</sup> This diagnostic provides an independent measure of nonuniformity in the target acceleration

although it is not expected to be as sensitive as the double-foil technique. Other diagnostics that will be fielded for the uniform ablation pressure studies include: x-ray imaging of the laser illuminated surface to check laser beam overlap; targets with imbedded high Z layers<sup>23,6</sup> to monitor uniformity of the mass ablation across the target; and imaging the light<sup>23,7</sup> and soft x-ray flux from the rear surface of the accelerated target and impact foil to assure that they are not excessively preheated.

## TARGET DIAGNOSTICS—RAYLEIGH TAYLOR EXPERIMENTS

The Rayleigh Taylor (RT) instability results in a redistribution in mass of the targets whereby the areal mass nonuniformity is enhanced. See Fig. 23.8. Detection of the growth of this areal mass nonuniformity will be the primary diagnostic for the instability. The classical growth rate for the instability is given by  $\gamma_c = \sqrt{(ka)}$  where  $k$  is the wavenumber and  $a$  is the target acceleration. With 200 to 300  $\mu\text{m}$  acceleration distances and 25 to 100  $\mu\text{m}$  instability wavelengths, there would be 5 to 12  $\gamma_c$

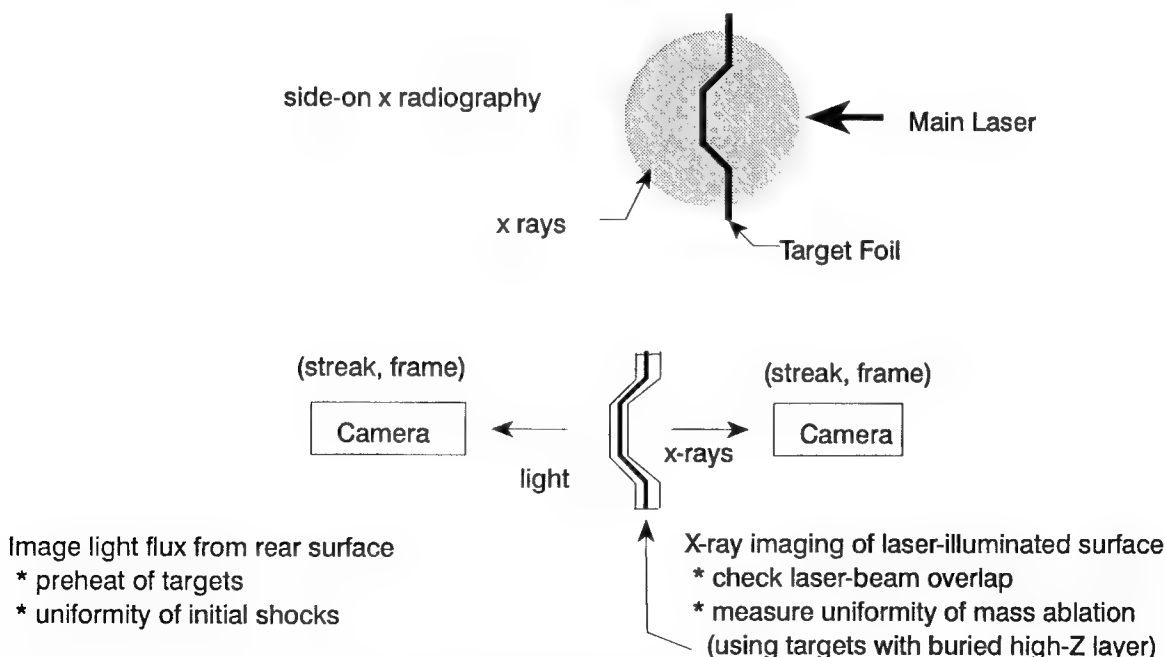


Fig. 23.6 — Complementary diagnostics to the double-foil technique for the uniform ablation pressure experiments including: x-ray sidelighting to determine the position of the accelerated target's mass; temporally and spatially resolved measurements of light and x-ray emission from targets; and use of layered targets.

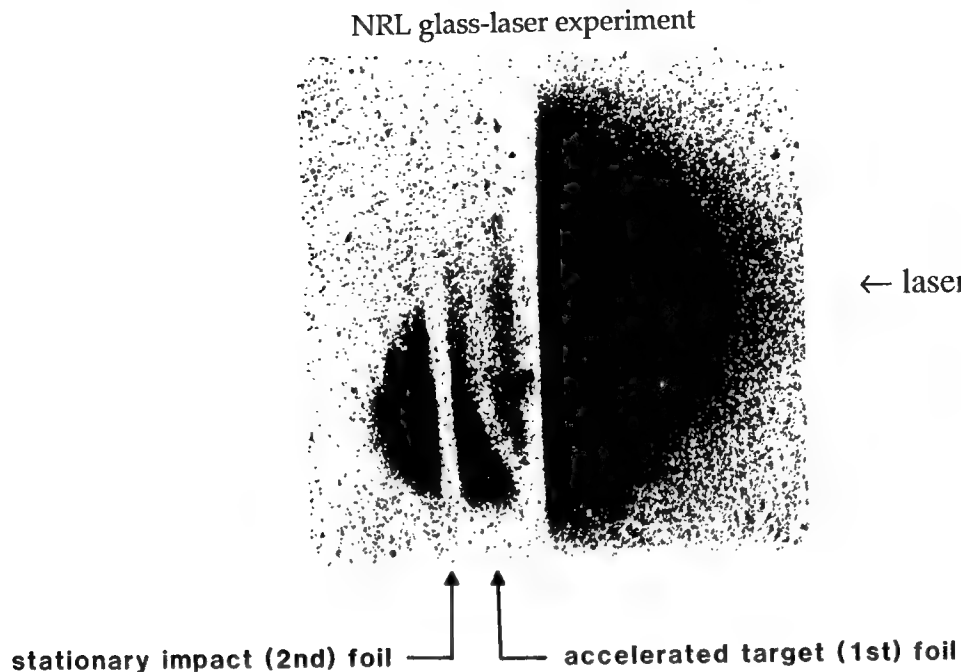


Fig. 23.7 — Flash x-ray sidelighting of a double-foil target just prior to impact.

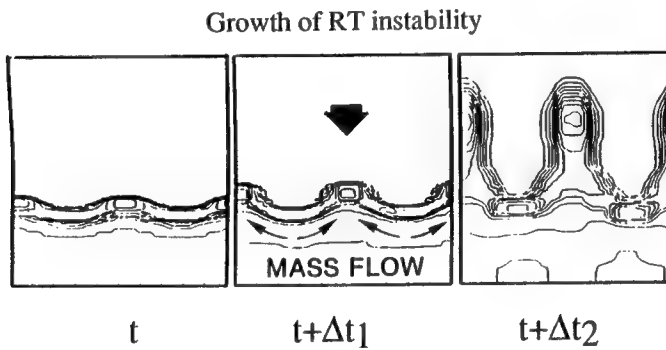


Fig. 23.8 — The Rayleigh-Taylor instability enhances areal mass nonuniformity.

exponentiations with Nike experiments. The instability should thus be easily observed in the Nike experiments even if factors of 2 to 3 reduction the growth rate below  $\gamma_c$  are achieved.

Figure 23.9 shows the diagnostic setup for the Nike Rayleigh-Taylor experiments. The main target is accelerated by 44 overlapped laser beams. For some experiments the target surface will be roughened or grooved to provide a seed for the instability. The auxiliary beams will be used to illuminate a backlighter for radiographing through the target, and a sidelighter for radiographing the target edge-on. This com-

bination of backlighter/sidelighter has been successfully used at NRL and elsewhere in earlier Rayleigh-Taylor experiments.<sup>23.8, 23.9, 23.10, 23.11</sup> The x-ray sidelighting provides the acceleration history of the target while the backlighting measures the growth of areal mass nonuniformity due to instability. X-ray streak or framing cameras provide the required spatial and temporal resolution. Figures 23.10 and 23.11 show representative results from sidelighter and backlighter experiments conducted at NRL using a glass laser and ISI beam smoothing. Figure 23.12 shows the measured growth of the mass nonuniformity deduced from the backlighting data.

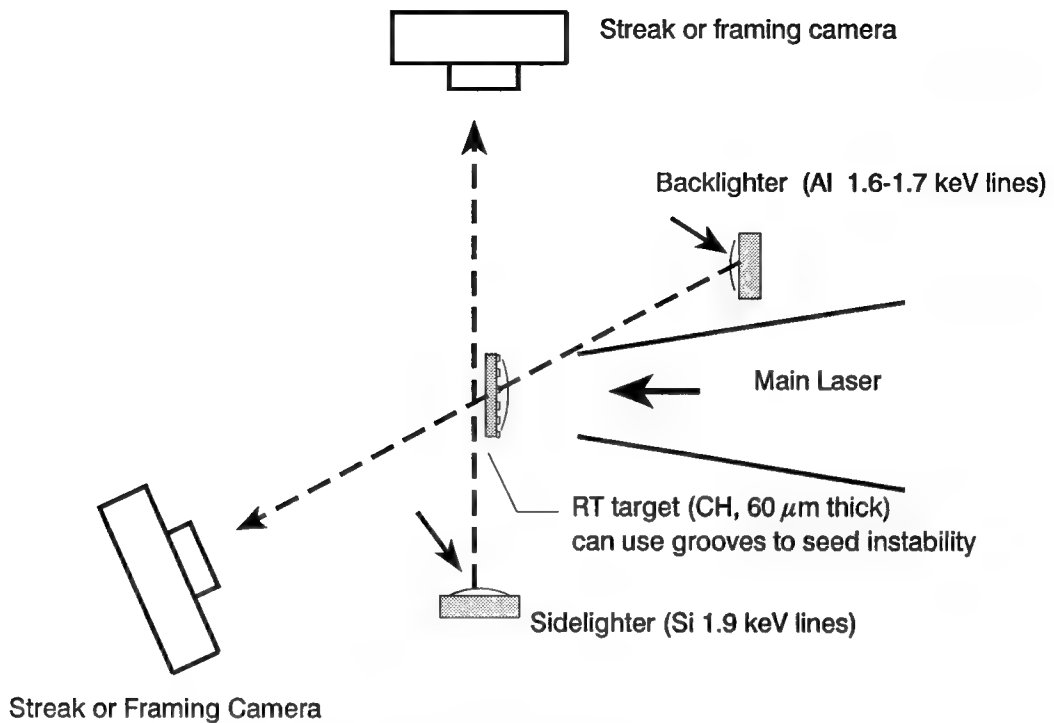


Fig. 23.9 — Arrangement of x-ray sidelighting and backlighting for Rayleigh-Taylor experiments.

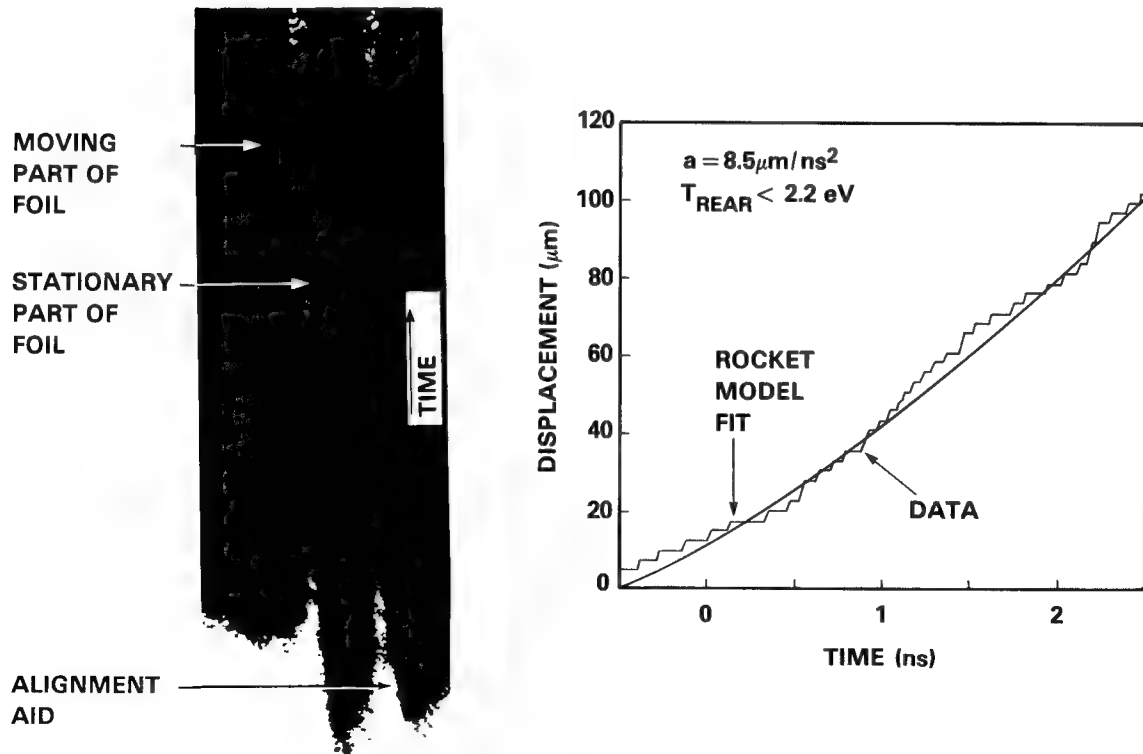


Fig. 23.10 — X-ray sidelighting measurement of target acceleration history from Ref. 23. 8.

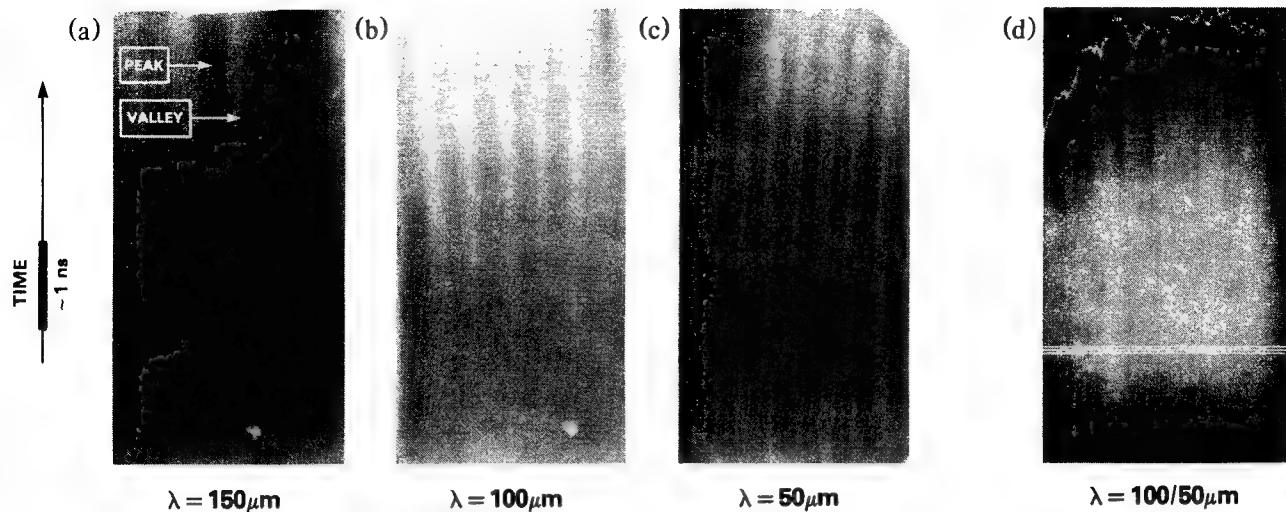


Fig. 23.11 — X-ray backlighting measurements of Rayleigh-Taylor instability growth from reference 23.8.  
Different grooves in the target seeded the instability.

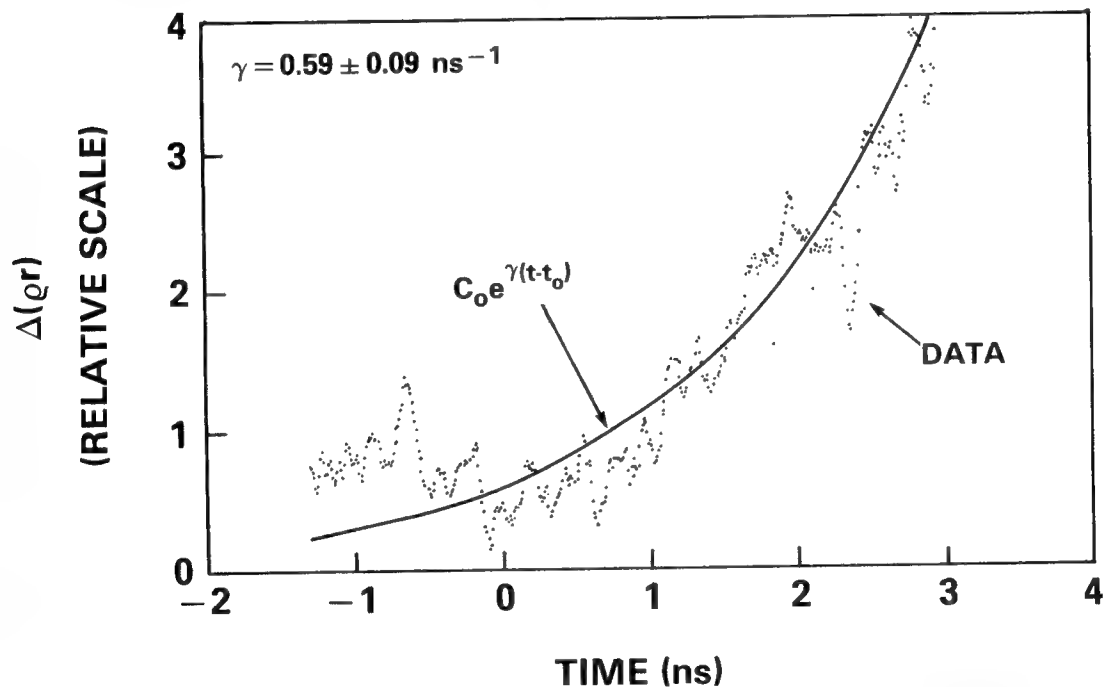


Fig. 23.12 — Exponential growth of seeded Rayleigh-Taylor deduced from backlighting.

The wavelength of the backlighter needs to be chosen to match the thickness and material of the Nike targets. One must obtain enough absorption to be sensitive to areal mass nonuniformity, yet obtain enough flux through the target to be detected. Line emission near 1.6 to 1.7 keV from aluminum targets appears to be a good match for the  $6 \text{ mg/cm}^2$  thick CH Nike targets.<sup>23,12</sup> Figure 23.13 shows simulations of

the growth of the areal mass nonuniformity and corresponding growth of the mass nonuniformity signal detected using an Al backlighter and a Si K edge filter. The simulation indicates that this backlighter will provide good contrast and signal for measurement of Rayleigh-Taylor growth. Numerical results from our hydrocode simulations of these experiments are discussed further in Section 24.

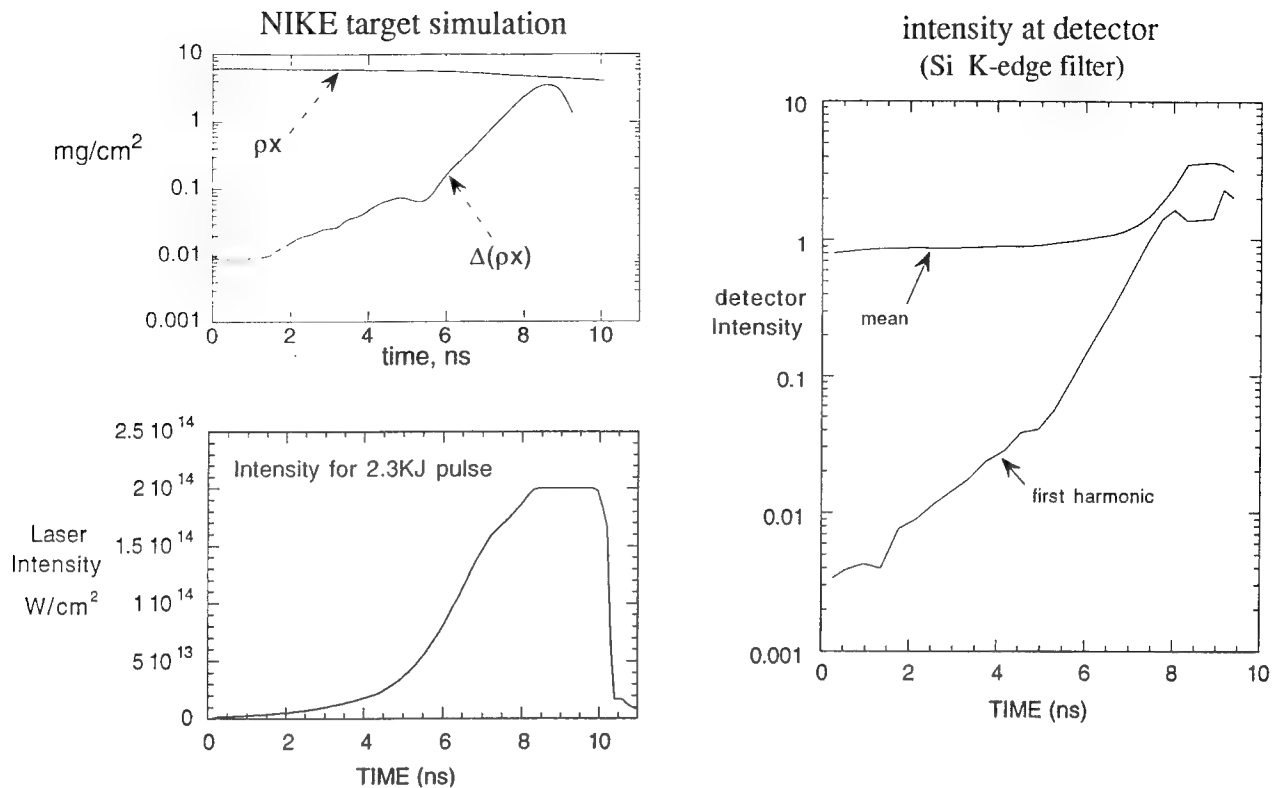


Fig. 23.13 — Simulation of measurement of Rayleigh-Taylor growth with an Al backscatterer.

## REFERENCES

- 23.1 S. P. Obenschain, J. Grun, B. H. Ripin, and E. A. McLean, Phys. Rev. Lett. **55**, 1402 (1981).
- 23.2 J. Grun, S. P. Obenschain, B. H. Ripin, R. R. Whitlock, E. A. McLean, J. Gardner, M. J. Herbst, and J. A. Stamper, Phys. Fluids **26**, 588 (1983).
- 23.3 S. P. Obenschain, R. R. Whitlock, E. A. McLean, B. H. Ripin, R. H. Price, D. W. Phillion, E. M. Cambell, M. D. Rosen, and J. M. Auerbach, Phys. Rev. Lett. **50**, 44 (1983).
- 23.4 R. Fabbro, B. Faral, F. Cottet and J. P. Romain, J. Appl. Phys. **56**, 3204 (1983).
- 23.5 R. R. Whitlock, S. P. Obenschain, J. Grun, J. A. Stamper, B. V. Sweeney, and B. H. Ripin, J. Appl. Phys. **61**, 131 (1987).
- 23.6 B. H. Ripin, R. R. Whitlock, F. C. Young, S. P. Obenschain, E. A. McLean and R. Decoste, Phys. Rev. Lett. **43**, 350 (1979).
- 23.7 E. A. McLean et al, Phys. Rev. Lett. **45**, 1246 (1980).
- 23.8 J. Grun, M. H. Emery, C. K. Manka, T. N. Lee, E. A. McLean, A. Mostovych, J. Stamper, S. Bodner, S. P. Obenschain, and B. H. Ripin, Phys. Rev. Lett. **58**, 2672 (1987).
- 23.9 M. Desselberger, O. Willi, M. Savage, and M. Lamb, Phys. Rev. Lett. **65**, 2997 (1990).
- 23.10 B. A. Remington, S. W. Haan, S. G. Glenndinning, J. D. Kilkenny, D. H. Munro, and R. J. Wallace, Phys. Fluids B **4**, 967 (1992).
- 23.11 S. G. Glenndinning, S. V. Weber, P. Bell, L. B. DaSilva, S. N. Dixit, M. A. Henesian, D. R. Kania, J. D. Kilkenny, H. T. Powell, R. J. Wallace, P. J. Wegner, J. P. Knauer, and C. P. Vernon, Phys. Rev. Lett. **69**, 1201 (1992).
- 23.12 F. Y. Young, "Design Considerations for Rayleigh Taylor Experiments", (unpublished memorandum, 1991)

## Section 24

### NIKE TARGET MODELING

John H. Gardner

*Laboratory for Computational Physics and Fluid Dynamics  
Naval Research Laboratory  
Washington, DC*

#### I. INTRODUCTION

Nike target experiments have two overall goals. The first is to demonstrate a uniform ablation pressure, with long wavelength ablation pressure variation of less than two percent. The second is to demonstrate an ablative Rayleigh-Taylor growth rate that is reduced to less than forty percent of its classical predicted value for wavelengths that are on the order of the target thickness. Achieving these goals will provide evidence that a direct-drive inertial confinement fusion [ICF] pellet can successfully survive the ablative acceleration phase of a high-gain implosion. This paper describes the numerical modeling efforts that are underway to predict the expected results of the experiments and to provide guidance in the design of the experiments. Most of the results were obtained with the NRL FAST2D laser-matter interaction code.<sup>24,1</sup> We will first describe the calculations in support of the double foil technique to measure ablation pressure uniformity and then describe our calculation in support of the Rayleigh-Taylor growth experiments.

#### II. UNIFORM ABLATION PRESSURE EXPERIMENTS

First we consider the uniform ablation pressure experiments, which are being designed to quantify Nike laser beam spatial uniformity. A schematic of the experimental set-up is shown in Fig. 24.1. A thicker foil, shown to the right, will be accelerated by the nearly uniform Nike laser beams until it collides with a thin witness

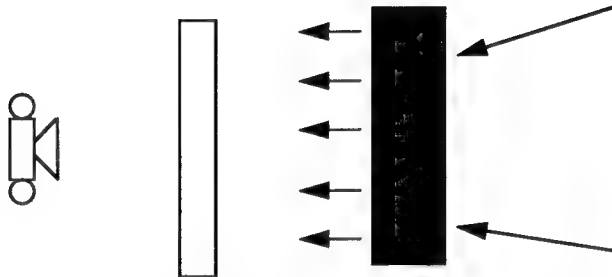


Fig. 24.1 — Schematic diagram of the experimental set up for the double foil experiment to measure laser uniformity.

foil. When the foils collide, a shock will be driven through the witness foil. As it exits, the shock will heat the rear surface of the witness foil causing that surface to emit detectable radiation in the far uv to soft x-ray bands of light. In the case of a perfectly spatially uniform laser beam we expect the accelerated foil and the shock it triggers to be uniform across the flat region of the focal spot diameter. The entire rear surface of the witness foil would light up simultaneously across this focal spot. However, if long wavelength nonuniformities exist in the driving ablation pressure these nonuniformities will directly perturb the accelerated foil. When the two foils collide, the shock generated in the witness foil by the impact of the accelerated foil will take on the shape of the nonuniform rear surface of the accelerated foil. The shock will thus exit the thinner witness foil over a range of times  $\delta t$ . The time span  $\delta t$  is directly proportional to the laser ablation pressure variation,  $\delta P$ . If  $\delta t$  can be measured, then a measure of the accelerated target nonuniformity and thus the laser ablation pressure nonuniformity will be provided.

From a target hydrodynamics point of view, the primary modeling issues for the uniform ablation pressure experiments are twofold. It is necessary to provide credible theoretical estimates for (a) the density of the accelerated foil that will trigger the shock in the witness foil; and, (b) the lateral spatial resolution of the diagnostic. The rise time of the emitted signal must also be short enough compared to the  $\delta t$  that the signal can be resolved.

We have used our radiation transport/hydrodynamic code to model plastic foils that are accelerated by the Nike KrF laser beam with a moderately shaped temporal history shown in Fig. 24.2a. The results indicate that the shock in the witness foil samples a density of greater than 0.2 g/cc in the foil. The pressure generated by a stagnating gas is proportional to  $\rho v^2$ . The velocity  $v$  is approximately that of the accelerated foil so the pressure builds up proportionately

to the density. Thus, the shock is dominated by the high density portion of the foil profile as long as the time of collision is short compared to the sound transit time through the witness foil. We illustrate with a one-dimensional calculation where both foils are polystyrene [CH]. The accelerated foil is 100  $\mu\text{m}$  thick, and is initially separated from the 15  $\mu\text{m}$  thick witness foil by a distance of 80  $\mu\text{m}$ , as can be seen from the  $x - t$  diagram, Fig. 24.2b. Density and temperature lineouts from  $x - t$  diagrams near the time the shock is triggered in the witness foil are shown in Figs. 24.2c-d, and at the time of shock breakout are plotted in Figs. 24.2e-f. Figure 24.2c shows that for these initial conditions and laser temporal history the shock in the witness foil is triggered by the laser-accelerated foil bulk with density greater than 0.2 g/cc and will thus be a measure of the acceleration of the bulk of the foil.

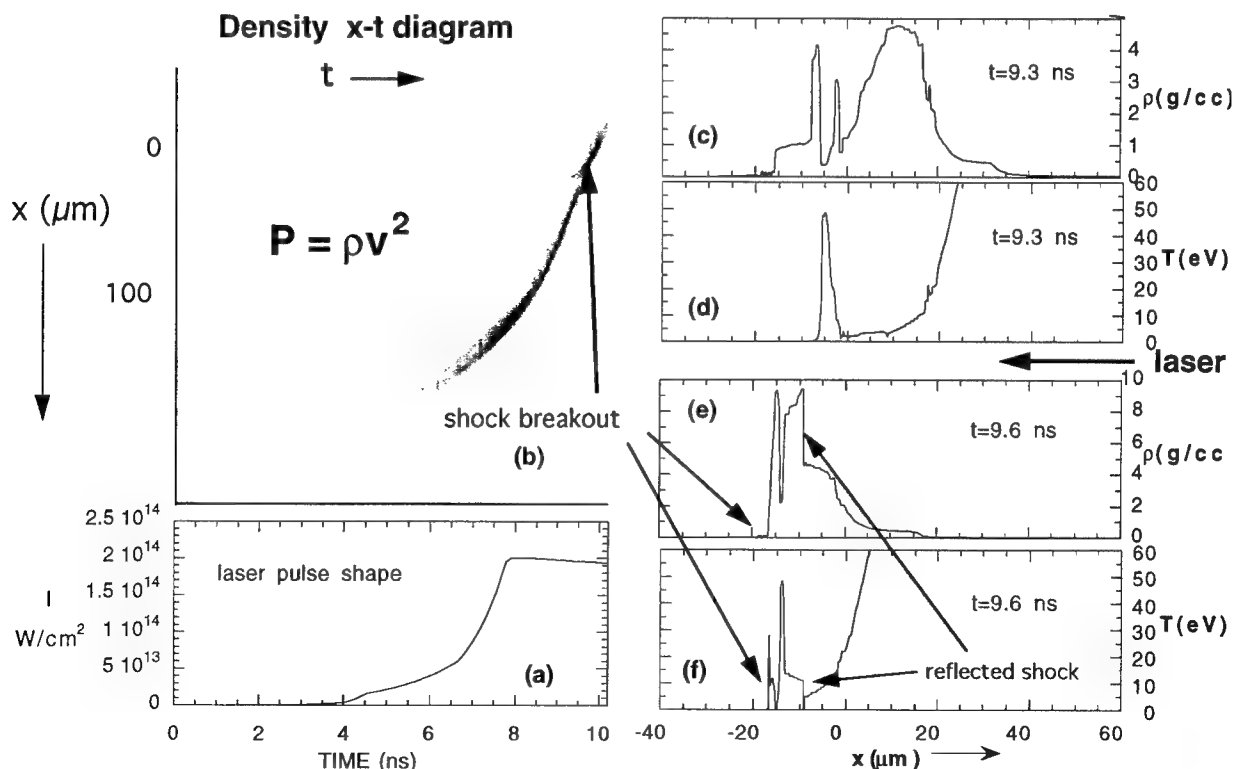


Fig. 24.2 — Results from a one dimensional simulation of one configuration for the double foil experiment: (a) laser pulse shape; (b)  $x - t$  diagram showing foil motion and shock evolution; (c) density lineout at time of shock formation due to foil collision; (d) temperature lineout at same time; (e) density profile at time of shock breakout from witness foil; and, (f) temperature profile at same time.

Nonuniformities in ablation pressure will lead directly to nonuniformities in acceleration and thus nonuniformities in the shock breakout time. This can be seen from the results of a series of hydrocode calculations shown in Fig. 24.3, a plot of witness-foil rear-surface temperature as a function of time. Each curve on the plot derives from a separate one-dimensional simulation where the driving laser peak intensity was varied by the percentage indicated. The witness foil temperature rise at the rear of the foil corresponding to a density of  $10^{21}$  g/cc (at an optical depth on the order of one) shows a sharp enough rise and sufficient separation to resolve one percent variations. The actual measurements will be of optical or soft x-ray fluxes, so in Fig. 24.4 we show the relative fluxes computed by our multigroup radiation transport package in flux bins in the (a) optical and (b) soft x-ray range. The optical data shows a sufficiently fast rise to resolve to the few percent level. In order to get preliminary data on the two dimensional (2d) effects, we performed 2d simulations with imposed laser non-uniformities of 2% and 3% with a spatial wavelength of 200  $\mu\text{m}$ . Figures 24.5a,b show the optical flux as would be seen by a streak

camera. Figures 24.5c,d show lineouts of the flux at the first and last shock arrival times. These results show that we should be able to measure laser nonuniformities down to the few percent level with at least 200  $\mu\text{m}$  resolution. Further work will determine the limits of the resolution.

A number of phenomena could limit the reliability of the radiation/hydrocode predictions of the shock breakout. Strongly coupled plasma effects at high mass density and uncertainties in the radiation opacities as well as significant lateral transport could modify these results. The preliminary multidimensional, single wavelength calculations indicate that excessive lateral transport will not occur. It is more difficult to estimate possible errors caused by neglecting (unknown) strongly coupled plasma effects.

### III. ABLATIVE RAYLEIGH-TAYLOR CONTROL EXPERIMENTS

We next address the second goal of Nike target experiments, to demonstrate an ablative Rayleigh-Taylor [RT] growth rate that is reduced to less than 40% of its classically predicted value for wavelengths that are on the

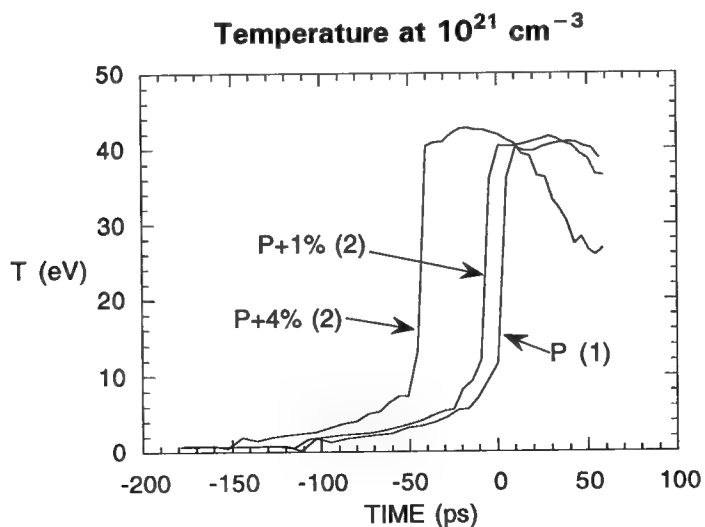


Fig. 24.3 — Evolution of the temperature during shock breakout at one optical depth from the rear of the witness foil for a baseline intensity and an intensity of 1% and 4% greater than the baseline intensity.

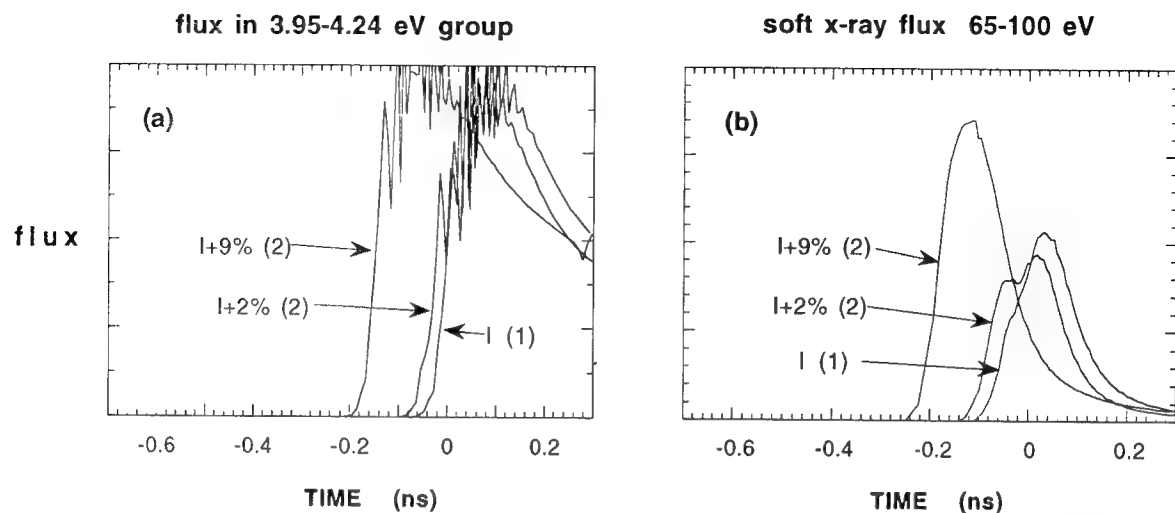


Fig. 24.4 — Evolution during shock breakout of the (a) optical flux in the 3.94-4.24 eV group; and, (b) soft x-ray group flux for a baseline intensity of  $2 \times 10^{14} \text{ W/cm}^2$  and intensities of 2% and 9% above the baseline.

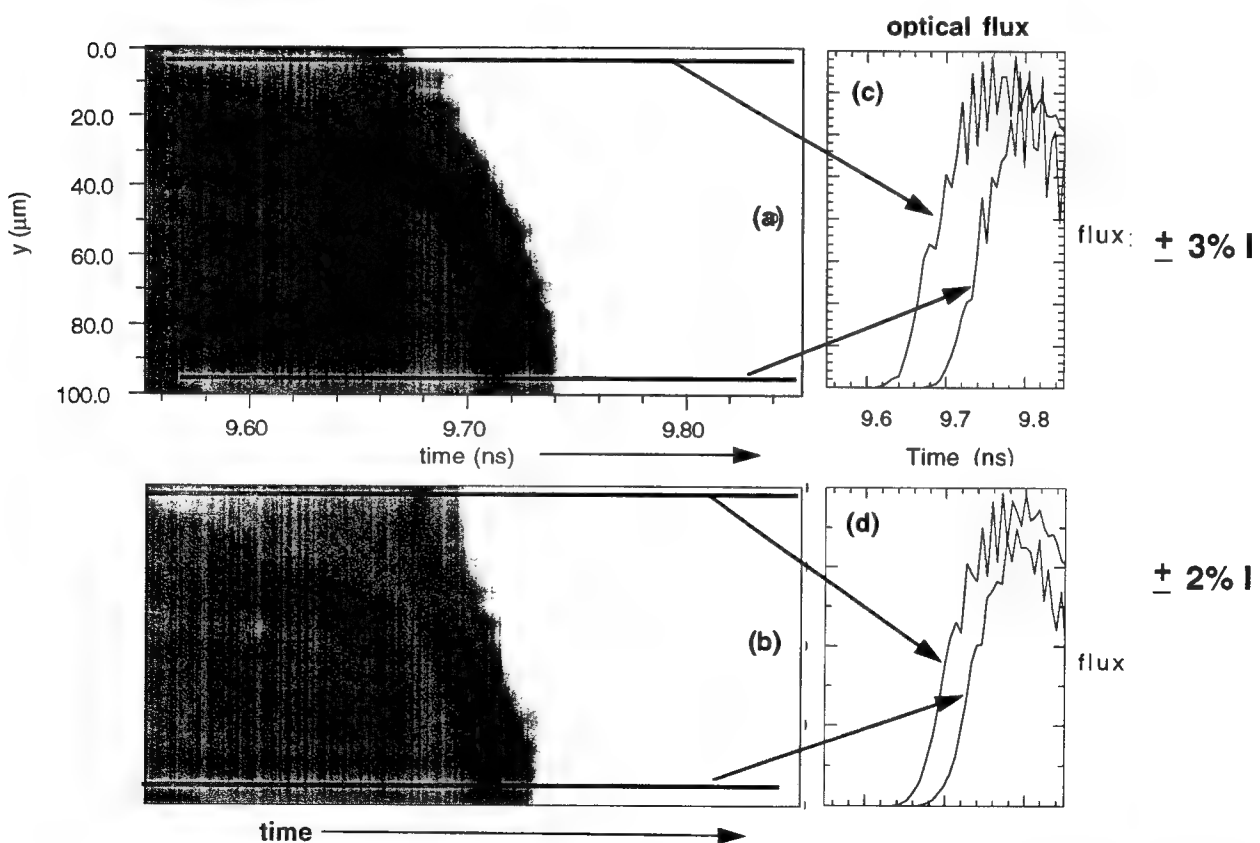


Fig. 24.5 — Optical flux as would be measured by a streak camera resulting from a 2d simulation of a  $200 \mu\text{m}$  wavelength: (a) 3% laser intensity variation; and, (b) 2% intensity variation. Lineouts through the earliest and latest shock breakout are shown in (c-d) indicating resolution to the few percent level at a  $200 \mu\text{m}$  resolution.

order of the accelerated target thickness. Since these targets are intended to model high-gain ICF pellet ablators, the reduced growth rates must be achieved while the target remains at low enough entropy that the comparable high-gain ICF pellet would compress sufficiently.

For these experiments, foils that closely approximate those of high-gain direct-drive ICF pellet ablators will be directly accelerated by the Nike laser beams with laser temporal histories that are similar to high-gain pulses. The foils will be accelerated for distances on the order of  $300 \mu\text{m}$  with spot diameters on the order of  $600 \mu\text{m}$  and laser intensities of a few times  $10^{14} \text{ W/cm}^2$ . Face-on radiography will be the primary diagnostic used to measure the Rayleigh-Taylor growth. A simple schematic of the experimental setup is shown in Fig. 24.6. The foil marked (a) is accelerated by the main laser beams. A few of the Nike beam lines are used to heat a backscatterer foil marked (b) which is placed slightly to one side of the main beam path. A camera is placed directly across the accelerated foil from the backscatterer which measures the relative attenuation through the foil of the x-rays generated by the backscatterer.

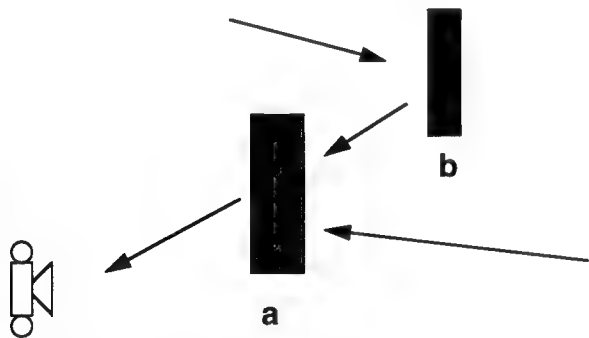


Fig. 24.6 — Schematic of the experimental setup for the Rayleigh-Taylor growth rate measurements.

The baseline accelerated foil is  $60 \mu\text{m}$  of plastic [CH]. A matrix of experiments are planned which span, on one axis, target composition and laser pulse temporal shape, which changes target entropy, and, on the other axis, the imposed RT perturbations. Since one hydrodynamic variable available to us is the atomic composition of the foil, we are considering a range of moderate Z dopants and surface layers

that should modify the radiation transport effects of the baseline target. These effects will alter the target entropy, in a spatially as well as temporally varying and controllable way, and thus will provide us with a means to control the RT growth rate. Another straightforward hydrodynamic variable is the laser pulse shape. Specified subnanosecond structures in the shape can drive shocks into the target which also will modify its entropy, thus providing another means of RT growth rate modification. The shape and amplitude of the RT perturbation that will be applied to the target when it is fabricated is another independent variable that will be varied.

Previous direct-drive RT experiments have been subject to significant driving laser beam difficulties: (a) beam spatial non-uniformities; and, (b) lack of enough pulse shaping to ensure low-entropy targets. For the RT perturbations to be studied in these cases, it was necessary for the imposed amplitudes to be large enough that the signal exceeded the noise of the laser beam imprinting effects, and that it was observable over the laser beam preheating effects. As a consequence, the initially imposed perturbations of successful experiments have been initialized with perturbations already in the early nonlinear stages of evolution. Thus, these experiments, while technologically superb, do not provide good measures of RT growth under realistic ICF conditions both in terms of perturbation amplitude and of target entropy. In particular the effects of Richtmyer-Meshkov (RM) growth in the foot of the laser pulse have not been adequately studied. We expect that the Nike laser will be sufficiently uniform to allow us to investigate the effects of actual ICF pellet surface finishes. Moreover, Nike is designed to provide good beam temporal history control (pulse shaping) which will give us the means to investigate a range of possible ICF driver and ablator conditions.

Simulation results from a typical baseline RT case are shown in Fig. 24.7. The laser pulse shape is shown in Fig. 24.7a. Figure 24.7b-d shows the 2d spatial evolution of a perturbed target, for three different times in the simulation. The expected nonlinear state of narrow spikes falling between wide, rising bubbles is

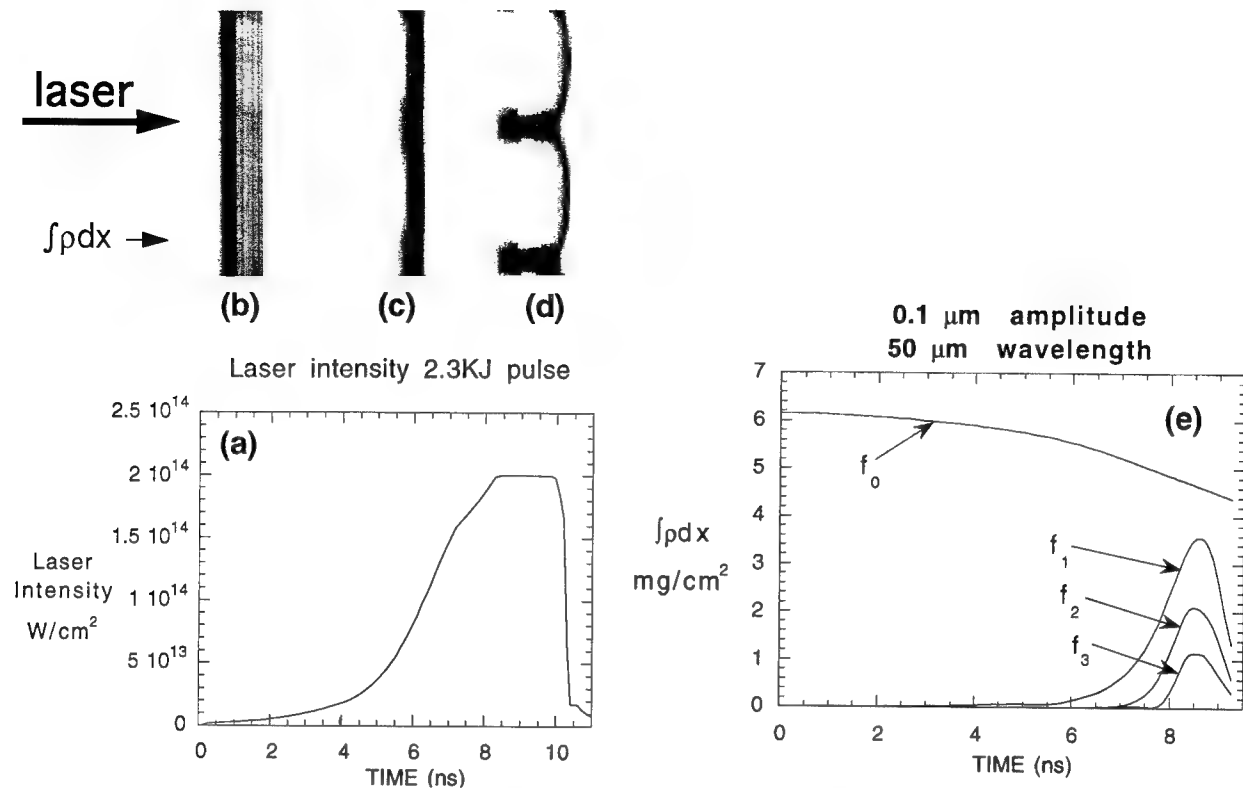


Fig. 24.7 — Results from a typical single mode Rayleigh-Taylor simulation: (a) laser pulse shape; (b) initial foil density profile; (c) density profile at the end of the linear stage; (d) density in the fully nonlinear stage showing well defined spikes and large bubbles; and, (e) Fourier coefficients of the areal mass through the target.  $f_0$  is the target mass and  $f_i$ ,  $i = 1, \dots$ , are the perturbation amplitudes. The initial target thickness was 60  $\mu m$ , the initial perturbation was a single mode of 50  $\mu m$  wavelength and 0.1  $\mu m/cc$  amplitude.

observed at the latest time, in Fig. 24.7d. In these simulations the basic Rayleigh-Taylor growth is measured from differences in target areal mass. The areal mass as a function of the direction transverse to the incident laser beam is obtained by  $\int_{x_1}^{x_2} \rho dx$ , for  $x_1$  a position far to the rear of the target, and  $x_2$  a position near the critical surface on the laser-illuminated side of the target. Separate modes of the Fourier transform of the areal mass are plotted in Fig. 24.7e, with  $f_0$  the mass of the target,  $f_1$  the amplitude of the initially perturbed mode, and  $f_j$ ,  $j = 2, \dots$ , the higher harmonics generated as a result of nonlinear growth at later times.

Experimentally there is no direct way to measure  $\int_{x_1}^{x_2} \rho dx$ . Instead what is measured is the attenuation of x-rays from a face-on backlighter source. We will be using line radiation as the first Nike backlighter source. This type of

source is to be preferred since for a narrow band source a narrow range of opacities are selected and can be more directly related to the absorption by the target. This makes interpretation of the x-ray absorption by the areal mass density more precise. The disadvantage is that it is more difficult to obtain a sufficiently bright source. Preliminary calculations indicate that the available laser energy will be sufficient to generate the necessary backlighter x-ray intensity. We initially plan to use line radiation from an aluminum source with a silicon filter to select x-rays in the 1.4-1.8 KeV range. There are two strong aluminum h- $\alpha$  lines in this region. Figure 24.8a<sup>24.2</sup> shows the fluency as a function of photon energy for the specific aluminum lines to be considered for the baseline RT experiments. The spectral intensity from the backlighter will be modulated by the variable opacity in the target and the silicone filter. Fourier transforms of intensity as a function of time are shown in

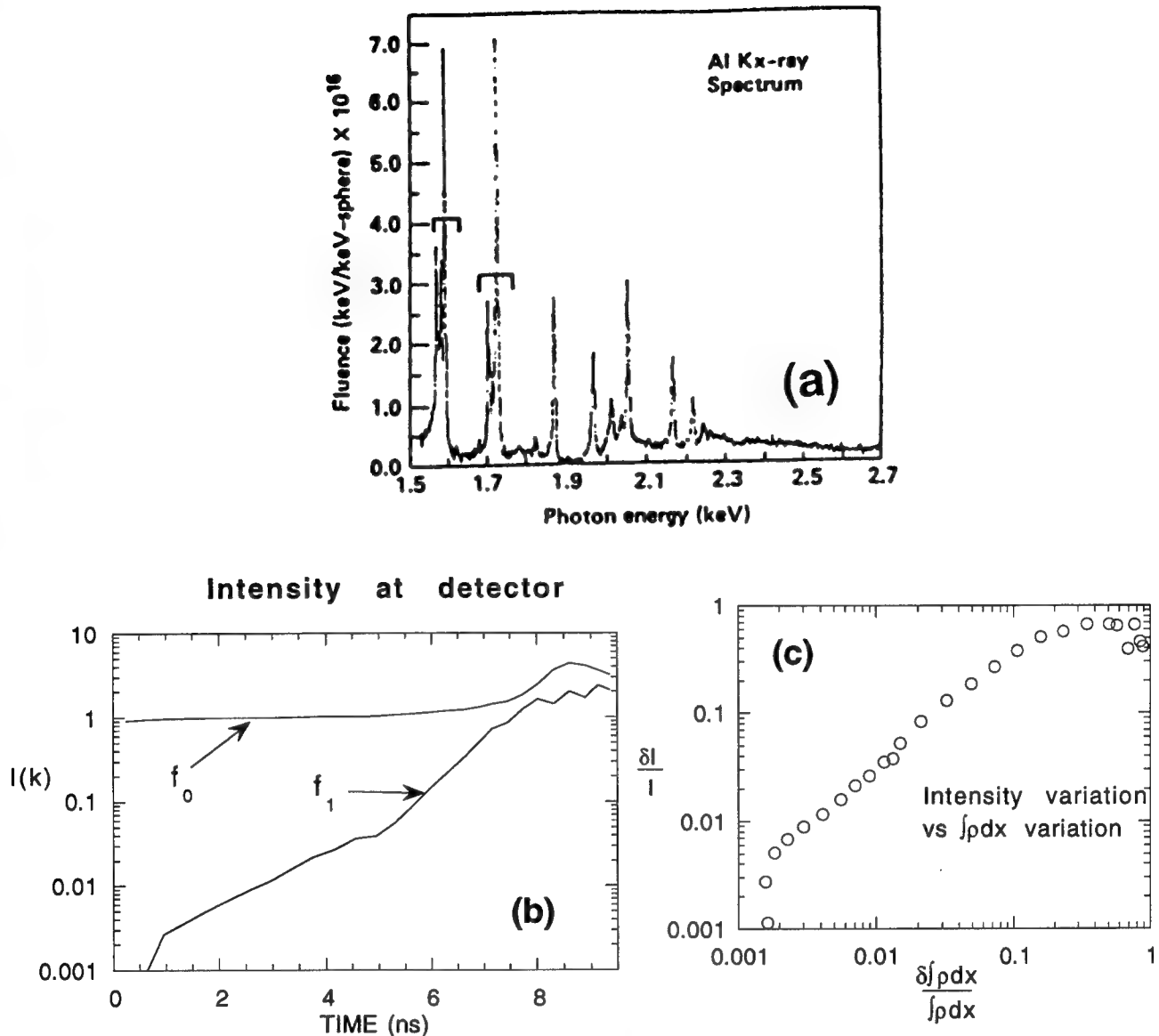


Fig. 24.8 — Results from the simulation of the backlighter intensity; (a) aluminum spectrum used in the simulation as the backlighter source; (b) Fourier coefficients of the radiation intensity at the detector plane (arbitrary units); and, (c) correlation of the intensity variation at the detector plane to the areal mass variation as computed in the simulation, indicating a dynamic range of two orders of magnitude for this diagnostic.

Fig. 24.8b. The zero order or mean intensity and the first harmonic are shown. In Fig. 24.8c the ratio of the first harmonic to the mean of the x-ray backlighter light is correlated to the ratio of the first harmonic to the mean of the areal mass density, during the entire pulse. The region of linear relationship shows that a dynamic range of more than two orders of magnitude is feasible with this diagnostic. This range should be adequate to measure both the linear growth phase and saturation.

With this diagnostic we will be able to investigate a number of fundamental hydrodynamic issues related to the RT and the RM instabilities. In order to achieve a realistic scaling, it is necessary to study the growth of instabilities using both laser and target response conditions that closely resemble those needed to drive actual direct-drive, high-gain ICF pellets. Figure 24.9a shows a typical shaped history necessary for a high-gain ICF implosion. The long foot is required to prepare the pellet fuel

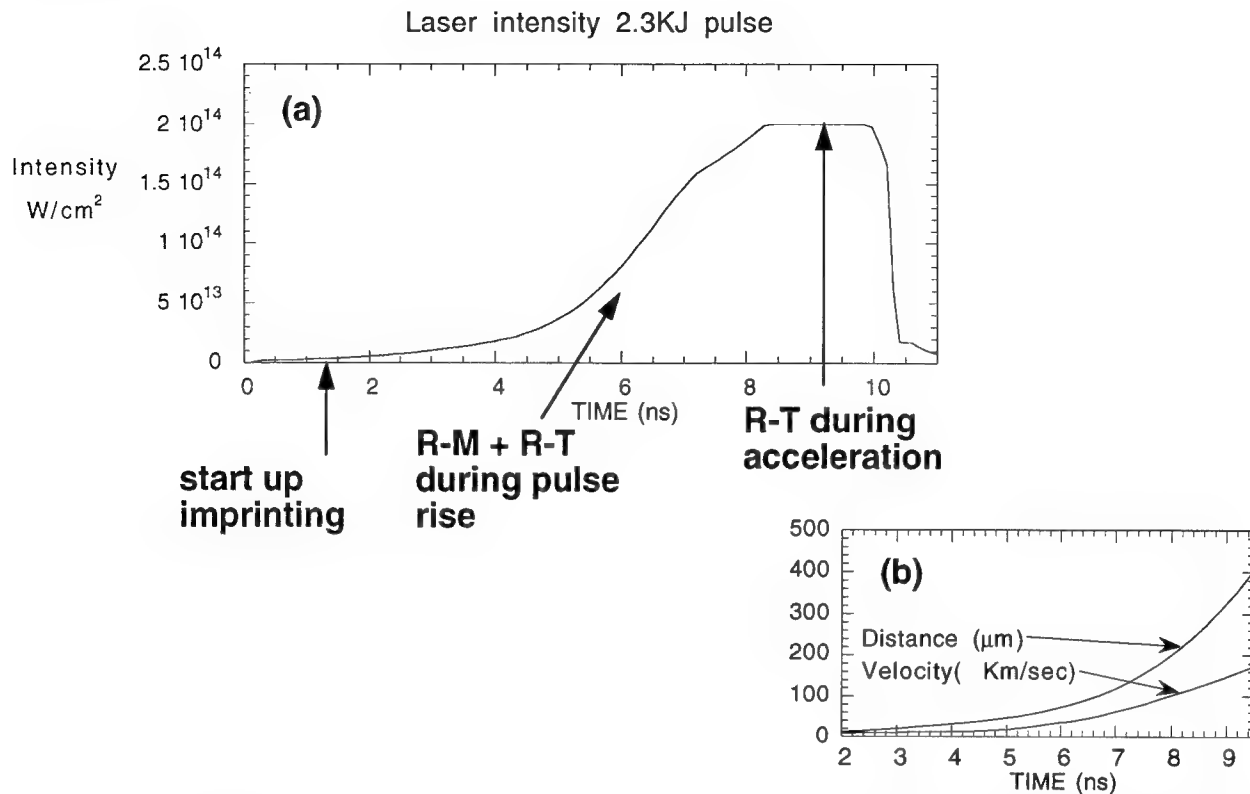


Fig. 24.9 — (a) Temporal pulse shape used for simulation of the baseline Rayleigh-Taylor experiments. This pulse shape is intended to mimic the pulse shape used in our high-gain pellet designs. (b) Distance traveled by the target and velocity of the target for the baseline Rayleigh-Taylor experiment.

on the correct low isentrope. Code predictions indicate that during this phase it is possible for initially small perturbations to grow an order of magnitude or more in amplitude due to the RM instability. We have observed that this growth is strongly dependent on the choice of ablator surface material. Since opacity and equation of state models are not well-characterized in this regime, issues related to imprinting during this "startup" phase must be experimentally investigated. During the early and rapidly rising portions of the pulse both RM and RT instability growth will occur simultaneously as a result of a combination of shock and continuous acceleration. Lastly, during the high intensity portion of the pulse instability growth will be dominated by the RT instability. Nike is being designed so that laser temporal histories shaped like the high-gain one shown in Fig. 24.9a are obtainable on the system. The distance the target will be pushed and the velocity the target will

achieve in a typical Nike experiment are shown in Fig. 24.9b. Although less than that needed for high-gain ICF, these quantities are sufficiently close to ICF conditions that extrapolations should be relatively straightforward.

The purpose of the experiments will be to determine what mechanisms will be required to control the hydrodynamic instabilities to a level tolerable for ICF success. There are a range of options that we will investigate: (0) do nothing; (1) dope the ablator with low to moderate Z materials to radiatively preheat the ablator material; (2) use a combination of shocks and rarefactions, as driven by a modified laser pulse shape, to preheat the ablator; (3) modify the laser pulse to induce dynamic stabilization. Although it is presently unclear which if any of these choices will bring sufficient control, Nike has sufficient beam quality that the entire range of questions such a list represents can be answered. With our numerical simulations we

are investigating the limits of the experimental program to determine what measurements are feasible.

Numerical simulations show that there is a direct correlation between perturbations induced by laser nonuniformity and those included in the initial target surface finish, in terms of the RT growth at later times. In Fig. 24.10a is plotted the amplitude of the 50  $\mu\text{m}$  perturbed mode as a function of time for two calculations. The curve marked 'initial amplitude' derives from a calculation in which a 60  $\mu\text{m}$  CH target is initially perturbed with a 0.5  $\mu\text{m}$  mass density perturbation, and then driven by a spatially uniform laser. The curve marked 'laser perturbation' derives from a calculation in which an unper-

turbed 60  $\mu\text{m}$  CH target is driven by a laser with a 5% sinusoidal spatial intensity modulation for all time. The curves overlap during the timespan in which the initially perturbed target exhibits RT growth. Similar behavior also occurs for smaller amplitudes, as shown in Fig. 24.10b. In both simulations the final amplitude is well into the nonlinear stage and exhibits saturation effects. Thus, experiments with highly shaped pulses with a long temporal foot and small initial target perturbations will require exceptional beam quality to avoid having the laser nonuniformity mask the effect of the initial target perturbation. Since with Nike such beam quality is possible, we expect to be able to investigate effects that evolve from surface

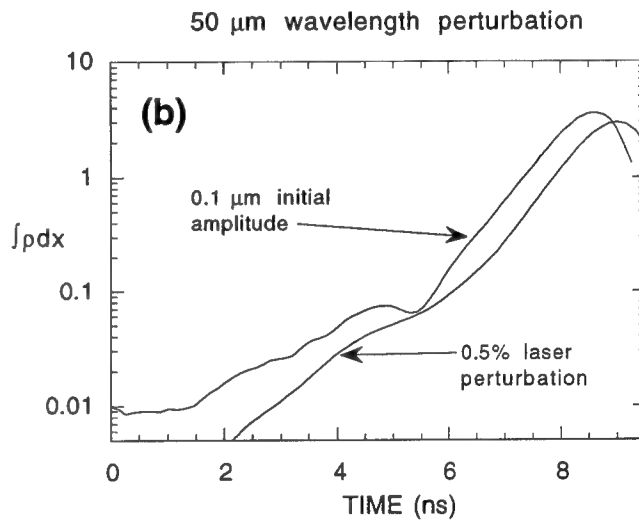
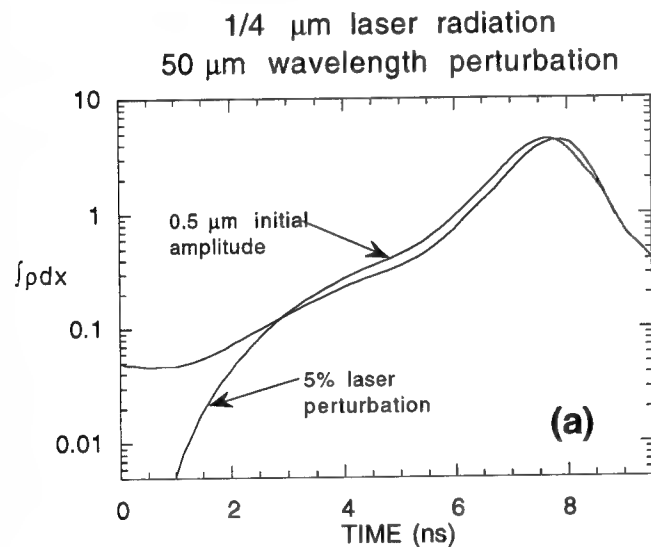
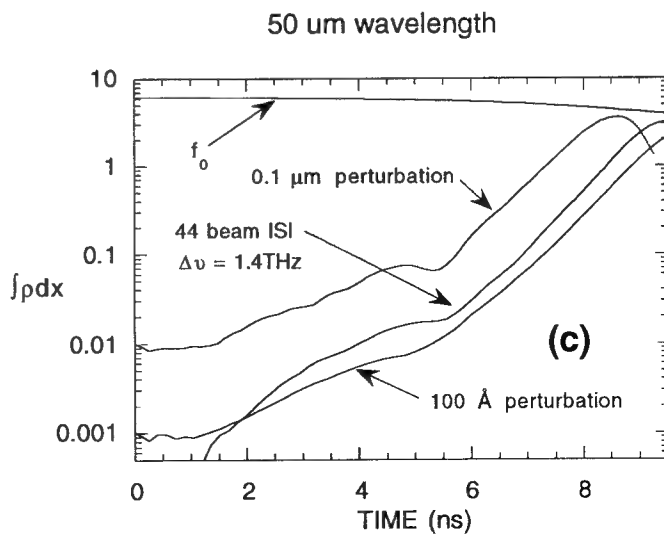


Fig. 24.10 — Results from the study of variation of initial perturbation amplitude and magnitude of laser nonuniformity on Rayleigh-Taylor growth: (a) 0.5  $\mu\text{m}$  g/cc initial perturbation amplitude and 5% laser nonuniformities show similar growth at late times; (b) smaller initial perturbation corresponds to an equivalently smaller laser nonuniformity; and (c) 44 beam ISI beam is equivalent to 100  $\text{\AA}$ -g/cc perturbation.



finishes on the order of those acceptable for a high-gain ICF pellet, *i.e.* on the order of a few hundred angstroms. In Fig. 24.10c, we show the results from a simulation where we have modeled the 44 overlapping ISI beams coming in at three distinct angles each representing 14 ISI beams. Results from this simulation show that RT growth due to beam nonuniformities is equivalent to that of a 100 Å surface finish in the same wavelength region.

There is computational evidence that the Nike laser imprint amplitude can be reduced further by the use of a small amount of x-radiation in the form of an x-ray flash at the start of the pulse. This generates a smooth ablation during the period before enough plasma has ablated

for thermal smoothing of the laser beam to be effective. When the ISI with 44 beam overlap calculation is repeated in the presence of early-time irradiation by a single joule of x-rays from a thulium x-ray source, the hydrodynamic instability effects of Nike imprinting drop to amplitudes below those generated from a 100 Å initial perturbation, as shown in Fig. 24.11a. This effect is not nearly so well pronounced when larger laser nonuniformities are considered. In Fig. 24.11 we show the results with the same x-ray flash but with imposed laser nonuniformities of 0.5% and 1%. In both cases the growth was nearly as large as without the x-ray flash.

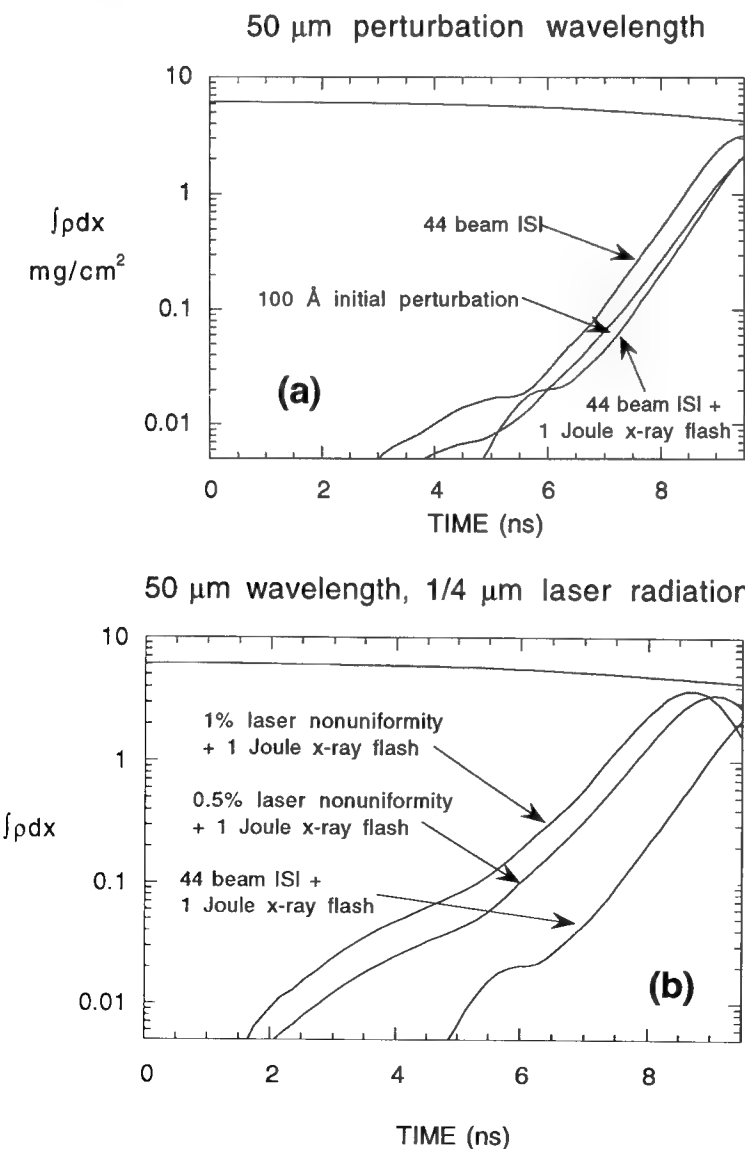


Fig. 24.11 — Results of using an x-ray flash to reduce the problem of initial imprinting: (a) with 44 beam ISI x-ray flash, which reduces growth to below 100 Å surface finish; and, (b) with a larger laser nonuniformity, when the x-ray flash is much less effective.

#### IV. SUMMARY

The two-fold goals of the Nike experimental program are being addressed computationally. Our design modeling indicates that the first goal, that of establishing the beam spatial uniformity, can successfully be addressed by experiment. Diagnostics exist which may confirm laser uniformities to better than two percent for low order modes. When the laser uniformity is established, the goal of controlling the Rayleigh-Taylor instability will be addressed. Several feasible techniques are proposed to control the instability. These techniques are being studied by numerical modeling. They will soon be evaluated by experiment in the Nike facility and compared to the modeling to help us improve further our modeling capabilities and give more confidence to the code predictions for high-gain designs.

#### ACKNOWLEDGEMENT

This work was performed in collaboration with Dr. J. P. Dahlburg in the Laboratory for Computational Physics and Fluid Dynamics, Naval Research Laboratory.

#### REFERENCES

- 24.1 M.H. Emery, J.H. Gardner, and J.P. Boris, *Appl. Phys. Lett.* **41**, 808 (1982); J.H. Gardner *et al.*, *Phys. Fluids* **29**, 1305 (1986).
- 24.2 D.L. Matthews *et al.*, *J. Appl. Phys.*, **54**, 4260 (1983).

## Section 25

### TARGETS FOR NIKE

J.D. Sethian

*Laser Plasma Branch  
Plasma Physics Division  
Naval Research Laboratory*

### INTRODUCTION

Very flat laser beams require very flat targets. All the effort expended in producing uniform laser focal profile would all go for naught if we could not generate comparably flat targets. Fortunately, our requirements on target flatness and uniformity, while more severe than those of an indirect drive target, are not so severe as to push the state of the art. Our targets are being developed by W J Schafer Associates as part of the DOE Target Fabrication Program.

### TARGETS

As described in Section 23, Nike will require a wide array of flat targets. These include single and double foils of pure CH, single foils with high Z-dopants, and rippled and contoured foils. The latter are used to determine the growth rate of targets with a "seeded" instability. The target thickness is determined by the available laser energy, and the target surface morphology is determined by the growth of the Rayleigh-Taylor instability. Typically the targets are 30 to 90  $\mu\text{m}$  thick, with the exception of the second foil in the double foil targets which are only 15  $\mu\text{m}$  thick. For the very uniform Nike beam, the peak to valley amplitude variation in the surface must be  $\pm 100 \text{ \AA}$  or better. This constraint applies over a spectral range of 2  $\mu\text{m}$  to 200  $\mu\text{m}$  in order to completely encompass the most unstable modes. To ensure the flat part of the beam illuminates the entire target simultaneously, the target curvature must be less than

4  $\mu\text{m}/\text{mm}$  over its width. Finally, the targets must be significantly larger than the laser spot size of 600  $\mu\text{m}$ . For ease of handling, we have specified the targets to be 2 mm  $\times$  2 mm.

The flat CH targets are produced by casting polystyrene film on flat silicon wafers. These wafers are extremely flat (less than 10  $\text{\AA}$  variation) and are commercially available from the semiconductor industry. Typically the wafers are 4 inches in diameter. To produce the films, a predetermined amount of polystyrene solution is applied from a syringe onto the wafer. The wafer is then covered with a watch glass to control the rate of evaporation. After the polystyrene has cured, the resulting film is cut into 2 mm  $\times$  2 mm targets. To date, flat films that meet the Nike specifications have been produced. Rippled and contoured targets can be produced by casting the films over a machined impression of the desired surface. Targets with random perturbations can be achieved by bead-blasting the silicon wafer, or by electrostatically depositing droplets of pure CH onto a wafer. The latter gives the targets an "orange peel" surface characteristic of the paint finish produced by low quality auto body shops. Doped targets can be fabricated either by chemically adding impurities to the CH mixture, or sputtering the impurities with a codeposition sputtering system. The latter technique allows layering of impurities and varying the dopant levels throughout the thickness of the target.

### TARGET MOUNTS

The targets must be mounted in a device that rigidly holds the film, yet allows free

unrestricted access to the target front, sides, and back, and still leave room for the x-ray back-lighter. The mount must be made of a low Z-material to prevent x-rays from the mount itself from obscuring the diagnostics, and, since the mount will be obliterated on each shot, it must be inexpensive. The target mount that meets all these criteria is shown in Fig. 25.1. They are cast from polystyrene on sprues following the same manufacturing techniques used to produce model airplane parts.<sup>25.1</sup> With a cost of roughly \$1.39 each we can afford to lose them on each shot. The targets are glued to the front face of the mount using a low viscosity UV cure cement. Double foil targets are produced by simply gluing a set of spacer strips (made of the same flat CH as the foil itself) on top of the first foil, and then gluing the second foil to the spacers. As the mounts are rather delicate, they are inserted into a thicker rigid plastic pylon. This pylon is in turn inserted in our target positioner. For ease of handling and shipping, the targets, mount, and pylon are preassembled before delivery.

## TARGET CHARACTERIZATION

One of the key elements of target fabrication is the characterization of the targets. The targets must meet a well defined list of specifications, and each target will be delivered with complete documentation of its characteristics.

The primary diagnostics for characterizing the targets are optical microscopy for measuring thickness and homogeneity, interferometry for measuring the film thickness and surface finish, and a photon tunneling microscope (PTM)<sup>25.2</sup> to measure the surface finish. The PTM is a newly developed technique that can allow detection of surface variations of 20 Å or more. It is based on the observation of Newton<sup>25.3</sup> who noted that not all the light that propagates at the critical angle from one medium to one of lower index of refraction is reflected. An evanescent wave is set up in the second medium whose amplitude decreases exponentially with distance from the interface. By placing an object in the second medium, and converting the reflected light with a gray scale imager, one can very accurately determine the distance from the sample to the interface. The PTM gives an image within a minute, and requires no sample preparation, no vacuum, and no physical contact. This is a very powerful tool, particularly considering the cost of the PTM with all the necessary electronics is around \$60,000. We also believe this technique can be used to characterize cryogenic surfaces.

## PRESENT STATUS

When applied to prototype foils, the PTM shows the cast CH method can produce foils with surface variations of less than  $\pm 50$  Å, with the required flatness. However a fair fraction of

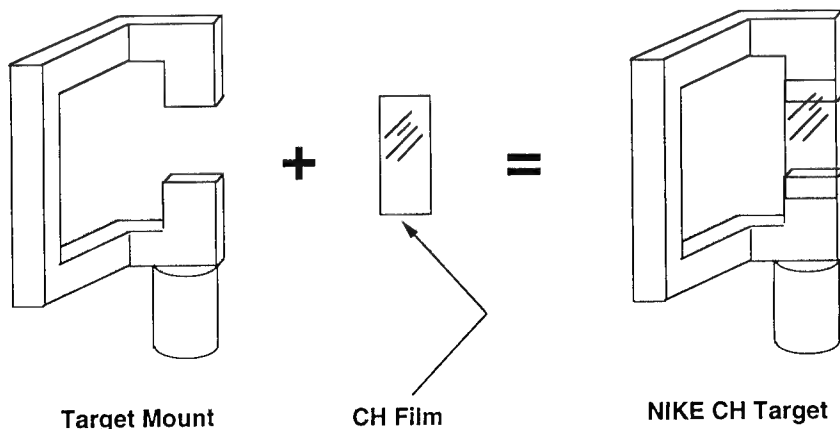


Fig. 25.1 — Fabrication of a NIKE target. A piece of precast CH film is micro-manipulated and glued to the edges of the target frame. In this view, the target is facing the laser beam.

the foils ends up with dust on the surface. This should be eliminated when the newly acquired clean room has been assembled. At that point we will commence production of both flat foil and double foil targets.

#### ACKNOWLEDGMENTS

Development and fabrication of targets for Nike has been carried out by W J Schafer Associates, including C. Hendricks, D. Bittner, M. McLellan, B. Motta, D. Schroen-Carey, and K. Shillito. Additional contributions have been made by C.J. Pawley, S.P. Obenschain, J. Dahlburg and J. Gardner of NRL.

#### REFERENCES

- 25.1 When polystyrene is injection molded, the liquid polymer is forced through a branched tubular network. The end of each branch terminates with a small hole followed with a cavity precisely machined to the shape of the desired part. This cavity serves as the female mold. When the polymer has hardened, the mold is opened, revealing a part cast at each end of a branching rod-like network. That rod-like network is called a sprue.
- 25.2 "Photon Tunneling Microscopy," J. M. Guerra, *Applied Optics*, **29**, 3741 (1990).
- 25.2 *Opticks*, I. Newton, Part I, P 193-224 (Dover, NY 1730, 1979).

# **Target Physics Modeling**

183 **Edge Effects**  
*Jill P. Dahlburg*

189 **STA Opacity Modeling**  
*Marcel Klapisch*

195 **Radiative Preheat in Strongly Coupled, Laser Accelerated Plasmas**  
*J. L. Giuliani, Jr.*

201 **Start-up Imprinting and Shock Dynamics**  
*Mark H. Emery*

211 **RAD3D\_CM**  
*David E. Fyfe*

215 **Three-Dimensional Multimode Results**  
*Jill P. Dahlburg*

## Section 26

### EDGE EFFECTS

Jill P. Dahlburg

*Laboratory for Computational Physics and Fluid Dynamics  
Naval Research Laboratory  
Washington, DC*

Laser systems have finite intensity spots in the directions transverse to the propagation of the beam. Initially planar laser targets accelerated by such beams develop large transverse deformations at the edge of the high-intensity region of the illumination spot. We are investigating the finite-spot, planar laser target system by means of numerical simulation. Our goal is to design laser-target experiments that maximize the laser energy available for target acceleration while minimizing edge effects.

This section reports results from our ongoing series of edge-effects hydrodynamics simulations in two-dimensional  $r, z$  geometry, where the beam emanates from  $z = +\infty$  and is finite in radius  $r$ . The NRL laser matter interaction code, *FAST2D*, is used for the simulations. *FAST2D* solves the hydrodynamic equations of compressible flow in conservation form using the FCT finite-volume method. Laser energy is deposited directly by means of inverse bremsstrahlung deposition and transported by classical Spitzer-Härm electron thermal conduction. The equations are closed with a real table-look-up equation of state.

When a high-intensity laser beam with a finite-sized spatial spot illuminates a thin target that has a transverse area larger than the spot, the illuminated part of the target is compressed and accelerated by the laser beam, and the unilluminated part of the target remains stationary. In this study we are most interested in the stretching part of the target between the stationary and fully accelerating limits—the ‘edge’ that can modify the hydrodynamics of the central, laser accelerated region where we expect to perform scalable experiments. Two-

dimensional [2d] simulation of this region can be performed best in the laboratory frame of reference, with cylindrical  $r, z$  symmetry. The biggest computational obstacle faced in edge effects calculations is the physical domain of the problem, the large spatial region that needs to be simulated with accuracy.

The temporal (Fig. 26.1a) and spatial (Fig. 26.1b) laser intensity profiles considered for this study fix the limits of the fine resolution in the physical  $r, z$  domain. These profiles are chosen to match closely those of the Nike laser system, with laser intensities ranging from 1 to  $3 \times 10^{14}$  W/cm<sup>2</sup>, energies of a few kilojoules, contrast ratios on the order of 300, and spot sizes of approximately 600  $\mu\text{m}$  in diameter. With the temporal profile as specified in Fig. 26.1a, a 60  $\mu\text{m}$  target will accelerate about 350  $\mu\text{m}$  in  $z$  during the time shown. In order to resolve the ablation front of the initially unmoving target, the target thickness in  $z$  and, the full distance the target will traverse, 500  $\mu\text{m}$  of fine  $z$ -resolution is nominally required. In  $r$  we need to resolve the full spot radius we can expect given the projected Nike energy and the peak intensity—about 400  $\mu\text{m}$ , when the spot ‘wings’ are included. For the accurate simulation of the Rayleigh-Taylor instability, the meshes would have to be about 0.25  $\mu\text{m}$  in  $z$  and no greater than eight times that in  $r$ . As the central portion of the target would be accelerated on the finely gridded mesh, most of the high-temperature, low-density blowoff would be resolved with 0.25  $\mu\text{m}$  zones. A severe and essentially unnecessary Courant limit would thereby be imposed on the timestep. An Eulerian, laboratory-frame edge effects calculation which would

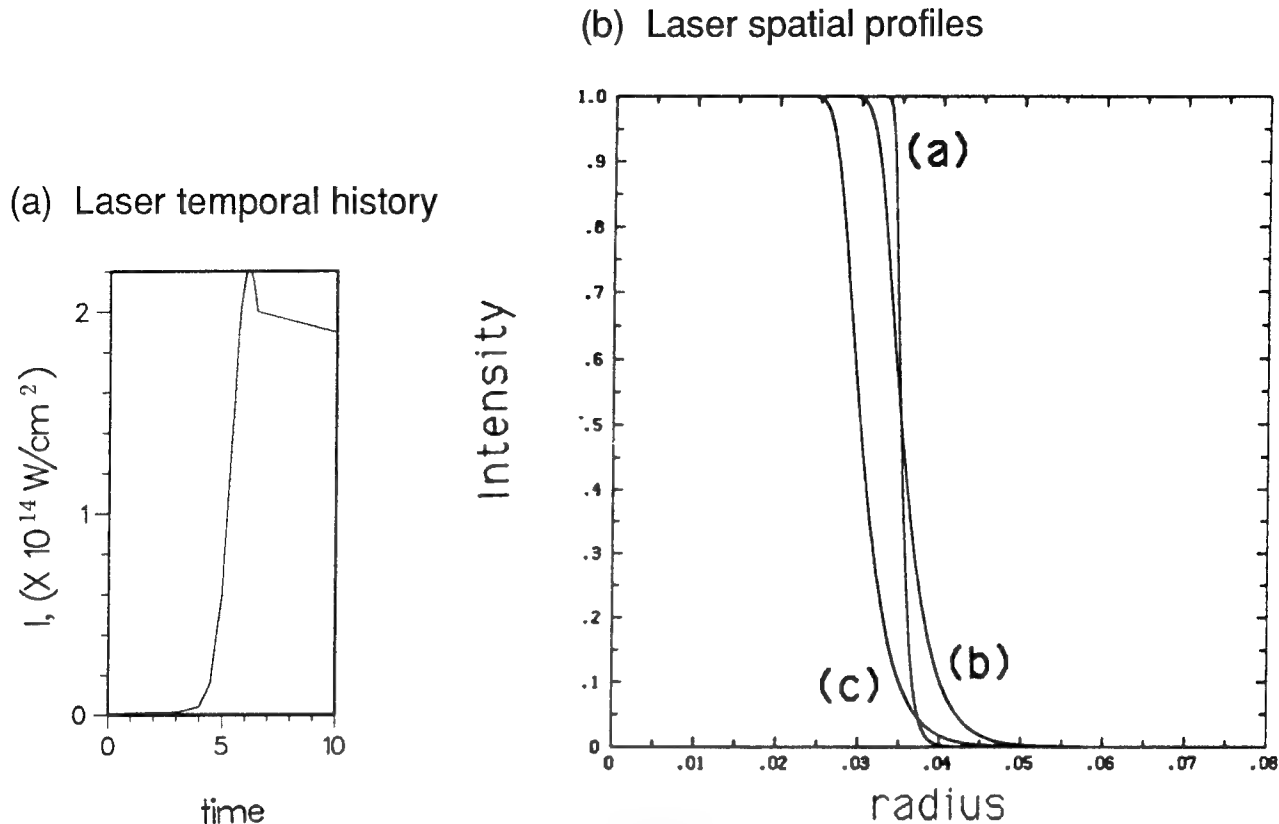


Fig. 26.1 — The laser profiles for the three calculations shown here. (a) The temporal laser history; and (b) the spatial laser intensity profile, or 'spot.'

model the target with sufficient numerical and physical accuracy to obtain the correct Rayleigh-Taylor growth rates will be extremely expensive, both in terms of the large number of spatial grids required and because of the resulting large number of timesteps.

Since the primary object of these edge-effects simulations is not to simulate the 'whole problem,' but instead to gain valid intuition about how to keep the finite sized laser spot from affecting target properties in the central, laser accelerated region, some gridding and physics compromises are made. We have included neither the *FAST2D* radiation transport package nor the oblique-angle laser ray trace. Currently, the parallel ray assumption is used to model the beam, with no spatial or temporal random intensity variation. The grid resolution is also relatively modest. In these calculations the  $z$  direction is resolved with  $0.525 \mu\text{m}$  meshes for  $315 \mu\text{m}$  (600 points), with an additional 150 points in that direction to account for the  $\pm z$  outflow boundary conditions and the

early-time laser deposition region, and the  $r$  direction is resolved with  $3 \mu\text{m}$  zones from  $r = 0$  to  $400 \mu\text{m}$ , with 20 more (stretched) meshes in  $r$  used to account for the unilluminated target at a radius outside the region of interest and to impose the outflow boundary conditions in  $r$ . Although this resolution is not sufficient for accurate Rayleigh-Taylor simulation—an anomalously high RT growth rate of modes seeded by grid noise will be observed in the results following—the computer time cost ( $\sim 20$  hours of Cray C-90 time per calculation) is low enough that a number of calculations can be performed to investigate the dominant hydrodynamic effects of laser spatial profiles of various shapes.

We discuss three calculations, as parameterized in Fig. 26.1b, and plotted in Figs. 26.2, 26.3 and 26.4. For all, velocity arrows are plotted every 10th point in  $r$ , with  $r = 0$  located half a cell beyond the lower boundary of the plots. The arrows are plotted every 25th point in the direction of the incident laser beam,  $z$ .

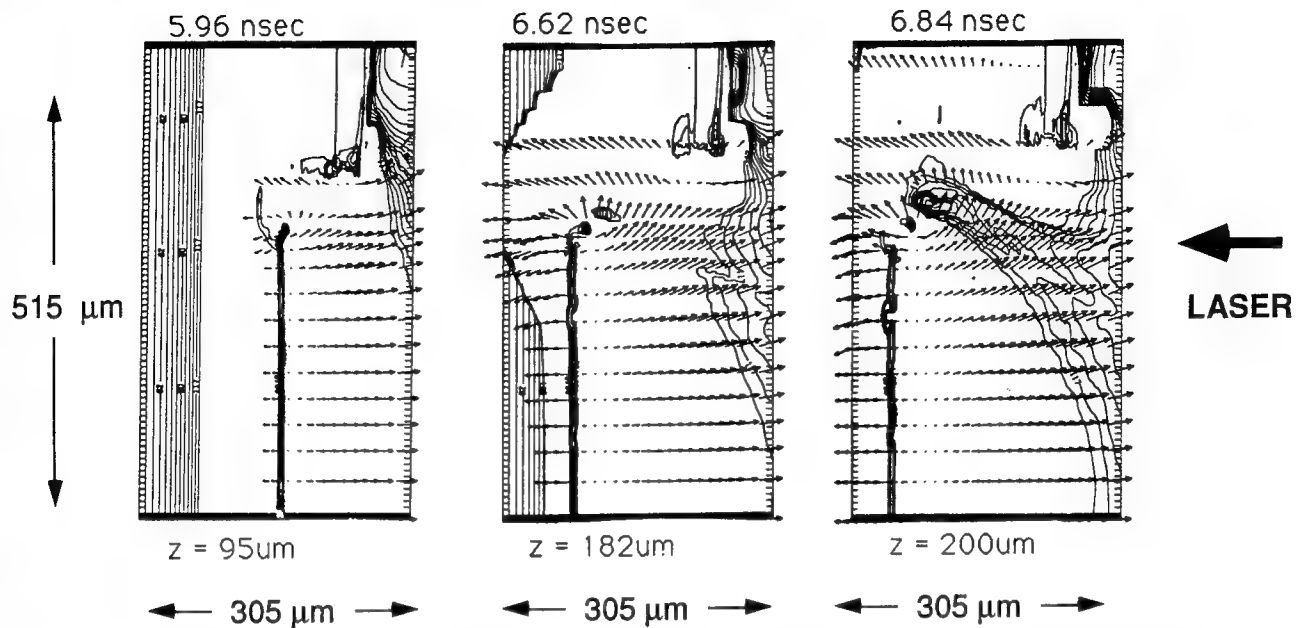


Fig. 26.2 — Velocity arrows overlaid on contours of constant density for case 'a' of Figure 26.1b, at three times: (a) at 5.96 nsec, when the average target velocity is  $9.0 \times 10^6$  cm/s; (b) at 6.62 nsec, when the average target velocity is  $1.5 \times 10^7$  cm/s; and, (c) at 6.84 nsec, when the average target velocity is  $1.7 \times 10^7$  cm/s. The z location of the moving target front surface is noted beneath each plot.

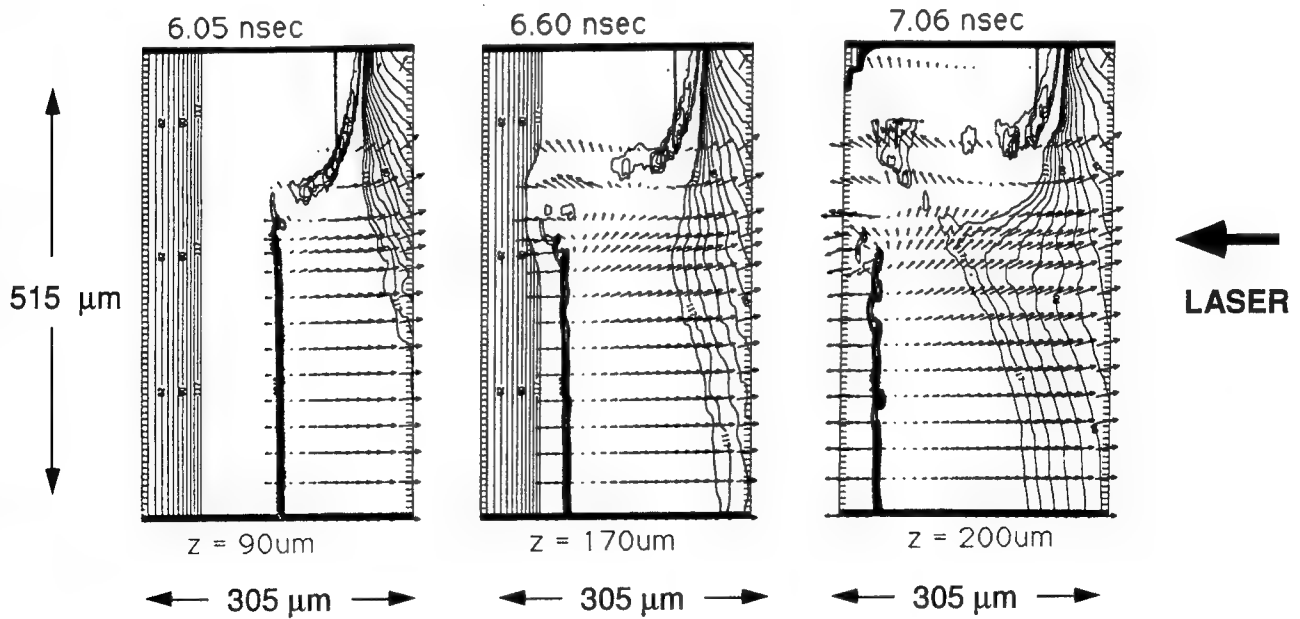


Fig. 26.3 — Velocity arrows overlaid on contours of constant density for case 'b' of Figure 26.1b, at three times: (a) at 6.05 nsec, when the average target velocity is  $8.5 \times 10^6$  cm/s; (b) at 6.60 nsec, when the average target velocity is  $1.2 \times 10^7$  cm/s; and, (c) at 7.06 nsec, when the average target velocity is  $1.5 \times 10^7$  cm/s. The z location of the moving target front surface is noted beneath each plot.

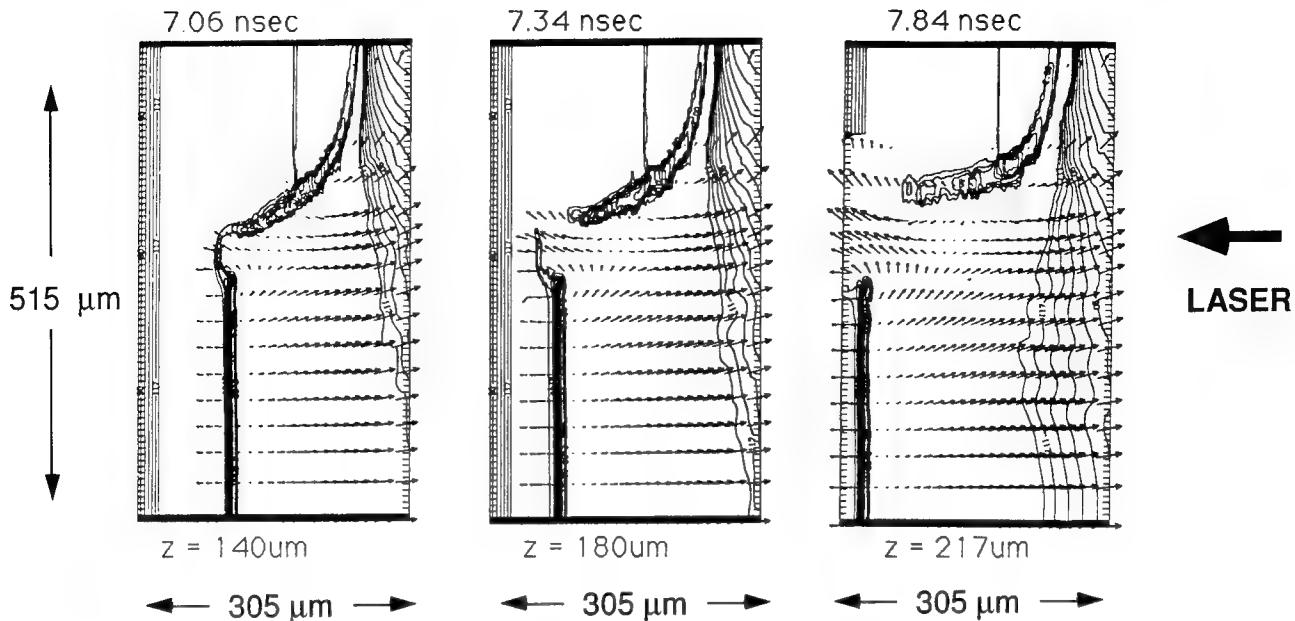


Fig. 26.4 — Velocity arrows overlaid on contours of constant density for case '(c)' of Figure 26.1b, at three times: (a) at 7.06 nsec, when the average target velocity is  $8.5 \times 10^6$  cm/s; (b) at 7.34 nsec, when the average target velocity is  $1.0 \times 10^7$  cm/s; and, (c) at 7.84 nsec, when the average target velocity is  $1.2 \times 10^7$  cm/s. The z location of the moving target front surface is noted beneath each plot.

The laser beam, schematically marked with an arrow, emanates from  $z = +\infty$ , which is located to the right of the plots. Two sets of mass density contours are plotted in each figure. One set, density contours of solid and higher densities, mark the target. The other set of contours mark surfaces of quarter critical density and lower; those to the right of the accelerating target show the spatial density variation in the laser deposition region.

The first calculation parameterized in Fig. 26.1b, labeled '(a),' uses a spatially sharp laser profile. With that beam a 45  $\mu\text{m}$  CH target is accelerated, as shown in Fig. 26.2. Early in time the target breaks at the 'edge'; see the first of Figs. 26.2, labelled 5.96 nsec. Subsequently, non-negligible lateral transport is observed around the broken edge of the accelerating target. At the latest time plotted, 6.84 nsec, the plasma in the laser deposition region is also very distorted, as can be seen from the contours at quarter critical density and below, in the plot at  $t = 6.84$  nsec.

The second calculation parameterized in Fig. 26.1b, labeled '(b),' uses a spatially more gentle laser profile. With that beam a 45  $\mu\text{m}$  CH target is again accelerated, as shown in Fig.

26.3. For this case, the target spatial profile matches that of the incident intensity. At the latest time plotted, when the accelerated part of the target has broken off from the 'edge,' non-negligible lateral transport and distortion of the plasma in the laser deposition region are visible. The effects are much less pronounced in this case than in the otherwise identical sharp profile case of Fig. 26.2.

The third calculation parameterized in Fig. 26.1b, labeled '(c),' is the same spatially more gentle laser profile as used in '(b).' The target accelerated in that calculation is an 85  $\mu\text{m}$  CH target. The laser beam diameter is reduced so that the same total laser energy is used over a longer run time. As in case '(b),' the target spatial profile matches that of the incident intensity; see Fig. 26.4. Increasing the target thickness delays breakthrough and keeps the target flatter, longer.

Our results indicate that planar laser targets are sensitive to sharp beam edge profiles. In the presence of a steep intensity fall-off (a "top-hat" profile) strong inward-directed flows quickly develop, inhibiting uniform planar acceleration in the region illuminated by the

high-intensity part of the spot. A similar effect is observed in cases where a thick ring of plastic encircles the central laser-target region.

However, in cases where the intensity profile is allowed to fall off more gently, with a scale-length on the order of 100  $\mu\text{m}$  or more,

there is much less interference of edge effects with the target bulk planar acceleration. The shear flow that develops in the edge region has a dominant outward radial component, and the target remains flat and accelerates uniformly in the flat central region of the laser spot.

## Section 27

### STA OPACITY MODELING

Marcel Klapisch  
ARTEP, Inc.  
Columbia, MD.

The amount and the distribution of radiation emitted and absorbed by each point of a plasma depends on the spectral opacity of matter. It turns out that hydrodynamic simulations are quite sensitive to opacities. But opacities depend on the temperature and density of the plasma, as well as on the charge state of the atoms, which in turn, is affected by the incident radiation. Therefore, exact computations should couple hydrodynamics, atomic physics and radiation transfer "on-line," and this is far beyond the reach of even the most powerful present computers. Consequently, approximations are used, but these can vary dramatically in accuracy. At a recent workshop in Garching, Germany (March 94) dedicated to the comparison between 20 opacity codes, it was shown that in some cases, group Rosseland means differed between codes by several orders of magnitude. The STA code came the closest to experimental data, whenever reliable experiments on LTE opacities were available. It was also the only code that could be applied without modification throughout the periodic table, and for a wide range of temperatures and densities.

#### I. THEORY

Atomic radiation is due to three types of transitions: Bound-bound, bound-free, and free-free. The most difficult part is the bound-bound, because for medium to heavy atoms in Local Thermodynamic Equilibrium (LTE), the number of states to be considered is enormous and make the problem not tractable. It is for this reason that the Super Transition Array (STA) concept was developed by A. Bar-Shalom [27.1-27.4],

as an extension of the Unresolved Transition Array (UTA) method [27.5]. The latter is based on the observation that for most ionized atoms, the great number of transitions between two configurations, in conjunction with line broadening, causes the lines to be lumped together in arrays that cannot be resolved (see Fig. 27.1). These arrays can be considered as distributions of transition energy, characterized by their moments:

$$\mu_n = \sum_{a \in A, b \in B} \frac{(E_a - E_b)^n w_{ab}}{w_{ab}}$$

where  $a, b$  are the states in configurations  $A$  and  $B$  respectively, and  $w_{ab}$  is a weight equal to the line strength. It turns out that these moments can be computed *exactly* in terms of universal coefficients and Slater integrals—the dipole integrals cancel out. Thus the position and width of an UTA can be evaluated very quickly with the effect of the fine structure, but without the full computation of the Hamiltonian and line strengths.

The STA method then goes a step further and defines a super configuration (SC) as a collection of "energetically near" configurations, with the same total number of electrons, for instance:  $(1s)^2(2s2p)^8(3s3p3d)^1$  meaning one electron outside closed shells either in  $3s$  or  $3p$  or  $3d$ . Then a Super Transition Array would be for instance all the transitions from  $(1s)^2(2s2p)^8(3s3p3d)^1$  to  $(1s)^2(2s2p)^7(3s3p3d)^2$ . It was shown by Bar-Shalom [27.1] that moments of STA can also be computed *exactly* if the populations of the configurations follow the Saha-Boltzman law.

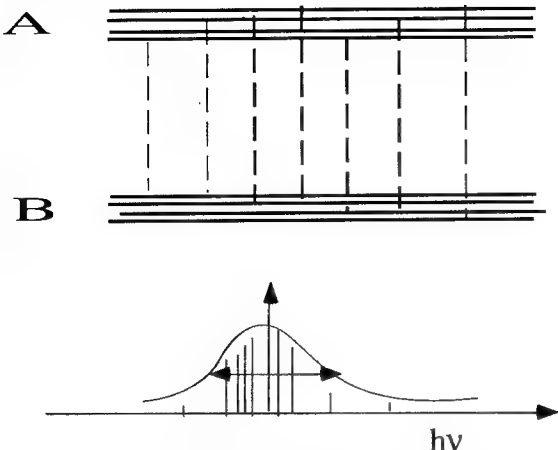


Fig. 27.1 — Two generic configurations A and B, and the distribution of all transitions between them.

A key characteristic of the STA method is that it is iterative: At first, the SCs are defined as relatively broad sets of configurations. The relevant STAs are computed, and a spectrum generated. Then, the SCs are broken up into smaller SCs, new STAs are computed, and a new spectrum is generated. The process is repeated until convergence on the spectrum is achieved.

Eventually, if the SCs are broken up into ordinary configurations, then UTAs are computed. However, in most cases, the number of STAs computed is orders of magnitude smaller than the number of UTAs that would be required. In this way, the effect of the fine structure is reproduced in an extremely efficient way, and without computing details that would not show up in the spectrum because of the line widths. For medium and heavy elements, this makes all the difference between a possible versus an impossible computation. For low  $Z$  atoms, the gain in computing time is not so dramatic, because the number of lines in an array is not so large. In principle, the STA model is valid for all  $Z$ , and actually, would converge to single configuration UTAs if the spectrum is sparse. As mentioned earlier, the moments of the UTAs are exact, so if there is but one line in an array, it will be reproduced very well. Comparison with more detailed codes like OPAL of Livermore, on low  $Z$  atoms shows that the agreement is remarkable, with running times typically an order of magnitude shorter.

For the actual computations, one needs energies and wavefunctions. These are obtained in the STA code by the parametric potential method [27.6-27.7] modified to include plasma effects [27.8-27.9]. This method turns out to be robust and reliable. It does not suffer like Hartree-Fock from convergence problems, and on the other hand, unlike many other approximate methods, it does not require an empirical form for the exchange potential. Its explicit foundation on perturbation theory [27.10] justifies the use of an analytical function for the potential in which the zero order wavefunctions are computed, at the condition that the matrix elements of the potential are subtracted from the first order contributions to the energies. The wavefunctions are obtained by solving the Dirac equation with this potential, and the parameters of the potential are modified until the first order energies of each superconfiguration are minimum.

## II. CODES

There are 2 codes available for Nike opacity computations:

(1) STA generates high resolution, high accuracy LTE opacity spectra for any atom, for a given grid of temperatures and densities, following the theory outlined above. Typical running times on workstations are 25 hours for light elements to 250 hours for high  $Z$ , for a grid of 60 densities by 40 temperatures. It generates binary files containing the spectra.

(2) MIX uses these results to compute group Rosseland and Planck means for any choice of "groups"—i.e., energy bins—and mixture of atoms, and prepares databases in a format compatible with the hydrodynamic codes. It involves an algorithm for the computation of effective density, or partial pressure, for each element of a mixture. This comes about because the equilibrium condition requires equality of the chemical potential of all the species in a mixture. This separation of tasks allows great flexibility in the definition of the groups, and the proportion of the elements in the mixture.

### III. COMPARISON WITH EXPERIMENTAL RESULTS

Recently, careful quantitative measurements of photoabsorption of an iron plasma were performed at Lawrence Livermore National Laboratory, using a backscatterer technique [27.11]. The plasma was prepared in such a way that LTE conditions were verified. The temperature and density of the plasma were measured simultaneously. Figure 27.2, reproduced from the above work, shows the experimental transmission data (gray line) for an Fe+NaF plasma of total density  $0.0113 \text{ g/cm}^3$ , 80.2% by weight Fe, and an areal density of  $339 \mu\text{g/cm}^2$ . The authors compared their measurements with the computations of several codes: (a) STA code for temperatures of 59 eV (solid line) and 57 eV (dotted line). The remaining model calculations assume a temperature of 59 eV. They were done with other codes in use at LLNL: (b) Monte Carlo with UTA (MCUTA) model, (c) OPAL with Detailed Term Accounting (DTA), (d) OPAL with UTA, (e) OPAL with Detailed Configuration Accounting (DCA) model.

The conclusion of the work is that STA comes closer to experiment than the other codes.

### IV. IMPROVEMENTS DURING 1993

Several valuable improvements were made this year to the STA and MIX codes.

#### *In STA:*

(i) We introduced an approximation to configuration interaction, which greatly improves the calculations of intensities, specially for light atoms [27.4]. In a relativistic framework, configuration interaction is the way to depart from pure  $jj$  coupling. For low  $Z$  atoms,  $jj$  coupling is not a good approximation, so configuration interaction is important. Now results for low  $Z$  atoms agree well with experimental spectra.

(ii) The treatment of orbital relaxation was improved. Now the potentials for the upper SC, as well as for the lower SC are optimized separately. This gives better transition energies.

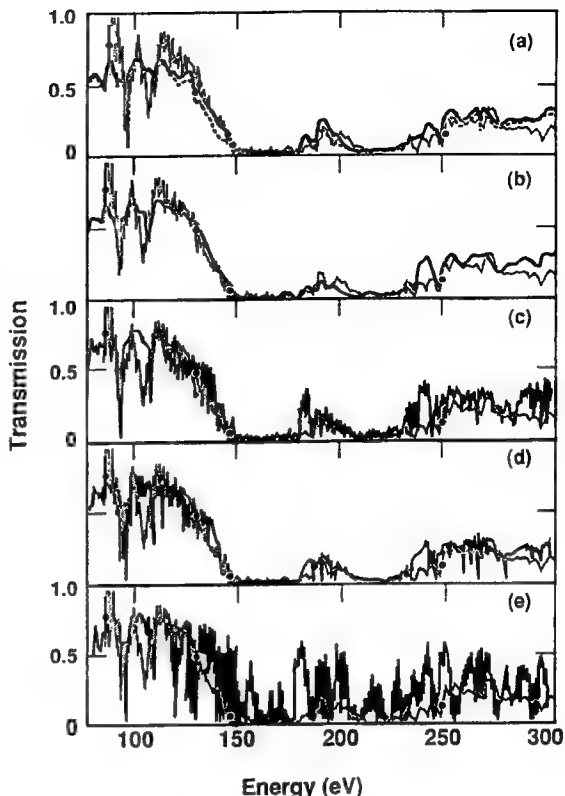


Fig. 27.2 — Experimental transmission data (gray line) for an Fe+NaF plasma compared with: (a) STA code for temperatures of 59 eV (solid line) and 57 eV (dotted line). (b) Monte Carlo with UTA (MCUTA) model, (c) OPAL with DTA, (d) OPAL with UTA, (e) OPAL with DCA model. Figure reproduced from ref. [27.11].

(iii) The way scattering is computed was improved by including correlation effects due to exchange and Coulomb interaction [27.12]. On the other hand, the effect of pair creation [27.13] was taken off, because it was felt that our plasma conditions will never give LTE at temperatures above 25 keV.

(iv) The numerical problems associated with low temperatures were solved. These problems were related to  $(E/kT)$ —where  $E$  is the energy of a configuration,  $kT$  is the Temperature in eV—being so large that there was a overflow/underflow in the exponential of the Boltzman factor. The problems did not exist on Cray supercomputers. They started appearing when we used DEC Alpha workstations, because the latter use less bits to hold the exponents. We had to factor out some exponents, and modify some algorithms.

(v) A new algorithm was introduced to compute the line shapes by the Voigt profile, improving significantly the stability and the accuracy, especially when the far wings of the lines contribute to the opacity—i.e. low  $Z$  with few lines. Before that, an isolated strong line could give negative contributions to the opacities.

*In MIX:*

A new algorithm was introduced to compute the partial pressure, or effective densities, of elements in a mixture. Instead of recomputing the Thomas Fermi equation for each temperature and density, we now use tables of chemical potentials as functions of density generated by the STA code, and inverse spline interpolation. Consequently, runs that took more than a hour now take only a few minutes, and the results are improved with respect to pure Saha Boltzman.

The computational scheme that we use is a little different than that in use in most other laboratories. Usually, the spectral opacities are computed on a photon energy range up to 20 or 30 times the temperature, on the justification that the weight function in the Rosseland and Planck means becomes very small above these energies. However, this can lead to missing some important features in case on a strong temperature gradient—i.e. high energy photons incident on a cold plasma cell. Also, it does not allow for enhancing resolution of special features. Consequently, we compute the spectra, at all temperatures on several fixed ranges, e.g.:  $0 \leq h\nu \leq 350\text{eV}$ ,  $0 \leq h\nu \leq 750\text{eV}$ ,  $0 \leq h\nu \leq 3000\text{eV}$  and  $0 \leq h\nu \leq 25000\text{eV}$ . This is one reason why we ran into numerical problems in STA, for low temperatures.

MIX was modified to accommodate any number of such spectral ranges.

## V. COMPUTATIONS PERFORMED

Databases were generated with the corrected versions of the programs, and on different spectra for the following elements: H, He, Be, C, Na, Al, Cl. In addition, some opacities for given temperatures and densities were calcu-

lated on a variety of rare earth elements like Samarium and Thullium. The aim here is the optimization of a backlighter source and a possible weak soft X-ray flash source near the target, for a moderate preheating.

## VI. CONCLUSION

The Nike Theory program is equipped with the most up to date and reliable codes for LTE opacities. These codes are in constant improvement and optimization. They are now well adapted to low and medium  $Z$  atoms that are of interest to Nike. A number of databases has been generated for many elements. Work is in progress to compute more databases, and to investigate the possibility of including non LTE effects in the codes.

## REFERENCES

- 27.1 A. Bar-Shalom, J. Oreg, W. H. Goldstein, D. Shvarts and A. Zigler, *Phys. Rev. A*, **40**, 3183(1989).
- 27.2 A. Bar-Shalom, W. H. Goldstein and J. Oreg, *IV<sup>th</sup> International Workshop on Radiative Properties of Hot Dense Matter*, (Sarasota, Fla, 1990) Ed. W. H. Goldstein, C. Hooper and R. Lee, World Scientific (1991) .
- 27.3 A. Bar-Shalom, J. Oreg and W. H. Goldstein, *Topical Conf. Atomic Processes in Plasmas*, (Portland, Maine, 1991) Ed. E. S. Marmar and J. L. Terry, AIP Conference Proceedings Nr.275 (1992) .
- 27.4 A. Bar-Shalom, J. Oreg and W. H. Goldstein, *J. Quant. Spectr. Radiat. Trans.*, **51**, 27(1994).
- 27.5 J. Bauche, C. Bauche-Arnoult and M. Klapisch, *Advance At. Mol. Phys.*, **23**, 131(1987).
- 27.6 M. Klapisch, *Comput. Phys. Comm.*, **2**, 239(1971).
- 27.7 M. Klapisch, J. L. Schwob, B. S. Fraenkel and J. Oreg, *J. Opt. Soc. Am.*, **67**, 148(1977).
- 27.8 D. Liberman, *Physical Review B*, **20**, 4981 (1979).
- 27.9 D. Liberman, *J. Quant. Spectr. Radiat. Trans.*, **27**, 335(1982).

27.10 M. Klapisch, *Thesis*, University of Paris, France (1969).

27.11 P. T. Springer, D. J. Fields, B. G. Wilson, J. K. Nash, W. H. Goldstein, C. A. Iglesias, F. J. Rogers, J. K. Swenson, M. H. Chen, A. Bar-Shalom and R. E. Stewart, *Phys. Rev. Lett.*, **69**, 3735(1992).

27.12 D. B. Boercker, *Astroph. J.*, **316**, L9-5(1987).

27.13 D. H. Sampson, *Astroph. J.*, **129**, 734(1959).

## Section 28

### RADIATIVE PREHEAT IN STRONGLY COUPLED, LASER ACCELERATED PLASMAS

J.L. Giuliani, Jr.

*Radiation Hydrodynamics Branch  
Plasma Physics Division  
Naval Research Laboratory*

#### ABSTRACT

A one-dimensional radiation hydrodynamics code is employed to model the interaction of the Nike KrF laser with a planar CH target. Three cases are compared to demonstrate the effects of radiative preheat: (a) the hydrodynamics of the laser target interaction with a high density equation-of-state (EOS) but without radiation; (b) the inclusion of radiation production and transport using collisional radiative equilibrium for the ionization dynamics; and (c) the addition of an approximate model for the pressure ionization and continuum lowering in the ionization dynamics. These last aspects are shown to significantly affect the results due to the strongly coupled plasma state of the compressed, accelerated target. As one moves from case (a) to (c) the density gradient near the ablation front is substantially reduced, implying a decrease in the Rayleigh-Taylor instability growth rates, but at the consequence of a hot and broad accelerating target. Furthermore, the photon spectra emerging from the rearside of the target is shifted in case (c) as compared to (b) toward higher energies and away from the absorption peak of neutral DT fuel.

#### INTRODUCTION

Control of the Rayleigh-Taylor instability in ablatively driven laser targets is one of the primary challenges in achieving high gain, direct drive laser fusion. One potential mechanism for inhibiting the instability is the deposition of high energy plasma radiation at the ablation

front in order to heat and thereby alter the density profile. A moderate atomic number material doped into the plastic target will, when heated in the corona, produce the penetrating x-rays absorbed by the dense layer. The ablative Rayleigh-Taylor formula for the growth rate  $\gamma$  is often written as<sup>28,1</sup>

$$\frac{\gamma}{\sqrt{kg}} = 0.9 \sqrt{\frac{\Delta}{k + \Delta}} - 3 \sqrt{\frac{k}{g}} \frac{\dot{m}}{\rho_{abl}}, \quad (28.1)$$

where  $k$  is the unstable wavenumber,  $g$  is the effective acceleration,  $\rho_{abl}$  is the density at the ablation surface,  $\Delta = |\nabla/\rho/\rho|_{abl}$ , and  $\dot{m}$  is the ablative mass flux. Stabilization might be achieved if the density as well as its gradient can be reduced at the ablation front by radiative preheat.

The choice of which dopant and how much to add to the target is central to this proposed solution for damping hydrodynamic instabilities. Due to the large range of possibilities, numerical simulations offer a viable means of discrimination. However, there are important physical issues which need to be considered in order to make a proper assessment. (a) Due to the high sound speed and electron degeneracy pressure of solids a realistic equation-of-state (EOS) is required. (b) The large range in density and temperature from the emitting corona to the absorbing target suggests the use of non-LTE ionization dynamics and radiative transfer rather than diffusion. (c) In high density regions such as the compressed, accelerating target, the

plasma can become strongly coupled. The importance of this last effect is typically estimated through the plasma coupling parameter:

$$\Gamma = \frac{\bar{Z}^2 e^2}{k_B T R_{IS}} \sim 5 \frac{\bar{Z}^2}{T_{eV}} \left( \frac{n_i}{10^{22} \text{ cm}^{-3}} \right)^{1/3}, \quad (28.2)$$

where  $e$  is the electron charge,  $k_B$  is Boltzmann's constant,  $T$  is the temperature,  $R_{IS}$  is the ion sphere radius for the ion density  $n_i$ , and  $\bar{Z}$  is the mean charge state. For  $\Gamma \geq 1$  the plasma ionization, radiation, and opacity can be altered, which in turn will alter the plasma dynamics. Furthermore, the spectrum of the radiation penetrating to the fuel may be affected and this is relevant to unwanted fuel preheat.

As part of a program to assess the radiative preheat effects NRL has been developing a one-dimensional Lagrangian radiation hydrodynamics code which includes the above physical processes for a range of materials. In the present report we will compare the density evolution of the target as the complexity of the model employed is increased in three stages: (a) a high density EOS, (b) plus a collisional-radiative equilibrium (CRE) ionization dynamics and probabilistic radiative transfer, (c) plus strongly coupled plasma effects. In each case the planar target is  $60 \mu\text{m}$  thick and composed of 50% carbon and 50% hydrogen. The incident laser corresponds to the KrF Nike laser system with  $0.264 \mu\text{m}$  light and an early version of the incident pulse as displayed in Fig. 28.1. The particular choice of the dopant material and model improvements will be addressed in future work.

#### CASE (A): HIGH DENSITY EOS

Let us first consider the target evolution when a high density EOS is coupled with the hydrodynamics, but radiative losses are neglected. The EOS consists of a Cowan ion model using the Debye and melt temperatures, the Thomas-Fermi electron cloud with  $Z$ -scaling for arbitrary compositions, and a Barnes correction to obtain the proper pressure during initial compression from the cold solid.<sup>28.2</sup> The thermal conductivity for the dense plasma includes

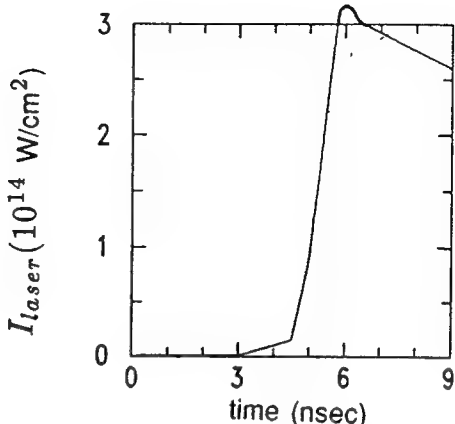


Fig. 28.1 — Profile of incident laser pulse used in the modeling.

electron degeneracy and corrections to the Coulomb logarithm according to Lee and More.<sup>28.3</sup>

Figure 28.2 shows the evolution of the density profile with the characteristic highly compressed, rearward accelerating region behind the ablation front. The steep density profile leading to the ablation front at peak density is highly Rayleigh-Taylor unstable.

#### CASE (B): IONIZATION-DYNAMICS AND RADIATION

The CRE model for the atomic populations uses rates for collisional and photoionization, 3-body, dielectronic, and radiative recombination, collisional excitation and photo-pumping, collisional de-excitation and radiative decay, and inner shell photo-absorption.<sup>28.4</sup> The detailed configuration accounting includes the stripped state for C and H, the ten principal quantum levels for H, six ground states and 48 excited levels for C. A probability-of-escape formalism is used for the bound-bound and bound-free radiation transport,<sup>28.5</sup> and a multi-frequency approach for the free-free radiation. Detailed comparisons of the EOS and CRE calculations established a demarcation line in the  $\rho$ - $T$  plane across which a smooth transition from the EOS charge state and pressure to the CRE values can be maintained.

The evolution of the density profile in Fig. 28.3 shows in comparison with case (a) a significant reduction in  $\rho$  and  $|\nabla\rho|$  at the ablation front, and an increase in the separation between

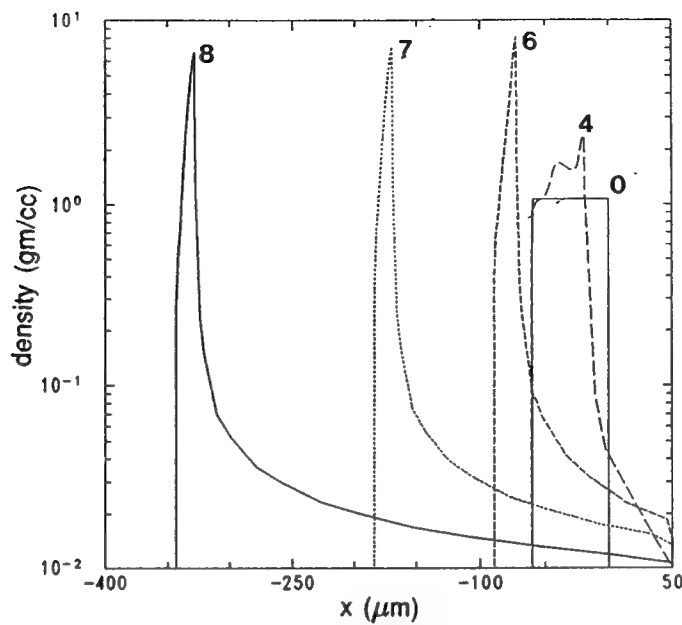


Fig. 28.2 — Evolution of the mass density at the listed times in nsec for case (a) of a high density EOS only. The incident laser enters from the right.

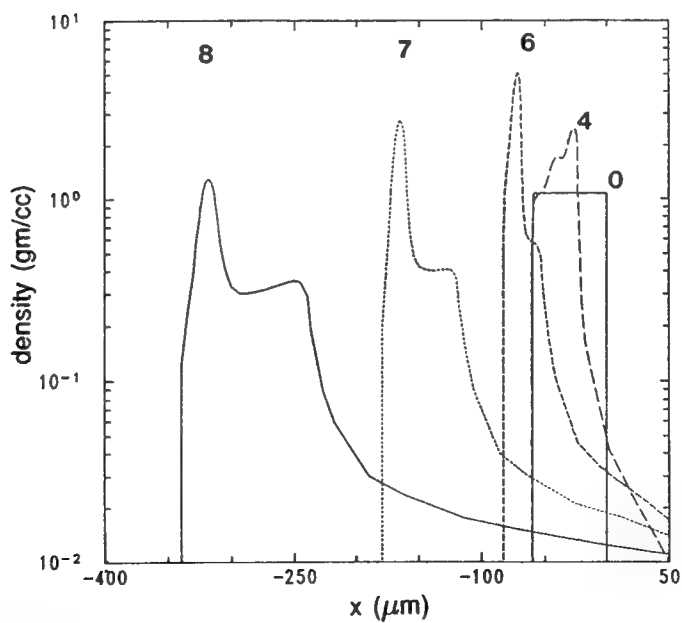


Fig. 28.3 — Evolution of the mass density at the listed times for case (b) with an EOS, CRE ionization dynamics, and radiation transfer.

the critical surface and the ablation front. The critical surface occurs roughly at the density 0.3 gm/cm<sup>3</sup>. In the present case,  $|\nabla\rho/\rho|_{abl}$  is reduced between 5 and 10, and by eqn. 28.1, the critical wavelength for instability would move to larger values. However, calculating  $\Gamma$  from eqn. 28.2 at the ablation surface shows that it is over 10 at the peak of the laser pulse, and remains above 2 even as late as 8 nsec. This suggests that strong coupling effects should be taken into account and we turn to this model next.

### CASE (C): STRONG COUPLING IN LASER PLASMAS

High density effects on plasma ionization dynamics have been an active area of research for several decades, yet a practical theory applicable in hydrodynamic simulations is still under development. The model we employ is based upon the work of Hummer and Mihalas.<sup>28,6</sup> The decrease in the population of a particular atomic level is accounted for smoothly and in a thermodynamically consistent manner through a reduction in the effective statistical weight  $g'_{nl}$  of that level. Pressure ionization is treated as an excluded volume correction through

$$g'_{nl} = g_{nl} \exp \{ -\mathcal{F}[r_{orb}(n)/R_{IS}]^3 \},$$

where  $r_{orb}(n)$  is the bound electron orbital radius for the level with principal quantum number  $n$  and  $\mathcal{F}$  is the fraction of neutral atoms. The microfield perturbations to the  $nl$  level of an ion of charge state  $Z_i$  is assumed to follow a Holtsmark distribution resulting in the further reduction

$$g''_{nl} = g'_{nl} \exp \left\{ -16 \left[ \frac{\sqrt{(Z_i + 1)e^2}}{\chi_{nl} R_{IS}} \right]^3 \frac{1}{Z_i^{3/2}} \right\},$$

where  $\chi_{nl}$  is the ionization potential of the level. To account for the electron screening in strongly coupled plasmas we include a continuum

energy lowering term which transitions from the Debye-Hückel to the ion-sphere forms:

$$\Delta E_{low} = \frac{\bar{Z}e^2}{\max\{2R_{IS}/3, R_{DH}\bar{Z}/(Z_i + 1)\}},$$

where  $R_{DH}$  is the Debye-Hückel radius.

Besides changing the effective statistical weight of a level one must also reduce the atomic physics rates to ensure that the proper equilibrium is attained at high densities. We follow the procedure of Busquet.<sup>28,7</sup>

The density evolution for the full model is shown in Fig. 28.4. The most surprising feature is the deterioration of the dense slab near the rear of the accelerating target and the consequent broad density profile. The strong coupling has reduced the allowed population in so many levels that the internal energy can no longer act as a heat sink. As a result, the rearside temperature and charge state are highest in case (c).

Another interesting feature is the radiation spectrum passing through the rearside of the target near peak laser intensity for cases (b) and (c) shown in Fig. 28.5. Note the stair-step feature of the emitted bound-free continuum radiation in case (b) reduces to fewer stairs when the strong coupling effects are included. Furthermore, the mean photon energy is smaller for case (b). This difference in the spectrum is significant for heating of the fuel. The fraction of the DT fuel which is neutral will be most opaque to  $\sim 15$  eV photons and the absorption cross-section decreases as the energy cubed above the threshold. In the present model, the inclusion of strong coupling effects drastically reduces the rearside spectrum in the 10 to 100 eV range and implies a reduction in the photo-absorption heating of the fuel.

### DISCUSSION

Comparison of Figs. 28.2, 28.3, and 28.4 demonstrate substantial changes in the target density as the complexity of the simulation is progressively increased. Case (b) indicates the importance of radiation even for targets composed of low atomic number material such

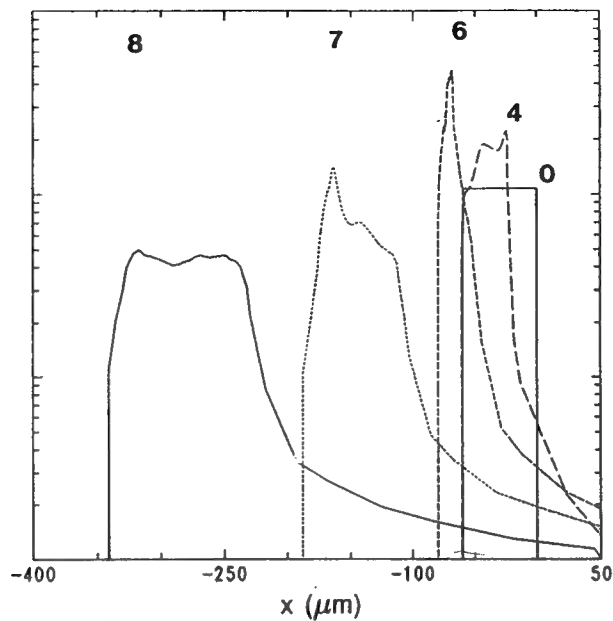


Fig. 28.4—Evolution of the mass density at the listed times for case (c) with the additional physics of strong coupling. Note the decrease in peak density and broadening of the density profile for the accelerated target in going from Figs. 28.2 to 28.4.

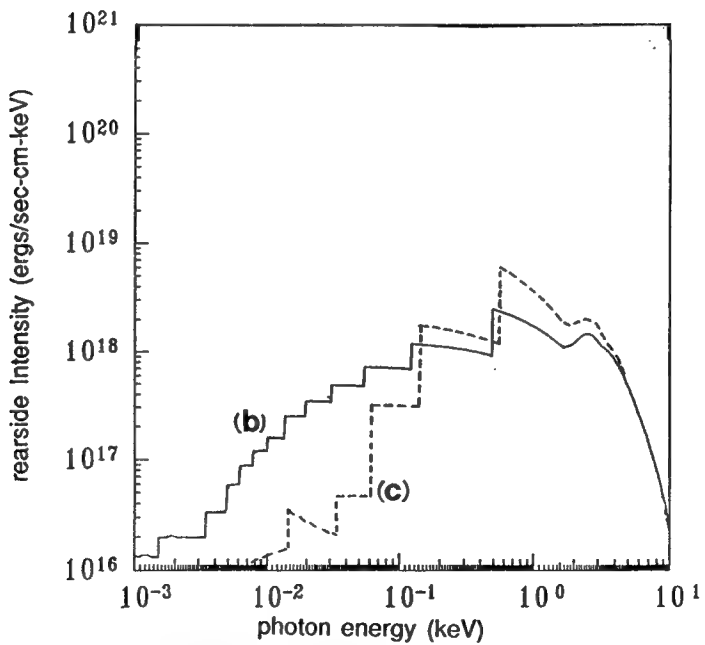


Fig. 28.5—The rearside time integrated radiation spectrum for cases (b) and (c) indicating depletion of photon energy in the 1 to 100 eV range due to strong coupling effects.

as carbon. This conclusion agrees with Duston, *et al.*,<sup>28.8</sup> who studied the problem with lower laser intensities and longer wavelengths. The role intended for doping by moderate Z-material appears already to be fulfilled by carbon in typical plastics. In case (c) the high density effects of pressure ionization, microfield perturbations, and continuum lowering, on atomic processes further accentuates the decrease in  $\rho_{abl}$  and the broadening of the density profile. The present results of including detailed non-LTE radiation and strong coupling effects suggest an inhibition of the ablative Rayleigh-Taylor instability in the accelerating target according to eqn. 28.1.

Furthermore, reduction of ions in excited states due to high densities shifts the backside spectrum toward higher photon energies and away from the strong absorption peak of neutral DT fuel. However, these potentially positive conclusions are offset by the extreme deterioration from a dense, cold, accelerated target [case (a)] to a more diffuse and hot one [case (c)].

Future work will need to concentrate on improving the microfield distribution to account for large  $\Gamma$ 's and allow for frequency shifts due to continuum lowering toward the red end in the bound-free emission. This last aspect, only feasible within a complete multi-frequency radiation transport, may alter some of the

present conclusions on the density profile and fuel preheat.

## ACKNOWLEDGMENT

This work was performed in collaboration with M. Mulbrannon and J. Davis, both of the Radiation Hydrodynamics Branch, Plasma Physics Division, Naval Research Laboratory.

## REFERENCES

- 28.1 J.H. Gardner, S.E. Bodner, & J.P. Dahlburg, *Phys. Fluids B*, **3**, 1070 (1991); and references therein.
- 28.2 R.M. More, K.H. Warren, D.A. Young, & G.B. Zimmerman, *Phys. Fluids*, **31**, 3059 (1988).
- 28.3 Y.T. Lee & R.M. More, *Phys. Fluids*, **27**, 1273 (1984).
- 28.4 D. Duston, R.W. Clark, J. Davis, & J.P. Apruzese, *Phys. Rev. A*, **27**, 1441 (1983).
- 28.5 J.P. Apruzese, *J. Quant. Spectrosc. Radiat. Transfer*, **34**, 447 (1985).
- 28.6 D.G. Hummer & D. Mihalas, *Astrophys. J.*, **331**, 794 (1988).
- 28.7 M. Busquet, *J. Quant. Spectrosc. Radiat. Transfer*, **43**, 91 (1990).
- 28.8 D. Duston, R.W. Clark, & J. Davis, *Phys. Rev. A*, **31**, 3220 (1985).

## Section 29

### START-UP IMPRINTING AND SHOCK DYNAMICS

Mark H. Emery

*Laboratory for Computational Physics and Fluid Dynamics  
Naval Research Laboratory  
Washington, D.C.*

#### I. INTRODUCTION

A high degree of ablation pressure uniformity is a necessary criterion for the success of laser-driven inertial confinement fusion. The ability of the recently developed random phase plate (RPP),<sup>29.1</sup> smoothing by spectral dispersion (SSD),<sup>29.2</sup> and induced spatial incoherence (ISI)<sup>29.3</sup> laser smoothing techniques to produce a nearly uniform ablation pressure is strongly contingent on the degree of thermal smoothing in the ablating plasma.<sup>29.3,29.4</sup> The SSD and ISI techniques benefit from temporal smoothing as a result of the broadband nature of the laser light but residual nonuniformities persist with all three methods.

The ability of the ISI concept to produce a smooth ablation pressure is based on a combination of (1) temporal smoothing (over 100's of coherence times) and (2) transverse thermal transport. Thermal diffusion in the pellet corona is necessary to smooth out the residual laser nonuniformities. For example, averaging over a thousand coherence times only reduces the laser flux nonuniformities by  $\sim\sqrt{1000}$ , to  $\sim 3\%$ . The thermal smoothing reduces the nonuniformities below 1%. This thermal smoothing is effective only if  $kd > 1$ , where "d" is the distance between the absorption surface and the ablation surface, and "k" is the wave number of the transverse disturbance. However at the beginning of the laser pulse the pellet is a solid, with no corona, and "d"  $\sim 0$ . It takes a few nanoseconds after the foot of the laser pulse turns on, for the plasma corona size "d" to grow large enough and become warm enough to

smooth out the laser nonuniformities. We therefore carried out an investigation of ISI during the initiation and foot of the laser pulse, when thermal smoothing is minimal.

We found that this early time behavior, which we called "start-up imprinting" can be very damaging unless the laser beam is extremely smooth. A laser nonuniformity of even a few percent produces an imprint that can grow linearly by a order of magnitude or more, depending on the target thickness, as a result of the Richtmyer-Meshkov instability before the target begins the rapid acceleration phase.<sup>29.4</sup> For a target to implode uniformly, the mass variations at this point in time must be  $\ll 1\%$ .

We present the results from a series of numerical simulations using the FAST2D Laser Matter Interaction Model. We investigate the impact of a shaped, reactor-like, ISI-smoothed laser beam on thick (hundreds of microns), solid DT and layered DT targets, and 60  $\mu\text{m}$  thick CH targets.

#### II. RESULTS

For most of the results presented here, we modeled the laser profile with a  $20 \times 20$  echelon array with an effective laser spot size  $d_{00} = 320 \mu\text{m}$  and a laser coherence time  $t_c = 1 \text{ psec}$ . The laser wavelength is  $0.264 \mu\text{m}$ . This corresponds to a lens with an  $F_{\text{number}} = 32$ . The laser spot is flat over the distance  $d_{00}$ . The transverse dimension is  $160 \mu\text{m}$ , represented by 80 zones, and there are 120 zones in the longitudinal direction. The ISI mode spectrum ranges between  $8 \mu\text{m}$  and  $160 \mu\text{m}$ . This compares

favorably with the envisioned reactor-like parameters:  $F_{\text{number}} \approx 30$ ,  $d_{00} = 600 \mu\text{m}$  and a  $60 \times 60$  echelon array. These conditions produce an ISI spectrum ranging between  $5 \mu\text{m}$  and  $300 \mu\text{m}$ . For the case presented here, the residual ISI nonuniformities were quite large:  $\sigma_{\text{RMS}} = 0.037$  with a maximum amplitude variation of  $\pm 8.6\%$ , which is characteristic of a single ISI laser beam.

These residual structures can be reduced in magnitude by lateral thermal smoothing as long as the distance between the ablation region and

the laser absorption region is larger than the scalelengths of the residual laser asymmetries. To test this hypothesis, we generated a moderately long scalelength plasma with a "perfect" laser beam before impacting the target with an ISI-smoothed laser beam. The temporal pulse shape is shown in Fig. 29.1a. The laser light is spatially uniform until 6 nsec, at which time the ISI spectrum is "turned on." Nearly all of the laser energy is absorbed between the 1/4 critical density ( $15 \mu\text{m}$  from the target surface) and critical density ( $1 \mu\text{m}$  from the target surface)

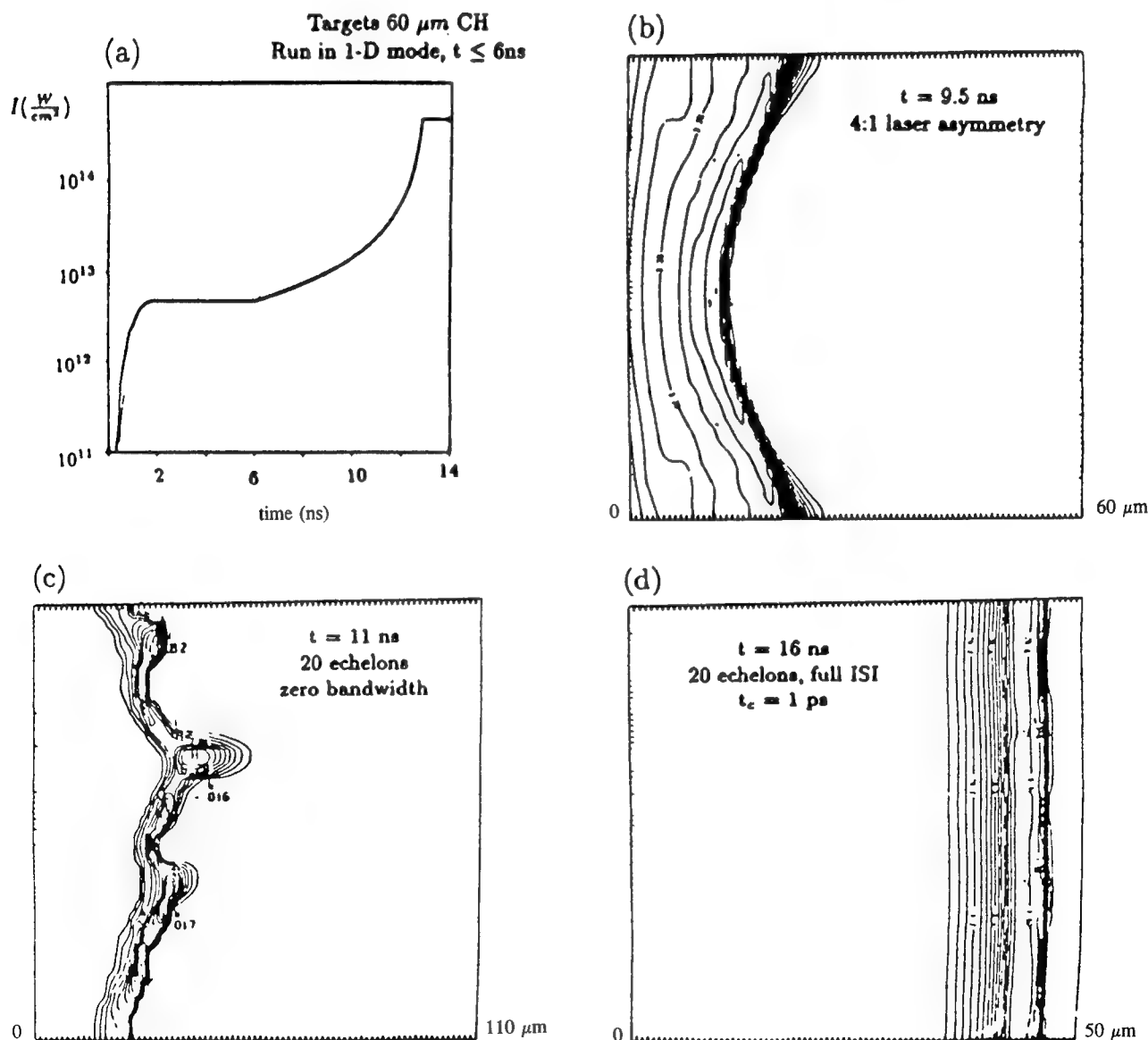


Fig. 29.1 — (a) Canonical power law laser profile. Isodensity contours responding to (b) 4:1 laser asymmetry, (c) RPP laser pulse, and (d) ISI laser pulse.

surfaces. Figure 29.1d shows the isodensity contours of an 80  $\mu m$  thick CH target at 16 nsec. The target is quite uniform well into the rapid acceleration phase. The mass perturbation at 16 nsec is  $\Delta m/m \approx 0.2\%$ . This density profile is to be contrasted with the case of a "frozen-in" 4:1 sinusoidal laser asymmetry shown in Fig. 29.1b at 9.5 nsec. The initial conditions are the same as the ISI case. A similar result is obtained with an ISI-like beam with zero bandwidth, a rough approximation to an RPP. In this case, at 6 nsec, the uniform laser profile shifts to a "frozen-in" ISI-profile. The target density contours are shown in Fig. 29.1c at 11 nsec.

Transverse thermal conduction is difficult to achieve with a reactor-like shaped laser pulse because of the long, low intensity "foot" prior to the main driving beam. The isodensity con-

tours for a 330  $\mu m$  thick frozen DT target illuminated with a shaped ISI laser beam is shown in Fig. 29.2 at 12 nsec. At this time the target mass variation  $\Delta(\rho r)/\langle \rho r \rangle$  is 22%. Early in the laser pulse, the laser energy is deposited directly onto the target surface. The highly nonuniform nature of the ISI beam results in spatially and temporally nonuniform shocks traversing the target. The target surface, itself, is perturbed and as the shock passes through the target it leaves residual mass perturbations in its wake. These residual variations grow linearly in time, in a Richtmyer-Meshkov-like manner, as the target drifts with a nearly constant velocity.

Several target designs were investigated in an attempt to mitigate the impact of the initial nonuniform shock structure. In one case, a 180  $\mu m$  thick solid DT target with a 100  $\mu m$

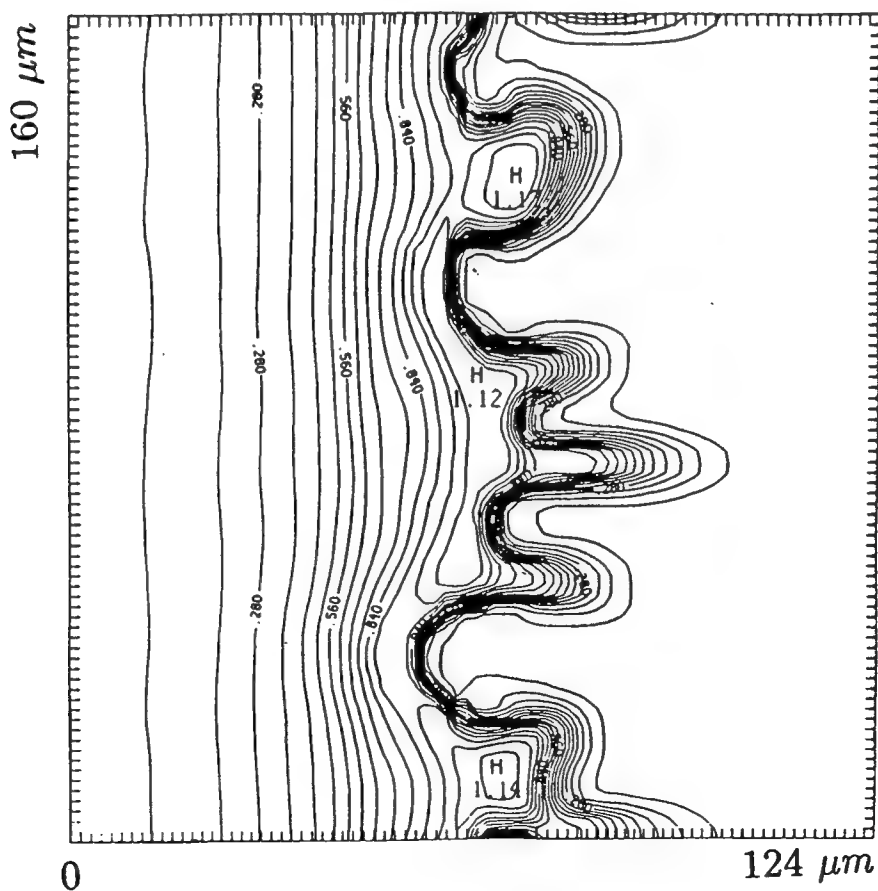


Fig. 29.2 — Isodensity contours at 12 nsec for 300  $\mu m$  DT target illuminated with ISI laser beam.

thick low density ( $0.08 \text{ gm/cm}^3$ ) DT layer was used. This layer reduces the perturbation on the shock front to some degree before the shock impacts the frozen DT target. The mass variation at 15 nsec is 21%.

In order to model layered, dissimilar materials, we incorporated a volume fraction method into the FAST2D Model. Figure 29.3 is an  $x - t$  diagram, isodensity contours of each material (spatially separated for visual clarity), illustrating the shock structure stemming from a typical power law laser pulse impacting a layered target of  $200 \mu\text{m}$  frozen DT ( $0.201 \text{ gm/cm}^3$ ),  $30 \mu\text{m}$  CH ( $1.04 \text{ gm/cm}^3$ ) and  $100 \mu\text{m}$  DT foam ( $0.08 \text{ gm/cm}^3$ ). The initial shock strikes the foam-CH interface at 5 nsec, sending a transmitted shock through the CH and a reflected shock back through the foam. The re-

flected shock strikes the free surface of the foam sending a rarefaction through the foam at about the same time (7 nsec) the transmitted shock strikes the CH-DT interface, sending a transmitted shock through the DT fuel and a rarefaction back through the CH. These rarefactions decompress the target by about a factor of two. The rarefaction strikes the CH-foam interface (10 nsec) sending another shock through the CH and subsequently through the DT fuel (12 nsec). The combination of the foam-CH layers eliminates most of the short wavelength mode structure stemming from the ISI beam and diminishes the mass perturbation,  $\Delta(\rho r)/\langle \rho r \rangle = 17\%$  at the peak of the laser pulse (15 nsec). This perturbation level is reduced to 9% by tailoring the laser pulse to rise somewhat more rapidly to eliminate the effect of the rarefaction.

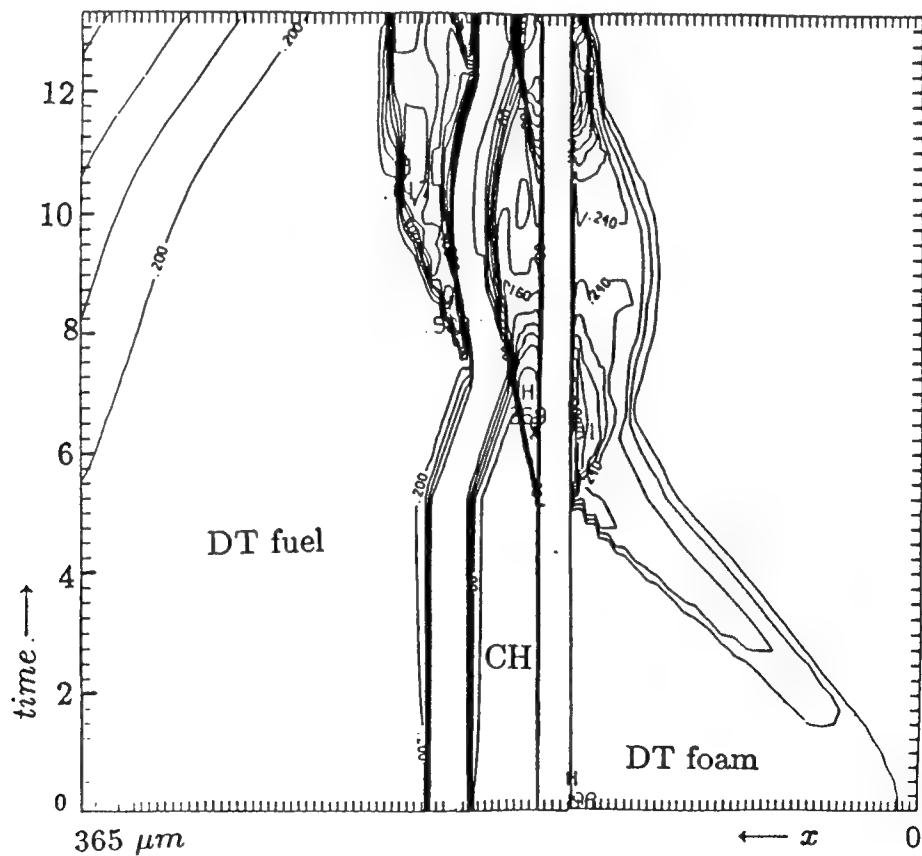


Fig. 29.3 —  $x - t$  diagram, resulting from 1d averaged isodensity contours in the center-of-mass frame, showing shock evolution in layered target.

The ablation to absorption distance can be increased by using longer wavelength laser light which would also result in an increase in the amount of thermal smoothing. However, longer wavelength laser light implies poorer laser-target coupling and reduced efficiency.<sup>29,5</sup> By combining long wavelength laser light at the beginning of the pulse with short wavelength laser light during the compression and acceleration phases, thermal smoothing would be enhanced during the early phase of the pulse and laser-target coupling would be enhanced during the acceleration phase. Using the same multi-layer target discussed above, the first 8 nsec of the laser beam is modeled as  $1.054 \mu\text{m}$  ISI laser light ( $t_c = 1 \text{ psec}$ ) which then smoothly evolves, over 1.5 nsec, to  $0.264 \mu\text{m}$  ISI laser light ( $t_c = 1 \text{ psec}$ ) for the rest of the laser pulse. At 15 nsec,  $\Delta(\rho r)/\langle \rho r \rangle = 4\%$ . The perturbation amplitude at this time includes  $\approx 1.5$  e-foldings of RT growth. At 12 nsec,  $\Delta(\rho r)/\langle \rho r \rangle = 0.9\%$ . Modeling the first 8 nsec of the  $1.054 \mu\text{m}$  beam as being perfectly uniform results in a mass variation of only 1.8% at 15 nsec (0.4% at 12 nsec). These perturbation levels are still too large to enable the target to implode uniformly.

A uniform blowoff plasma could be generated by coating the target with a thin ( $O(\text{few } 100 \text{ \AA})$ ) high-Z material and striking the target with a very short burst of X rays. We have approximated this interaction by depositing  $1/4 \text{ J}$  of energy directly onto the surface of a frozen DT target during a  $250 \text{ psec FWHM}$  pulse. The target is  $330 \mu\text{m}$  thick. This energy pulse produces a very weak shock,  $O(10\text{'s of kbar})$ , and at 10 nsec after the "x-ray flash," the density scalelength, at critical density for  $1/4 \mu\text{m}$  laser light, is  $\approx 100 \mu\text{m}$ . The target is then illuminated with a  $0.264 \mu\text{m}$  ISI - smoothed laser beam at a  $30^\circ$  angle of incidence (with respect to the normal). For this case, the laser pulse has a 5 nsec Gaussian rise to an intensity of  $10^{12} \text{ W/cm}^2$  which then evolves into a power law-pulse which peaks at  $3 \times 10^{14} \text{ W/cm}^2$  at 15 nsec. A plot of the rays incident at an angle of  $30^\circ$  at the peak of the laser pulse is shown in Fig. 29.4a. The turning point of the rays is just outside of the critical surface and the plasma continues to absorb energy from the rays until each ray contains  $< 1\%$  of its initial energy.

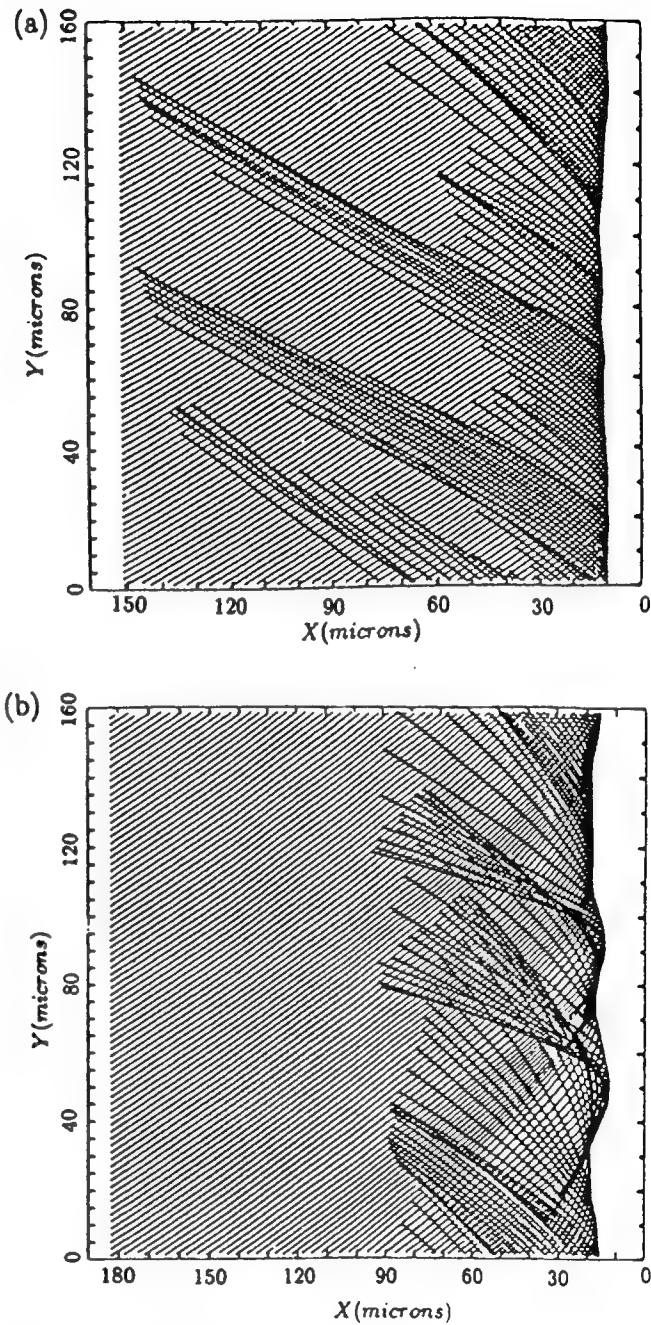


Fig. 29.4 — (a) Plot of the rays incident at an angle of  $30^\circ$  on a  $330 \mu\text{m}$  thick DT target at the peak of the laser pulse after the target was illuminated with an artificial "X-ray flash." (b) Plot of the rays at the same angle of incidence and at the same time as (a) but without the "X-ray flash." Note that there is some evidence for self-focusing.

The maximum mass variation of the target,  $\Delta(\rho r)/\langle \rho r \rangle$ , is 4.8% at 15 nsec. The mass perturbations are larger than the layered, multiple laser wavelength cases, but significantly smaller than the nonlayered, normal incident cases.

Figure 29.4b illustrates the rays at the same time and angle of incidence as above but without the initial "X-ray flash." Note that there appears to be some evidence for self-focusing.

The results of this series of calculations is summarized in Fig. 29.5 in the form of a histogram. The maximum mass perturbation level (in per cent) and the time at which perturbation level is measured are denoted as well as the target and laser pulse characteristics. These numerical results indicate that cold, low density foam layers, multiple wavelength lasers and initial X-ray flashes can significantly reduce the mass perturbation level stemming from the initial imprint of an ISI-smoothed laser beam. There is also experimental evidence that an initial X-ray flash can eliminate plasma jetting generated by the initial imprint of an ISI-smoothed laser.<sup>29,6</sup> The numerical results, however, indicate that the perturbation level at the beginning of the drive portion of the pulse (several percent) is still too large to enable the target to implode uniformly.

Since it is the first shock which is the culprit here, it may be possible to compress the target adiabatically—without any shocks except for the final drive portion of the pulse—and circumvent the problem. This would entail a very long, slowly rising laser pulse. A pulse of this shape would generate kilobar-like pressures in the target and thus compressive stress, shear stress, elastic response and plastic flow become important considerations. We have developed an elastic-plastic-hydrodynamic numerical model to account for these phenomena and now apply this model to the study of an ISI-smoothed laser pulse on targets similar to those envisioned for the initial set of experiments for the Nike Laser System.

For the first case, the ISI-smoothed laser pulse has the canonical power-law profile with a 1/2 nsec rise to  $10^{12} \text{ W/cm}^2$ , a  $t^{5/4}$  rise to  $3 \times 10^{14} \text{ W/cm}^2$  at 6 nsec, followed by a 3 nsec drive at this intensity. The target is 60  $\mu\text{m}$  of CH, and the laser wavelength is 1/4  $\mu\text{m}$  with a coherence time of 1 psec. The target mass

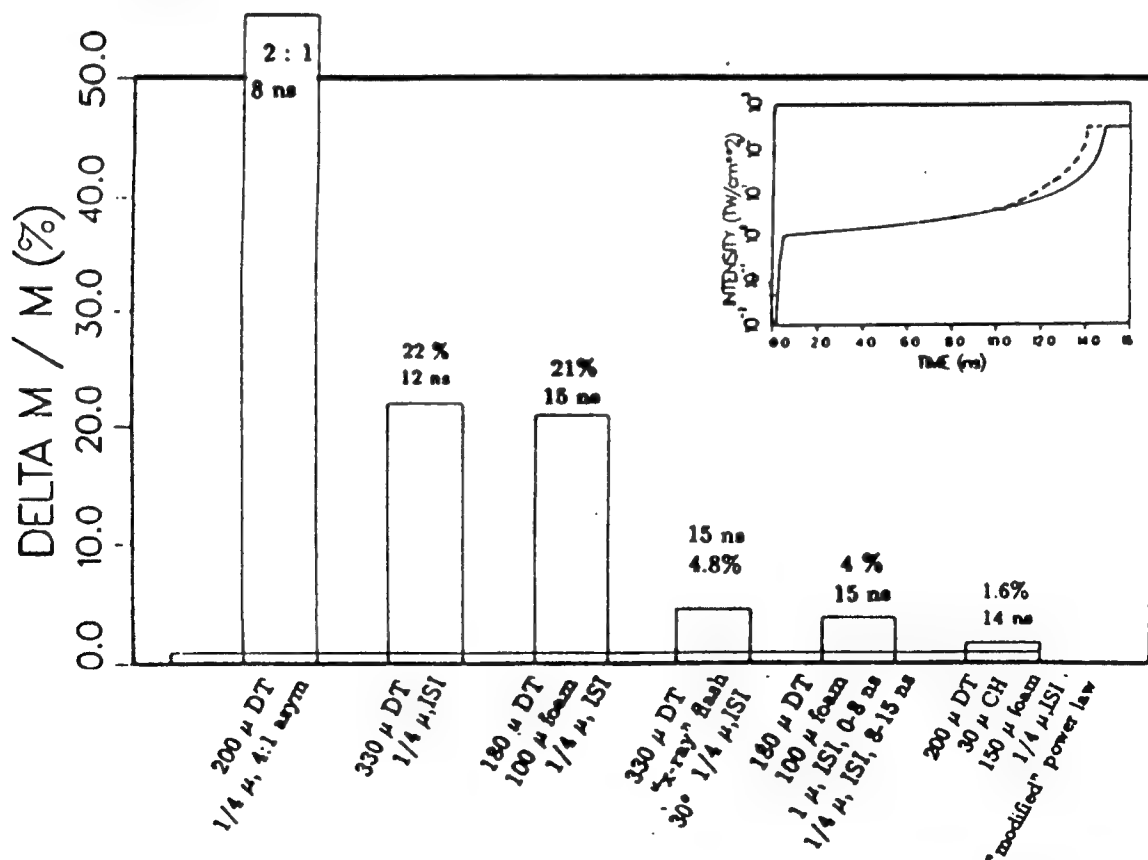


Fig. 29.5 — Histogram comparing the mass perturbation levels for various target designs and laser scenarios using a 15 nsec shaped ISI laser pulse. The dashed line illustrates the "modified" laser pulse.

variation at the beginning of the drive portion of the pulse (6 nsec) is 3.6%. This is comparable to the mass variation (3.8%) attained with the pure hydrodynamic version of the code under the same pulse shape conditions. This is to be expected as the first shock stemming from this laser pulse is  $O(1 \text{ Mbar})$  and the elasticity/plasticity of the material does not play a role. The target would soon fracture as a result of the RT instability with an initial mass perturbation of this magnitude. The total energy density of

the laser pulse (9 nsec) is  $970 \text{ kJ/cm}^2$  and the target velocity at 9 nsec is  $2.5 \times 10^7 \text{ cm/s}$ .

For the shock-free pulse, the laser intensity starts at  $10^7 \text{ W/cm}^2$  and increases very slowly reaching  $3 \times 10^{14} \text{ W/cm}^2$  at 28 nsec. See Fig. 29.6a. Shown in Fig. 29.6b is an  $x-t-\rho$  plot illustrating the target response. A small compression wave begins propagating through the target at  $\approx 20$  nsec; the total stress has reached an amplitude of  $\approx 20 \text{ kbar}$  at this time. The peak compressed density is  $8.2 \text{ gm/cm}^3$ .

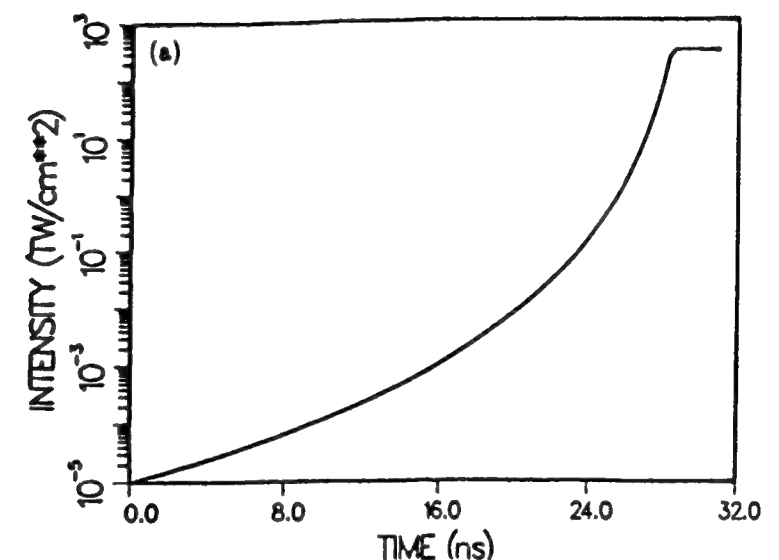
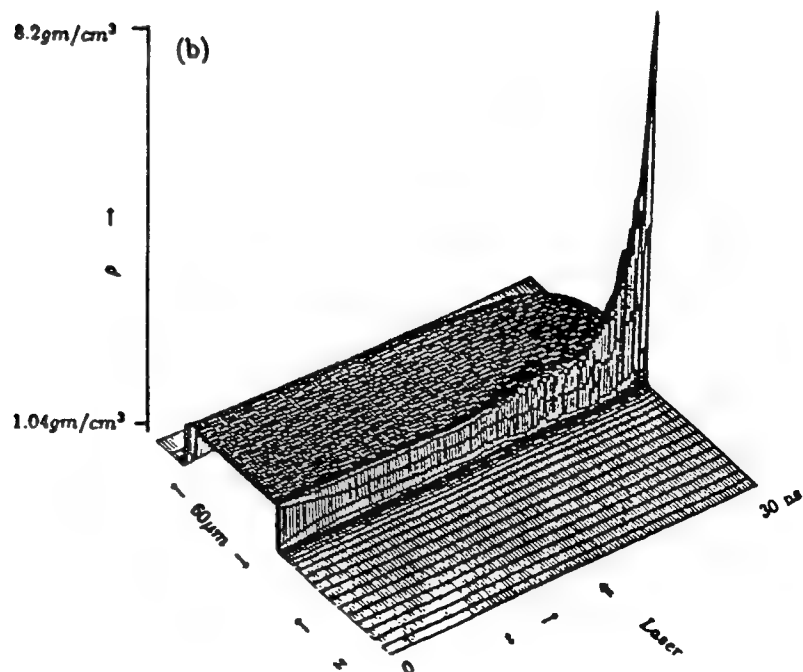


Fig. 29.6 — (a) Intensity profile for the temporally long, slowly rising laser pulse. (b)  $x-t-\rho$  plot for the  $60 \mu\text{m}$  thick plastic target (in the center-of-mass frame) for the slowly rising laser pulse.



which is 12% larger than for the 6 nsec pulse case. Figure 29.7 illustrates the target isodensity contours at 28 nsec the beginning of the drive portion of the pulse. The amplitude of the maximum density variation is only 0.5%. This is close to the requirement ( $O(0.1\%)$ ) for uniform implosion. Note that a portion of this growth, an e-folding or so, is due to RT growth as the target begins to rapidly accelerate at  $\approx 27$  nsec. For this case, the total energy density of the laser pulse (31 nsec) is 1200  $\text{kJ/cm}^2$  and the target velocity at 31 nsec is  $2 \times 10^7 \text{ cm/s}$ .

There are several reasons why the mass perturbation level for the shock-free case is reduced. The elastic wave speed depends only upon the material properties not on the stress loading and the CH relaxes back to its initial

state once the elastic compression wave has passed. Plastic flow does not begin until the elastic distortion energy exceeds the von Mises yield condition; i.e., stresses  $> 30 \text{ kbar}$ . At this time ( $t \approx 24 \text{ nsec}$ ), the laser intensity is in the mid  $10^{11} \text{ W/cm}^2$  range and the distance between the absorption region and the target surface " $d$ "  $> 7 \mu\text{m}$  which provides some thermal smoothing. The elastic wave is followed by a plastic wave which travels more slowly. When stress is released (at random times and positions, due to the ISI profile) an elastic tension wave is generated, which catches up to the plastic wave and reduces its amplitude. By the time the shock is generated,  $t \approx 26 \text{ nsec}$ , and " $d$ "  $> 15 \mu\text{m}$ , which leads to significant thermal smoothing.

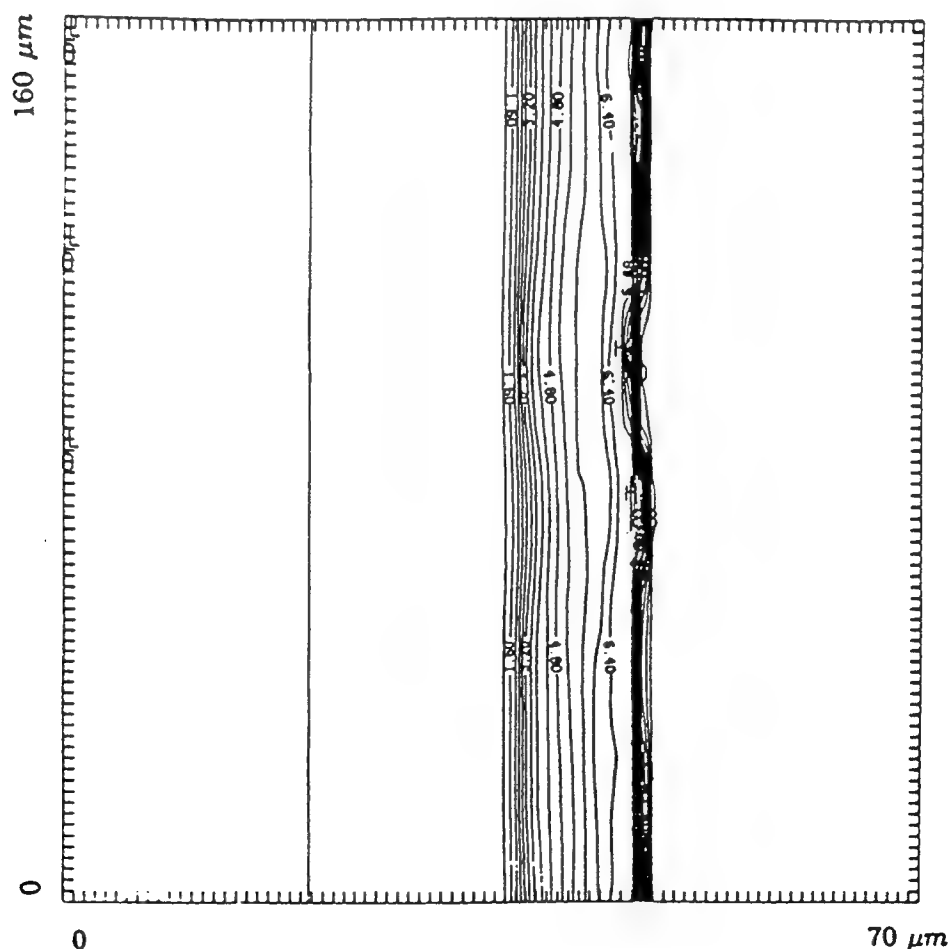


Fig. 29.7 — Isodensity contours of the  $60 \mu\text{m}$  thick CH target at 28 nsec impacted with the slowly rising laser pulse. The maximum mass variation at this time is 0.5%.

### III. SUMMARY AND CONCLUSIONS

In summary, we have shown that it is possible to influence the impact of the residual nonuniformities inherent in a nonperfect laser beam during the start-up phase. Cold, low density layers, multiple laser wavelengths, shallow angles of incidence, and thin high-Z ablators can all significantly reduce the perturbations stemming from an imperfect laser beam. The perturbation level may be minimized by eliminating the first shock in the laser pulse by designing a temporally long, slowly rising, truly adiabatic laser pulse. A small price is paid in laser energy and hydrodynamic efficiency, but the net result is that the perturbation level is reduced by nearly an order of magnitude below the level attained with the canonical power-law pulse or with other target designs.

However in all cases, a laser nonuniformity with an rms flux variation of 3.7% after 1000 coherence times produces an unacceptable imprinting on the target. We conclude that the laser quality needs to be much better. Note that all simulations modeled a single laser beam and, with the exception of one case, at normal incidence. The Nike system, with multiple overlapping beams at various angles of incidence, is designed to produce approximately 0.4% flux nonuniformity in this time interval, and other

calculations indicate that this degree of uniformity should suffice.

### ACKNOWLEDGMENTS

The author gratefully acknowledges fruitful discussions with J. Gardner, R. Lehmberg, and S. Obenschain.

### REFERENCES

- 29.1 Y. Kato, K. Mima, N. Miyanaga, S. Arinaga, Y. Kitagawa, M. Nakatsuka, and C. Yamanaka, *Phys. Rev. Lett.* **53**, 1057 (1984).
- 29.2 S. Skupsky, R. W. Short, T. Kessler, R. S. Craxton, S. Letzring, and J. M. Soures, *J. Appl. Phys.* **66**, 3456 (1989).
- 29.3 R. H. Lehmberg and S. P. Obenschain, *Opt. Commun.* **46**, 27 (1983); R. H. Lehmberg, A. J. Schmitt, and S. E. Bodner, *J. App. Phys.* **62**, 2680 (1987).
- 29.4 M. H. Emery, J. H. Gardner, R. H. Lehmberg, and S. P. Obenschain, *Phys. Fluids B* **3**, 2640 (1992).
- 29.5 J. H. Gardner, and S. E. Bodner, *Phys. Rev. Lett.* **47**, 1137 (1981).
- 29.6 M. Desselberger, T. Afshar-rad, F. Khattak, S. Viana, and O. Willi, *Phys. Rev. Lett.* **68**, 1539 (1992).

## Section 30

### RAD3D\_CM

David E. Fyfe

*Laboratory for Computational Physics and Fluid Dynamics  
Naval Research Laboratory  
Washington, DC*

#### ABSTRACT

*RAD3D\_CM*,<sup>30.1</sup> an efficient and accurate variable Eddington multigroup radiation transport hydrodynamics code, has been developed by members of the Laboratory for Computational Physics & Fluid Dynamics [LCP&FD] at NRL. This code, which runs in data parallel mode on the NRL CM-5, has been tested on a variety of nonlinear three-dimensional [3d] problems. In particular, we have performed the first series of well-resolved 3d multimode laser matter interaction [LMI] simulations of the time-dependent hydrodynamic behavior of a laser irradiated plastic [CH] target.<sup>30.2</sup> In these *RAD3D\_CM* simulations, the laser target is accelerated using the NRL Nike KrF Laser Facility prototype inertial confinement fusion [ICF] driver conditions<sup>30.2</sup> to relevant velocities and throw distances. Ablative Rayleigh-Taylor [RT] laser target simulations of these conditions, using *RAD3D\_CM*, contain the essential dynamics of a fusion-regime laser-accelerated ablator.

#### BACKGROUND

Radiation transport hydrodynamics codes have many applications in high temperature physics. One relevant example is the LMI problem, with investigations ranging from design of high-gain ICF pellets to the design and diagnosis of near-term laboratory experiments at such facilities as the NRL Nike KrF Laser Facility and the NOVA laser at LLNL. The most dangerous hydrodynamic instability to affect laser ablatively-accelerated targets is the ablative RT instability, which acts during the

target acceleration phase.<sup>30.3</sup> Realistic LMI simulations of the ablative RT instability offer one of the best means of studying RT in relevant regimes, and of learning how to control it to effect the survival of ICF targets.

The equations governing radiation transport hydrodynamics describe several physical processes: hydrodynamic transport, thermal diffusion, laser energy deposition and radiation diffusion. For the LMI simulations of the ablative RT instability, we consider a small region surrounding a small section of the target so that Cartesian geometry is valid. We take the direction of the incident laser beam as the *x*-direction. In the directions normal to the laser, (*y,z*), we employ periodic boundary conditions.

#### SERIAL IMPLEMENTATION

The serial code uses an operator splitting approach to solve the hydrodynamic equations, basically solving each physical process separately and combining the result. The hydrodynamic transport is solved using an operator-split Flux-Corrected-Transport [FCT] algorithm.<sup>30.4</sup> FCT is a high order monotone explicit algorithm well-suited for compressible flows. The laser radiation is treated as a source term in the energy equation. We also assume that the scattering of laser energy normal to the laser direction is small so that the amount of energy deposited in the material at a given location is determined only by the amount of laser energy reaching that location from the *x*-direction.

The thermal diffusion step is discretized implicitly in time and with finite volumes in space. This produces a system of non-linear

equations in which each equation involves the seven nearest neighbors. These equations are solved iteratively. Linearization of the equations produces a block banded matrix equation. The iteration process treats the diagonal and the non-diagonal elements of this matrix associated with the  $x$ -direction discretization implicitly and the other four bands explicitly. As a result the algorithm iteratively updates and inverts a set of tridiagonal matrices.

Finally, a real equation of state for hydrodynamic transport as well as the calculation of opacities are done through a table look-up and logarithmic interpolation.

## CM-5 ARCHITECTURE

The CM-5 is a scalable parallel multi-processor system.<sup>30,5</sup> It can be scaled to 16K processors. The CM-5 at NRL has 256 processing nodes. Each node consists of a SPARC processor and four optional vector units. The CM-5 at NRL is equipped with the vector units. A CM-5 nodes may be divided into several partitions. The NRL CM-5 currently runs with a single 256-node partition. The peak speed of a processing node with vector units is 128 MFLOPS for multiply-adds. The NRL CM-5 also has 64 Mbytes of memory per processing node. The CM-5 supports both SIMD and MIMD programming models. However, effective use of the vector units on the CM-5 is most easily accomplished within the SIMD programming model. The CM-5 supports the SIMD programming model with the data parallel language CM\_FORTTRAN. CM\_FORTTRAN implements data parallelism through the FORTRAN-90 array syntax.

The CM-5 has two internal communication networks.<sup>30,6</sup> The control network supports operations that require global communications. The data network is used for node-to-node communication. The CM-5's communications network is in the form of a tree-based structure. Several other communication topologies can be embedded within the CM-5 network. In particular, a toroidal mesh is useful for the structured grid calculations of the *RAD3D* algorithm. Within CM\_FORTTRAN, one specifies the preferred data layout and in effect

the communications network desired through the CMF\$LAYOUT compiler directive.

## PARALLEL IMPLEMENTATION

For an explicit algorithm such as FCT, data parallelism is easily accomplished up to boundary conditions. Periodic boundary conditions are ideal for SIMD computing since the equations at each point look the same and the toroidal mesh communications network for the CM-5 makes the exchange of neighbor data uniform across processors. Only the  $x$ -direction requires special processing for the boundary conditions. Hence, the transport phase of the calculation will benefit from a data layout that places all of the  $x$ -direction within processor and the  $y,z$ -directions across processors. This can be accomplished within CM\_FORTTRAN using the CMF\$LAYOUT directive, specifying that each 3d array be (:SERIAL, :NEWS, :NEWS), where the :SERIAL axis is associated with the  $x$ -direction. In order to make efficient use of a 256-node partition, we must also have adequate resolution in the (:NEWS, :NEWS) direction. A typical ablative RT LMI calculation uses a 128  $\times$  128 grid in the  $(y,z)$  directions, thus placing one  $x$ -direction pencil in each vector unit of a 256-node partition. Each vector unit then operates on vectors which are the length of the :SERIAL direction. Finally, a standard split scheme FCT code algorithm<sup>30,7</sup> integrates one pencil at a time, and thus uses only one-dimensional arrays for scratch storage. In order to utilize the SIMD nature of the algorithm and because of the large memory on the CM-5, these arrays were promoted to three dimensions.

The laser energy deposition also benefits from this pencil layout of data. Since we assume no transverse scattering, all data dependencies in the algorithm involve multiply-scan operations along the  $x$ -direction, while depositing energy at each location. By placing  $x$ -direction pencils within processor, each pencil is processed in parallel. The multiply-scan operations terminate at the surface of the target, where energy is deposited and a reflected multiply-scan operation begins. Within this model the surface of the target is denoted by a  $x$ -position function of the transverse coordinates. Location of this

position is done with a search down the  $x$ -pencils until the appropriate density change is encountered. Again the (:SERIAL, :NEWS, :NEWS) layout allows this search to be conducted in parallel.

The iteration process in the thermal diffusion step also can be solved in parallel. Since the tridiagonal matrices involved in this step only couple data in the serial  $x$ -direction, all the data for inverting the tridiagonal lies within processor. Furthermore each tridiagonal is the same length, hence solving this set of tridiagonals can proceed in a SIMD fashion. The only communication needed in this step is for the explicit update of the coefficients and the right-hand-sides of the tridiagonal system.

Table look-up can be a difficulty for distributed memory computers. Our equation of state table consist of a few thousand entries, while the opacity tables involve a few hundred entries per frequency band. The memory capacity of each processor on the CM-5 is such that we can store a copy of each table on each processing node (SPARC plus four vector units). The four vector units on each processing node use the same table. The CM-5 software libraries include routines for building and accessing these duplicate tables in a SIMD fashion.

## DISCUSSION

We have recently adapted a running Cray code, *RAD3D*,<sup>30,8</sup> for efficient simulation on a variety of SIMD parallel platforms, among them the NRL CM-200 and NRL CM-5. *RAD3D\_CM* is essentially a new simulation code. When running on the CM-5 *RAD3D\_CM* exhibits more than a seventy-fold increase in speed over its serial XMP-running predecessor *RAD3D*. Such a significant speed-up, combined with the CM-5 attributes of massive amounts of memory and the ability to handle table look-ups of opacity and equation of state databases, is enabling us to begin to simulate a wide range of 3d multimode problems that have hitherto been impossible to address. With this code we are performing 3d numerical calculations which investigate in the realistic multimode regime the effects of RT perturbation shape. Our results are

directly applicable to experiment on the NRL Nike prototype ICF acceleration-phase experiments.

(i) *RAD3D\_CM* is a compressible hydrodynamics code which contains the following effects relevant for the simulation high-temperature plasmas such as ICF-regime RT unstable laser targets: classical Spitzer thermal conduction; real (table look-up) equation-of-state with either separate or identical electron and ion temperatures; multigroup variable Eddington radiation transport; and, inverse bremsstrahlung deposition of the incident laser beam. Our code is the only 3d simulation code extant which includes these effects, and it provides us with a unique and powerful tool for our research into high temperature plasmas in which the effects of radiation transport are important, such as the control of the ablative RT instability.

(ii) We are currently using *RAD3D\_CM* to simulate the evolution of CH ablator targets, accelerated with prototype Nike ICF driver conditions. Particularly, as discussed in Section 31, we address the question: Does an initial three-dimensional RT perturbation directly determine target survival or do multimode nonlinear effects come to dominate on a timescale shorter than would be expected from single-mode simulations<sup>30,9</sup> and 2nd-order multimode theory?<sup>30,10</sup>

## SUMMARY

The code *RAD3D\_CM* is the first parallel 3d LMI radiation transport hydrodynamics code. This code allows for accurate and efficient investigation of high temperature hydrodynamics in which effects of radiation transport are important. *RAD3D\_CM* has been tested on a variety of low Z planar LMI problems with conditions appropriate to Nike. The calculations performed with *RAD3D\_CM* should be generally useful in validating radiation transport models and one- and two-dimensional hydrocode predictions.

## ACKNOWLEDGEMENT

This work was performed in collaboration with Jill Dahlburg and John Gardner, both of

the Laboratory for Computational Physics and Fluid Dynamics of the Naval Research Laboratory.

## REFERENCES

30.1 D. E. Fyfe, J. P. Dahlburg, & J. H. Gardner, 23rd Anomalous Absorption Conference, Wintergreen, VA (June, 1993).

30.2 J. P. Dahlburg, J. H. Gardner, & D. E. Fyfe, 23rd Anomalous Absorption Conference, Wintergreen, VA (June, 1993).

30.3 D. H. Sharp, *Physica* **12D**, 3, (1984).

30.4 J. Boris and D. Book, *J. Comp. Phys.* **11**, 38, (1973).

30.5 Z. Bozkus, S. Ranka, and G. Fox, *IEEE proceedings*, (1992).

30.6 R. Ponnusamy, A. Choudhary, and G. Fox, *IEEE proceedings*, (1992).

30.7 J. Boris, *NRL Memorandum Report* 3237, (1976).

30.8 J. P. Dahlburg, & J. H. Gardner, *Bull. Am. Phys. Soc.* **37**, 1471, (1992).

30.9 J. P. Dahlburg, J. H. Gardner, S.W.Haan, & G. D. Doolen, *Phys. Fluids B*, **5**, 571 (1993).

30.10 S. W. Haan, *Phys. Fluids B*, **3**, 2349 (1991).

## Section 31

### THREE-DIMENSIONAL MULTIMODE RESULTS

Jill P. Dahlburg

*Laboratory for Computational Physics and Fluid Dynamics  
Naval Research Laboratory  
Washington, DC*

The three-dimensional multimode simulation work is motivated by the idea that no real surface has a finish that can be represented by decomposition into a unidirectional Fourier series. Physical surfaces have imperfections that range from small round bumps to long striations, with varying amplitudes and locations. In the inertial confinement fusion [ICF] problem, pellet surface finishes will undoubtedly be as complex as the ones we see regularly. Pellet surface imperfections, as well as variations in the incident laser intensity, will act as perturbation seeds for the Rayleigh-Taylor [RT] instability.<sup>31.1</sup> They will consequently be determining factors in the success of ICF.

The single mode, ablative RT instability has been studied for many years. The range of wavenumbers generally considered in the single mode studies are those on the order of the initial target thickness. For most high-gain pellet designs, modes much shorter than the ablator thickness (wavelength =  $\lambda < 15 \mu\text{m}$ ) are stabilized by density gradients. Modes much longer than the ablator thickness ( $\lambda > 150 \mu\text{m}$ ) tend to buckle the shell but in general will not grow large enough during the pellet acceleration phase to destroy the pellet during that phase. Modes on the order of the shell thickness ( $25 \mu\text{m} \leq \lambda \leq 125 \mu\text{m}$ ) are considered to be the most dangerous in terms of the ablative RT instability. The ablative stabilization of the linear growth of single Fourier mode perturbations in this range has been well-characterized.<sup>31.2</sup> Extending the two-dimensional [2d] single mode work to realistic surface finishes in three dimensions [3d] is important for a number of reasons.

First, we have found by previous simulation that the shape of a Rayleigh-Taylor perturbation is significant in the early nonlinear development of the instability.<sup>31.3</sup> The simulation geometry we used for the single-mode, 3d shape calculations, and the one we are using in the current multimode study, is shown in Fig. 31.1. Results from the single-mode study are synopsized in Fig. 31.2, a plot of the time dependence of the minimum target mass ( $\rho R \equiv \int_{x_{\min}}^{x(\rho_c)} \rho(x, y, z) dx$ , where  $\rho$  is the mass density;  $x_{\min}$  is a point far behind the target; and,  $x(\rho_c)$  is the location of the critical surface to the laser side of the target) for the various perturbation shapes imposed. This plot is accompanied by surface plots of target solid density, at the moderately late nonlinear time of 3.25 nsec. The only difference among the perturbed simulations is the initial density perturbation shape. All one-dimensional [1d] parameters of the runs are identical, as well as the initial perturbation amplitudes and the

perturbation wavenumber  $k$  (for  $k = \sqrt{k_y^2 + k_z^2} = 2\pi/\lambda$  with  $\lambda$  the perturbation wavelength). The RT bubbles—the rising, hotter, fluid that penetrates the finite-thickness, denser and colder target—seem to be the key to the differences among the minimum values of  $\rho R$ . The more spherical the bubble, the faster it burns through the target.

Second, there is the question: how do many modes of neighboring wavelengths in the ‘most dangerous’ wavelength range interact under conditions relevant to ICF? Two-dimensional multimode RT theory and simulation results<sup>31.4</sup> suggest that there will be insufficient time for

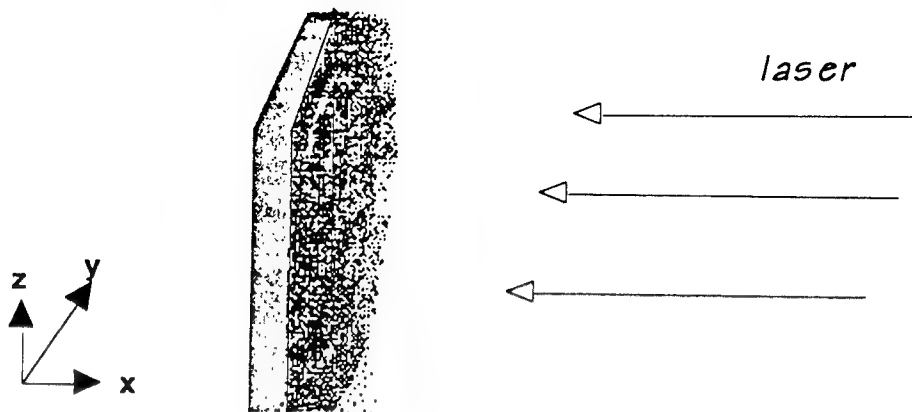
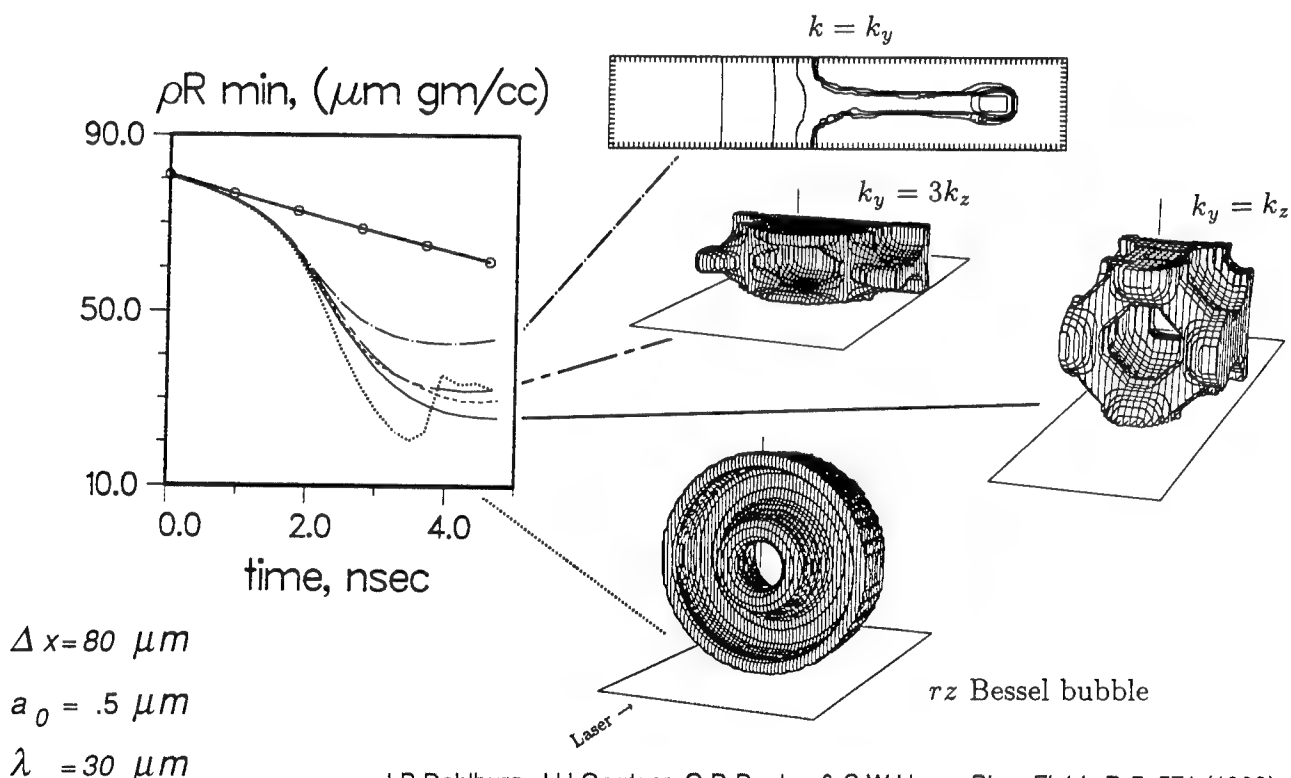
Fig. 31.1 — The cartesian  $x, y, z$  geometry of the three-dimensional simulations.

Fig. 31.2 — Synopsized results from four perturbed calculations, in which it is apparent that the more spherical the perturbation bubble, the faster a finite-thickness target is burned through. The fifth curve, marked with open circles, is the target mass ( $\rho R$ ) time history from the comparable unperturbed run. In all perturbed cases, only the shape of the imposed single mode perturbation is varied. The surface plots are CH solid density, at time = 3.25 nsec.

mode coupling to dominate multimode RT perturbations on a target that is optimized for laser fusion. In light of our previous single-mode results (Fig. 31.2, *e.g.*), the implication of this conjecture is: the subset of RT unstable modes (*a*) that evolve to those with more spherical bubbles (*b*) that are of the highest wavenumber not subject to strong density gradient stabilization, and, (*c*) which are present from very early times, are likely to be most dangerous to the target survival. However, another scenario is also possible. Results from nonablative turbulent mixing simulations in 2d and in 3d show that the mixing region grows faster in 3d than in 2d.<sup>31.5</sup> If the non-ablative mixing result holds in the presence of ablation, then it is possible that the transition to the time when the ablative RT perturbation forgets its origins may occur at lower overall amplitudes in 3d than in 2d. If the first conjecture is correct, then individual small spherical bubbles in the initial perturbation seed will dominate at late times. Otherwise, the target will deform in ways that cannot be determined from the initial perturbation by means other than full 3d nonlinear simulation. The goal of the present set of simulations is to determine which of the two scenarios is more likely.

For this investigation, it is necessary to use a highly parallelized simulation code on a high-performance computing machine; we use *RAD3D\_CM*<sup>31.6</sup> on the NRL CM-5, as described in Section 30. The 3d single mode simulations were run on a Cray-XMP with the Cray version *RAD3D* on a mesh that was  $20 \times 20$  points in *y* and *z*, the directions transverse to the laser, and much longer (200 - 240 points) in *x*, the laser direction. In order to resolve even a modest range of perturbation wavelengths on the order of the target thickness, the mesh has to be at least six times bigger in *y* and *z*. We use  $220 \times 128 \times 128$  point *x,y,z* meshes for the current multimode study, with  $y_{max} = z_{max} = 128 \mu\text{m}$ . A non-radiative, ideal gas calculation with this mesh takes about sixty hours of NRL CM-5 time; the Cray-XMP code would have taken an impossible 70 times longer for a comparable run! This mesh precludes any effect from wavelengths much shorter than or much longer than the target thickness. Both of the omitted length scales can be relevant in the nonlinear

regime. Wavelengths shorter than  $15 \mu\text{m}$  can help to stabilize the longer wavelengths,<sup>31.7</sup> and wavelengths longer than  $150 \mu\text{m}$  can be critical during pellet implosion. It will be very interesting to see how the moderate wavelength perturbations feed into both those scales—provided we have a target that survives the first few nanoseconds of evolution. We expect to address these issues with a radiation-stabilized ablator in future studies.

We consider two *RAD3D\_CM* calculations for this study. Spitzer-Härm thermal conduction and inverse bremsstrahlung laser deposition of  $0.249 \mu\text{m}$  (KrF) laser light are included, although we ran the simulations using the ideal gas equation of state and no radiation transport. In both calculations, plastic targets in hydrodynamic near-steady state<sup>31.3</sup> accelerating at  $4 \times 10^{15} \text{ cm/sec}^2$  are perturbed with the same random amplitude density perturbation. The perturbation is imposed randomly from  $k_y/(2\pi/128 \mu\text{m}) = 1, \dots, 6$  and  $k_z/(2\pi/128 \mu\text{m}) = 1, \dots, 6$ . A number of  $k_y, k_z$  pairs are not perturbed, so that mode coupling theories can be tested. The target perturbation is constrained by two things: spectrally, it is flat through  $k^2 = 8$  and then falls off with a  $k^{-2}$  power law to  $k_{max}^2 = 72$ ; and, the subsequent amplitudes are scaled so that the initial rms density variation of the perturbation is  $0.1 \mu\text{m g/cc}$ . The first target, the ‘thinner target,’ is  $67 \mu\text{m g/cc}$  of CH when the perturbation is imposed; this target is accelerated by a KrF laser with intensity  $2 \times 10^{14} \text{ W/cm}^2$ . The second, ‘thicker target,’ is  $130 \mu\text{m g/cc}$  of CH, and it is accelerated by a KrF laser with intensity  $4.5 \times 10^{14} \text{ W/cm}^2$ .

Since we are most interested in the effects of the RT perturbations on the target bulk, our main diagnostic is the *x*-integrated  $\rho R(y,z)$ . In Fig. 31.3 are plots of  $\rho R(y,z)$  at three times in the thinner target evolution. By 3.5 nsec (Fig. 31.3c), the target has evolved into a state with many nearly spherical bubbles rising in a ‘honeycomb’<sup>31.1</sup> of narrow, falling spikes. The word ‘honeycomb’ is apt—the preferred nonlinear state seems to be one in which the bubbles tile the target *y,z* plane as fully as possible, with narrow, elongated surrounding spikes. In the  $\rho R$  plot of Fig. 31.3c, bubbles of polygonal cross section with diameters that are about 1/6 of the

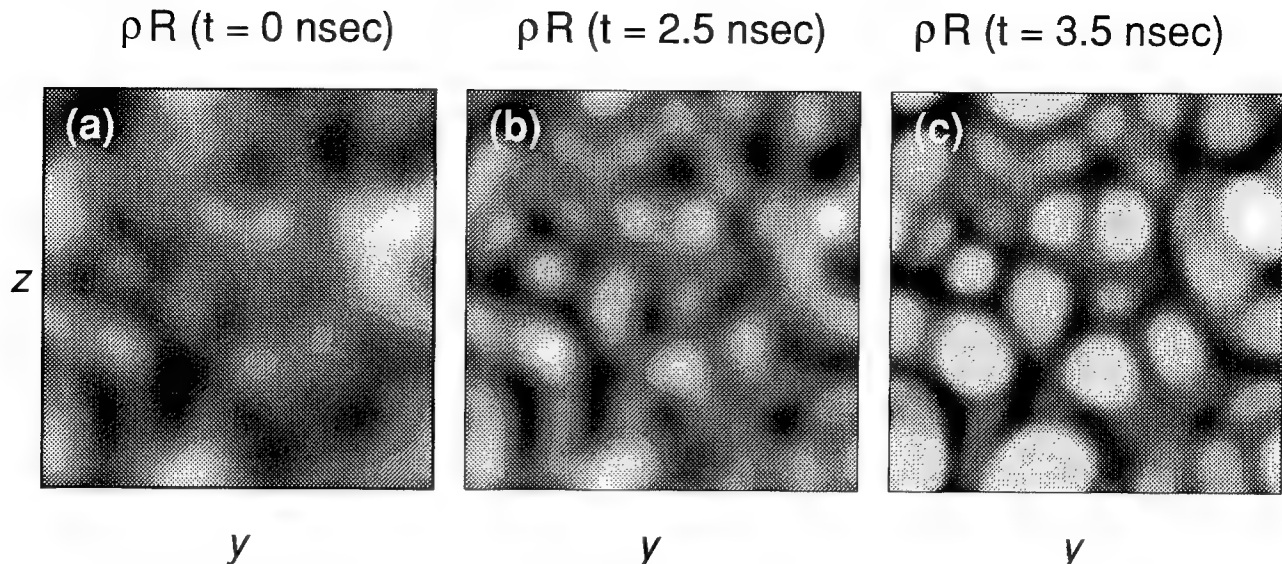


Fig. 31.3 — The spatial integral of the target mass for the thinner target case ( $\rho R = \int_{x_{\min}}^{x(\rho)} \rho(x, y, z) dx$ ), integrated through the target in the direction of the incident laser: (a) initially, showing the imposed perturbation; (b) after 2.5 nsec of evolution. Since the evolution is still nearly linear, the smaller scale structures are growing faster than the larger scales and are most visible to the eye; and, (c) after 3.5 nsec of hydrodynamic evolution, displaying the expected<sup>31.1,31.3</sup> late-time (nonlinear) state of rising spherical bubbles in a honeycomb of narrow, falling spikes. In these plots, darkest shades of greyscale indicate regions of greatest  $\rho R$ .

full 128  $\mu\text{m}$  length in  $y$  or  $z$  dominate at nonlinear times, in full agreement with our previous, less-resolved multimode results.<sup>31.8</sup> The average diameter of the dominant bubbles is the shortest wavelength seeded by the initial random perturbation; it is also the approximate in-flight thickness of the comparable 1d target.

The evolution of the thicker target is similar to that of the thinner target as plotted in Fig. 31.3, through 3.5 nsec. By 4 nsec, however, the thinner target has ‘burned through’ (target density at the minimum  $\rho R$  is about 0.1 g/cc, with a temperature greater than 50 eV), while on the thicker target the perturbations still have ample unperturbed target mass to grow into; see Fig. 31.4. A plot of the thicker target  $\rho R$  at 4.7 nsec (Fig. 31.5) demonstrates nonlinear evolution on the thicker target. Compare Fig. 31.5 with Fig. 31.4b; ‘bubble merger,’ the transfer of RT perturbation excitation to longer length scales at later times, is evident. In the thinner target case the dominant bubbles were polygons on the order of the in-flight target thickness when the problem ‘was over,’ *i.e.*, when the target burned through. Since there is more target mass in the thicker target case, there is time for the

dominant RT perturbation excitation to transfer from polygons of that order to those of lower wavenumbers. This transfer takes two routes: (a) the polygonal bubbles that were dominant at 3.5 nsec are nonlinearly merging; and (b) the linearly slower growing, initially-seeded bubbles of larger diameter are independently getting bigger. The process is reminiscent of an inverse cascade in two-dimensional hydrodynamic turbulence.<sup>31.9</sup>

It is interesting to look at the spectral properties of the simulations. We consider the thinner target calculation through 4 nsec. Figure 31.6 shows the Fourier mass density spectra ( $\log_{10}[\rho R(k)]$ ) plotted as a function of wavenumber  $k$  at four times. At 1 nsec the spectrum looks very similar to the initial condition. By 2 nsec, the excitations are growing overall, with some excitation at the smaller scales. If RT growth rates are measured at this time, the initially perturbed modes are growing approximately as expected from single-mode, linear-regime simulations<sup>31.2</sup> and the modes arising from mode-coupling are growing with rates that are consistent with Haan’s second-order theory.<sup>31.4</sup> By 4 nsec the spectrum has evolved into

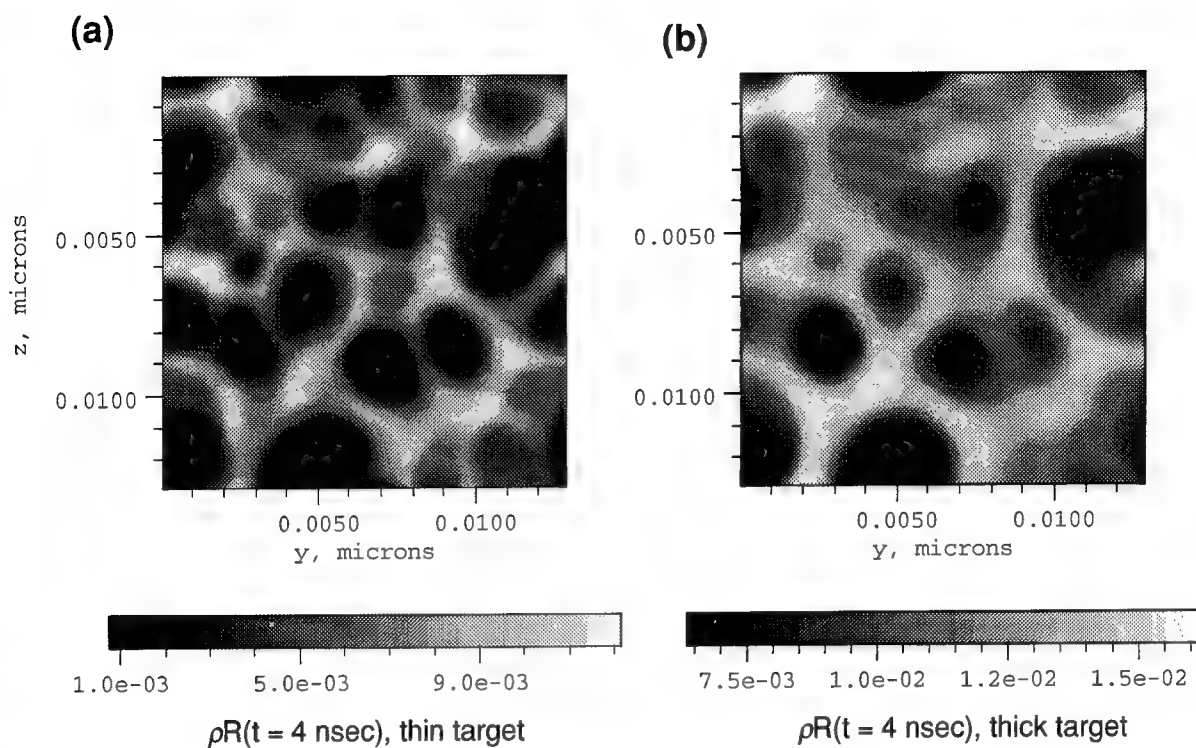


Fig. 31.4 — Comparison of  $\rho R$  between the thinner (a) and thicker (b) targets, at 4 nsec when the thinner target has burned through. In these plots, darkest shades of greyscale indicate regions of least  $\rho R$ .

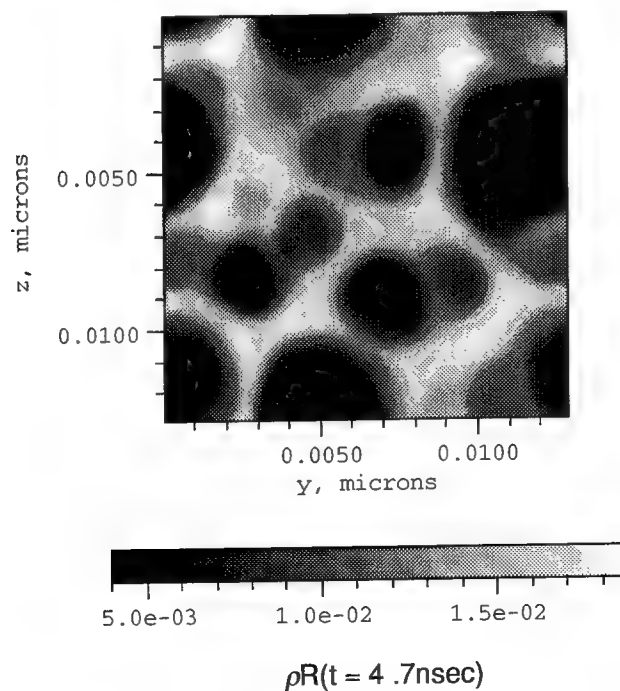


Fig. 31.5 — Thicker target  $\rho R$  at 4.7 nsec. Compare with Fig. 31.4b to see 'bubble merger.' In this plot, darkest shades of greyscale indicate regions of least  $\rho R$ .

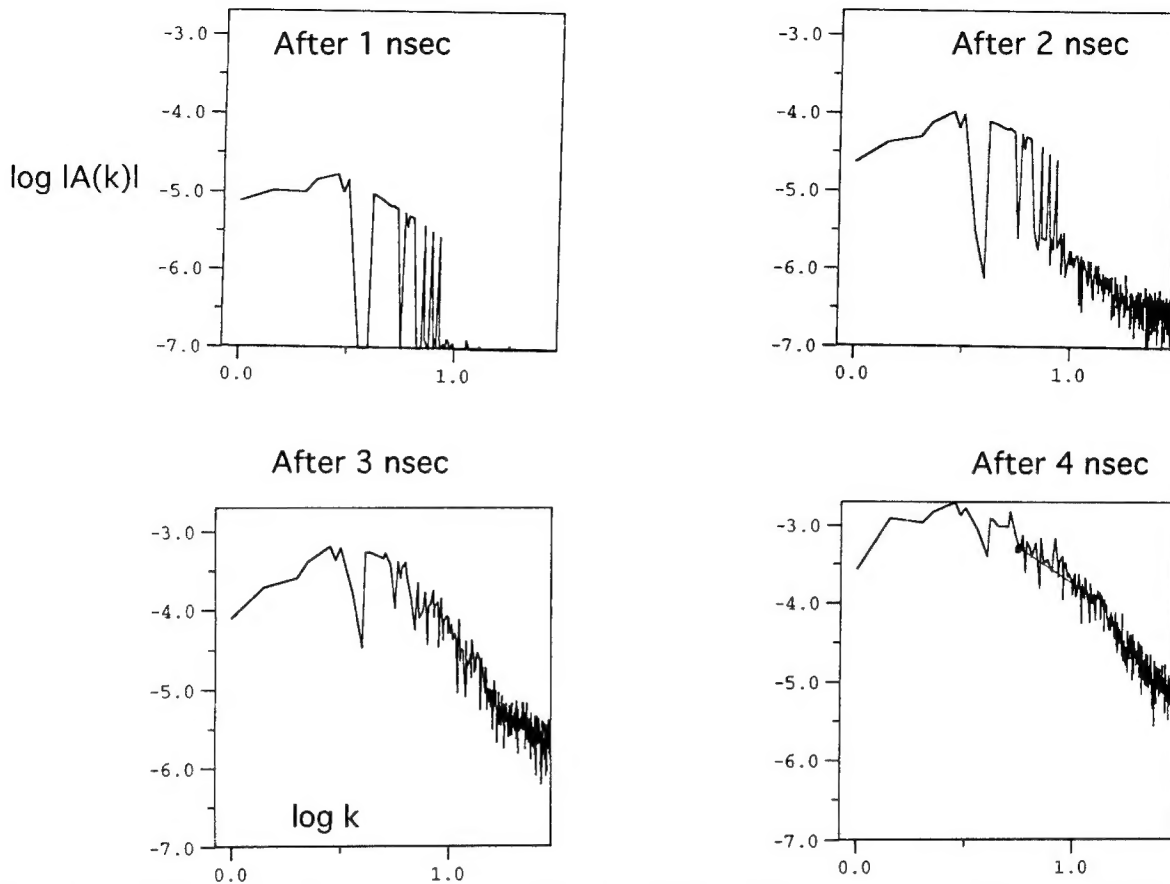


Fig. 31.6 — Fourier density spectra,  $\log_{10}[\rho R(k)]$ , plotted as a function of wavenumber  $k$  at four times in the thinner target evolution. The line traced on the fourth plot (4 nsec) marks a  $k^{-5/3}$  spectrum in the neighborhood of  $k = 10$ .

one that is virtually indistinguishable from a traditional ‘turbulence spectrum,’ with ‘energy-containing’ modes at the low wavenumbers, an ‘inertial range’ at moderate  $k$ , and a spectrum that falls off with a slope steeper than  $k^{-5/3}$  in the high wavenumber ‘dissipation range.’ If we really had ‘turbulence’ in this calculation, then one would expect a significant amount of fluctuation in the spectrum at wavenumbers greater than those in the energy-containing range, on timescales short compared to those over which the longest scales evolve. If we assume that an average ‘turbulent eddy’ is about 1/10th of the box, or  $12.8 \mu\text{m}$ , and that the average velocity of that eddy is about  $5 \times 10^6 \text{ cm/s}$ , then the eddy turnover time—a ballpark estimate of an expected fluctuation timescale—is about 3.9 nsec. In 3.9 nsec, however, the thinner target has burned through. This crude analysis indicates that in the ablative RT problem on ICF-relevant targets there is not enough of a separa-

tion of timescales between the ones which determine the bulk properties of the target evolution, and the fluctuation timescales, for turbulence to be effective even in 3d. This is another way of saying what we observed in Fig. 31.3c above, and posed as a possible scenario at the beginning of the article. For targets that are relevant to existing high-gain ICF pellet designs, the most dangerous ablative Rayleigh-Taylor modes have the following characteristics: they develop approximately spherical bubbles; their wavenumbers are comparable to the target in-flight thickness; and, they are present from very early times.

#### ACKNOWLEDGEMENT

This article reports work that is a continuing effort. It is a pleasure to acknowledge my collaborators: John H. Gardner, David E. Fyfe, Steve W. Haan, and Gary D. Doolen.

## REFERENCES

31.1 D. H. Sharp, *Physica* **12D**, 3, (1984).

31.2 J. H. Gardner, S. E. Bodner, & J. P. Dahlburg, *Phys. Fluids B*, **3**, 1070-10-74, (1991); and references within.

31.3 J. P. Dahlburg, J. H. Gardner, S. W. Haan, & G. D. Doolen, *Phys. Fluids B*, **5**, 571 (1993).

31.4 S. W. Haan, *Phys. Fluids B*, **3**, 2349 (1991).

31.5 D. L. Youngs, *Phys. Fluids A*, **3**, 1312 (1991).

31.6 D. E. Fyfe, J. P. Dahlburg, & J. H. Gardner, 23rd Anomalous Absorption Conference, Wintergreen, VA (1993);

31.7 J. P. Dahlburg, J. H. Gardner, & M. H. Emery, *Bull. Am. Phys. Soc.* **35**, 1969 (1990).

31.8 J. P. Dahlburg, J. H. Gardner, & G. D. Doolen, 19th Annual Anomalous Absorption Conference, Durango, CO, (1989).

31.9 D. E. Fyfe, D. C. Montgomery, & G. Joyce, *J. Plasma Phys.* **17**, 369 (1977); J. P. Dahlburg, R. B. Dahlburg, J. H. Gardner, & J. M. Picone, *Phys. Fluids A*, **2**, 1481 (1990).

also see Section 30, this issue; J. P. Dahlburg, D. E. Fyfe, J. H. Gardner, S. W. Haan, & G. D. Doolen, in prep., (1994).

# Author Index

## Author Index

Barr, O., 147  
Bodner, S., 3, 7, 9, 15  
Dahlburg, J., 183, 215  
Deniz, A., 71  
Emery, M., 201  
Fyfe, D., 211  
Gardner, J., 65, 165

Giuliani, J., 195  
Guzdar, P., 47  
Hardgrove, J., 135  
Klapisch, M., 189  
Lehecka, T., 61, 131  
Lehmburg, R., 19, 53  
McGeoch, M., 89

Mostovych, A., 33  
Obenschain, S., 57, 69, 155  
Pawley, C., 113  
Pronko, M., 75  
Schmitt, A., 21  
Sethian, J., 123, 177  
Stamper, J., 139